DOCTORAL THESIS

Development of Light-Responsive Co-Crystals and Salts as Photo-Mechanical Materials

Tristan H. Borchers

Supervisors: Christopher J. Barrett, Tomislav Friščić

A thesis submitted to McGill University in partial fulfillment of the requirements of the degree of Doctor of Philosophy

December 2022

Table of Contents

Chapter 2: Cold Photo-Carving of Dye-Volatile Halogen-Bonded Co-Crystals Using Low-Powered Visible light

Statement of Objectives

This thesis aims to investigate how the photo-responsive properties of organic chromophore co-crystals and multi-component salts are affected by volatile or unstable molecules within the crystalline material. More specifically, the photo-mechanical properties of these crystalline materials are studied, including experimental and theoretical results suggesting a mechanism of controlled photo-decomposition occurring in the crystalline materials on irradiation. We investigate a total of seven organic co-crystals and study how different volatile components and differing chromophores affect the photo-mechanical response of the crystalline materials. Additionally, two thermally unstable salt complexes are studied to investigate the photo-responsive nature of hypohalite ions in the solid state.

Abstract

Development of Light-Responsive Co-Crystals and Salts as Photo-Mechanical Materials

My Thesis research makes contributions in the areas of crystal engineering and photo-responsive materials. It is based on co-crystals containing azobenzene dyes (Chapters 2–4) or mixed inorganic salts (Chapter 5). The Thesis investigates a new photo-responsive phenomena coined 'cold photo-carving' (CPC), a response seen in co-crystals containing a photo-responsive dye and a volatile co-crystal former (coformer). Upon irradiation with low intensity visible light the crystals undergo selective disassembly in which the volatile coformer evaporates out of the co-crystal and the azobenzene recrystallizes at the edge of the irradiated area, resulting in a precise hole or other controlled pattern in the crystal coincident with the laser irradiation. This unique response was previously unreported in prior literature of either crystalline azobenzene or volatile co-crystals. Chapter 2 reports the initial discovery of CPC, provides insight into the mechanism, focusing on a pair of *trans*-azobenzene co-crystals. The chapter outlines a proposed mechanism of disassembly through detailed analysis using powder X-ray diffraction, and Raman spectroscopy. Chapter 3 builds on the foundations laid out in Chapter 2, focusing on the subsequent *cis*-azobenzene co-crystals that undergo different responses depending on the intensity of the laser light: photo-chromic, photo-mechanical, or photo-carving. The various photo-responses are rationalized throughout the chapter with periodic density functional theory (DFT), used to calculate the stability of the co-crystals studied in Chapters 2 and 3. Additionally, there was found to be a disconnect between thermal studies and photo-responsive studies, in which one proceeds *via* isomerization prior to desolvation (photo) and the other proceeds by desolvation followed by isomerization

(thermal). Such findings further prove that CPC is a photo-specific effect. Chapter 4 introduces a new form of photo-response in a co-crystal that contains a second chromophore class acting as the volatile conformer, where the co-crystal display two different wavelength dependent responses to light. When using green/blue visible light the co-crystal will undergo CPC, however, when irradiated with IR light, epitaxial growth of yellow/orange crystals is visible from the location of irradiation, enabling a material that can selectively produce two separate responses, triggered by changing the wavelength of the excitation laser. Chapter 5 outlines the first example of CPC used on a non-organic system, and without an azobenzene dye. Hypohalites (sodium hypobromite and sodium hypochlorite) were shown to oxidize upon irradiation, with hypobromite or hypochlorite converting to chlorite and bromite. The conversion was specific to the solid state, a finding that was hypothesized as due to the near linear alignment of hypohalite anions in their respective crystal structures. In summary this Thesis introduces CPC as new functional photo-response achievable by crystal engineering, with 4 distinct studies outlining the mechanism, the wavelength dependence, and the laser intensity dependence, using both experimental and theoretical methods to give insight into the process.

Abrégé

Development of Light-Responsive Co-Crystals and Salts as Photo-Mechanical Materials

Mes recherches de thèse apportent des contributions dans les domaines de l'ingénierie des cristaux et des matériaux photo-réactifs. Elle est basée sur des co-cristaux contenant des colourants azobenzènes (chapitres 2–4) ou des sels inorganiques mixtes (Chapitre 5). La Thèse étudie un nouveau phénomène de photo-réaction appelé photo-gravure à froid, une réponse observée dans les co-cristaux contenant un colourant photorécepteur et un agent de formation de co-cristaux volatile (coformateur). Lors de l'irradiation par une lumière visible de faible intensité, les cristaux subissent un désassemblage sélectif au cours duquel le coformateur volatil s'évapore du co-cristal et l'azobenzène recristallise au bord de la zone irradiée, ce qui donne un trou précis ou un autre motif contrôlé dans le cristal coïncidant avec l'irradiation laser. Cette réponse unique n'a jamais été rapportée dans la littérature antérieure, que ce soit pour l'azobenzène cristallin ou les co-cristaux volatils. Le Chapitre 2 donne un aperçu et rapporte la découverte initiale de la photo-gravure à froid, en se concentrant sur une paire de co-cristaux d'azobenzène *trans*. Le chapitre présente une proposition de mécanisme de désassemblage, à travers une analyse détaillée utilisant la diffraction des rayons X sur poudre et la spectroscopie Raman. Le Chapitre 3 s'appuie sur les bases établies dans le Chapitre 2, en se concentrant sur les co-cristaux de *cis*-azobenzène suivants qui subissent différentes réponses en fonction de l'intensité de la lumière laser : photo-chromique, photo-mécanique, ou photo-sculpture. Les différentes photo-réponses sont largement rationalisées tout au long du Chapitre à l'aide de la théorie fonctionnelle de la densité périodique, utilisée pour calculer la stabilité des co-cristaux étudiés aux Chapitres 2 et 3. En outre, on a constaté une

déconnexion entre les études thermiques et les études photo-réactives, dans lesquelles l'une procède par isomérisation avant désolvatation (photo) et l'autre procède par désolvatation suivie d'isomérisation (thermique). Ces résultats prouvent une fois de plus que la photogravure à froid est un effet photo-spécifique. Le Chapitre 4 présente une nouvelle forme de photo-réponse dans un co-cristal qui contient un second chromophore agissant en tant que conformateur volatil ; où le co-cristal présente deux réponses différentes à la lumière en fonction de la longueur d'onde. Le co-cristal présente deux réponses différentes à la lumière en fonction de la longueur d'onde. Lorsqu'il est exposé à la lumière visible verte/bleue, le co-cristal subit une photogravure à froid, mais lorsqu'il est exposé à la lumière infrarouge, la croissance épitaxiale du cristal jaune/orange est visible à l'endroit de l'irradiation, ce qui permet d'obtenir un matériau capable de produire sélectivement deux réponses distinctes, déclenchées par le changement de la longueur d'onde du laser d'excitation. Le Chapitre 5 présente le premier exemple de photo-gravure à froid utilisé sur un système non organique, et sans colourant azobenzène. Il a été démontré que les hypohalites (hypobromite de sodium et hypochlorite de sodium) s'oxydent sous l'effet de l'irradiation, l'hypobromite ou l'hypochlorite se transformant en chlorite et en bromite. La conversion était spécifique à l'état solide, une découverte qui a été supposée être due à l'alignement quasi linéaire des anions hypohalites dans leurs structures cristallines respectives. En résumé, cette thèse présente la photo-gravure à froid comme une nouvelle photo-réponse fonctionnelle réalisable par l'ingénierie cristalline, avec 4 études distinctes décrivant le mécanisme, la dépendance de la longueur d'onde et de l'intensité du laser, en utilisant des méthodes expérimentales et théoriques pour donner un aperçu du processus.

Acknowledgements

There are many people who have contributed to my growth as a researcher and as an individual over these last six years of my life. If it weren't for the friendships and the pleasant working environment they created, this thesis would not have of been possible. For that, I am extremely grateful to have been surrounded by such wonderful people.

First and foremost, the largest thanks go to my two amazing PhD supervisors, Prof. Christopher J. Barrett and Prof. Tomislav Friščić. Without their support and advice this thesis would not have been possible. They created an environment in which I could explore ideas and follow my curiosities with freedom to choose what I studied. They always provided a helping hand while simultaneously avoiding to add the pressure of deadlines. I could not have asked for two better supervisors, and for that I will always be extremely grateful.

Thanks also go to the other members of the Barrett and Friščić groups, both past and present. Thank you for your continuous friendship during this time and playing an integral role in creating the research environment where grad-students, under-grads, and postdocs bounce ideas off each other and help during difficult times. Thanks go out to Friščić group members: Yong, Joe, Dylan, Cameron, Linda, Lori, Luzia, Sandra, Farshid, Louis, Galen, Thomas, Mike, Blaine, Igor, and Pat. Thanks also go out to Barrett group members: Jan, Mikel, Victoria, Tom, Alex, Kayrel, Shayne, and Mikhail. A special thank you goes out to Filip, he played the role as a 3rd supervisor at times, introducing me to the world of crystallography and acting as a friend throughout my Ph.D. Additional thanks go out to my good friend and colleague Jorgidas; our Ph.D.'s will forever be linked through our collaborations. I couldn't have asked for a better lad to work with.

I would like to also thank the friendships I made along the way: Alex, Brandon, and Aidan, the Preston boys! I will forever cherish our weekly pints at Benelux, talking about science, football and politics. A special thank you goes to Big Red, who not only became a great friend, but will also be one of my groomsmen next September.

Finally, I would like to thank my family for their continued support and belief in me. Dad, Mom, Sophia, and Sammie, thank you for always being there. I could not have done any of this without the emotional and financial support of my beautiful and brilliant fiancé, Coralie. I love you so much and I dedicate this thesis to you.

Contributions to Original Knowledge

This thesis contains a number of original scholarly contributions, with Chapters 2–5 published, submitted, or in the process of being submitted to peer-reviewed journals at the time of submission of this Thesis.

Chapter 2 introduces two novel halogen-bonded co-crystals that undergo a previously unreported photo-mechanical phenomenon coined ‘Cold Photo-Carving’ (CPC). The process of CPC was investigated in detail through a variety of analytical methods, including Raman spectroscopy, powder X-ray diffraction (PXRD), scanning electron microscopy (SEM), and the use of a high-speed camera. The analysis from these methods allowed us to propose a mechanism of the controlled photo-decomposition of the co-crystals.

Chapter 3 expands on the CPC studies conducted in Chapter 2, introducing two additional novel halogen-bonded co-crystals that undergo CPC. The co-crystals exhibited a unique intensity-dependent response to visible light, leading to a material that exhibits three distinct photo-responses. In addition to once again investigating the process of CPC experimentally, it was also investigated theoretically, leading to a better understanding of the relationship between halogen-bond strength and the experimental decomposition studies.

Chapter 4 continues investigating the process of CPC with an additional three halogen-bonded co-crystals. The use of a second chromophore within two of the co-crystals produced a material that undergoes two separate photo-responses, dependent on the wavelength of light. Additionally, this Chapter introduces halogen-bonding to π-systems as a new approach to develop materials that will undergo CPC.

Chapter 5 is the first photo-responsive study to date of solid state hypohalites. The process of photo-decomposition of hypohalite ions was studied both experimentally and theoretically. It was shown that the hypobromite ion undergoes a similar process to CPC, in which the crystal can be cut, carved, and engraved.

Contributions of Authors

Chapter 1: Introduction and Literature Review of Photo-Responsive Crystalline Materials

Chapter 1 was researched and written entirely by Tristan H. Borchers, with Prof. Barrett and Prof. Friščić helping with final editing of the text.

Chapter 2: Cold Photo-Carving of Dye-Volatile Halogen-Bonded Co-crystals Using Low-Power Visible Light

Reprinted (adapted) with permission from: Borchers, T. H., Topić, F., Christopherson, J.-C., Bushuyev, O. S., Vainauskas, J., Titi, H. M, Friščić, T., & Barrett, C. J. "Cold photo-carving of halogen-bonded co-crystals of a dye and a volatile co-former using visible light" *Nature Chemistry* **14**, 574–581 (2022).

Project design, synthesis, material preparation, laser experiments, powder X-ray diffraction, and Raman analysis were conducted by Tristan H. Borchers. Dr. Filip Topić performed single crystal X-ray analysis. Jan-Constantine Christopherson and Dr. Oleksandr S. Bushuyev of our Group discovered the initial CPC co-crystal (*trans*-azo)(dioxane), Jorgidas Vainauskas advised on crystallization experiments, Dr. Hatem M. Titi advised on best practices of thermal analysis. The initial manuscript was written by Tristan H. Borchers, with Prof. Barrett and Prof. Friščić helping with final editing and manuscript submission.

Chapter 3: Three-In-One: Dye-Volatile Co-crystals Exhibiting Intensity-Dependent Photo-Chromic, Photo-Mechanical and Photo-Carving Response

Reprinted (adapted) with permission from: Borchers, T. H., Topić F., Arhangelskis, M., Vainauskas, J., Titi, H. M., Bushuyev, O. S., Barrett, C. J., & Friščić., T. "Three-in-one: dye-volatile co-crystals exhibiting intensity-dependent photo-chromic, photo-mechanical and photo-carving response" *ChemRxiv*. (2022), and in preparation for peer-reviewed journal submission.

Project design, synthesis, material preparation, laser experiments, powder X-ray diffraction analysis, Raman analysis, and theoretical calculations were conducted by Tristan H. Borchers. Dr. Filip Topić performed single crystal X-ray analysis. Jorgidas Vainauskas advised on crystallization experiments, Dr, Hatem M. Titi advised on best practices of thermal analysis, Dr. Oleksandr S. Bushuyev advised on photo-mechanical studies. The initial manuscript was written by Tristan H. Borchers, with Prof. Barrett and Prof. Friščić helping with final editing and manuscript submission.

Chapter 4: Multi-Component Crystals with Wavelength Dependent Response to Visible and IR Light

Project design, synthesis, material preparation, laser experiments, *in-situ* powder X-ray diffraction analysis, single crystal X-ray diffraction analysis, and theoretical calculations were conducted by Tristan H. Borchers. Jorgidas Vainauskas finalized the crystallographic information files (CIF). Dr. Hatem M. Titi advised on the best practices on *in situ* powder X-ray diffraction analysis. Initial manuscript was written by Tristan H. Borchers, with Prof. Barrett and Prof. Friščić helping with final editing of the manuscript.

Chapter 5: New Photochemistry of Hypohalites: a Topochemical, Light-Induced Solid State Conversion of Hypohalites (ClO^-, BrO^-) into Halites (ClO_2^-, BrO_2^-)

Project design, laser experiments, bandgap experiments, Raman analysis, and theoretical calculations were conducted by Tristan H. Borchers. Joseph M. Marrett assisted in the synthesis of hypobromite. Dr. Dylan J. Shields assisted in the gas-phase calculations. . Initial manuscript was written by Tristan H. Borchers, with Prof. Barrett and Prof. Friščić helping with final editing of the manuscript.

Chapter 6: Discussion, Summary, and Conclusions

Chapter 6 was written entirely by Tristan H. Borchers, with Prof. Barrett and Prof. Friščić helping with final editing of the text.

List of Figures

List of Tables

List of Abbreviations

ADP: Anisotropic displacement parameters

API: Active pharmaceutical ingredient

Azu: azulene

***cis*-azo:** *cis*-4,4'-diodoperfuluoroazobenzene

Co-crystal: Multi-component crystals

Coformer: Co-crystal former

CPC: Cold photo-carving

DFT: Density functional theory

DPA: Diphenylacetylene

DMAAM: Dimethyl-2(3-(anthracene-9-yl)allylidene)malonate

DSC: Differential scanning calorimetry

DVAAM: 2-(3-(anthracene-9-yl0allylidene)malononitrile

FIB: Focused ion beam

FPS: Frames per second

GC: Gas chromatography

HOMO: Highest occupied molecular orbital

IR: Infrared

LUMO: Lowest unoccupied molecular orbital

MS: Mass spectrometry

Naph: Naphthalene

NIR: Near-infrared

OLED: Organic light emitting diode

PAC: Photo-carving of azo-volatile co-crystals

PAH: Polyaromatic hydrocarbon

PXRD: Powder X-ray diffraction

SEM: Scanning electron microscopy

SCXRD: Single crystal X-ray diffraction

***trans*-azo:** *trans*-4,4'-diodoperfuluoroazobenzene

***trans*-azo I:** *trans*-azo polymorph **I**

***trans*-azo II**: *trans*-azo polymorph **II**

***trans*-iodo-Fazo:** *trans*-4,4'-diodoperfuluoroazobenzene

***trans*-bromo-Fazo:** *trans*-4,4'-dibromoperfuluoroazobenzene

TCQDM: 7,7,8,8-tetracyanooquinodimethane

TFIB: Tetra-fluoro-iodo-benzene

TGA: Thermogravimetric analysis

THF: Tetrahydrofuran

TMCQD: 7,7,8,8-tetrakis(methoxycarbonyl)-quinodimethane

TS: *trans*-stilbene

UV: Ultraviolet

Vis: Visible

XB: Halogen bond

Introduction and Literature Review of Photo-Responsive Crystalline Materials

T. H. Borchers, T. Friščić, and C. J. Barrett**

Department of Chemistry, McGill University, Montreal, QC, Canada

1.1 Abstract

This introduction summarizes the recent advances in the development and understanding of crystalline materials that exhibit unique responses to light, be that optical, mechanical, or solid state photochemical transformations. Special focus is paid to various methods of how to tune solid state optical and photo-responsive properties of molecules in the solid state, including co-crystallization and the use of halogen bonding as a versatile supramolecular interaction for the assembly of structures with interesting properties. Furthermore, this Chapter is more specifically focus on the fundamentals of azobenzene photo-switches in crystal engineering, and how these types of systems have recently been used in the development and discovery of optical and photo-responsive solid state materials. The use of crystal engineering and molecular chromophores allows for physicists, chemists, material scientists and crystal engineers to develop a wide range of new optical and light responsive materials, including luminescence, dichroic, photo-actuating materials, and more.

1.2 Light matter interactions in molecular materials

Controlling the properties and behaviour of matter by light is a highly attractive concept in the advancement of engineering, medicine, and materials science. The majority of materials or biological systems are considered to be inherently non-photo-responsive to visible light,[1] and inducing this type of behaviour necessitates the inclusion of a photo-active unit, such as a molecule, into the system of interest. For example, once organic molecules are identified to exhibit interesting photo-responsive behaviour, the strategies can, in principle, be developed for their inclusion into polymer matrices or biological systems, either through covalent bond formation,[2] assembly *via* intermolecular interactions,[3] or simply by doping into the system.[4] These molecules, referred to as photo-switches,[5] are generally inexpensive[6] to make and have already been used in holographic writing materials,[7] mass transport systems,[8] and photo-mechanical actuators.[9] Photo-switches have also found use in biological systems involved in cavity opening or closing.[10] In materials design, the use of such photo-switches have been shown as promising strategy to control surface properties, *via* on and off cell adhesion,[11] control of tunneling distance in electrodes,[12] and controlling self-assembly and self-organization.[13]

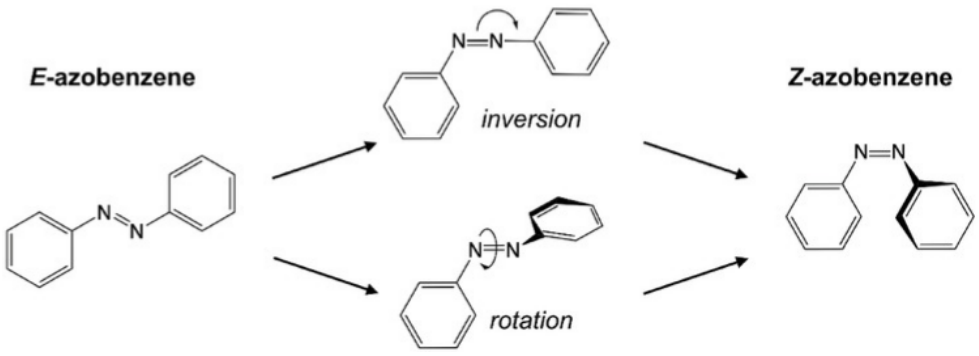

Scheme 1.1. Schematic of *trans*- to *cis*-azobenzene isomerization occurring through potential pathways: rotation or inversion mechanisms (reproduced from reference [14]).

Azobenzenes are a unique class of molecular photo-switches, which exhibit two isomers: a more stable *trans*- (*E*-), and a metastable *cis*- (*Z*-) isomer. Generally, these isomers are known to interconvert upon ultraviolet (UV) irradiation, which causes *trans*→*cis* isomerizations, while visible light irradiation or introduction of thermal energy will cause the reverse *cis*→*trans* isomerization (**Scheme 1.1)**. This class of photo-switchable molecules is easily tunable, as the introduction of substituent groups to the azobenzene backbone will often have a profound effect on the absorbance of the molecule, as well as the excitation wavelength and the rate of thermal relaxation from *cis*→*trans*. Traditionally, azobenzene molecules are divided into three broad classes of derivatives; azobenzenes, amino-azobenzenes, and pseudo-stilbene azobenzenes (**Figure 1.1a)**.[15] The amino-azobenzene system includes an electron-donating group substituted onto the benzene ring, which results in red-shifting of the absorbance and an increase in the relaxation rate of the *cis*-isomer. The pseudo-stilbene type of azobenzenes is considered to be a 'push-pull' system, where one of the benzene rings is substituted with an electron-withdrawing group, while the second one contains an electron-donating substituent. The presence of both electron-withdrawing and -donating groups on the molecules results in further red-shifting of the absorbance and increase in the rate of relaxation relative to the amino-azobenzene systems. The most significant benefit in the development of either the amino- or pseudo-stilbene type of azobenzenes is that a lower frequency light is required to induce isomerization from the *trans*- to the *cis*-isomer, allowing for the use of green/blue visible lasers as opposed to UV lasers in materials science,[16] and biological applications.[17] This lower energy irradiation reduces the potential for damage or destruction of the surrounding environment of the material or tissue. However, the azobenzenes of the amino- and pseudo-stilbene types exhibit a reduced *cis*-isomer lifetime, which results in the lower overall conversion to the *cis*-isomer. This reduction in half-life is a downside,

as it limits the use of such azobenzene derivatives. Nevertheless, altering the substituent groups of the azobenzene allows for control of the photo-response of a material by rational design (examples are shown in **Figure 1.2)**. Azobenzenes have so far been used in a number of systems, including liquid crystals,[18-20] photo-mechanical actuators,[9,18,20-22] mass transport systems,[7,8,23,24] nano-tweezers,[25] photo-switchable nanoparticle aggregation,[26] photo-responsive surfaces,[13,27-29] biological systems,[30,31] and solid state crystalline materials.[32,33]

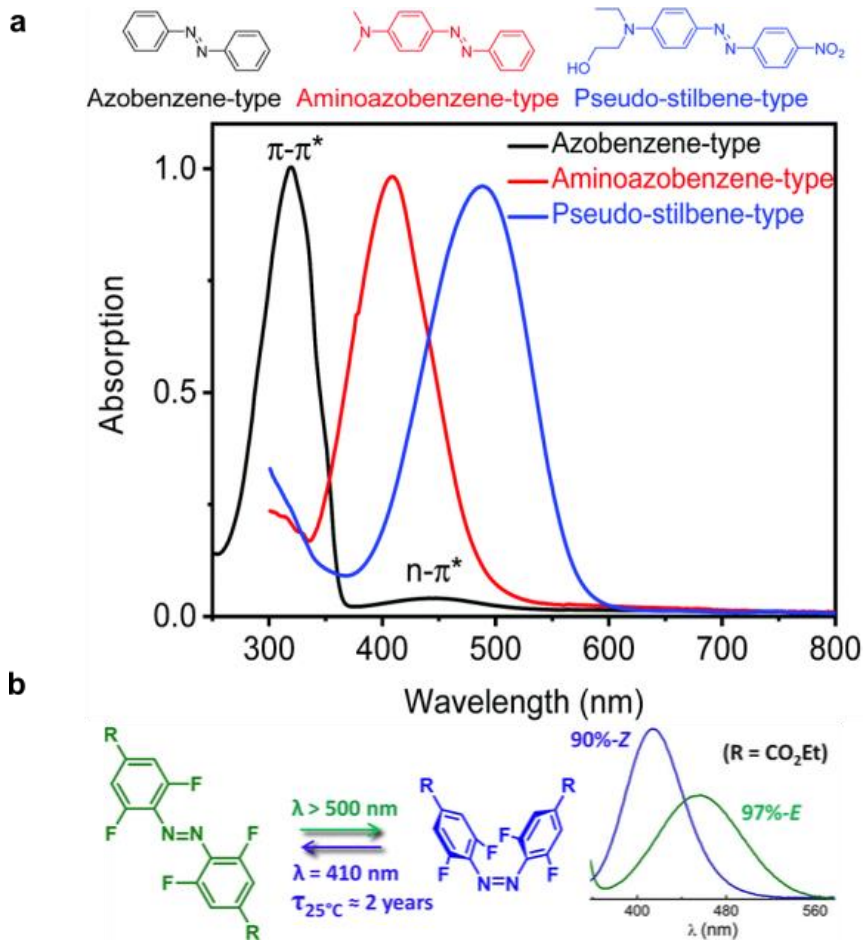

Figure 1.1. Illustration of different classes of azobenzene molecules. a) Typical chemical structures and UV/Vis absorption spectra of the three traditional types of azobenzenes (reproduced from reference [34]). **b)** Chemical structures and n-π* absorbance transitions of *ortho*-fluorine functionalized azobenzenes (reproduced from reference [35]).

Recent advances have now produced a new class of azobenzenes (azos) in which the *ortho*-positions of the benzene rings are fluorinated, which impacts the azobenzene in three distinct ways (**Figure 1.1b)**. First, *ortho*-fluorination leads to the stabilization of the *cis*-isomer, which is unusual and contrary to other substituent effects, and can permit the isolation of *cis*-azobenzenes in the crystalline solid state. Second, fluorination of the aromatic *ortho*-position, red-shifts the wavelength required to induce the $E \rightarrow Z$ isomerization.[35] Lastly, *ortho*-fluorination of the azobenzene core has an effect on the reverse process of $Z \rightarrow E$ photo-isomerization, as it leads to a reduced overlap of the $n \rightarrow \pi^*$ transitions of the *cis* and *trans* isomers. The latter is important, as it allows for quantitative isomerization of the azobenzene in either *Z*- or *E*-direction using visible light. So far, such *ortho*-fluorinated azobenzene molecules have been used in a variety of ways in the fields of biological and material sciences, such as *in vivo* studies,[36] and as photo-actuators,[37] and surface relief gratings,[38] respectively. Fluorination of the benzene rings of the azobenzene core additionally produces an electron-withdrawing moiety, which gives rise to the possibility to use such molecules as halogen-bond donors when appropriately substituted with heavy halogen atoms (I or Br).

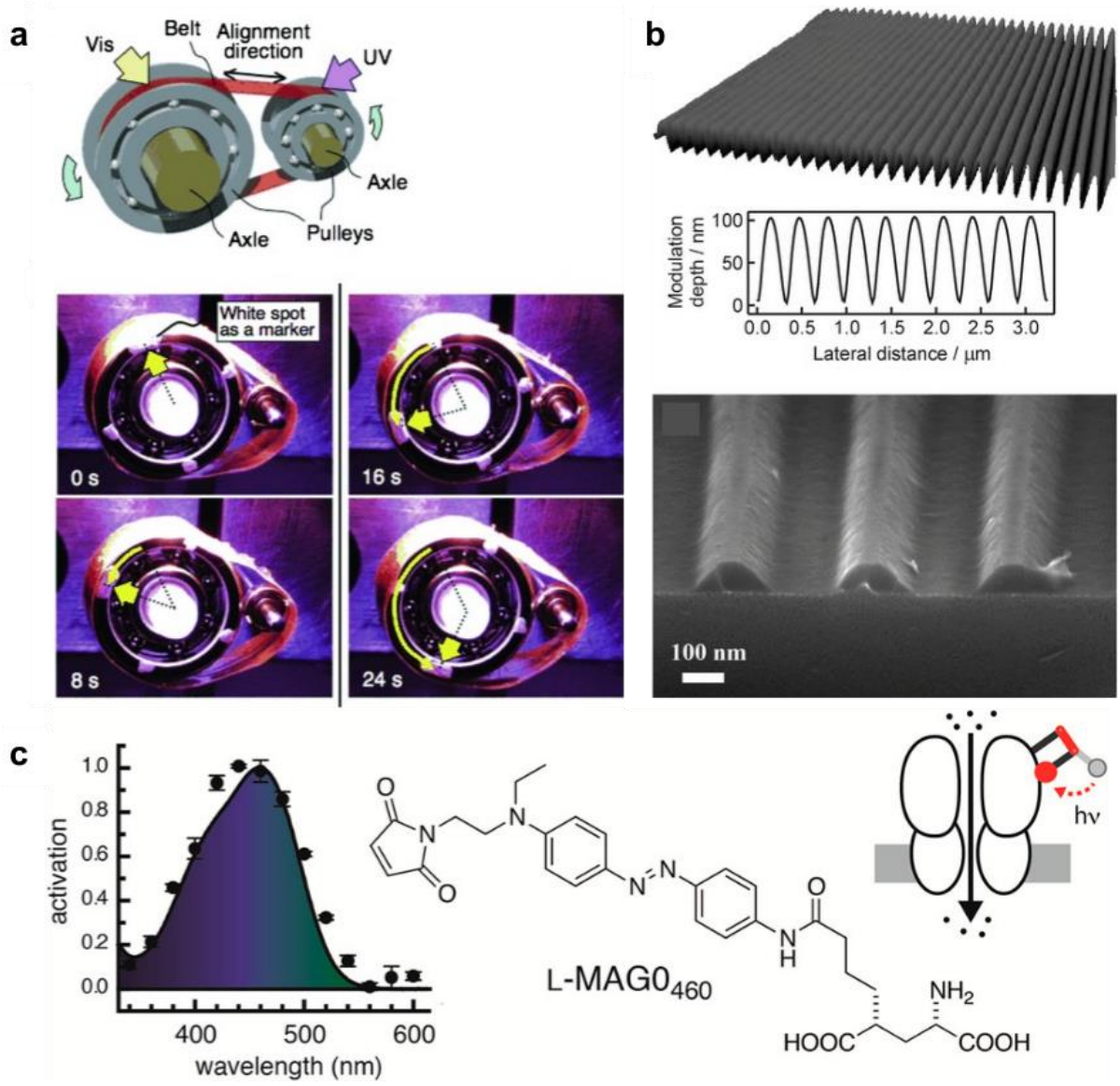

Figure 1.2. Selected advances in materials and biological sciences when incorporating azobenzene molecules. a) A molecular machine built through an azo-polymer in which the system will isomerize from the *trans* to the *cis* form and *vice versa* forming a molecular motor (reproduced from reference [21]). **b)** Surface relief gratings produced on the surface of silicon by using an azo-polymer coating (reproduced from reference [39]). **c)** Photo-chromic blockers of potassium ion channels, produced by a red-shifted absorbing azobenzene dye (reproduced from reference [10]).

1.3 Crystal engineering

The control of solid state materials with desired physical or chemical properties is the essence of crystal engineering.[40,41] The main strategies involve the development of multi-component solids, such as co-crystals, in which functionalities of the components are combined to get solids with tunable and/or desired physiochemical properties.[42,43] This strategy has been used in pharmaceuticals,[44-46] photo- or thermo-responsive materials,[47] tunability of optical properties,[48,49] or conductive properties of solids.[50] One of the main tools of crystal engineering is the use of intermolecular interactions to form co-crystals, primarily using π-π stacking,[51] hydrogen,[52] halogen,[53] or coordination bonding.[54]

Hydrogen bonding is generally defined as an electrostatic interaction between a hydrogen bond donor, which is a functional group containing a hydrogen that is bonded to electronegative atom, and a hydrogen bond acceptor, an electronegative atom.[55] The strength of such intermolecular bonding varies from 4–170 $kJ \cdot mol^{-1}$,[55] and hydrogen bonding is generally seen as a directional interaction.[56,57] Hydrogen bonds can form using a large variety of different hydrogen bonding moieties (OH···O, NH···O, etc), and the directionality of the interactions can sometimes allow for the qualitative prediction of the orientation of the molecules within a solid state structure.[58] The combination of certain hydrogen bond moieties as functional groups on a molecular skeleton will generate hydrogen bonding synthons[58,59] (examples seen in **Figure 3)**. An advantage of using hydrogen bonding when forming a co-crystal is that it enables the ability to alter physiochemical properties of pharmaceuticals directly through co-crystallization with an active pharmaceutical ingredient (API) and a co-crystal former, typically denoted as a coformer,[44,45] altering properties such as solubility,[60] shelf-life,[61] thermostability,[62] and

biovailability.[63] In addition, hydrogen bonding has been used as a tool to enable co-crystallization of two non-photo-responsive solids to produce a unique photo-responsive material.[64]

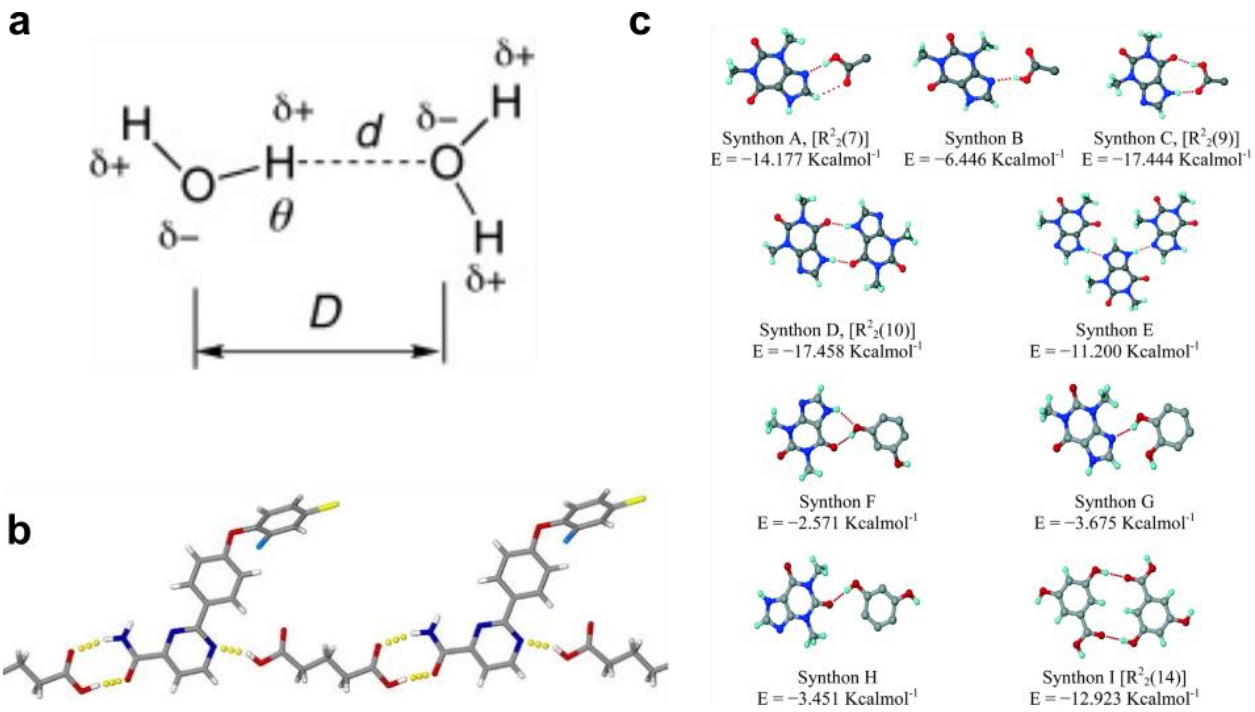

Figure 1.3. Examples of hydrogen-bonding synthons. a) Example of a hydrogen bond dimer, water (reproduced from reference [55]). **b)** Glutaric acid/API co-crystal dimer hydrogen bonds formed from carboxylic acid groups on the glutaric acid and amide and pyridine groups on the drug molecule (reproduced from reference [63]). **c)** A selection of hydrogen bonding synthons and their respective interaction energy, the dimers had been taken from crystallographic structures outlined in Sarma *et al*.[65] (reproduced from reference [65]).

Halogen bonding, similar to hydrogen bonding, is an electrostatic interaction between an electronegative atom, known as the halogen bond acceptor, and a region of positive electron potential that is generated on a polarized halogen atom, identified as the halogen bond donor, through proximity of the halogen to electron withdrawing groups.[66,67] The area of positive potential is referred to as a σ-hole due to spatial overlap with the area of the σ* orbital associated with the

covalent bond between the halogen atom and the adjoining atom (**Figure 1.4c**). Larger polarizability of the halogen atom leads to a larger σ-hole and, consequently, a stronger halogen bonding interaction.[68] As a result, the σ-hole is more pronounced for heavier, more diffuse and polarizable halogen atoms, such as iodine and bromine. In general, the halogen bond strength is anticipated to increase with the size of the halogen atom: F < Cl < Br < I (**Figure 1.4b**).[68] An atom of iodine or bromine can be readily polarized when connected through a variety of electron-withdrawing groups, including fluoro- or nitro-substituted aromatic rings, perfluoroalkyl groups, alkynes, etc. As for the design of halogen bond acceptors, there is a variety of options available including, but not limited to, the use of heteroatoms such as N, O, S, F, etc.,[68] as well as other electron-rich species, such as aromatic π-systems.[69]

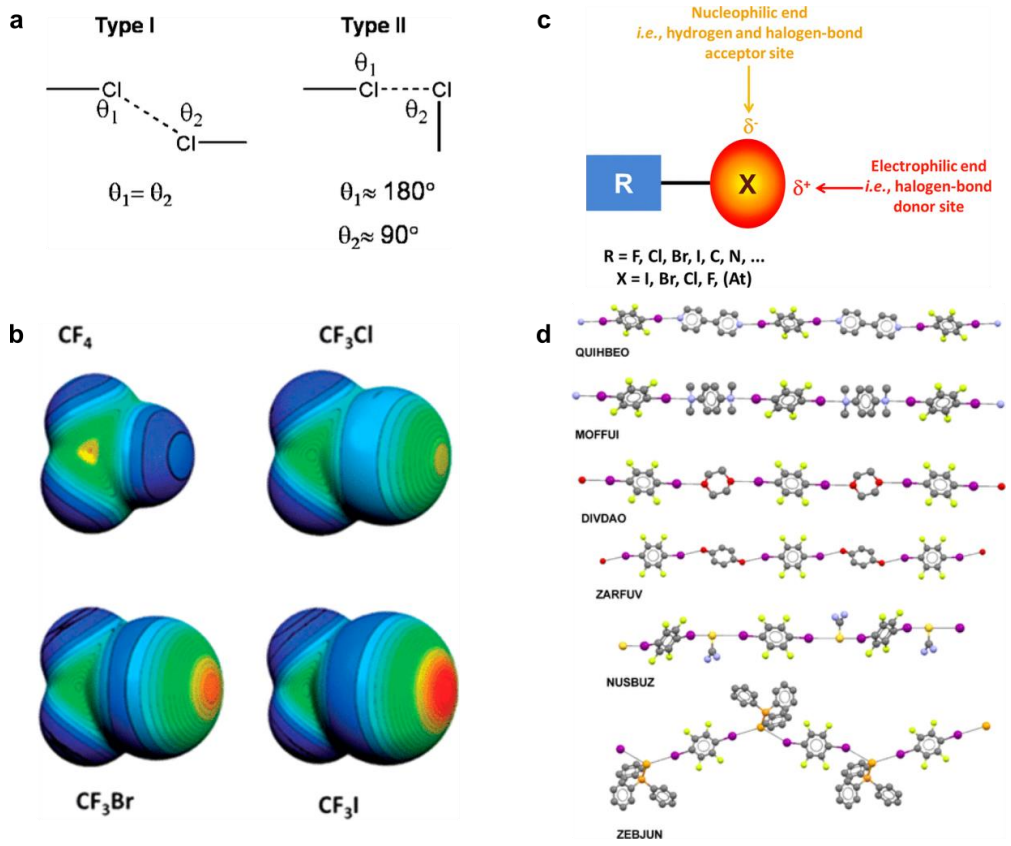

Figure 1.4. Depiction of halogen-bonding. a) Type I and Type II Cl···Cl contacts (reproduced from reference [66]). **b)** Electrostatic potential diagrams of various XCF_3 molecules, showing the sigma hole size dependence on the size of the halogen. **c)** Schematic of the anisotropic distribution of the electron density around a halogen atom covalently bonded to an electron withdrawing group. **d)** Halogen-bonded chains in various co-crystals of the 1,4-diiodotetrafluorobenzene halogen bond donor, with atoms shown in a ball-and-stick representation (**b–d** have been reproduced from reference [67]).

One of the properties of the halogen bond (XB) that is of particular value in the context of crystal engineering is the directionality of the interaction, which is seen as nearly linear with bonding angles nearing 180^0.[70] The bonding energies of halogen bonds have been evaluated to range from 10–200 $kJ{\cdot}mol^{-1}$.[71] On the other hand, halogen-halogen contacts (X···X contacts)

appear in two types; Type 1 is considered to be a non-halogen bonding interaction, while Type 2 occurs through two halogen atoms interacting *via* a halogen-bonding interaction accomplished between the positive σ-hole of one halogen atom, and the nucleophilic end in the equatorial region of the second one (**Figure 1.4a**). Consistent with being halogen bonds, the Type 2 halogen···halogen interactions also show a directionality to them. Rather than being linear, as is typically seen in halogen bonds, type II X···X interactions occur as nearly orthogonal (≈90 ^{0}).[72] Type I and Type II (XB, or X···X) interactions are found throughout many structures of crystalline halogenated organic compounds, and have been utilized in crystal engineering as a tool to form predicable assemblies of halogen-bonded co-crystals.[66,73]

A large range of functional groups has been shown to engage in halogen bonding, including halogen bonding acceptor groups like sulfur,[74] selenium,[75] and antimony[76] —heavy elements that rarely if ever partake in hydrogen bonding. Additionally, it has been shown that halogen bonding is energetically favourable, while exhibiting better directionality and orthogonality than hydrogen bonding.[77] A wide number of available halogen bond acceptors also makes available a large range of potential intermolecular geometries, that could be used to design a diversity of materials including organic solids,[78] metal-organic solids,[79] host-guest systems,[80] and liquid crystals.[81] Several of these materials have exhibited photo- or optical properties, including photo-mechanical bending,[37] dichroism,[82] photo-emission,[83] mass-transport,[38,84] and more.

1.4 Bond formation

1.4.1 Photo-dimerization reactions

Crystal engineering has been used to direct reactions in the solid state,[41] using either hydrogen or halogen-bonding templates to assemble reactants at appropriate distances, ensuring reactivity. This is especially important in light-driven [2+2] photo-dimerization reactions of olefins, in which the molecular arrangement must satisfy the criteria laid out by Schmidt, *i.e.* the olefin C=C bonds need to be aligned in parallel and at a separation of 4.2 Å or less to undergo a light-driven conversion into a cyclobutane product.[85-87] Due to this clear geometrical criteria there are crystal engineering tools to engineer reactive structures, such as using either hydrogen,[88] halogen,[89] or coordination bonding,[90] to ensure reactants are an appropriate distance to ensure that the olefin will undergo [2+2] photo-dimerizations.

MacGillivray *et al*.[64] have shown the use of templates to influence the crystalline structure when intermolecular interactions are used to obtain a stacking motif of olefins, within the criteria set by Schmidt (**Figure 1.5a**). In one case, the authors used resorcinol as a co-crystal former (coformer) in combination with *trans*-1,2-bis(4-pyridyl)ethylene (4,4'-bpe) (**Figure 1.5b**), an olefin which in pure solid form adopts a layered structure in which the C=C bonds are separated by 6.52 Å, and should not be conducive to [2+2] photo-dimerization. Hydrogen-bonding between the hydroxyl moiety and the nitrogen atom on the pyridyl substituent forms a 2:2 resorcinol:4,4'-bpe solid state complex in which the two olefins are separated by a 3.65 Å, and upon light irradiation the desired photo-product is produced.

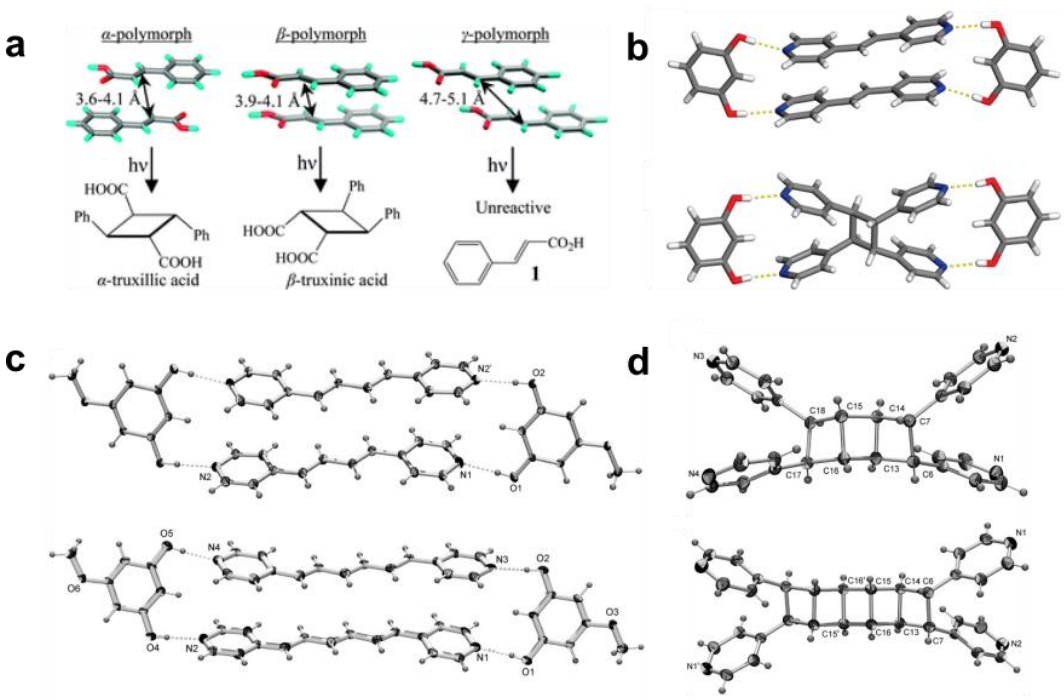

Figure 1.5. Examples of template assisted [2+2] photo-dimerizations. a) Schematic of cinnamic acid polymorphs (α, β, and γ) and their respective distance between olefin groups in the solid state, highlighted is their potential photo-reactivity (reproduced from reference [41]). **b)** Hydrogen-bonded template created by resorcinol co-crystalized with *trans*-1,2-bis(4-pyridyl)ethylene and the resultant photo-product (reproduced from reference [47]). **c)** Crystallographic hydrogen-bonded template of precursors to [n]ladderanes. **d)** Resultant photo-product of the templated reaction, showing two examples of [n]ladderanes produced through using hydrogen-bonded templates (**c–d** reproduced from reference [91]).

Additionally, the template approach has also been used to make ladderane molecules, based on a sequence of edge-fused cyclobutane moieties, by using conjugated olefins as reactants in [2+2] photo-dimerization (**Figures 1.5c,d**).[91] Coordination bonds have also successfully been used to template the arrangement of molecules into orientations suitable for a topochemical [2+2] photo-dimerization.[92] This is illustrated through the use of 2-dimensional (2D) coordination polymers

which can undergo [2+2] photo-dimerization to form a three-dimensional (3D) structure (**Scheme 1.2**),[93] or the use of gold atoms which will coordinate to the nitrogen atoms of *trans*-1,2-Bis(4-pyridyl)ethane (4,4-bpe),[94] and will successfully undergo a [2+2] photo-dimerization. Additionally, chalcogen-bonding interactions can also coordinate to the nitrogen of 4,4'-bpe,[95] and undergo a photo-dimerization.

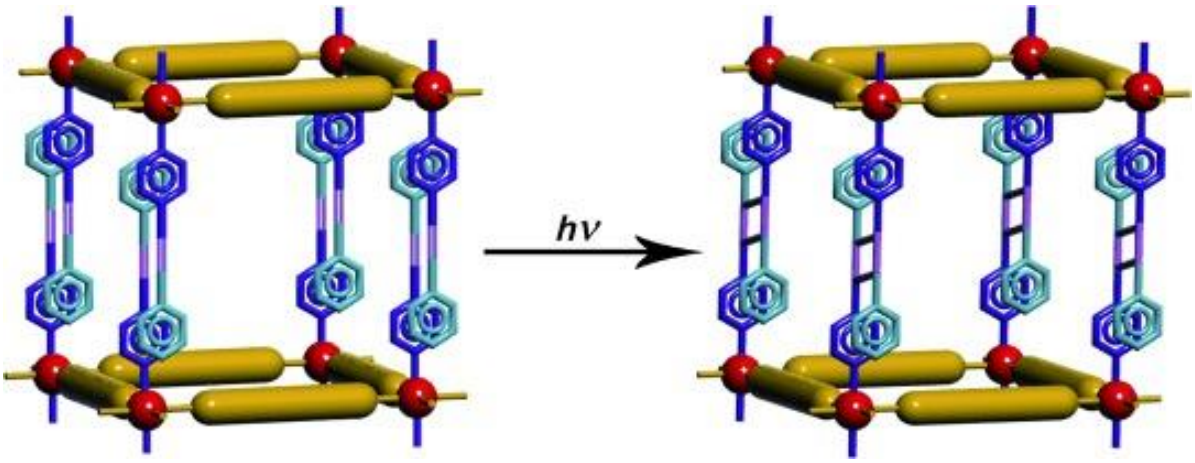

Scheme 1.2. Schematic of photo-induced structural change in which a 2D interdigitated layer is converted into a 3D MOF structure, through a topochemical [2+2] photo-dimerization (reproduced from reference [93]).

Halogen bonding was used as an interaction to template the arrangement of substrate molecules for a [2+2] photo-dimerization.[89] Using a halogen bond donor as a coformer with 2,4'-bpe acting as a halogen bond acceptor, two olefins can induced to undergo a dimerization to form a cyclobutane ring due to their close proximity in the crystal structure.[96] Similarly, the reactive olefin substrate can be used as the halogen bond donor. This is seen when the photo-stable olefin *trans*-1,2-bis(4-iodotetrafluorophenyl)ethene is combined with 1,8-di(4-pyridyl)naphthalene as the halogen-bonding template (**Figure 1.6**).[89] The resulting co-crystal is composed of discrete

assemblies in which the olefin and the template are halogen-bonded in a 2:2 stoichiometry, through halogen bonds of N···I type. The resulting assemblies exhibit olefin groups arranged in parallel and at a separation of 3.68 Å, enabling the [2+2] photo-dimerization leading to quantitative formation of the cyclobutane product upon irradiation with UV light.

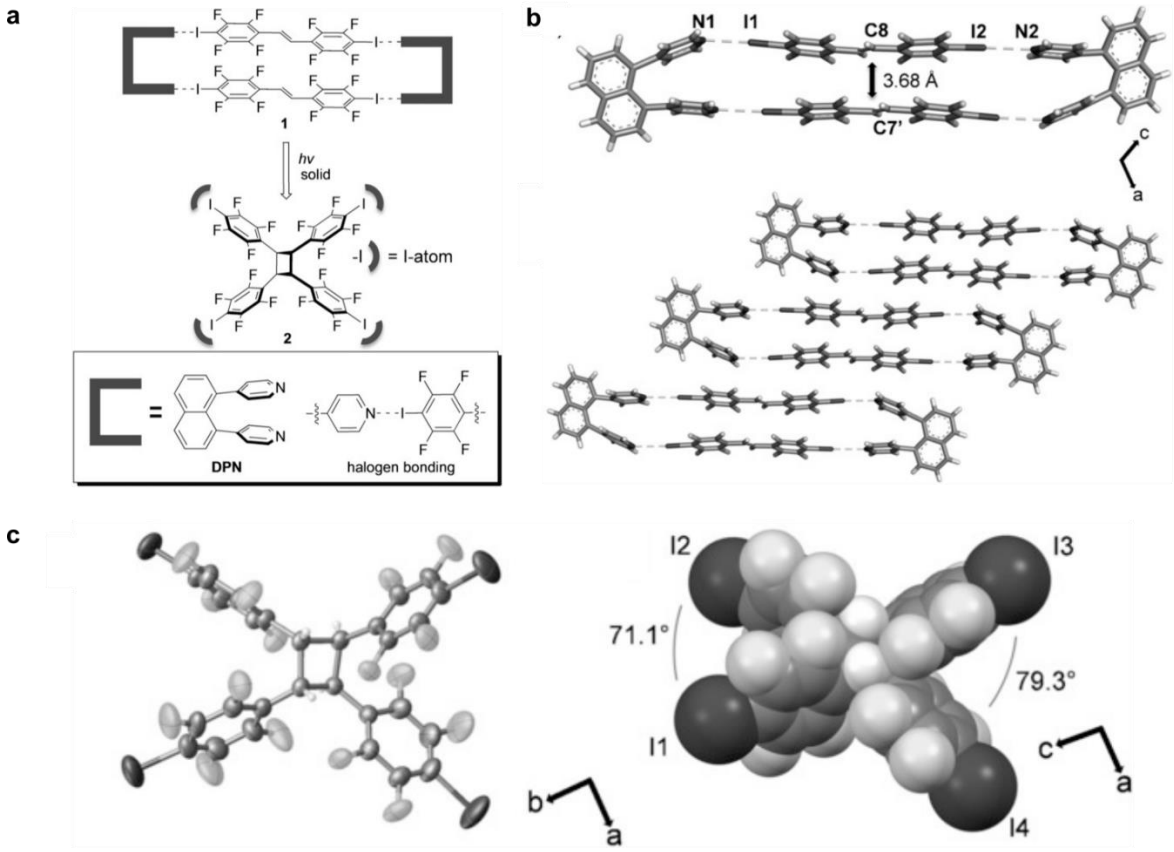

Figure 1.6. Halogen-bonding template used to mediate [2+2] photo-cycloadditions in the solid state. a) Schematic of templated solid state photo-dimerization to form the photo product. **b)** The crystallographic structure of the fluorinated olefin and coformer, showing the halogen bonding template (top), and extended packing (bottom). **c)** X-ray crystal structure of the photo-product in ORTEP (left) and space-fill model (right) (Images reproduced from reference [89]).

Similarly to topochemical [2+2] photo-dimerizations, [4+4] cycloadditions can also occur in the solid state. They require proximity between the reacting molecules to induce bond formation by light.[97] Chemical modification of anthracene molecules has been a popular technique to induce such cycloadditions, as introduction of substituents is an effective albeit unpredictable means to alter the solid state packing of reactive molecular cores. When modified appropriately, the anthracene molecules can act as monomers in a polymerization.[98] This could lead to a change in crystalline habit, allowing the crystals to function as photo-actuators.[99]

1.4.2 Topochemical polymerizations

Co-crystallization has been shown as a crystal engineering method to enable topochemical polymerization through hydrogen bonding, π-π interactions, or host-guest interaction systems. These interactions have been used for solid state polymerization of diacetylenes, triacetylenes, dienes and trienes.[100-104] Co-crystallization can also be used to enable the solid state formation of alternating copolymers, as seen by the application of two molecules 7,7,8,8-tetrakis(methoxycarbonyl)-quinodimethane (**TMCQD**) and 7,7,8,8-tetracyanooquinodimethane (**TCQDM**) (**Figures 1.7a,b)**.[105] The monomers pack in an alternating fashion of **TMCQD** and **TCQDM,** allowing for polymerization under UV-light irradiation, forming a polymer based on alternating monomers with composition (poly(**TMCQD** · **TCQDM**)).

Halogen bonding has also been used to template topochemical polymerizations.[102,103] Using diiodobutadiyne as a monomer, in combination with a variety of self-assembled halogen bond acceptors has enabled Sun *et al*. to achieve controlled solid state synthesis of poly(diiododiacetylene). The synthesis of this halogenated polymeric carbon backbone requires the use small molecule templates that are specifically chosen and designed to self-assemble into extended structures in which the halogen bond accepting groups are arranged at repeat distances

suitable for light- and/or heat-induced diacetylene polymerization. These examples described show how co-crystallization can be used to engage otherwise non-reactive monomers and use (supra)molecular templates to arrange them in a way conducive to solid state topochemical polymerization.

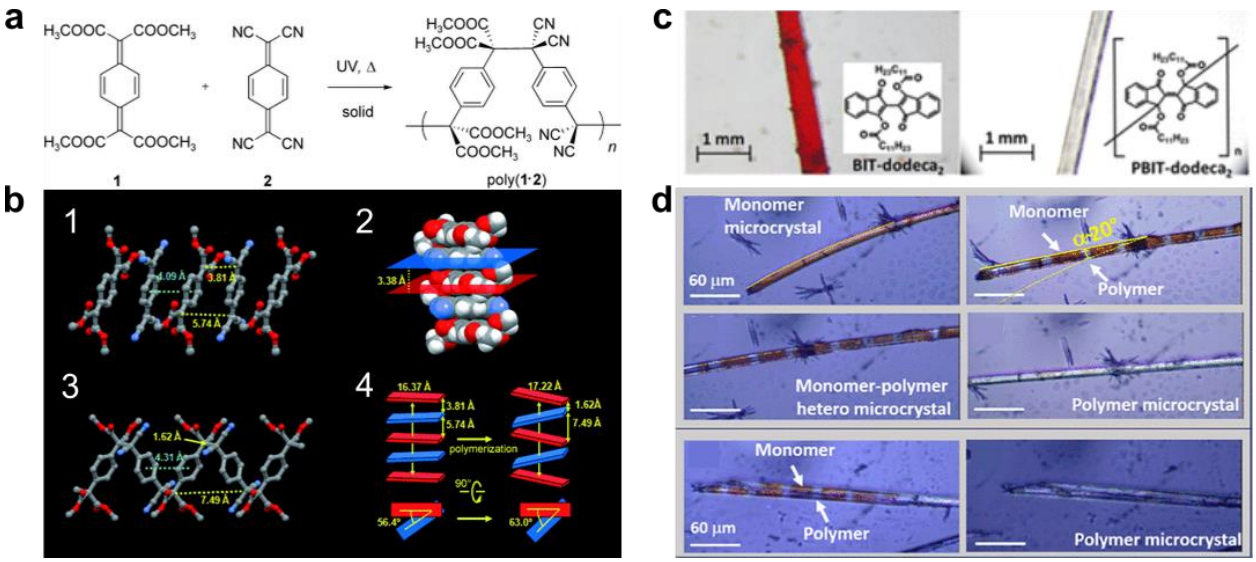

Figure 1.7. Selected examples of topochemical polymerizations. a) Schematic of photo-induced co-polymerization of two separate monomers. **b)** Molecular packing of the co-crystals in ball-stick and space fill models (panels 1 and 2). Crystal packing of the co-polymer crystal (panel 3), and schematic of crystallographic changes occurring *via* photo-induced polymerization (panel 4). (**a,b** reproduced from reference [105]). **c)** Single crystals and molecular diagram of the monomer and polymer. **d)** Confocal optical images of the monomer-polymer heterostructure formation (**c,d** reproduced from reference [106]).

Topochemical polymerization in the solid state can also change the optical properties of the material. This is especially interesting when the polymerization is reversible,[106] allowing for optical control and development of functional materials that can be used for information storage,

optical writing, and, for example, photo-patternable paper.[107] In a notable example, Reddy *et al.*[106] have described a monomer single crystal of 1,1'dioxo-1H-2,2'-biindene-3,3'-diyldidodecanoate that was found to undergo a single-crystal-to-single-crystal polymerization upon photo-irradiation (**Figures 1.7c,d**). Upon polymerization, the crystal appearance was observed to change from bright red to transparent, showing a unique photo-chromic effect. As the crystal is heated the polymer reverts back to repeating units of the monomer, with the colour of the crystal returning from transparent to red. The reversibility of the colour is seen both in studies on individual single crystals, as well as on polycrystalline films of the material. The authors additionally showed light induced patterning of a single crystal, in which there where specific domains associated to the polymer and the monomer.

1.5 Crystals active in the optical region

The design of single or multi-component crystals that exhibit unique optical properties such as photo-chromism,[108,109] is important in a variety of engineering and material science fields. Crystalline materials have been used as organic light emitting diodes (OLEDs),[110] waveguides,[111] components for non-linear optics,[112] and as dichroic,[113] or pleochroic,[114] materials.

1.5.1 Dichroic materials

Dichroic materials exhibit differing absorbances of plane-polarized light dependent on the orientation of the light source to the sample.[115] Dichroism of a material is directly related to the crystallographic structure, *i.e.* the arrangement of molecules in the crystalline solid state. For instance, in a crystal structure that consists of molecular chromophores organized with their distinct transition dipole moments aligned in a parallel, linear fashion, to the transition dipole

(whose magnitude is related to molecular dimension, where the longest molecular axis roughly approximates the direction of the largest transition dipole moment).[116,117] Their dipole moments would appear in a single plane, increasing the dependence of light-matter interactions such as transmission and/or absorbance, depending on the polarization orientation of the light source. On the other hand, if such chromophores are packed in a fashion in which the transition dipole moments of neighbouring molecules are not aligned, the dependence that the absorbance or transmission has on the polarization orientation of light is greatly reduced.

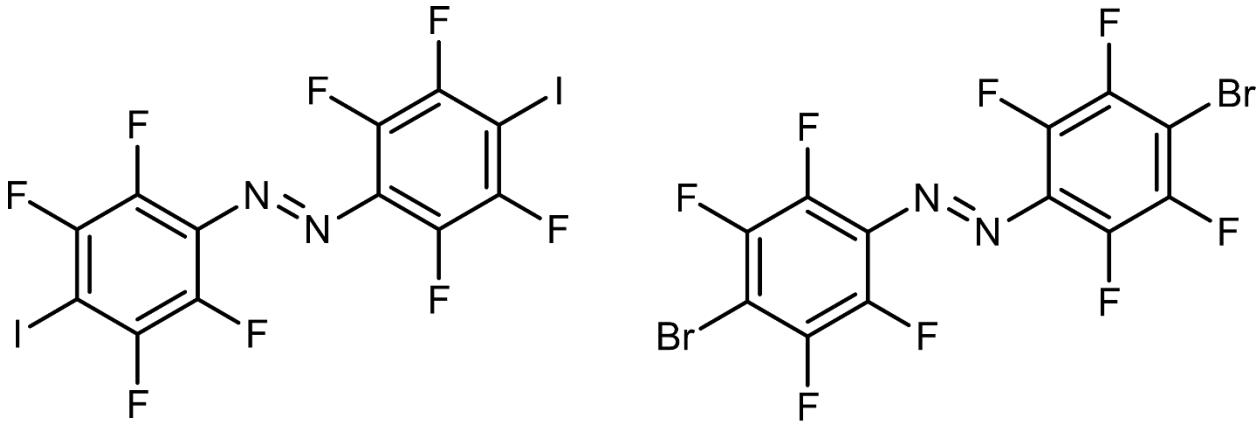

trans-4,4'-diiodoperfluoroazobenzene *trans*-4,4'-dibromoperfluoroazobenzene

Scheme 1.3. Fluorinated azobenzene chromophores of *trans*-iodo-Fazo (left) and *trans*-bromo-Fazo (right).

Bushuyev *et al.* have demonstrated a strategy to induce and tune dichroism of molecular solids through halogen bond-driven co-crystal formation.[82] In particular, the strategy presented by Bushuyev and co-workers rests on the use of linear ditopic halogen bond donors and acceptors that are anticipated to self-assemble into parallel halogen-bonded supramolecular chains of alternating XB donor and acceptor molecules. This simple approach provides a means to, at least in two dimensions, ensure a linear, parallel arrangement of chromophores in a crystalline solid.

Specifically, as halogen bond donors were investigated two separate chromophores; *trans*-4,4′-diiodo- and 4,4′-dibromoperfluoroazobenzene (*trans*-iodo-Fazo, *trans*-bromo-Fazo, **Scheme 1.3**). Despite similarities in their molecular structures, the two compounds exhibited remarkably different dichroic properties as pure crystalline solids. Specifically, while *trans*-bromo-Fazo derivatives would undergo a noticeable change in transmission colour upon variation of the orientation of polarized light, *trans*-iodo-Fazo exhibited little change upon variation of polarized light orientation. The reason for the difference in observed dichroic properties was explained through differences in the crystallographic arrangement of the molecules for the two compounds. *Trans*-bromo-Fazo was found to assemble in the solid state in a linear fashion, aligning the molecules on a similar plane. In contrast, *trans*-iodo-Fazo molecules would arrange in a herringbone-type crystal structure. However, upon co-crystallization of *trans*-iodo-Fazo with various linear ditopic halogen bond acceptors, the dichroic behaviour was greatly enhanced (**Figure 1.8a**), due to an all-parallel orientation of the chromophores related to the formation of halogen-bonded chains with the coformer. This crystal engineering concept for the design of dichroic solids was revisited through combining *trans*-iodo-Fazo with halogen bond acceptor dicyanoaurate(I) ion in a four-component co-crystal salt solvate, containing the azobenzene, $KAu(CN)_2$, and in the presence of crown ether (15-crown-5).[113] The linear ditopic halogen bond acceptor forms anionic chains with *trans*-iodo-Fazo, leading to a highly dichroic material.

Coordination bonds have also been used as a crystal engineering tool to enhance dichroism of a chromophore that exhibited poor dichroism as a single component crystal. For example, 4-phylazopyridine acts as a Lewis base and coordinates orthogonally to the electron-deficient boron atom in tris(pentafluorophenyl)borane.[118] Together, they self-assemble into molecular helices with the chromophores aligned linear and parallel, leading to a strongly dichroic crystalline material.

Vainauskas *et al.* have shown that the co-crystallization of multiple chromophores can be developed into a rational design of pleochroic materials: solids that will switch between different transmitted colours depending on their orientation with respect to plane-polarized light (**Figure 1.8b**).[114] The design presented by Vainauskas and co-workers relied on the use of halogen bonding to combine in the solid state two different types of chromophores, *trans*-iodo-Fazo (red dye) acting as a halogen bond donor, and an aromatic compound azulene (blue dye) acting as halogen bond acceptor. The two chromophores will co-crystalize into one of two supramolecular motifs: a ladder-like motif in a 2:1 azobenzene:azulene stoichiometry, and a second motif containing discrete $(azulene)_2(azobenzene)_2$ moieties and an additional azulene molecule sitting between two moieties. In the ladder-like motif the azobenzene molecules, as well as the azulene molecules, are aligned parallel to each other along the major transition dipole moment. However, the major transition dipole moment of the azulene is perpendicular to that of the azobenzene. Therefore, when varying the polarization of the light, the crystal will change colours from red to blue. While the second structure also exhibits pleochroic behaviour, it is not as pronounced as the ladder-like motif. This could be due to the slight offset of the chromophores, making them less parallel than those seen in the first structure.

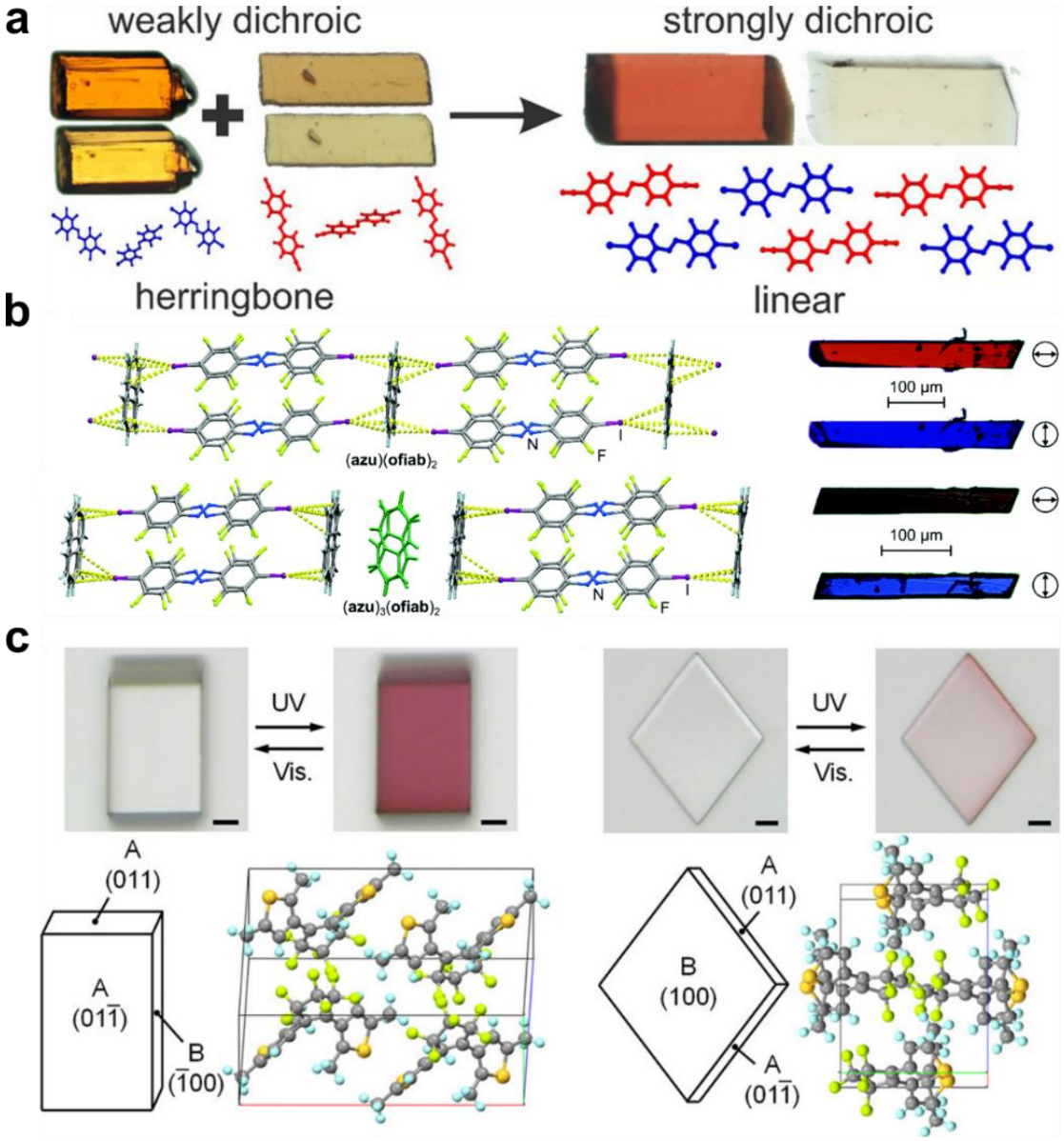

Figure 1.8. Optically responsive crystals and co-crystals. a) Example of crystal engineering to induce dichroism by taking two components that are weakly dichroic and forming a strongly dichroic co-crystal, and how those crystals pack (reproduced from reference [82]). **b)** Two sets of pleochroic crystals that appear as different colours under varying polarization and their respective crystal packing (reproduced from reference [114]). **c)** Optical images of the diarylethene crystals before and after their photo-induced ring closing/opening reaction and their respective crystal structures (reproduced from reference [119]).

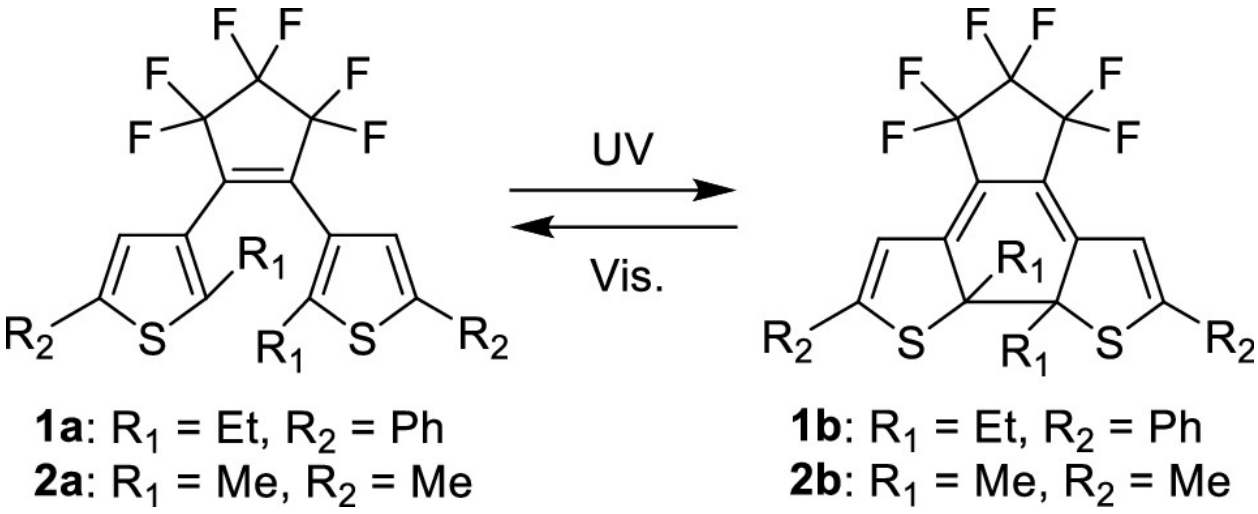

Scheme 1.4. Molecular structures of diarylethenes (reproduced from reference [119]).

As previously stated, one or more types of chromophores can be incorporated within a crystal to develop dichroic or pleochroic materials, respectively, but the birefringence of a crystalline material can be altered by isomerizing a photo-switch itself. Morinoto *et al*. have demonstrated the ability to alter the transmittance and polarizability anisotropy of diarylethylenes single crystals (**Scheme 1.4**) by isomerizing them with UV or visible light (**Figure 1.8c**).[119] The authors found that the intensity of transmitted light through the crystals can be either increased or decreased depending on the ring opening/ring closing of the diarylethene.

1.5.2 Luminescent crystals

Organic crystalline materials are highly attractive when developing flexible organic optoelectronics,[120] due to their periodic structures, anisotropic photophysical properties, and intense luminescence.[121] Recent studies have characterized flexible crystalline materials that, rather than cracking under stress, will bend away from the stress through either reversible (elastic),[111,122,123] or irreversible (plastic) deformation.[124] Such crystals can function as

waveguides[125] — active *via* transmission of fluorescence, or passive *via* transmission of unaltered input light,[126] optical transducing media, thermal sensers,[127] and lasing media.[128]

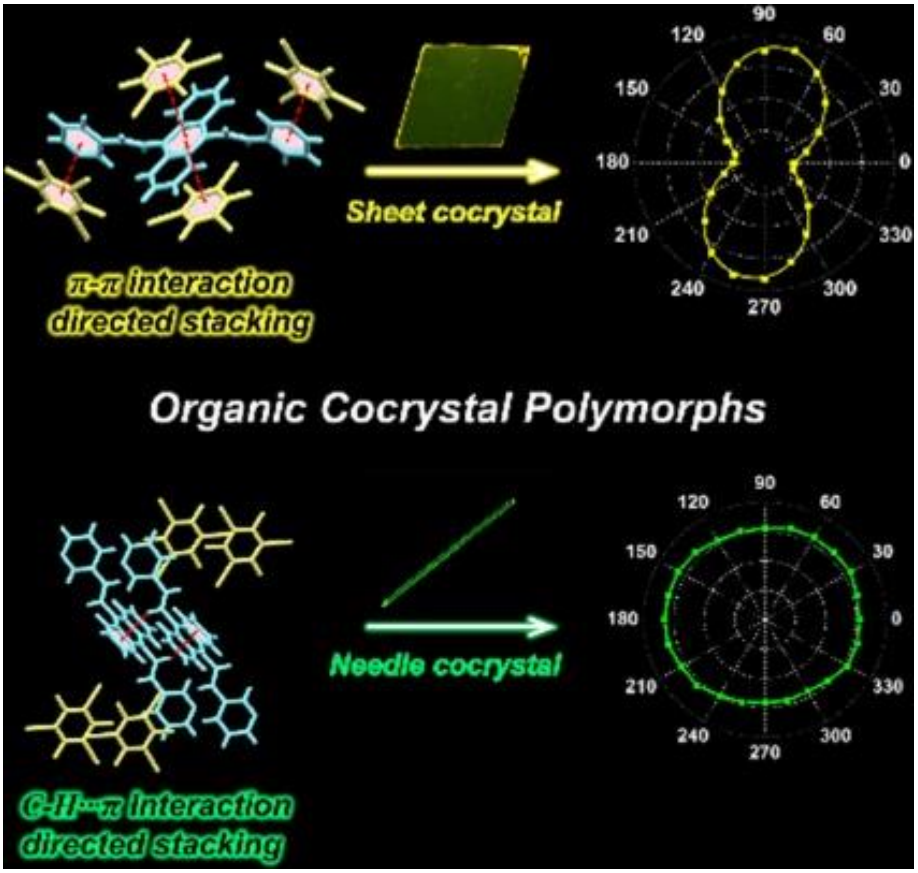

Figure 1.9. Polymorphs of organic co-crystals exhibiting differing crystalline habits and different luminescence properties based on a variety of interactions directing the crystallographic arrangement. Polymorph 1 (top) molecules are arranged through π-stacking leading to sheet-like crystalline habit, with yellow polarization dependent luminescent properties. Polymorph 2 (bottom) molecules are arranged through C-H···π interactions leading to needle-like crystalline habit, with green luminescent properties (reproduced from reference [129]).

Co-crystallization can also be used as a crystal engineering tool to develop either passive or active waveguides, for instance by combing desired physical properties such as high elasticity, with luminescence properties, allowing for their use as active waveguides. As an example, Du *et al.* have described two differing optical waveguides composed of the same crystalline components (organic polymorphs) (**Figure 1.9**).[129] Polymorphs have been shown to exhibit differing emission properties,[130] and in the study of Du *et al.* one of the co-crystals (polymorph 1), molecules were arranged through π-π interactions, resulting in a material exhibiting an overall sheet-like crystal morphology, with yellow-like luminescence properties. In the second polymorph molecules arranged through CH-π interactions forming a needle-like crystalline habit, with green luminescence. Both co-crystals showed significant light propagation throughout the crystal, with light traveling upwards of 5 mm in the second polymorph. Interestingly the two polymorphs' emission properties exhibited differing amounts of polarization dependence. The first polymorph emission intensity had no dependence on the polarization, while the second polymorph emission intensity was strongly dependent on the angle of polarization at the emitting (011) plane.

Ma *et al*. synthesized various co-crystals of tetra(*tert*-butyl)perylene and phthalonitrile isomers for application as tunable waveguides.[131] The three co-crystals were isostructural, yet exhibited remarkably different luminescence properties, with green, orange, and red photo-luminescence emissions (**Figure 1.10a**). The authors showed that the crystal growth rate can be modulated to obtain varying crystalline habits. While slow growth leads to single crystals appearing in a rod-like crystalline habit, faster growth showed the crystallites will begin branching off perpendicular to an existing rod. This allows for the co-crystals to act as either 1 or 2 dimensional waveguides.

Co-crystallization of chromophores with diverse coformers is an excellent and simple way to tune the emissive properties of a solid (**Figure 1.10b**).[132-134] In particular, halogen bonding-based co-crystallization has been shown as a robust tool to control solid state luminescence (**Figure 1.10c**).[135,136] For example, Yan *et al*. used halogen bonding, as well as other intermolecular interactions, to modify the solid state optical properties of 1,4-bis(4-cyanostyryl)benzene chromophores,[134] showing that co-crystalization can vary the absorbance, colour, and fluorescence emission of the chromophore. These optical changes were explained through changes or the arrangement of the molecules in the crystallographic structure. The authors also recognized that varying the crystal size, as well as temperature, affected luminescence properties such as fluorescence lifetime and fluorescence intensity. Additionally, temperature had a direct effect on the I···N and Br···N halogen bond distances, rationalizing the effect temperature has on the emission intensity of the co-crystals.

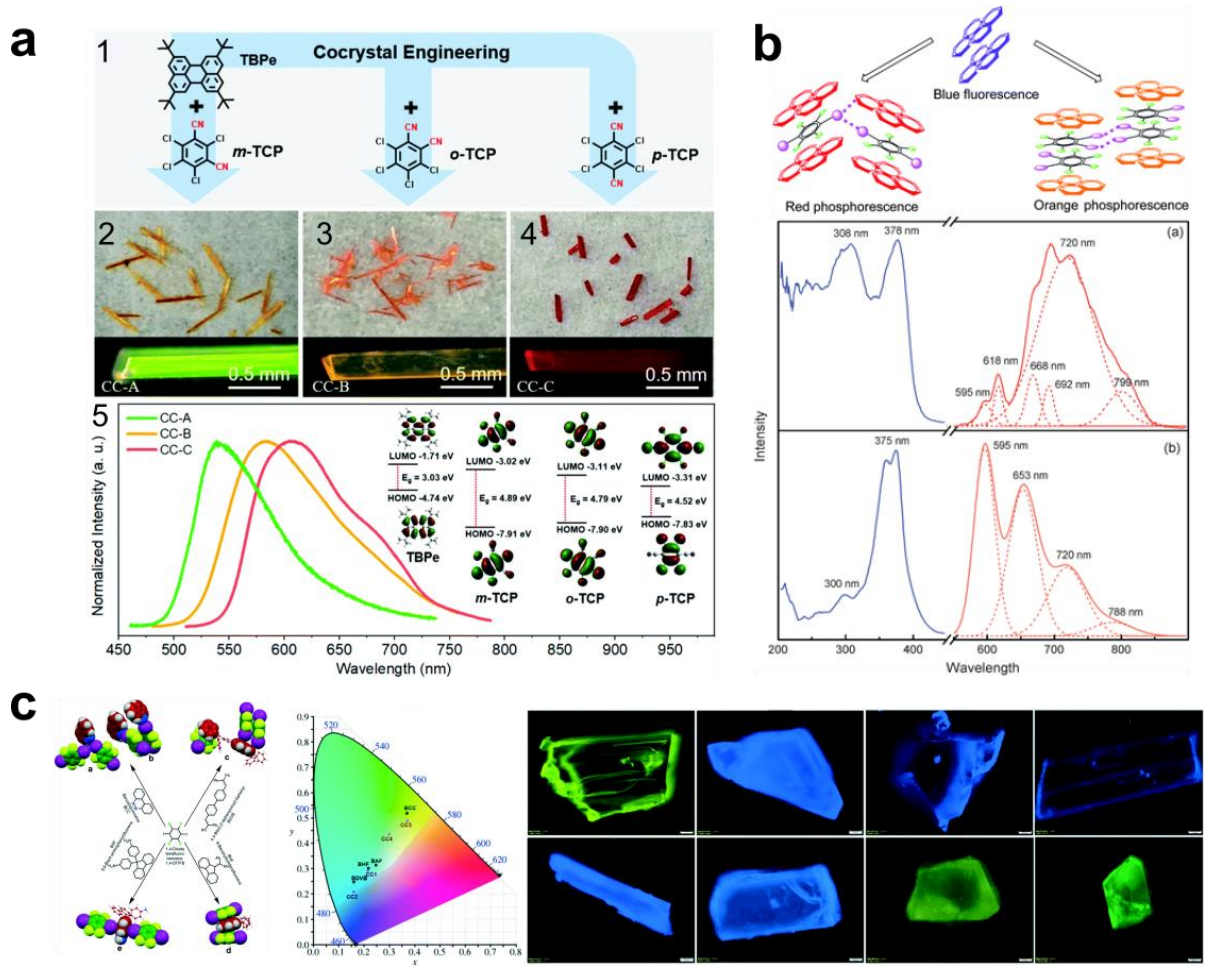

Figure 1.10. Using co-crystallization to alter luminescence properties by changing the packing of emissive molecules. a) Schematic representation of co-crystals used in the study (1), optical and fluorescent images of single crystals (2–4), and their respective photo-luminescence spectra with calculated HOMO-LUMO orbitals (5) (reproduced from reference [131]). **b)** Schematic of co-crystallization of pyrene with either 1,4-TFIB or 1,2-TFIB and their respective excitation and emission spectra (reproduced from reference [132]). **c)** Schematic of co-crystallization with 1,4-TFIB and various emissive molecules, undergoing a variety of intermolecular interactions (left), CIE colour coordinates of the differing co-crystals and the single crystal aromatic components (mid), as well fluorescent microscopy images of the co-crystals (top) and the single crystal aromatic components (bottom) (reproduced from reference [135]).

Halogen bonding to π-systems has also been shown to modulate the luminescence properties of a solid state chromophore. For example, d'Agostino *et al*. have showed the ability to alter the photo-luminescence of either diphenylacetylene (DPA) or *trans*-stilbene (TS) by varying the stoichiometric composition of two C-I···π halogen-bonded co-crystal systems (**Figure 1.11a**).[137] Using DPA or TS as halogen bond acceptors, and 1,4-TFIB as the halogen bond donor, the authors developed 4 novel co-crystals: stiochomers (DPA)(1,4-TFIB), (DPA)(1,4-TFIB)$_2$ and stiochomers (TS)(1,4-TFIB), (TS)(1,4-TFIB)$_2$. Both chromophores DPA and TS showed intense fluorescence emission at 358 nm and 366 nm respectively, however both sets of co-crystals altered the emission properties of the solid. While the DPA co-crystal (DPA)(1,4-TFIB) showed a weak fluorescence emission accompanied with a weak yet clear phosphorescence signal, its stoichomer (DPA)(1,4-TFIB)$_2$ completely suppresses the fluorescence signal while retaining the red-shifted phosphorescence signal. The changes in emission properties of the second co-crystal were either due to the higher coformer stoichiometry, or to the different packing of the DPA molecules. The second system ((TS)(1,4-TFIB) and (TS)(1,4-TFIB)$_2$) was similar to the DPA co-crystals, with even greater promotion of phosphorescence, but an overall weaker signal. Both systems showed the role that the stoichiometry of a coformer can play in the tuning of emission properties of a system *via* quenching fluorescence and promoting phosphorescence.

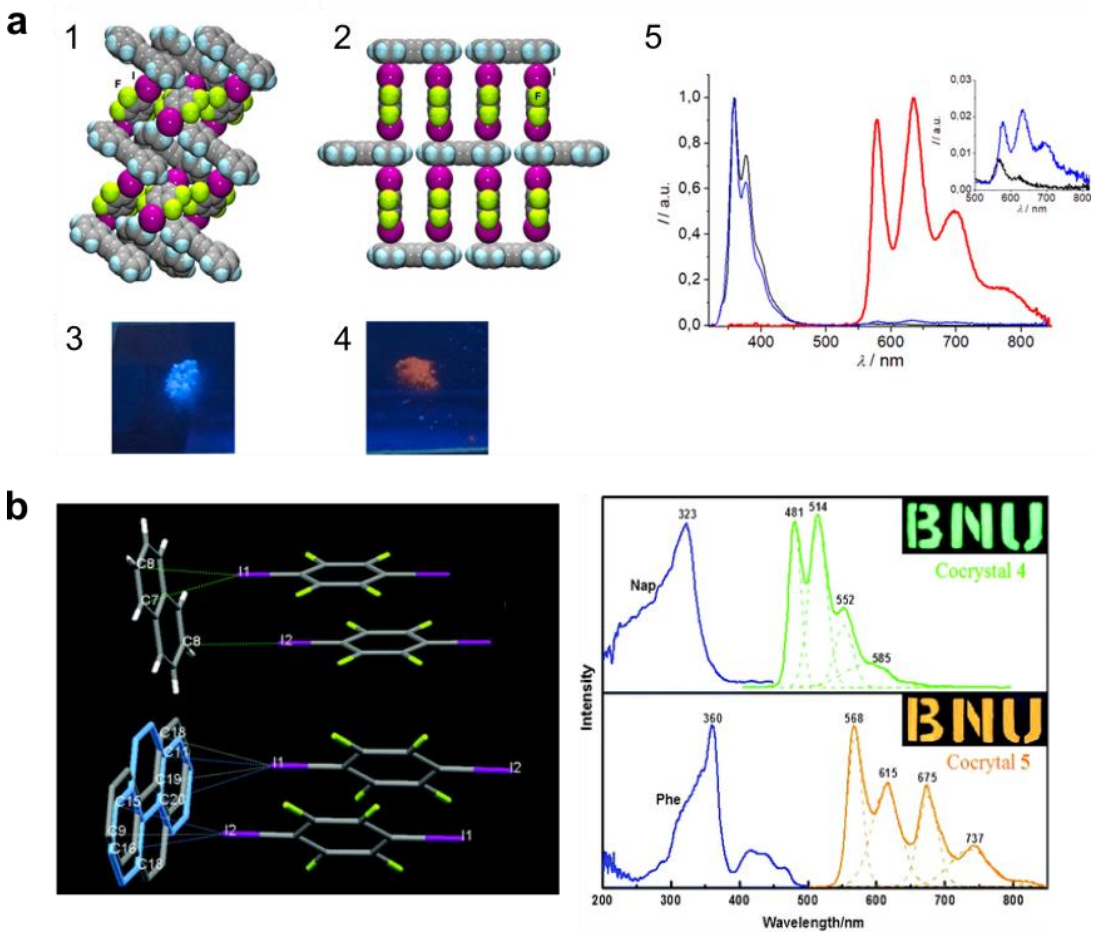

Figure 1.11. Luminescence properties of co-crystals formed through halogen-bonding to π-systems. a) Illustration of the arrangement of molecules in crystal structures of co-crystals formed from tolane XB acceptor and 1,4-TFIB as the XB donor, with stoichiometric compositions of (1) (DPA)(1,4-TFIB) and (2) (DPA)(1,4-TFIB)$_2$, luminescence images of the (3) (DPA)(1,4-TFIB) and (4) (DPA)(1,4-TFIB)$_2$ co-crystals and (5) their respective normalized emission profiles ((DPA)(1,4-TFIB) co-crystal blue trace, (DPA)(1,4-TFIB)$_2$ co-crystal red trace) (reproduced from reference [137]). **b)** C-I···π halogen bonding of 1,4-TFIB with phenanthrene and naphthalene (left) and their respective emissive properties (blue trace; starting material (naphthalene top and phenanthrene bottom), green trace naphthalene:1,4-TFIB co-crystal and orange trace phenanthrene:1,4-TFIB co-crystal) (reproduced from reference [138]).

There have been other examples of using C-I···π halogen bonding to alter emission properties of molecules, which were achieved by co-crystallization of 1,4-TFIB with either biphenyl, naphthalene (Nap), or phenanthrene (Phen) (**Figure 1.11b**).[138] These polyaromatic hydrocarbons (PAHs) typically have strong luminescence structural units, however the emission tends to be blue or green as it is most commonly fluorescent. Phosphorescence for PAHs is difficult to observe due to transition between singlet to triplet states being spin forbidden. While co-crystallization of 1,4-TFIB with biphenyl showed no emission properties due to the biphenyl existing in a nonplanar form in the crystal structure, the other two co-crystals (Nap-1.4-TFIB) and (Phen-1,4-TFIB) exhibited strong green and red phosphorescence. The 1,4-TFIB affects the emission properties of the solid in multiple ways. For instance, it allows for transitions from the normally forbidden singlet to triplet states due to the strong spin-orbital coupling of the heavy iodine atom, as well as diluting the concentration of Nap or Phen in the crystalline solid, which prevents self-quenching.

1.6 Photo-mechanical crystals

Crystalline solids that change shape by hopping, twisting, bending, shattering, growing, or shrinking upon external stimuli such as heat, pH, or light are considered mechanical crystals.[139] Such dynamic crystals can be used in a variety of applications, including molecular machines,[140] artificial muscles,[141] and electric fuses.[142] Using a molecular photo-switch that will undergo a change of conformation upon photo-irradiation is a common tool to develop such dynamic crystals, as a small change on the molecular level can produce a profound effect on larger length scales from μm to cm, due to the cumulative strain produced through the cooperative action of the molecules found in the ordered crystals. Additionally, the use of light rather than other external

stimuli allows for remote and directional operation without the need for physical contact with the actuator.

1.6.1 Photo-mechanical actuation of organic photo-switches

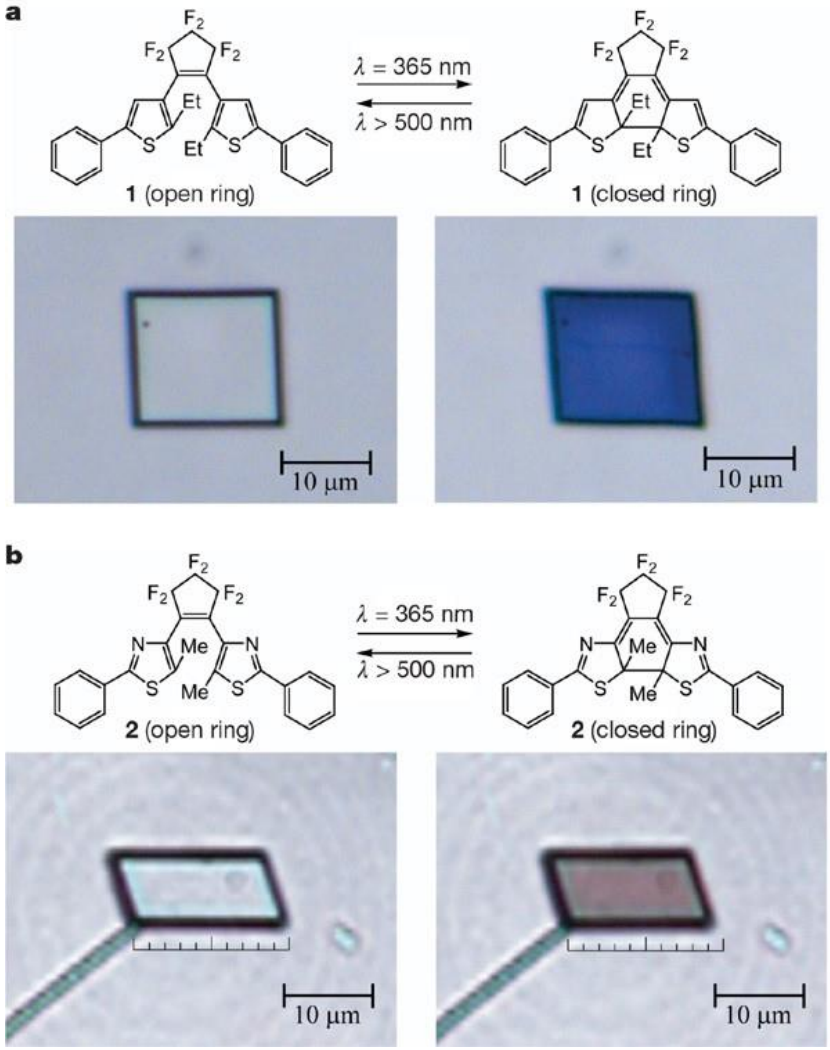

Figure 1.12. Crystals and molecular structures of two ring closing photo-isomerizations. a) Molecular structure and crystal of 1,2-bis(2-ethyl-5-phenyl-3-thienyl)perfluorocyclopentene before and after photo-isomerization. **b)** Molecular structure and crystal of 1,2-bis(5-methyl-2-phenyl-4-thiazolyl)perfluorocyclopentene before and after photo-isomerization. (reproduced from reference [143]).

Various photo-switches have been used in developing photo-mechanical crystals that can perform a variety of tasks, depending on the photo-switch, its crystallographic packing and crystalline habit. Such photo-responsive crystals can reversibly or irreversibly photo-mechanically change, relaxing to the initial configuration thermally, photochemically, or with other external stimuli. Using diarylethene chromophores as a photo-switch, Kobatake *et al*. developed a reversible photo-switch in which the single crystal of 1,2-bis(2-ethyl-5-phenyl-3-thienyl)perfluorocyclopentene crystalline habit will change from a square shape to a lozenge-like shape upon irradiation with UV-light (**Figure 1.12**).[143] The process occurs through ring closure of the diarylethene compound, resulting in a change of crystal shape, accompanied with an optical colour change. The resultant crystal will revert to the square shape upon irradiation with visible blue light. The authors further expanded their study by using a second diarylethene molecule; 1,2-bis(5-methyl-2-phenyl-4-thiazolyl)perfluoro-cyclopentene. The molecules crystalize to produce solids with two differing crystalline habits, one of which was rod-like and showed the ability to undergo reversible photo-mechanical bending upon exposure to UV and visible light, while the 2nd was plate-like and had similar photo-responsive behaviour as the 1,2-bis(2-ethyl-5-phenyl-3-thienyl)perfluorocyclopentene crystal. The rod-like crystal converted light to mechanical work by moving a gold micro-particle that was 90 times its weight.

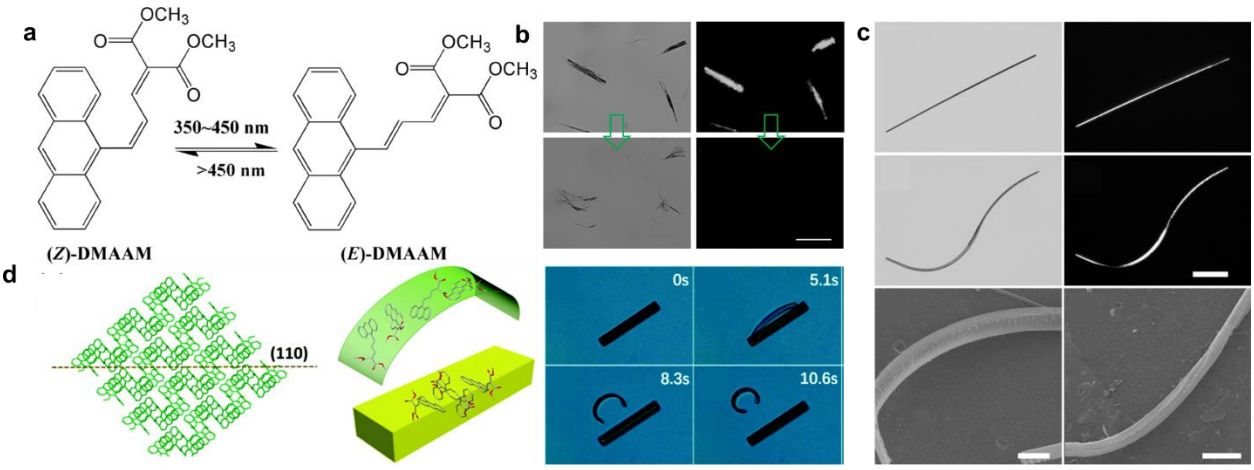

Figure 1.13. Photo-actuation of functional anthracenes. a) Schematic of the isomerization of *cis*-DMAAM to *trans*-DMAAM. **b)** Optical microscopy images of DMAAM nanowires before (top) and after (bottom) photo-irradiation under linear (left) and cross polarized light (right) (**a**–**b** are reproduced from reference [144]), **c)** DVAAM nano-wires before (top) and after (mid, bottom) irradiation, shown to undergo photo-induced crawling, linear (left) and cross (right) polarized microscopy represent the first 4 panels SEM images the bottom two (reproduced from reference [145]). **d)** *cis*-DMAAM single crystals undergoing a photo-induced peeling effect upon photo-irradiation, (left) schematic of the reaction occurring and crystalline packing, (right) the optical images of the crystal undergoing a peeling effect at different irradiation times (reproduced from reference [146]).

Similar to azobenzenes, stilbenes can also undergo a photo-induced isomerization from the more stable *trans*- into the metastable *cis*-isomer, providing potential to function as light-powered molecular-level actuators. However, unlike azobenzenes, stilbenes have been shown to undergo either [2+2] or [4+4] dimerizations, depending on the solid state crystalline arrangement of molecules. In that context, crystal engineering is essential in designing photo-actuators when using stilbenes. For example, Tong *et al*. used a stilbene anthracene derivative *cis/trans*-dimethyl-2(3-

(anthracene-9-yl)allylidene)malonate (*cis/trans*-DMAAM), which has been shown to undergo large changes in crystal shape upon photo-induced isomerization of crystalline nanowires (**Figures 1.13a,b**).[144] The authors showed that nanowires of either the *cis* or the *trans* isomer will undergo a photo-induced coiling upon exposure to a pulse of visible light with wavelength in the range of 450 nm to 550 nm. Interestingly, the shape of the crystal continued to change after the irradiation source was removed. It was determined that the nanowires collapse into a coil, due to the mixture of the *trans* and *cis* isomers. However, it was later shown that if *cis*-DMAAM was grown from aqueous surfactant solutions, the micrometer sized crystals had a different effect upon irradiation, as compared to the nanowires (**Figure 1.13d**).[146] Rather than coiling, a fraction of the crystal peels from the existing block. It was determined that light converts a fraction of the molecules on the surface of the crystal from the *cis* isomer to the *trans* isomer (*trans*-DMAAM), as the concentration of *trans*-DMAAM increases as a photo-stationary state is reached containing a mixture of *cis* and *trans* isomers. The mixture of isomers causes no periodic order and this amorphous phase will then separate from the remaining *cis*-DMAAM crystalline block. It was suggested that the separation was due to loss of order, or possibly solvent penetration. Similar to DMAAM crystalline nanowires, DVAAM ((E,Z)-2-(3-(anthracene-9-yl)allylidene)malononitrile) nanowires undergo a unique photo-induced curling upon photo-irradiation (**Figure 1.13d**).[145] Tong *et al*. showed that these anthracene derivatives will undergo deformations that mimic the motion of biological flagella, allowing the crystals to 'swim' through water. The motion is centered around the reversible $E \rightarrow Z$, which oscillates back and forth as irradiation continues, moving the crystals through water.

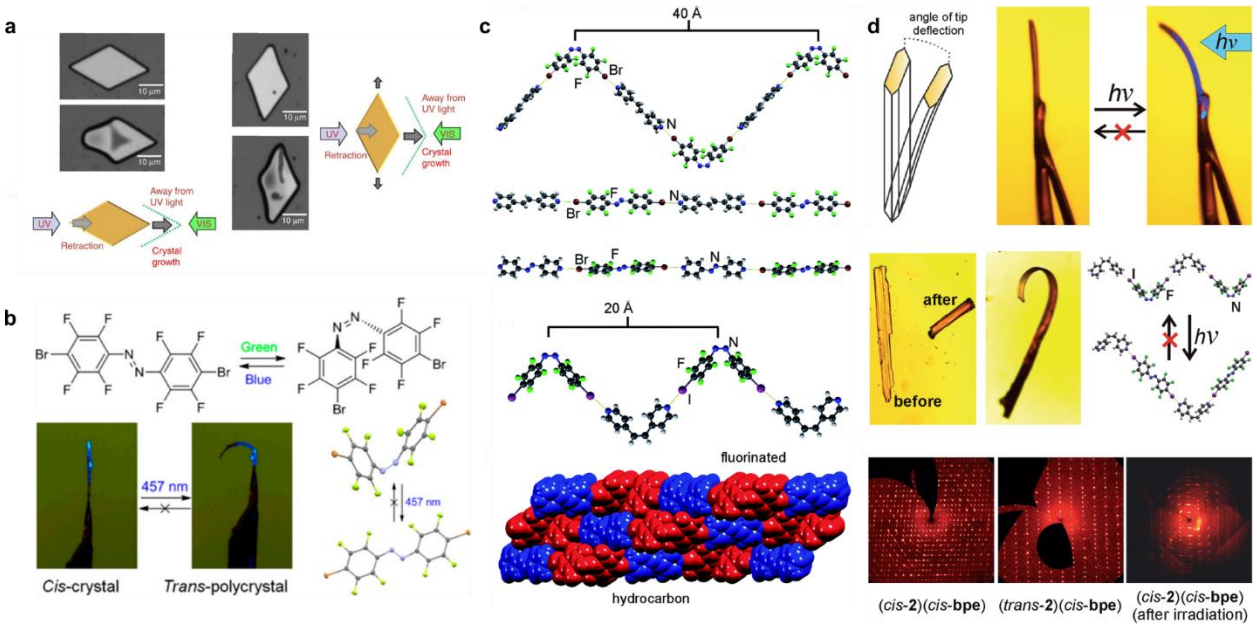

Figure 1.14. Azobenzene crystals and co-crystals that will bend and crawl. a) A single crystal of an azobenzene molecule undergoing a photo-induced change to the crystal that will result in the single crystal crawling away from the light irradiation (reproduced from reference [147]). **b)** *o*-fluorinated azobenzene crystals that will undergo a *cis* to *trans* isomerization resulting in photo-mechanical bending of the crystal (reproduced from reference [148]). **c)** Crystallographic packing of *trans* or *cis o*-fluorinated azobenzene co-crystals, shown as linear and zig-zig halogen-bonded chains. **d)** A single crystal of a *cis*-azobenzene co-crystal before and after photo-irradiation, showing significant photo-mechanical bending as it isomerizes to the *trans* co-crystal (top), precession images of the *cis* co-crystal before and after irradiation and *trans* co-crystal shown as a reference (images **c)** and **d)** are reproduced from reference [37]).

Azobenzene molecules have been used to form multiple different crystalline actuators. These actuators can either be reversible through *trans*→*cis* isomerization, followed by thermal relaxation or photo-induced isomerization, from *cis*→*trans*, or irreversibly, in which the crystal will not revert back to its starting crystalline habit. Bushuyev *et al*. published an in-depth study on

how crystalline packing will affect photo-actuation of azobenzene crystals, by using various commercially available dyes, with differing functional groups.[149] All five crystal systems studied would undergo various amounts of photo-mechanical bending, through *trans*→*cis* isomerization. The authors suggested that there was a relationship between the crystal packing and the photo-responsive properties of the crystal, resulting in differences of deflection angle between the different crystals studied. It was found that the density of the crystal plays a large role in the photo-mechanical bending, as those with the lowest density had the greatest angle of deflection while those with the highest density had the lowest angle of deflection. Their findings highlight the importance that density of the crystal plays into the photo-responsive nature of a crystal.

Fluorinated azobenzenes exhibit enhanced stability of the *cis* isomers (*cis*-Fazo),[35] enabling their crystallization to form solid state photo-actuators. *Cis*-Fazo single crystals formed long thin needles through azo···π stacking.[150] When the needles were irradiated with blue (457 nm) light the molecules within the crystal began to isomerize from *cis* azo to *trans* azo, resulting in the crystal undergoing a large range of motion (**Figure 1.14b**).[148] Due to the chemical isomerization going from the meta-stable *cis* isomer to the more stable *trans* isomer this process is irreversible, and the resultant crystal remains curved after irradiation. Interestingly, the crystals of the *trans* isomer exhibited no photo-mechanical response. Due to the azobenzenes containing either iodine or bromine in the *para*-position of the benzene rings, these molecules can act as halogen bond donors. Bushuyev *et al*. used the molecules as halogen bond donors with multiple different halogen bond acceptors, to tune the photo-response of the crystals (**Figures 1.14c,d**). It was found that the use of different coformers can lead to co-crystal materials of different calculated densities, which affects both the deflection angle and the laser power required to induce the photo-response. The co-crystallization exhibited additional effects including stabilizing the thermodynamic properties

of the crystals, with single crystals of the *cis*-azobenzenes converting to *trans*-azobenzene by heating through a melt and recrystallization, while the co-crystals do not undergo this melt and instead just isomerize. The authors also monitored the transitions between the *cis* co-crystals and the *trans* co-crystals *in situ* by single crystal X-ray diffraction, with experiments performed at room temperature and at 200 K. The room temperature experiments showed new crystallographic reflections assigned as the *trans* co-crystal, while the low temperature experiments showed the complete disappearance of reflections, suggesting that the single-crystal-to-single-crystal experiment occurs *via* an amorphous intermediate which will recrystallize into the *trans* co-crystal.

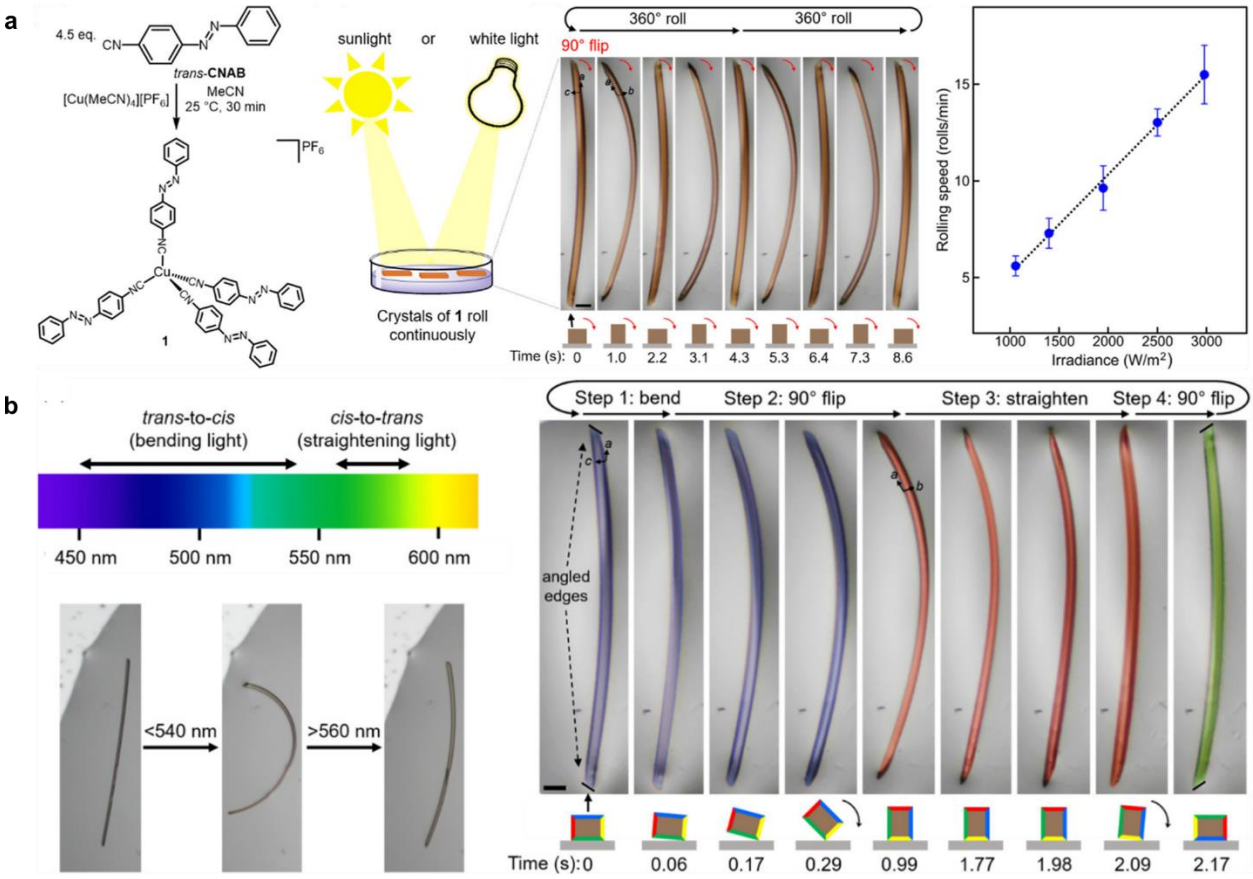

Figure 1.15. Photo-induced rolling of a highly strained azobenzene crystal. a) Schematic of an azobenzene functionalized molecule, a demonstration of a single crystal of the copper complex rolling upon photo-irradiation and the rotational speed dependence on irradiance. **b)** Example of visible light that induces either bending of the single crystal (*trans* to *cis*) or straightening of the single crystal (*cis* to *trans*) (left), and irradiation by a broad light source inducing rolling of a single crystal through reversible *trans* to *cis* and *cis* to *trans* isomerization (**a, b** reproduced from reference [151]).

Photo-induced changes of shape for an azobenzene-based crystal do not necessarily involve bending, as shown by the report of Uchida *et al*. which describes a crystalline material that will retract away from the area of UV light irradiation and grow towards the area of visible irradiation (**Figure 1.14a**).[147] The resultant photo-induced motion leads to translational crawling of the

crystal. This motion is induced by rapid isomerization from *trans*→*cis* by the UV light, and *cis*→*trans* by the visible light. Such crawling crystals can be used as remote-controlled micrometre-sized vehicles. Similarly, continuous motion of azobenzene single crystals upon light irradiation has been shown in a Cu(I)-isocyanoazobenzene complex (**Figure 1.15**).[151] This multicomponent crystal packs in the solid state with a highly twisted azobenzene ligand forming a coordination bond to the copper atom. When the single crystal is irradiated under white light, the crystal will continuously roll, which was associated to ongoing *trans*→*cis* and *cis*→*trans* isomerization processes. Rolling was found to be a consequence of continuous bending and straightening of the crystal: blue light of wavelength in the range 450–530 nm was found to induce crystal bending due to *trans*→*cis* isomerization, while light with wavelength in the 560–580 nm range was found to result in *cis*→*trans* isomerization and straightening of the crystal.

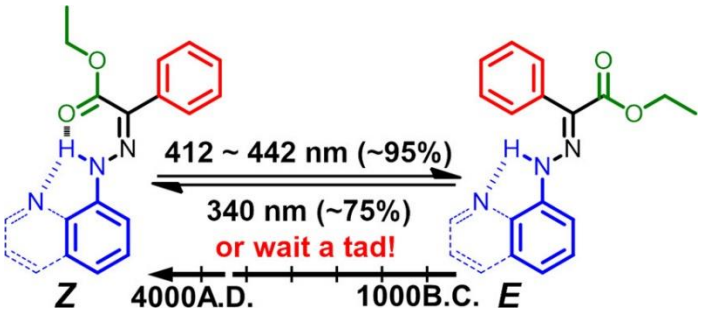

Scheme 1.5. Example of hydrazone photo-isomerization and stability (reproduced from reference [152]).

Hydrazone molecular photo-switches have two distinct isomers, a thermodynamically favorable *Z*- and a meta-stable *E*-form. The two isomeric forms can interconvert upon light irradiation, or the *E* isomer will thermally convert to the *Z*. Hydrazone-based molecular photo-switches are of interest due to the high stability of both these isomers, with the *E*-isomers of many hydrazone derivatives exhibiting half-lives longer than 1000 years.[152] Due to such high stability,

the hydrazone systems have been used as photo-actuators in which photo-induced isomerization causes the material to bend away from the light irradiation. As the irradiation stops, however, the bent material will retain its current shape rather then recoiling back.[153] The material can then be reversed *via* the back isomerization. Although these molecules have been used in developing solid state on/off fluorescent probes,[154,155] when developing photo-actuators, the molecules have been limited to polymeric and liquid crystalline materials. This allows for a unique opportunity for future crystal engineers to develop photo-actuators based on crystalline materials.

1.6.2 Photo-salient crystals

In addition to the photo-mechanical crystals that have been highlighted already, where the molecules can bend, twist, crawl, etc., other dynamic crystals can undergo a substantial size change either growing or shrinking upon light, and potentially even jumping. Similar to thermo-salient crystals that gain or lose size upon heating resulting in jumping,[156] these photo-salient crystals will undergo a size change or jumping effect either reversible or irreversible, through either a polymorphic transition, isomerizations, or chemical bond formation. A photo-salient effect is considered a photo-mechanical phenomenon in which stress is developed in response to a mechanical force created inside a crystal due to changes of the structure as a result of photochemical reaction or polymorphic switching culminating in a stochastic release of energy.

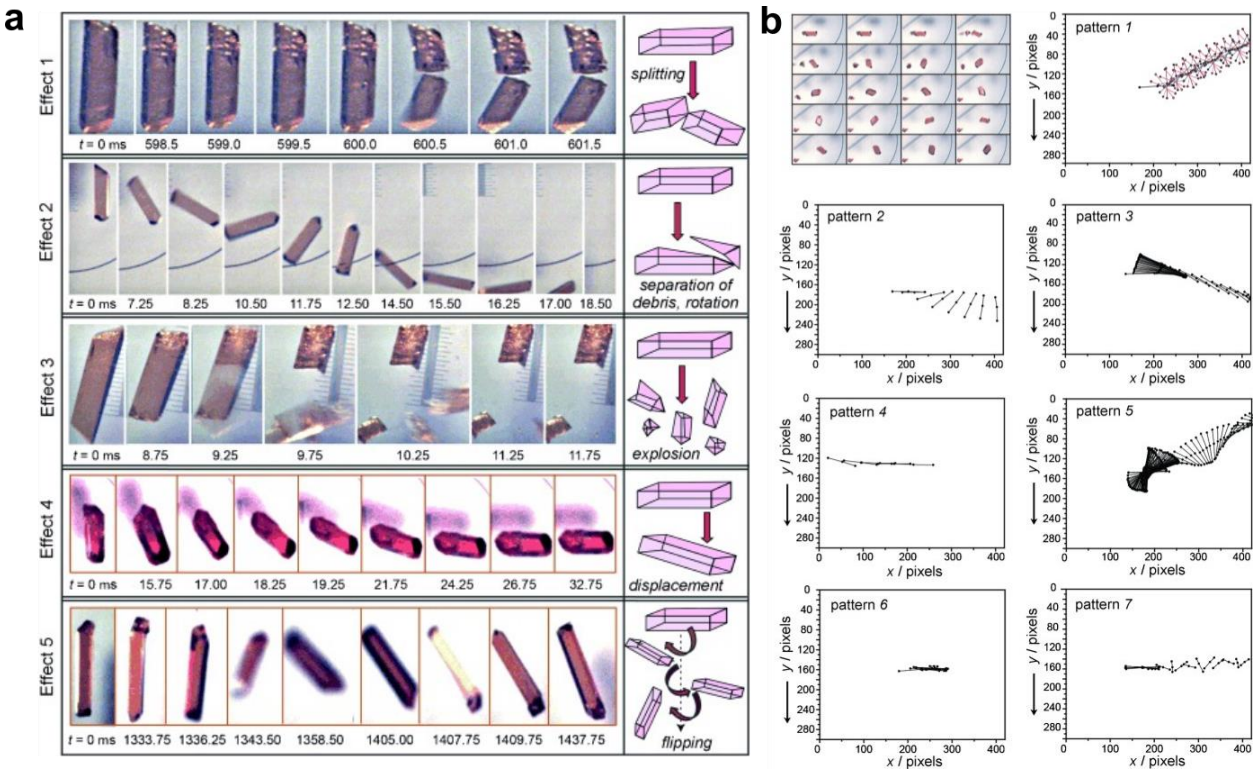

Figure 1.16. Example of a photo-salient crystal. a) Differing effects that will occur upon photo-induced irradiation of the cobalt complex. **b)** Descriptions of the motion of single crystals upon photo-irradiation (reproduced from reference [157]).

Naumov *et al.* proposed that molecular single crystals could be used to mimic some motions in biological systems such as tissues, or organs.[157] Specifically, this work focused on single crystals of the monomeric coordination complex $[Co(NH_3)_5(NO_2)]Cl(NO_3)$ that were found to jump up to 10^2–10^5 times their own length upon irradiation by high intensity UV light (**Figure 1.16**). These cobalt complexes have been shown to undergo intramolecular linkage isomerization, which causes strain and stress at the area of irradiation which causes cracking and breakage of the crystal. The authors here discovered a second crystalline habit which, rather than cracking or breaking, would undergo hopping suddenly in a random manner in random directions. Therefore, the authors found that a small extent of a macroscopic photochemical reaction can cause

centimetre-scale changes in the form of mechanical motion. In another report by Seki *et al.*, a gold(I) isocyanide complex was found to undergo a photo-induced polymorphic transition upon irradiation with a high-powered UV light source.[38,158] The polymorphic change is accompanied with a shortening of the Au···Au bond distance, and change of the emission profile of the solid. Interestingly also the crystals will exhibit a salient effect due to changes in the unit cell, causing the crystal to jump when irradiated.

The photo-salient effect has additionally been found to be triggered by [2+2] cycloadditions.[159] The packing of several coordination metal complexes are such that the distance between olefins are within 4.2 Å, allowing for the possibility to form a photo-induced [2+2] dimerization. Interestingly, the formation of the new bonds alters the packing of the molecules and therefore puts enough strain on the crystalline habit to cause a salient effect. The authors reported that even when using low powered light the crystals would pop "violently". The crystals exhibited 3 different kinematic effects, shown to be dependent on the crystal size. While larger crystals would roll, medium samples would break at a point of the crystal causing the intact part to be propelled away, and small crystals would explode into smaller pieces, showing that careful control over crystal shape and size is important in the design of photo-actuating systems. This work was expanded by Medishetty *et al*. highlighting that salient effects are more common for [2+2] cycloadditions than originally realized.[160] The authors used nine differing photo-reactive gold complexes, of which six of the nine exhibit a photo-salient response whether it was hopping, popping, or leaping. The authors concluded that the photo-salient nature of the crystals relied heavily on the crystal packing of the system. Therefore crystal engineering contributes a large role in the photo-actuation properties of these systems.

1.7 Conclusions and future outlook

Throughout this Introduction section many recent advances have been highlighted in the development of photo-responsive molecular solids, with the aim to illustrate how concepts of crystal engineering and solid state supramolecular chemistry can be used to alter the optical or photo-responsive properties of crystalline solids. Among these examples, particular attention has been given to systems based on halogen bonding, which enabled the assembly of molecular building blocks to generate and enhance solid state properties, such as dichroism, luminescence properties, photo-actuation, and ability to undergo topochemical solid state [2+2] photo-cycloadditions.

While this review has covered a wide range of different types of photo-responsive behaviour, there are still areas of the field that continue to grow, either by studying new photo-switches and their specific photo-response such as hydrazones, or by finding completely new types of photo-responsive behaviour by clever design of the crystalline structure. The subsequent Thesis Chapters will focus on the latter approach, and will detail the design of a series of co-crystals focused around a previously reported ortho-substituted fluorinated azobenzenes which are co-crystalized with a variety of volatile coformers. The crystallization of a light responsive dye and a volatile component allows for micrometer precision cutting of the material using low-powered visible light. This is a similar process to traditional light-induced chemical surface etching known as photo-lithography, which has been applied to polymeric resins,[161] hyperbolic metamaterials,[162] nanostructures,[163] photonic crystals[164] and co-crystal thin films,[165] yet these traditional methods require significantly higher energy and higher power than what we employed to our organic co-crystals. The development of such photo-carvable co-crystals is an advance in both photo-

responsive materials and crystal engineering, introducing molecular organic solids as a new class of materials that can be precision machined.

The research described in this Thesis begins with Chapter 2, outlining the discovery of photo-carvable co-crystals, highlighting the mechanism of decomposition occurring, and discussing ways of tuning the properties by selecting appropriate coformers. This research is further advanced in Chapter 3, where the photo-responsive *trans* azo dye is replaced with its meta-stable *cis* isomer, and the resultant co-crystals are shown to undergo three different photo-responses: photo-chromic, photo-mechanical, and photo-carving. These responses were found to be selectively light intensity driven, and additionally theoretical studies were performed to analyze the stability of the co-crystals covered in Chapters 2 and 3. Chapter 4, continues the research of photo-carvable co-crystals, in which we study the effect that replacing the volatile component with a blue absorbing dye will have on the system. The new co-crystals were found to undergo two separate photo-responses dependent on the wavelength of the excitation laser. Finally Chapter 5 introduces new photochemistry occurring in solid state hypohalites, in which the resultant photo-product is a direct result of the crystallographic arrangements of hypohalite ions in the solid state. A discussion of all the findings is provided in Chapter 6, with conclusions, and a summary of how overall this thesis highlights the power of crystal-engineering, and the effects that crystallographic arrangements of dye and volatile conformer molecules have on a variety of photo-responses of these materials in the solid state.

1.8 References

1. Szymański, W., Beierle, J. M., Kistemaker, H. A. V., Velema, W. A. & Feringa, B. L. Reversible Photocontrol of Biological Systems by the Incorporation of Molecular Photoswitches. *Chem. Rev.* **113**, 6114-6178, (2013).

2. Andjaba, J. M., Rybak, C. J., Wang, Z., Ling, J., Mein, J., & Uyeda, C. Catalytic Synthesis of Conjugated Azopolymers from Aromatic Diazides. *J. Am. Chem. Soc.* **143**, 3975-3982, (2021).

3. Fang, L. Zhang, H., Li, Z., Zhang, Y., Zhang, Y., & Zhang, H. Synthesis of Reactive Azobenzene Main-Chain Liquid Crystalline Polymers via Michael Addition Polymerization and Photomechanical Effects of Their Supramolecular Hydrogen-Bonded Fibers. *Macromolecules* **46**, 7650-7660, (2013).

4. Thum, M. D., Ratchford, D. C., Casalini, R., Wynne, J. H. & Lundin, J. G. Azobenzene-Doped Liquid Crystals in Electrospun Nanofibrous Mats for Photochemical Phase Control. *ACS Appl. Nano Mater.* **4**, 297-304, (2021).

5. Russew, M.-M. & Hecht, S. Photoswitches: From Molecules to Materials. *Advan. Mater.* **22**, 3348-3360, (2010).

6. Hemmer, J. R., Poelma, S. O., Treat, N., Page, Z. A., Dolinski, N. D., Diaz, Y. J., Tomlinson, W., Clark, K. D., Hooper, J. P., Hawker, C. & Read de Alaniz, J. Tunable Visible and Near Infrared Photoswitches. *J. Am. Chem. Soc.* **138**, (2016).

7. Kim, D. Li, L., Jiang, X. L., Shivshankar, V., Kumar, J., & Tripathy, S. K. Polarized laser induced holographic surface relief gratings on polymer films. *Macromolecules* **28**, 8835-8839 (1995).

8. Yager, K. G. & Barrett, C. J. All-optical patterning of azo polymer films. *Current Opinion in Solid State and Materials Science* **5**, 487-494, (2001).

9. Barrett, C. J., Mamiya, J.-i., Yager, K. G. & Ikeda, T. Photo-mechanical effects in azobenzene-containing soft materials. *Soft Matter* **3**, 1249-1261, (2007).

10. Banghart, M. R., Mourot, A., Fortin, D. L., Yao, J. Z., Kramer, R. H., & Trauner, D. Photochromic Blockers of Voltage-Gated Potassium Channels. *Angew. Chem. Int. Ed.* **48**, 9097-9101, (2009).

11. Liu, D., Xie, Y., Shao, H. & Jiang, X. Using Azobenzene-Embedded Self-Assembled Monolayers To Photochemically Control Cell Adhesion Reversibly. *Angew. Chem. Int. Ed.* **48**, 4406-4408, (2009).

12. Ferri, V. Elbing, M., Pace, G., Dickey, M. D., Zharnikov, & M., Samori, P. Light-Powered Electrical Switch Based on Cargo-Lifting Azobenzene Monolayers. *Angew. Chem. Int. Ed.* **47**, 3407-3409, (2008).

13. Wang, Y., Han, P., Zu, H., Wang, Z., Zhang, X., & Kabonov, A. V. Photocontrolled Self-Assembly and Disassembly of Block Ionomer Complex Vesicles: A Facile Approach toward Supramolecular Polymer Nanocontainers. *Langmuir* **26**, 709-715, (2010).

14. Baroncini, M., Groppi, J., Corra, S., Silvi, S. & Credi, A. Light-Responsive (Supra)Molecular Architectures: Recent Advances. *Adv. Opt. Mater.* **7**, 1900392, (2019).

15. Bandara, H. D. & Burdette, S. C. Photoisomerization in different classes of azobenzene. *Chem. Rev.* **41**, 1809-1825, (2012).

16. Castellanos, S. Goulet-Hanssens, A., Zhao, F., Dikhtiarenko, A., Pustovarenko, A., Hect, S., Gascon, J., Kapteijn, F., & Bleger D. Structural Effects in Visible-Light-Responsive Metal–Organic Frameworks Incorporating ortho-Fluoroazobenzenes. *Eur. J. Chem.* **22**, 746-752, (2016).

17. Goulet-Hanssens, A. & Barrett, C. J. Photo-control of biological systems with azobenzene polymers. *Journal of Polymer Science Part A: Polymer Chemistry* **51**, 3058-3070, (2013).

18. Lee, K. M., Koerner, H., Vaia, R. A., Bunning, T. J. & White, T. J. Relationship between the Photomechanical Response and the Thermomechanical Properties of Azobenzene Liquid Crystalline Polymer Networks. *Macromolecules* **43**, 8185-8190, (2010).

19. Ikeda, T. & Tsutsumi, O. Optical switching and image storage by means of azobenzene liquid-crystal films. *Science* **268**, 1873-1875 (1995).

20. Pang, X., Lv, J.-a., Zhu, C., Qin, L. & Yu, Y. Photodeformable Azobenzene-Containing Liquid Crystal Polymers and Soft Actuators. *Adv. Mater.* **31**, 1904224, (2019).

21. Yamada, M., Kondo, M., Mamiya, J.-I., Yu, Y., Kinoshita, M., Barrett, C. J., Photomobile Polymer Materials: Towards Light-Driven Plastic Motors. *Angew. Chem. Int. Ed.* **47**, 4986-4988, (2008).

22. Zeng, H., Wani, O. M., Wasylczyk, P. & Priimagi, A. Light-Driven, Caterpillar-Inspired Miniature Inching Robot. *Macromolecular Rapid Communications* **39**, 1700224, (2018).

23. Tanchak, O. M. & Barrett, C. J. Light-Induced Reversible Volume Changes in Thin Films of Azo Polymers: The Photomechanical Effect. *Macromolecules* **38**, 10566-10570, (2005).

24. Kim, K., Park, H., Park, K. J, Park, S. H., Kim, H. H., & Lee, S. Light-Directed Soft Mass Migration for Micro/Nanophotonics. *Adv. Opt. Mater.* **7**, 1900074, (2019).

25. Liang, X., Nishioka, H., Takenaka, N. & Asanuma, H. A DNA Nanomachine Powered by Light Irradiation. *ChemBioChem* **9**, 702-705, (2008).

26. Klajn, R., Wesson, P. J., Bishop, K. J. M. & Grzybowski, B. A. Writing Self-Erasing Images using Metastable Nanoparticle "Inks". *Angew. Chem. Int. Ed.* **48**, 7035-7039, (2009).

27. Landry, M. J., Gu, K., Harris, S. N., Al-Alwan, L., Gutsin, L., De Biasio, D., Jiang, B., Nakamura, D., S. Corkery, T. C., Kennedy, T. E., & Barrett, C. J. Tunable Engineered Extracellular Matrix Materials: Polyelectrolyte Multilayers Promote Improved Neural Cell Growth and Survival. *Macromol Biosci.* **19**, 1900036, (2019).

28. Landry, M. J., Applegate, M. B., Bushyev, O., S., Omenetto, F. G., Kaplan, D. L, Cronin-Golomb, M., & Barrett, C. J. Photo-induced structural modification of silk gels containing azobenzene side groups. *Soft Matter* **13**, 2903-2906, (2017).

29. Comstock, M. J., Levy, N. Kirakosian, A., Cho, J., Lauterwasser, F., Harvey, J. H., Strubbe, D. A., Frechet, J. M. J., Trauner, D., Louie, S. G., & Crommie, M. F. Reversible Photomechanical Switching of Individual Engineered Molecules at a Metallic Surface. *Phys. Rev. Lett.* **99**, 038301, (2007).

30. Borowiak, M., Nahoboo, W., Reynders, M., Nekolla, K., Jalinot, P., Hasserodt, J., Rehberg, M., Delattre, M., Zahler, S., Vollmar, A., Trauner, D., & Thorn-Seshold, O. Photoswitchable Inhibitors of Microtubule Dynamics Optically Control Mitosis and Cell Death. *Cell* **162**, 403-411, (2015).

31. Fortin, D. L., Banghart, M. R., Dunn, T. W., Borges, K., Wagenaar, D. A., Gaudry, Q., Karakossian, M. H., Otis, T. S., Kristan, W. B., Trauner, D. & Kramer, R. H. Photochemical control of endogenous ion channels and cellular excitability. *Nat. Methods* **5**, 331-338, (2008).

32. Koshima, H. & Ojima, N. Photomechanical bending of 4-aminoazobenzene crystals. *Dyes Pigm* **92**, 798-801, (2012).

33. Taniguchi, T., Asahi, T. & Koshima, H. Photomechanical Azobenzene Crystals. *Crystals* **9**, 437 (2019).

34. Sun, S., Liang, S., Xu, W.-C., Xu, G. & Wu, S. Photoresponsive polymers with multi-azobenzene groups. *Polym. Chem.* **10**, 4389-4401, (2019).

35. Bléger, D., Schwarz, J., Brouwer, A. M. & Hecht, S. o-Fluoroazobenzenes as Readily Synthesized Photoswitches Offering Nearly Quantitative Two-Way Isomerization with Visible Light. *J. Am. Chem. Soc.* **134**, 20597-20600, (2012).

36. Aggarwal, K., Kuka, T. P., Banik, M., Medellin, B. P., Ngo, C. Q., Xie, D., Fernandes, Y., Dangerfield, T. L., Ye., E., Bouley, B., Jounson, K. A., Zhang, Y. J., Eberhart, J. K., & Que, E. L. Visible Light Mediated Bidirectional Control over Carbonic Anhydrase Activity in Cells and in Vivo Using Azobenzenesulfonamides. *J. Am. Chem. Soc.* **142**, 14522-14531, (2020).

37. Bushuyev, O. S., Corkery, T. C., Barrett, C. J. & Friščić, T. Photo-mechanical azobenzene cocrystals and in situ X-ray diffraction monitoring of their optically-induced crystal-to-crystal isomerisation. *Chem. Sci.* **5**, 3158-3164, (2014).

38. Stumpel, J. E., Saccone, M., Dichiarante, V., Lehtonen, O., Virkki, M., Metrangolo, P. & Priimagi, A. Surface-Relief Gratings in Halogen-Bonded Polymer–Azobenzene Complexes: A Concentration-Dependence Study. *Molecules* **22**, 1844 (2017).

39. Kravchenko, A., Shevchenko, A., Ovchinnikov, V., Priimagi, A. & Kaivola, M. Optical Interference Lithography Using Azobenzene-Functionalized Polymers for Micro- and Nanopatterning of Silicon. *Adv. Mater.* **23**, 4174-4177, (2011).

40. Desiraju, G. R. Crystal Engineering: From Molecule to Crystal. *J. Am. Chem. Soc.* **135**, 9952-9967, (2013).

41. Biradha, K. & Santra, R. Crystal engineering of topochemical solid state reactions. *Chem. Soc. Rev.* **42**, 950-967, (2013).

42. Mir, N. A., Dubey, R. & Desiraju, G. R. Strategy and Methodology in the Synthesis of Multicomponent Molecular Solids: The Quest for Higher Cocrystals. *Acc. Chem. Res.* **52**, 2210-2220, (2019).

43. Aitipamula, S. *et al.* Polymorphs, Salts, and Cocrystals: What's in a Name? *Cryst. Growth Des.* **12**, 2147-2152, (2012).

44. Thakuria, R. & Sarma, B. Drug-Drug and Drug-Nutraceutical Cocrystal/Salt as Alternative Medicine for Combination Therapy: A Crystal Engineering Approach. *Crystals* **8**, 101 (2018).

45. Duggirala, N. K., Perry, M. L., Almarsson, Ö. & Zaworotko, M. J. Pharmaceutical cocrystals: along the path to improved medicines. *Chem. Commun.* **52**, 640-655, (2016).

46. Kavanagh, O. N., Croker, D. M., Walker, G. M. & Zaworotko, M. J. Pharmaceutical cocrystals: from serendipity to design to application. *Drug Discov. Today* **24**, 796-804, (2019).

47. MacGillivray, L. R. Papaefstathiou, G., Friščić, T., Hamilton, T. D., Bucar, D.-K., Chu, Q., Varshney, D. B., & Georgiev, I. G. Supramolecular Control of Reactivity in the Solid State: From Templates to Ladderanes to Metal−Organic Frameworks. *Acc. Chem. Res.* **41**, 280-291, (2008).

48. Lu, B., Fang, X. & Yan, D. Luminescent Polymorphic Co-crystals: A Promising Way to the Diversity of Molecular Assembly, Fluorescence Polarization, and Optical Waveguide. *ACS Appl. Mater. Interfaces* **12**, 31940-31951, (2020).

49. Christopherson, J. C., Topić, F., Barrett, C. J. & Friščić, T. Halogen-Bonded Cocrystals as Optical Materials: Next-Generation Control over Light–Matter Interactions. *Cryst. Growth. Des.* **18**, 1245-1259, doi:10.1021/acs.cgd.7b01445 (2018).

50. Liu, C.-H., Niazi, M. R. & Perepichka, D. F. Strong Enhancement of π-Electron Donor/Acceptor Ability by Complementary DD/AA Hydrogen Bonding. *Angew. Chem. Int. Ed.* **58**, 17312-17321, (2019).

51. Bora, P., Saikia, B. & Sarma, B. Regulation of π···π Stacking Interactions in Small Molecule Cocrystals and/or Salts for Physiochemical Property Modulation. *Cryst. Growth. Des.* **18**, 1448-1458, (2018).

52. Karki, S., Friščić, T. & Jones, W. Control and interconversion of cocrystal stoichiometry in grinding: stepwise mechanism for the formation of a hydrogen-bonded cocrystal. *CrystEngComm* **11**, 470-481, (2009).

53. Cinčić, D., Friščić, T. & Jones, W. Isostructural Materials Achieved by Using Structurally Equivalent Donors and Acceptors in Halogen-Bonded Cocrystals. *Chem. Eur. J.* **14**, 747-753, (2008).

54. Xiao, Y., Liu, Y. Q., Li, G. & Huang, P. Microwave-assisted synthesis, structure and properties of a co-crystal compound with 2-ethoxy-6-methyliminomethyl-phenol. *Supramol Chem.* **27**, 161-166, (2015).

55. Steiner, T. The hydrogen bond in the solid state. *Angew. Chem. Int. Ed.* **41**, 48-76 (2002).

56. Gilli, G. & Gilli, P. *The nature of the hydrogen bond: outline of a comprehensive hydrogen bond theory*. Vol. 23 (Oxford university press, 2009).

57. Kollman, P. A. & Allen, L. C. Theory of the hydrogen bond. *Chem. Rev.* **72**, 283-303 (1972).

58. Desiraju, G. R. Supramolecular Synthons in Crystal Engineering—A New Organic Synthesis. *Angew. Chem. Int. Ed.* **34**, 2311-2327, (1995).

59. Saikia, B., Bora, P., Khatioda, R. & Sarma, B. Hydrogen Bond Synthons in the Interplay of Solubility and Membrane Permeability/Diffusion in Variable Stoichiometry Drug Cocrystals. *Cryst. Growth Des.* **15**, 5593-5603, (2015).

60. Bavishi, D. D. & Borkhataria, C. H. Spring and parachute: How cocrystals enhance solubility. *Prog. Cryst. Growth. Charact. Mater.* **62**, 1-8, (2016).

61. Bolla, G. & Nangia, A. Pharmaceutical cocrystals: walking the talk. *Chem. Commun.* **52**, 8342-8360, doi:10.1039/C6CC02943D (2016).

62. Gala, U., Chuong, M. C., Varanasi, R. & Chauhan, H. Characterization and Comparison of Lidocaine-Tetracaine and Lidocaine-Camphor Eutectic Mixtures Based on Their Crystallization and Hydrogen-Bonding Abilities. *AAPS PharmSciTech* **16**, 528-536, (2015).

63. McNamara, D. P. *et al.* Use of a Glutaric Acid Cocrystal to Improve Oral Bioavailability of a Low Solubility API. *Pharm. Res.* **23**, 1888-1897, (2006).

64. MacGillivray, L. R., Reid, J. L. & Ripmeester, J. A. Supramolecular Control of Reactivity in the Solid State Using Linear Molecular Templates. *J. Am. Chem. Soc.* **122**, 7817-7818, (2000).

65. Sarma, B. & Saikia, B. Hydrogen bond synthon competition in the stabilization of theophylline cocrystals. *CrystEngComm* **16**, 4753-4765, (2014).

66. Mukherjee, A., Tothadi, S. & Desiraju, G. R. Halogen Bonds in Crystal Engineering: Like Hydrogen Bonds yet Different. *Acc. Chem. Res.* **47**, 2514-2524, (2014).

67. Cavallo, G. *et al.* The Halogen Bond. *Chem. Rev.* **116**, 2478-2601, (2016).

68. Clark, T. Halogen bonds and σ-holes. *Faraday. Discuss.* **203**, 9-27 (2017).

69. Forni, A., Pieraccini, S., Rendine, S., Gabas, F. & Sironi, M. Halogen-Bonding Interactions with π Systems: CCSD(T), MP2, and DFT Calculations. *ChemPhysChem* **13**, 4224-4234, (2012).

70. Huber, S. M., Scanlon, J. D., Jimenez-Izal, E., Ugalde, J. M. & Infante, I. On the directionality of halogen bonding. *Phys. Chem. Chem. Phys.* **15**, 10350-10357, (2013).

71. Metrangolo, P., Meyer, F., Pilati, T., Resnati, G. & Terraneo, G. Halogen Bonding in Supramolecular Chemistry. *Angew. Chem. Int. Ed.* **47**, 6114-6127, (2008).

72. Metrangolo, P. & Resnati, G. Type II halogen···halogen contacts are halogen bonds. *IUCrJ* **1**, 5-7, (2014).

73. Siram, R. B. K., Karothu, D. P., Guru Row, T. N. & Patil, S. Unique Type II Halogen···Halogen Interactions in Pentafluorophenyl-Appended 2,2′-Bithiazoles. *Cryst. Growth. Des.* **13**, 1045-1049, (2013).

74. Ford, M. C., Saxton, M. & Ho, P. S. Sulfur as an Acceptor to Bromine in Biomolecular Halogen Bonds. *J. Phys. Chem. Lett.* **8**, 4246-4252, (2017).

75. Daniliuc, C. G., Hrib, C. G., Jones, P. G. & du Mont, W.-W. Directed Selenium–Iodine Halogen Bonding and Se···H–C Contacts in Solid Iododiisopropylphosphane Selenide. *Cryst. Growth. Des.* **12**, 185-188, (2012).

76. Lisac, K. *et al.* Halogen-bonded cocrystallization with phosphorus, arsenic and antimony acceptors. *Nat. Commun.* **10**, 61, (2019).

77. Robertson, C. C. *et al.* Hydrogen bonding vs. halogen bonding: the solvent decides. *Chem. Sci.* **8**, 5392-5398, (2017).

78. Gullo, M. C., Baldini, L., Casnati, A. & Marchiò, L. Halogen Bonds Direct the Solid State Architectures of a Multivalent Iodopropargylcalix[4]arene. *Cryst. Growth Des.* **20**, 3611-3616, (2020).

79. Gurbanov, A. V. *et al.* Halogen bonding in cadmium(ii) MOFs: its influence on the structure and on the nitroaldol reaction in aqueous medium. *Dalton Trans.* **51**, 1019-1031, (2022).

80. Amombo Noa, F. M., Bourne, S. A., Su, H., Weber, E. & Nassimbeni, L. R. Hydrogen Bonding versus Halogen Bonding in Host–Guest Compounds. *Cryst. Growth Des.* **16**, 4765-4771, (2016).

81. Saccone, M. *et al.* Photoresponsive Halogen-Bonded Liquid Crystals: The Role of Aromatic Fluorine Substitution. *Chem. of Mater.* **31**, 462-470, (2019).

82. Bushuyev, O. S., Friščić, T. & Barrett, C. J. Controlling Dichroism of Molecular Crystals by Cocrystallization. *Cryst. Growth Des.* **16**, 541-545, (2016).

83. Xiao, L. *et al.* Room-Temperature Phosphorescence in Pure Organic Materials: Halogen Bonding Switching Effects. *Chem. Eur. J.* **24**, 1801-1805, (2018).

84. Priimagi, A. *et al.* Halogen Bonding versus Hydrogen Bonding in Driving Self-Assembly and Performance of Light-Responsive Supramolecular Polymers. *Adv. Funct. Mater.* **22**, 2572-2579, (2012).

85. Hirshfeld, F. L. & Schmidt, G. M. J. Topochemical control of solid-state polymerization. *Journal of Polymer Science Part A: General Papers* **2**, 2181-2190, (1964).

86. Cohen, M. D. & Schmidt, G. M. J. 383. Topochemistry. Part I. A survey. *Journal of the Chemical Society (Resumed)*, 1996-2000, (1964).

87. Cohen, M. D., Schmidt, G. M. J. & Sonntag, F. I. 384. Topochemistry. Part II. The photochemistry of trans-cinnamic acids. *Journal of the Chemical Society (Resumed)*, (1964).

88. Bhogala, B. R., Captain, B., Parthasarathy, A. & Ramamurthy, V. Thiourea as a Template for Photodimerization of Azastilbenes. *J. Am. Chem. Soc.* **132**, 13434-13442, (2010).

89. Sinnwell, M. A. & MacGillivray, L. R. Halogen-Bond-Templated [2+2] Photodimerization in the Solid State: Directed Synthesis and Rare Self-Inclusion of a Halogenated Product. *Angew. Chem. Int. Ed.* **55**, 3477-3480, (2016).

90. Liu, D. *et al.* Single-Crystal-to-Single-Crystal Transformations of Two Three-Dimensional Coordination Polymers through Regioselective [2+2] Photodimerization Reactions. *Angew. Chem. Int. Ed.* **49**, 4767-4770, (2010).

91. Gao, X., Friščić, T. & MacGillivray, L. R. Supramolecular Construction of Molecular Ladders in the Solid State. *Angew. Chem. Int. Ed.* **43**, 232-236, (2004).

92. Rath, B. B. & Vittal, J. J. Single-Crystal-to-Single-Crystal [2 + 2] Photocycloaddition Reaction in a Photosalient One-Dimensional Coordination Polymer of Pb(II). *J. Am. Chem. Soc.* **142**, 20117-20123, doi:10.1021/jacs.0c09577 (2020).

93. Medishetty, R., Koh, L. L., Kole, G. K. & Vittal, J. J. Solid-State Structural Transformations from 2D Interdigitated Layers to 3D Interpenetrated Structures. *Angew. Chem. Int. Ed.* **50**, 10949-10952, (2011).

94. Li, C., Campillo-Alvarado, G., Swenson, D. C. & MacGillivray, L. R. Exploiting Aurophilic Interactions in a [2 + 2] Photocycloaddition: Single-Crystal Reactivity with Changes to Surface Morphology. *Inorg. Chem.* **58**, 12497-12500, (2019).

95. Alfuth, J., Jeannin, O. & Fourmigué, M. Topochemical, Single-Crystal-to-Single-Crystal [2+2] Photocycloadditions Driven by Chalcogen-Bonding Interactions. *Angew. Chem. Int. Ed.* **61**, e202206249, (2022).

96. Quentin, J., Reinheimer, E. W. & MacGillivray, L. R. Halogen-Bond Mediated [2+2] Photodimerizations: A la Carte Access to Unsymmetrical Cyclobutanes in the Solid State. *Molecules* **27**, 1048 (2022).

97. Li, M., Schlüter, A. D. & Sakamoto, J. Solid-State Photopolymerization of a Shape-Persistent Macrocycle with Two 1,8-Diazaanthracene Units in a Single Crystal. *J. Am. Chem. Soc.* **134**, 11721-11725, (2012).

98. Servalli, M., Trapp, N. & Schlüter, A. D. Single-Crystal-to-Single-Crystal (SCSC) Linear Polymerization of a Desymmetrized Anthraphane. *Chem. Eur. J.* **24**, 15003-15012, (2018).

99. Morimoto, K. *et al.* Correlating Reaction Dynamics and Size Change during the Photomechanical Transformation of 9-Methylanthracene Single Crystals. *Angew. Chem. Int. Ed.* **61**, e202114089, (2022).

100. Matsumoto, A., Nagahama, S. & Odani, T. Molecular Design and Polymer Structure Control Based on Polymer Crystal Engineering. Topochemical Polymerization of 1,3-Diene Mono- and Dicarboxylic Acid Derivatives Bearing a Naphthylmethylammonium Group as the Countercation. *J. Am. Chem. Soc.* **122**, 9109-9119, (2000).

101. Nagahama, S., Inoue, K., Sada, K., Miyata, M. & Matsumoto, A. Two-Dimensional Hydrogen Bond Networks Supported by CH/π Interaction Leading to a Molecular Packing Appropriate for Topochemical Polymerization of 1,3-Diene Monomers. *Cryst. Growth Des.* **3**, 247-256, (2003).

102. Sun, A., Lauher, J. W. & Goroff, N. S. Preparation of Poly(diiododiacetylene), an Ordered Conjugated Polymer of Carbon and Iodine. *Science* **312**, 1030-1034, (2006).

103. Luo, L. *et al.* Poly(diiododiacetylene): Preparation, Isolation, and Full Characterization of a Very Simple Poly(diacetylene). *J. Am. Chem. Soc.* **130**, 7702-7709, (2008).

104. Xu, R., Schweizer, W. B. & Frauenrath, H. Perfluorophenyl–Phenyl Interactions in the Crystallization and Topochemical Polymerization of Triacetylene Monomers. *Chem. Eur. J.* **15**, 9105-9116, (2009).

105. Itoh, T. *et al.* Cis-Specific Topochemical Polymerization: Alternating Copolymerization of 7,7,8,8-Tetrakis(methoxycarbonyl)quinodimethane with 7,7,8,8-Tetracyanoquinodimethane in the Solid State. *Angew. Chem. Int. Ed.* **50**, 2253-2256, (2011).

106. Samanta, R. *et al.* Mechanical Actuation and Patterning of Rewritable Crystalline Monomer−Polymer Heterostructures via Topochemical Polymerization in a Dual-Responsive Photochromic Organic Material. *ACS. Appl. Mater. Interfaces* **12**, 16856-16863, (2020).

107. Qi, A. *et al.* Hydroxypropyl Cellulose Methacrylate as a Photo-Patternable and Biodegradable Hybrid Paper Substrate for Cell Culture and Other Bioapplications. *Adv. Healthc. Mater.* **3**, 543-554, (2014).

108. Scott, J. L. & Tanaka, K. Photochromic Crystals: Toward an Understanding of Color Development in the Solid State. *Cryst. Growth Des.* **5**, 1209-1213, (2005).

109. Irie, M., Fukaminato, T., Matsuda, K. & Kobatake, S. Photochromism of Diarylethene Molecules and Crystals: Memories, Switches, and Actuators. *Chem. Rev.* **114**, 12174-12277, (2014).

110. Li, X., Xu, Y., Li, F. & Ma, Y. Organic light-emitting diodes based on an ambipolar single crystal. *Org. Electron.* **13**, 762-766, (2012).

111. Huang, R., Wang, C., Wang, Y. & Zhang, H. Elastic Self-Doping Organic Single Crystals Exhibiting Flexible Optical Waveguide and Amplified Spontaneous Emission. *Adv. Mater*. **30**, 1800814, (2018).

112. Cariati, E. *et al.* Tuning second-order NLO responses through halogen bonding. *Chem. Commun.* 2590-2592, (2007).

113. Christopherson, J.-C. *et al.* Assembly and dichroism of a four-component halogen-bonded metal–organic cocrystal salt solvate involving dicyanoaurate(I) acceptors. *Faraday Discuss.* **203**, 441-457, (2017).

114. Vainauskas, J., Topić, F., Bushuyev, O. S., Barrett, C. J. & Friščić, T. Halogen bonding to the azulene π-system: cocrystal design of pleochroism. *Chem. Commun.* **56**, 15145-15148, (2020).

115. Natansohn, A. & Rochon, P. Photoinduced Motions in Azo-Containing Polymers. *Chem. Rev.* **102**, 4139-4176, (2002).

116. Zhao, Y. & Ikeda, T. *Smart light-responsive materials: azobenzene-containing polymers and liquid crystals*. (John Wiley & Sons, 2009).

117. Schönhoff, M., Mertesdorf, M. & Lösche, M. Mechanism of photoreorientation of azobenzene dyes in molecular films. *J. Phys. Chem.* **100**, 7558-7565 (1996).

118. Campillo-Alvarado, G., Liu, R. J., Davies, D. W. & Diao, Y. Enhancing Single-Crystal Dichroism of an Asymmetric Azo Chromophore by Perfluorophenyl Embraces and Boron Coordination. *Cryst. Growth Des.* **21**, 3143-3147 (2021).

119. Morimoto, K., Tsujioka, H., Kitagawa, D. & Kobatake, S. Photoreversible Birefringence Change of Diarylethene Single Crystals as Revealed by Change in Molecular Polarizability Anisotropy. *J. Phys. Chem. A* **124**, 4732-4741, doi:10.1021/acs.jpca.0c02774 (2020).

120. Liu, H., Lu, Z., Zhang, Z., Wang, Y. & Zhang, H. Highly Elastic Organic Crystals for Flexible Optical Waveguides. *Angew. Chem. Int. Ed.* **57**, 8448-8452, (2018).

121. Gierschner, J. *et al.* Luminescence in Crystalline Organic Materials: From Molecules to Molecular Solids. *Adv. Opt. Mater.* **9**, 2002251, (2021).

122. Tang, S. *et al.* Organic Crystalline Optical Waveguides That Remain Elastic from −196 to ≈200 °C. *Adv. Opt. Mater.* 2200627, (2022).

123. Hayashi, S. & Koizumi, T. Elastic Organic Crystals of a Fluorescent π-Conjugated Molecule. *Angew. Chem. Int. Ed.* **55**, 2701-2704, (2016).

124. Panda, M. K. *et al.* Spatially resolved analysis of short-range structure perturbations in a plastically bent molecular crystal. *Nat. Chem.* **7**, 65-72, (2015).

125. Lan, L. *et al.* Organic Single-Crystal Actuators and Waveguides that Operate at Low Temperatures. *Adv. Mater.* **34**, 2200471, (2022).

126. Karothu, D. P. *et al.* Mechanically robust amino acid crystals as fiber-optic transducers and wide bandpass filters for optical communication in the near-infrared. *Nat. Commun.* **12**, 1326, (2021).

127. Di, Q. *et al.* Fluorescence-based thermal sensing with elastic organic crystals. *Nat. Commun.* **13**, 5280, (2022).

128. Chu, X. *et al.* Engineering Mechanical Compliance of an Organic Compound toward Flexible Crystal Lasing Media. *J. Phys. Chem. Lett.* **11**, 5433-5438, (2020).

129. Du, S., Ma, S., Xu, B. & Tian, W. Optical Waveguide and Photoluminescent Polarization in Organic Cocrystal Polymorphs. *J. Phys. Chem. Lett.* **12**, 9233-9238, (2021).

130. Shao, B. *et al.* Luminescent switching and structural transition through multiple external stimuli based on organic molecular polymorphs. *J. Mater. Chem. C* **7**, 3263-3268, (2019).

131. Ma, Y.-X., Wei, G.-Q., Chen, S., Lin, H.-T. & Wang, X.-D. Self-assembled organic homostructures with tunable optical waveguides fabricated via "cocrystal engineering". *Chem. Commun.* **57**, 11803-11806, (2021).

132. Feng, Q. *et al.* Tuning solid-state fluorescence of pyrene derivatives via a cocrystal strategy. *CrystEngComm* **15**, 3623-3629, (2013).

133. Shen, Q. J., Wei, H. Q., Zou, W. S., Sun, H. L. & Jin, W. J. Cocrystals assembled by pyrene and 1,2- or 1,4-diiodotetrafluorobenzenes and their phosphorescent behaviors modulated by local molecular environment. *CrystEngComm* **14**, 1010-1015, (2012).

134. Yan, D. *et al.* A Cocrystal Strategy to Tune the Luminescent Properties of Stilbene-Type Organic Solid-State Materials. *Angew. Chem. Int. Ed.* **50**, 12483-12486, (2011).

135. Bhowal, R., Biswas, S., Adiyeri Saseendran, D. P., Koner, A. L. & Chopra, D. Tuning the solid-state emission by co-crystallization through σ- and π-hole directed intermolecular interactions. *CrystEngComm* **21**, 1940-1947, (2019).

136. Salunke, J. K. *et al.* Halogen-Bond-Assisted Photoluminescence Modulation in Carbazole-Based Emitter. *Sci. Rep.* **8**, 14431, (2018).

137. d'Agostino, S., Grepioni, F., Braga, D. & Ventura, B. Tipping the Balance with the Aid of Stoichiometry: Room Temperature Phosphorescence versus Fluorescence in Organic Cocrystals. *Cryst. Growth Des.* **15**, 2039-2045, (2015).

138. Shen, Q. J. *et al.* Phosphorescent cocrystals constructed by 1,4-diiodotetrafluorobenzene and polyaromatic hydrocarbons based on C–I···π halogen bonding and other assisting weak interactions. *CrystEngComm* **14**, 5027-5034, (2012).

139. Naumov, P. *et al.* The Rise of the Dynamic Crystals. *J. Am. Chem. Soc.* **142**, 13256-13272, (2020).

140. Vogelsberg, C. S. & Garcia-Garibay, M. A. Crystalline molecular machines: function, phase order, dimensionality, and composition. *Chem. Soc. Rev.* **41**, 1892-1910, (2012).

141. Yu, Q. *et al.* Photomechanical Organic Crystals as Smart Materials for Advanced Applications. *Chem. Eur. J.* **25**, 5611-5622, (2019).

142. Khalil, A., Ahmed, E. & Naumov, P. Metal-coated thermosalient crystals as electrical fuses. *Chem. Commun.* **53**, 8470-8473, (2017).

143. Kobatake, S., Takami, S., Muto, H., Ishikawa, T. & Irie, M. Rapid and reversible shape changes of molecular crystals on photoirradiation. *Nature* **446**, 778-781 (2007).

144. Tong, F., Liu, M., Al-Kaysi, R. O. & Bardeen, C. J. Surfactant-Enhanced Photoisomerization and Photomechanical Response in Molecular Crystal Nanowires. *Langmuir* **34**, 1627-1634, (2018).

145. Tong, F., Kitagawa, D., Bushnak, I., Al-Kaysi, R. O. & Bardeen, C. J. Light-Powered Autonomous Flagella-Like Motion of Molecular Crystal Microwires. *Angew. Chem. Int. Ed.* **60**, 2414-2423, (2021).

146. Tong, F., Al-Haidar, M., Zhu, L., Al-Kaysi, R. O. & Bardeen, C. J. Photoinduced peeling of molecular crystals. *Chem. Commun.* **55**, 3709-3712, (2019).

147. Uchida, E., Azumi, R. & Norikane, Y. Light-induced crawling of crystals on a glass surface. *Nat. Commun.* **6**, 7310, (2015).

148. Bushuyev, O. S., Tomberg, A., Friščić, T. & Barrett, C. J. Shaping Crystals with Light: Crystal-to-Crystal Isomerization and Photomechanical Effect in Fluorinated Azobenzenes. *J. Am. Chem. Soc.* **135**, 12556-12559, (2013).

149. Bushuyev, O. S., Singleton, T. A. & Barrett, C. J. Fast, Reversible, and General Photomechanical Motion in Single Crystals of Various Azo Compounds Using Visible Light. *Adv. Mater.* **25**, 1796-1800, (2013).

150. Bushuyev, O. S. *et al.* Azo...phenyl stacking: a persistent self-assembly motif guides the assembly of fluorinated cis-azobenzenes into photo-mechanical needle crystals. *Chem. Commun.* **52**, 2103-2106, (2016).

151. Bartholomew, A. K., Stone, I. B., Steigerwald, M. L., Lambert, T. H. & Roy, X. Highly Twisted Azobenzene Ligand Causes Crystals to Continuously Roll in Sunlight. *J. Am. Chem. Soc.* (2022).

152. Qian, H., Pramanik, S. & Aprahamian, I. Photochromic Hydrazone Switches with Extremely Long Thermal Half-Lives. *J. Am. Chem. Soc.* **139**, 9140-9143, (2017).

153. Ryabchun, A., Li, Q., Lancia, F., Aprahamian, I. & Katsonis, N. Shape-Persistent Actuators from Hydrazone Photoswitches. *J. Am. Chem. Soc.* **141**, 1196-1200, (2019).

154. Shao, B., Qian, H., Li, Q. & Aprahamian, I. Structure Property Analysis of the Solution and Solid-State Properties of Bistable Photochromic Hydrazones. *J. Am. Chem. Soc.* **141**, 8364-8371, (2019).

155. Shao, B. *et al.* Solution and Solid-State Emission Toggling of a Photochromic Hydrazone. *J. Am. Chem. Soc.* **140**, 12323-12327, (2018).

156. Karothu, D. P. *et al.* Exceptionally high work density of a ferroelectric dynamic organic crystal around room temperature. *Nat. Commun.* **13**, 2823, (2022).

157. Naumov, P., Sahoo, S. C., Zakharov, B. A. & Boldyreva, E. V. Dynamic Single Crystals: Kinematic Analysis of Photoinduced Crystal Jumping (The Photosalient Effect). *Angew. Chem. Int. Ed.* **52**, 9990-9995, (2013).

158. Seki, T., Sakurada, K., Muromoto, M. & Ito, H. Photoinduced single-crystal-to-single-crystal phase transition and photosalient effect of a gold(i) isocyanide complex with shortening of intermolecular aurophilic bonds. *Chem. Sci.* **6**, 1491-1497, (2015).

159. Medishetty, R. *et al.* Single Crystals Popping Under UV Light: A Photosalient Effect Triggered by a [2+2] Cycloaddition Reaction. *Angew. Chem. Int. Ed.* **53**, 5907-5911, (2014).

160. Medishetty, R., Sahoo, S. C., Mulijanto, C. E., Naumov, P. & Vittal, J. J. Photosalient Behavior of Photoreactive Crystals. *Chem Mater.* **27**, 1821-1829, (2015).

161. Yao, Y., Zhang, L., Leydecker, T. & Samorì, P. Direct Photolithography on Molecular Crystals for High Performance Organic Optoelectronic Devices. *J. Am. Chem. Soc.* **140**, 6984-6990, (2018).

162. Sun, J. & Litchinitser, N. M. Toward Practical, Subwavelength, Visible-Light Photolithography with Hyperlens. *ACS Nano* **12**, 542-548, (2018).

163. Desbiolles, B. X. E., Bertsch, A. & Renaud, P. Ion beam etching redeposition for 3D multimaterial nanostructure manufacturing. *Microsyst.Nanoeng.* **5**, 11, (2019).

164. Wang, Z. *et al.* Patterning Organic/Inorganic Hybrid Bragg Stacks by Integrating One-Dimensional Photonic Crystals and Macrocavities through Photolithography: Toward Tunable Colorful Patterns as Highly Selective Sensors. *ACS Appl. Mater. Interfaces* **4**, 1397-1403, (2012).

165. Ghorai, S. *et al.* From co-crystals to functional thin films: photolithography using [2+2] photodimerization. *Chem. Sci.* **4**, 4304-4308, (2013).

Rationale for Chapter 2

As emphasized in Section 1.7, the study of photo-responsive crystals is continuously growing, with a strong emphasis on developing materials with new types of photo-responsive behaviour by design of the crystalline structure. The following Chapter takes a crystal engineering approach to develop a crystalline solid which exhibits a new photo-response unique to this material, through the combination of a volatile co-crystal former (coformer) and a light absorbing dye. This Chapter focuses on a new form of photo-response called 'Cold Photo-Carving' (CPC) analogous to laser beam machining (LBM) used to cut, shape, and engrave materials, yet performed at room temperature *via* a photo- and not a thermal process. We highlight two novel co-crystals which undergo the process of CPC upon irradiation with low-power visible light, and additionally we discuss the mechanism of this controlled photo-decomposition of the co-crystals in the following Chapter.

Chapter 2 was reproduced with permission from Nature springer publishing group.

Citation: Borchers, T. H., Topić, F., Christopherson, J.-C., Bushuyev, O. S., Vainauskas, J., Titi, H. M, Friščić, T., & Barrett, C. J. Cold photo-carving of halogen-bonded co-crystals of a dye and a volatile co-former using visible light. *Nature Chemistry* **14**, 574–581 (2022).

Cold Photo-Carving of Dye-Volatile Halogen-Bonded Co-Crystals Using Low-Power Visible Light

T. H. Borchers, F. Topić, J.-C. Christopherson, O. S. Bushuyev, J. Vainauskas, H. M. Titi, T. Friščić, and C. J. Barrett**

Department of Chemistry, McGill University, Montreal, QC, Canada

2.1 Abstract

The formation of multi-component crystals (co-crystals) by the assembly of molecules with complementary molecular recognition functionalities is a popular strategy to improve and design a range of solid state properties, from pharmaceuticals, photo- or thermo-responsive materials, to organic electronics. Here, we report halogen-bonded co-crystals of a fluorinated azobenzene with a volatile component dioxane or pyrazine, that can be cut, carved, or engraved with low-powered visible light. This cold photo-carving (CPC) process is enabled by co-crystallization of a light-absorbing azo dye with a volatile component, giving rise to materials that can be selectively disassembled with micrometer precision using low-power, non-burning free-laser irradiation, or a commercial confocal microscope The ability to shape and even machine co-crystals in 3D using laser powers between 0.5–20 mW, several orders of magnitude lower compared to those used for machining metals, ceramics or polymers, is rationalized by CPC targeting the disruption of weak supramolecular interactions, rather than covalent bonds or ionic structures targeted by conventional laser beam or focused ion beam machining processes.

2.2 Introduction

The formation of multi-component crystals (co-crystals) by the assembly of molecular building blocks with complementary molecular recognition functionalities is a well-developed strategy for improving solid state physicochemical properties of molecular solids[1–3] such as pharmaceuticals[4] and photo- or thermo-responsive materials,[5–7] as well as for tuning optical[8,9] or conducting properties of organic materials,[10] and stabilizing volatile compounds.[11] Halogen bonding[12,13] has been used as a design element to generate dynamic co-crystals[14] with potential applications in stabilization or separation[15] of volatile molecules, as a tool for constructing amphidynamic[16,17] and liquid crystals,[18] for templating solid state reactions,[19] and other uses in materials chemistry.[20,21]

Stimuli-responsive behaviour of molecular crystals has recently attracted great interest,[22] and in particular a wide range of light-matter interactions has been achieved, including chemical reactions (*e.g.* isomerization,[23,24] dimerization,[25,26] or polymerization[27,28]); photo-mechanical motion,[22,29–31] photochromism,[32] and waveguide behaviour.[33,34] Additionally, photodimerization in co-crystals with volatile co-crystal formers (coformers)[35] provides an ability to purify reaction product *via* sublimation.[36] While traditional light-induced chemical surface etching (photolithography) has been applied to polymeric resins,[37] hyperbolic metamaterials,[38] nanostructures,[39] photonic crystals[40] and co-crystal thin films,[41] the ability to accurately shape, or machine, organic crystalline solids using low-powered visible or ultraviolet (UV) light has yet to be achieved. Materials machining and lithography have been reported using high-energy beam techniques, such as focused ion beam (FIB) milling,[42] electron beam lithography, or femtosecond laser beam machining.[43] These methods, however, operate at beam intensities (on the order of kiloWatts per mm^2 to gigaWatts per mm^2)[44] that will produce chemical damage to molecular

organic materials, and are most commonly used for organic polymers and inorganic materials.[45–48]

Here we describe co-crystallization as a route to obtain crystalline organic materials that can be engraved, cut, and/or punctured without chemical damage, with micrometer-scale precision, using a laser beam with output powers in the milliwatt range (0.5–20 mW) and a maximum beam intensity between 200–2500 $mW \cdot mm^{-2}$ (Supplementary **Figure 7**), *i.e.* orders of magnitude lower in comparison to conventional beam machining techniques, such as femtosecond laser beam machining ($\approx 10^3$–10^9 $W \cdot mm^{-2}$).[44] The herein reported co-crystals are based on a photo-responsive building block (*trans*-4,4'-diiodooctafluoroazobenzene, *trans*-azo, **Figure 1a)** combined with dioxane or pyrazine (**Figure 1a**) as a loosely-bound halogen bond acceptor, and their susceptibility to machining using a low-energy laser beam represents a property emergent from co-crystal formation. Light exposure is thought to induce a localized evaporation event of the volatile coformer due to the photochromic behaviour of the azobenzene. The resulting azobenzene molecules recrystallize near the edge of the irradiation area. This work demonstrates gentle room-temperature photo-machining of a molecular crystal with micrometer precision, and introduces a technique for laser micro-shaping of co-crystals, analogous to laser beam machining yet using energies far below the threshold of chemical damage, as a methodology to shape organic crystals. As irradiation of azobenzenes in the solid state is expected to lead to only minor increases in temperature[49], we term this process cold photo-carving (CPC).

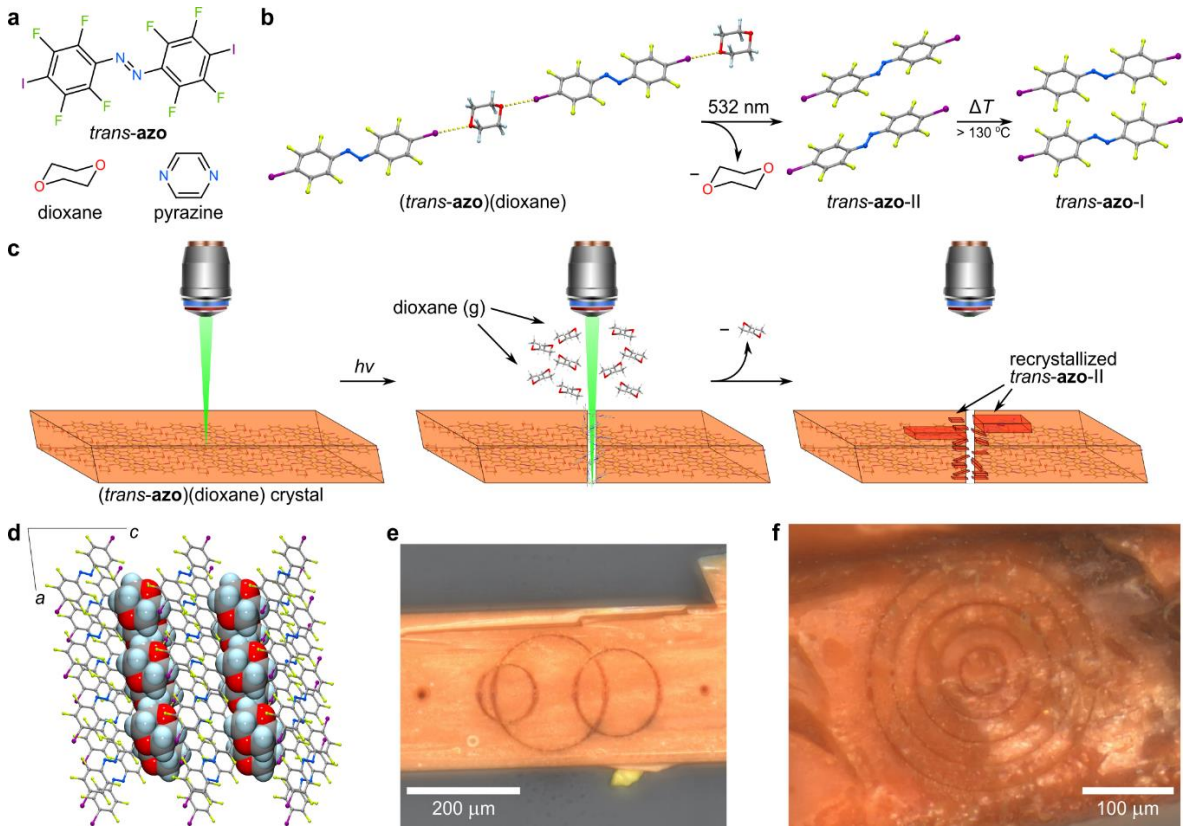

Figure 2.1. Illustration of cold photo-carving (CPC) of a halogen-bonded co-crystal. a) Molecular structures of *trans*-azo, (1,4)-dioxane, and pyrazine. **b)** Illustration of the herein observed co-crystal dissociation process underlying cold photo-carving of (*trans*-azo)(dioxane**) (Atom labels: F, green; O, red; N, blue; I, purple). c)** Illustration of the photo-carving and/or engraving of (*trans*-azo)(dioxane) co-crystal using a confocal microscope system, highlighting the proposed explanation of the room-temperature photo-carving process based on the loss of the volatile component dioxane, and recrystallization of remaining azo-dye as *trans*-azo **II** near the surface of irradiation. **d)** Fragment of the crystal structure of (*trans*-azo)(dioxane) co-crystal, viewed along the crystallographic [010] direction. **e-f**) Examples of detailed cold photo-carving of the surface of a (*trans*-azo)(dioxane) co-crystal using low-powered 532 nm light, illustrating the creation of holes, as well as surface engraving of circles (1 mW power and 1 s irradiation was used for engraving circles, 2 mW power and 1 s irradiation was used for making holes).

2.3 Results and discussion

2.3.1 Laser cold photo-carving of the (*trans*-azo)(dioxane) co-crystals

The co-crystal (*trans*-azo)(dioxane) was synthesized as a part of our research program towards controlling the optical and photo-mechanical behaviour of crystalline molecular solids based on azobenzene (azo) dyes, which can photo-isomerize between *trans* and *cis* geometries reversibly with low-power visible light.[6,9,23,50] Single crystal X-ray diffraction analysis revealed that the crystal structure of (*trans*-azo)(dioxane) is based on zig-zag chains held by I···O halogen bonds occupying the equatorial positions of the oxygen atoms (d(I···O) = 2.981(3) Å, R_{XB} = 0.852) (**Figure 1b**).[51,52] Single crystals of (*trans*-azo)(dioxane) exhibit strong dichroism under plane-polarized light, changing from dark red to almost completely colourless, reflecting the parallel alignment of azo-chromophores in the structure (**Supplementary Figure 2.8**).[9]

Unexpectedly, irradiating the largest (010) face (**Figure 2.1c**) of the thin, lath-shaped crystals of (*trans*-azo)(dioxane) (thickness ~5–100 μm) using a low-power diode green laser (532 nm wavelength, 2–20 mW power with a variable beam width of ~100–500 μm and thus a corresponding beam intensity between 200–2500 mW·mm^{-2}, see Methods, **Supplementary Figure 2.7**) resulted in cutting and the appearance of visible holes or slits at the spot of irradiation (**Supplementary Figure 2.9 and 2.10**). Cutting was readily observed even for much thicker crystal samples (ca. 250 μm, **Supplementary Figure 2.11**), at a comparable laser power (15 mW), and was not observed to depend on the face being directly cut. This laser machining behaviour contrasts with previous reports on crystalline azobenzenes which, if photoactive, exhibit either reversible or irreversible bending upon exposure to UV or visible light.[6,23,33,53] In order to gain further insight into the observed light-induced machining, we turned to spectroscopic observation

using confocal Raman microscopy.[54] Due to the larger numerical aperture (reducing the beam width to 5–50 μm), the confocal Raman microscope setup enabled the machining of (*trans*-azo)(dioxane) crystals at even lower power levels, down to 0.5 mW, and with fine computer spatial control that permitted improved (micrometer-scale) engraving precision (**Figure 2.1e**). By combining an optical microscope and a Raman spectrometer, this technique also allowed the real-time visualization and spectroscopic monitoring of molecular and physical changes during crystal machining, with a spatial resolution below 1 μm, and using a laser probe with either a 532 nm or 785 nm wavelength. Focusing the analysis on the spectral region above 150 cm^{-1}, associated with intramolecular vibrations, it was further possible to distinguish between the pure *trans*-azo and the corresponding co-crystals.

Analysis by confocal Raman microscopy showed that the irradiation of (*trans*-azo)(dioxane) using near-infrared (NIR) laser light (785 nm) resulted in no visual changes to the material, even at the maximum power setting (70 mW), contrasting the machining effect observed with low-power green (532 nm) light. To confirm this observation, we collected consecutive Raman spectra for 150 seconds using either the 785 nm NIR laser at the 25 mW power setting, or the 532 nm green laser at the power setting of 5 mW (**Figure 2.2a, b, and c**). Irradiation at 785 nm did not lead to any noticeable changes to the spectra, whereas spectral peaks acquired using 532 nm radiation were found to diminish over time, consistent with the creation of a hole coincident with the irradiation. Specifically, the normalized intensity of the ν(N=N) Raman band was constant upon irradiation of the crystal with 785 nm light, but rapidly decayed upon exposure to 532 nm light. The band intensity plateaued after 60 seconds, with the residual signal assigned to scattering from the edges of the beam profile (**Figure 2.2c**). No new Raman signals appeared during or after the disappearance of the ν(N=N) band, indicating the absence of new chemical

species or chemical degradation. The sensitivity of (*trans*-azo)(dioxane) to irradiation at 532 nm, but not to 785 nm, is consistent with the absorption behaviour of *trans*-azo, which exhibits a $n \rightarrow \pi^*$ transition absorption maximum centered at 460 nm (**Supplementary Figure 2.1**). Similar experiments were visualized using a laboratory laser system (**Figure 2.2d**), where irradiation of a single crystal with a 633 nm laser at 30 mW power for a duration of 2 minutes, resulted in no visual change to the crystal. This was followed by irradiation of the crystal by a 532 nm laser with an output power of 10 mW over a duration of 2 seconds, resulting in clean cutting of the crystal.

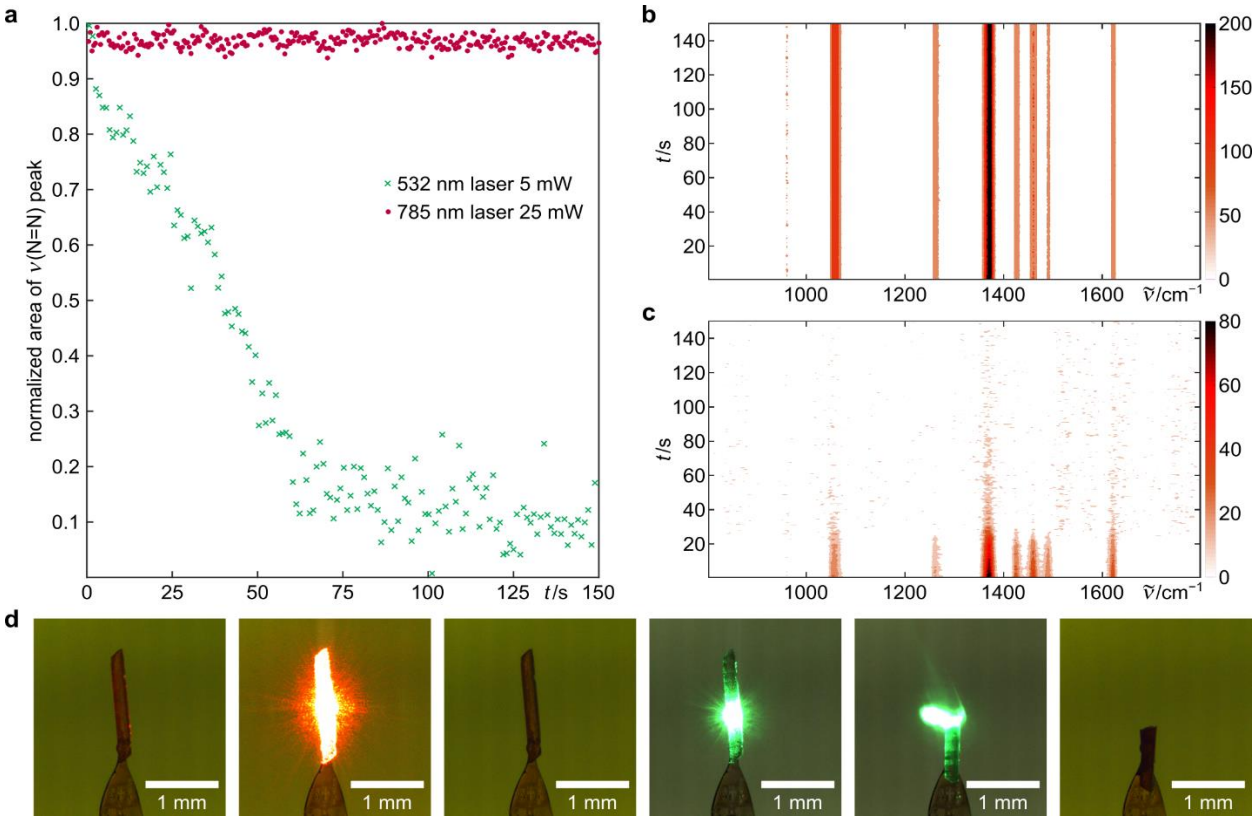

Figure 2.2. Wavelength dependence of the machining of (*trans*-azo)(dioxane) co-crystal with visible light. a) Normalized area of the *ν*(N=N) Raman band (1372 cm^{-1}) over time, for both 785 nm (red) and 532 nm (green) studies. Contour plots of the change in Raman absorption bands over time for co-crystal (*trans*-azo)(dioxane) at different laser wavelengths and power, yet with the same beam width: **b)** 785 nm wavelength and 25 mW power, **c)** 532 nm wavelength and 5 mW power. **d)** Behaviour of a single crystal of (*trans*-azo)(dioxane) upon irradiation *via* two separate laser systems, with a constant beam width of 150 μm (left-to-right): prior to irradiation, during irradiation with a 633 nm laser at 30 mW for a total duration of 2 mins, the resulting crystal after 633 nm irradiation, during irradiation of the crystal with a 532 nm laser at 10 mW for a total duration of 2 s which led to photo-carving, the crystal immediately after being cut, and the resulting crystal following irradiation with a 532 nm laser.

The crystal machining effect was associated with loss of the volatile dioxane, as evidenced by Raman spectra obtained using the 785 nm probe before and after exposing a fresh crystal of (*trans*-azo)(dioxane) to a 1 mW 532 nm 1 second laser pulse. Spectra acquired before and after the pulse showed the disappearance of a Raman band at 830 cm^{-1}, associated with the ν(ring breathing) vibration of dioxane, assigned with the help of the calculated gas-phase vibrational spectra of dioxane and *trans*-azo (Methods, **Supplementary Figure 2.12**, **Supplementary Table 2.2**). This suggests the loss of dioxane upon irradiation (**Supplementary Figure 2.13**). A Raman spectrum recorded from the edge of a hole previously carved with a 532 nm laser beam also revealed the absence of the band at 830 cm^{-1}, again indicating dioxane loss (**Supplementary Figure 2.14**). We investigated the possibility of some of the *trans*-azo component also transferring to the gas phase by mass spectrometry (MS) analysis of the headspace over a sample of several irradiated (*trans*-azo)(dioxane) crystals, but were not able to detect any signal probably due to the low quantity of the sample (**Supplementary Figure 2.48**).

Utilizing the confocal microscope-guided laser beam, a variety of more complex patterns could be gently inscribed onto single crystals of (*trans*-azo)(dioxane) (**Figure 2.3**), either by fully penetrating through the crystal or by deep engraving of the crystal surface. Examples in Figure 3 demonstrate the precision of such photo-carving on the order of microns (μm) and illustrate the variety of techniques that can be used to create (embossing and outline carving) and view (optical and fluorescence microscopy) the obtained patterns. Additionally, adjusting the power of the incident light (15, 10, 5, 2 mW) changed the diameter of the desired hole (17, 16, 14, 12 μm respectively, **Figure 2.3d**). The inscribed images do not exhibit any significant fading upon prolonged standing (**Supplementary Figure 2.15**).

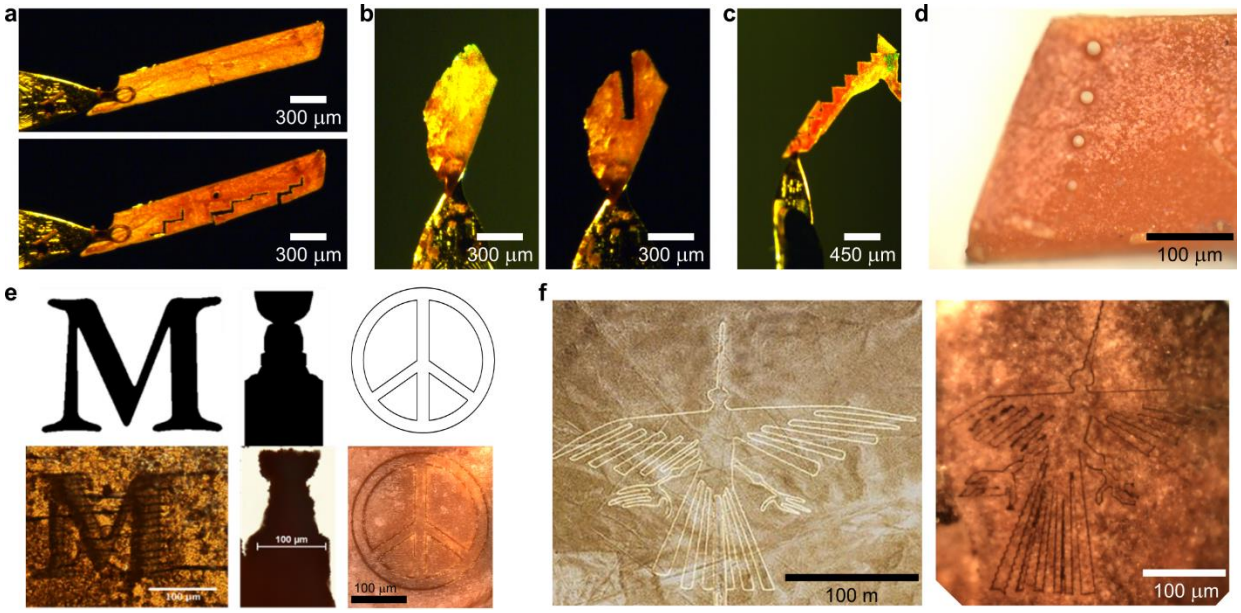

Figure 2.3. Detailed patterns inscribed onto the surface of a (*trans*-azo)(dioxane) co-crystal using either a laboratory laser setup (a–c), or a confocal microscope system (d,f). a) Lines and holes inscribed into a crystal with low-power 532 nm wavelength laser. **b**) Illustration of larger slits machined into a crystal by changing the distance between the crystal and the focal point of the laser. **c**) A crystal manually machined in the shape of a staircase. **d**) A sequence of holes with decreasing diameters machined into the crystal by changing the power of the laser with a confocal microscope system (From top to bottom: 15, 10, 5, 2 mW). **e)** Top: Desired test outlines, Bottom: (left to right) Achieved outcomes of an embossed letter "M", shown in transmission mode of an optical microscope; Microscopy image of a crystal that was cut into the iconic 'Stanley Cup' hockey trophy shape, by irradiating a crystal covered with a mask; Embossed image of a peace sign. **f**) Image (left) of the Condor of the Nazca desert (Peru, left, Credit: iStock.com/digitalg) and an analogous, approximately million-fold reduced, image (right) imprinted onto the surface of a (*trans*-azo)(dioxane) crystal.

The micrometer precision of the cold photo-carving process was confirmed *via* scanning electron microscopy (SEM), in which cuts and holes can be seen in greater detail. The SEM images (**Figure 2.4a**, **Supplementary Figures 2.42–2.45**) revealed only gentle (~ 1 μm height) build-up of material around a hole made by 532 nm irradiation, suggesting the relocation of the non-volatile *trans*-azo upon irradiation. Analysis by SEM also revealed micro-sized crystals growing from the edge of the irradiated hole or cut area, indicating high mobility of molecules that is reminiscent of the fluidization effect seen in azo-containing polymers.[54–56]

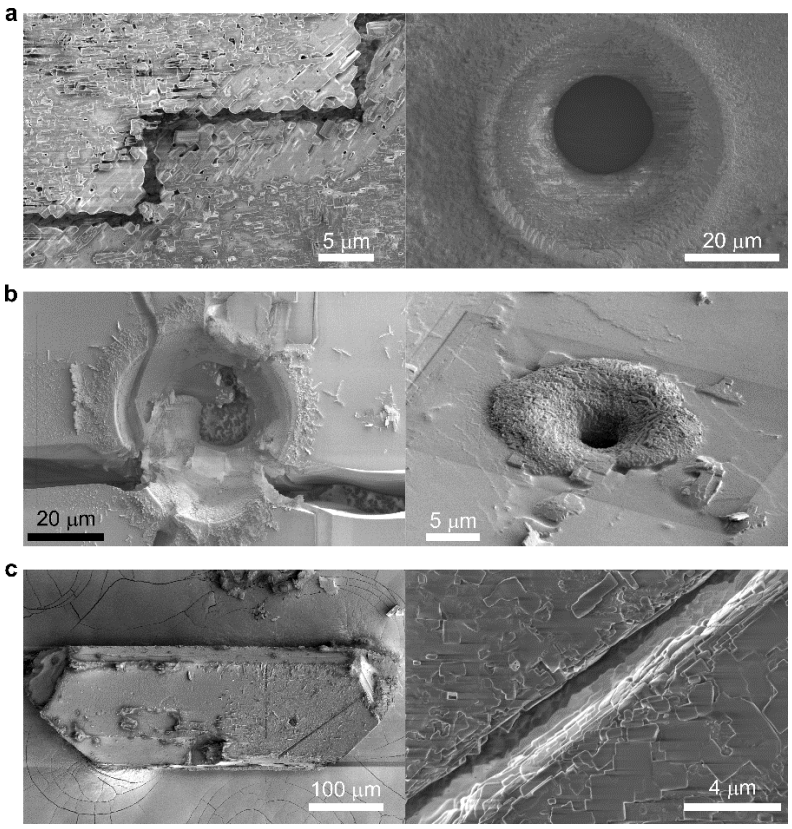

Figure 2.4. Comparison of the outcomes of the cold photo-carving process on the co-crystal (*trans*-azo)(dioxane) and irradiation of a crystal of *trans*-azo, based on SEM. a) (left) Micrometer-sized lines cut into the surface of a (*trans*-azo)(dioxane) crystal using a 1 mW, 532 nm confocal laser, demonstrating the appearance of crystals along the cut, attributed to *trans*-azo polymorph II; (right) a hole of ca. 20 μm diameter cut through a (*trans*-azo)(dioxane) co-crystal using a 10 mW, 532 nm confocal laser. **b)** (left) The surface of a *trans*-azo crystal irradiated with a 15 mW, 532 nm confocal laser, demonstrating significant disruption of the surface and crystal cracking and (right) irradiated with a 5 mW, 532 nm confocal beam, again demonstrating significant disruption of the surface. **c)** (left) Image of a co-crystal of (*trans*-azo)(pyrazine) with a micrometer-sized line and a hole created on the right side of the crystal using a 1.5 mW, 532 nm confocal laser and (right) a magnified image of the line cut into the crystal, illustrating micrometer-scale thickness of the cut.

Single-crystal Raman spectroscopy indicated that the clean machining of thin (*trans*-azo)(dioxane) crystals is associated with dioxane loss, which was also supported by powder X-ray diffraction (PXRD) studies of the bulk microcrystalline powder of the material. PXRD analysis of a polycrystalline sample of (*trans*-azo)(dioxane) before and after 2 hours irradiation with dispersed 37 mW LED light of 532 nm wavelength revealed complete disappearance of the X-ray reflections of the co-crystal, and the appearance of signals not consistent with the reported *trans*-azo crystal structure (herein termed *trans*-azo **I**, **Supplementary Figure 2.16**). Specifically, the PXRD pattern of the irradiated material changed rapidly to reveal another crystalline phase which was subsequently identified as a polymorph of *trans*-azo, herein termed *trans*-azo **II**, and was obtained as diffraction-quality single crystals by rapid recrystallization from diethyl ether.

Thermogravimetric analysis coupled with differential scanning calorimetry (TGA/DSC) of (*trans*-azo)(dioxane) revealed a mass loss step taking place between 70 and 90 °C, consistent with a low temperature barrier for dioxane loss (calculated for dioxane: 13.2, measured: 14.7%). A small exothermic signal was observed in the DSC trace between 140 and 150 °C, which was attributed to the polymorphic transition *trans*-azo **II** → *trans*-azo **I**. This is followed by a larger endothermic signal at 200 °C corresponding to the melting of *trans*-azo **I** (**Supplementary Figure 2.17**). The interpretation of DSC data was validated by variable-temperature PXRD analysis (**Supplementary Figure 2.18**). A PXRD pattern collected at 25 °C was an excellent match to the one simulated for (*trans*-azo)(dioxane). Upon heating to 115 °C, the pattern showed a mixture of phases dominated by *trans*-azo **II** which, upon heating to 160 °C, fully converted to *trans*-azo **I**. Investigation by optical hot-stage microscopy reveals that thermally induced loss of dioxane from a (*trans*-azo)(dioxane) crystal does not significantly perturb its shape (**Supplementary Figure**

2.19). This observation, which is consistent across several explored crystals, is likely to be critical for the high regularity of co-crystal machining.

To monitor the changes upon photo-carving of (*trans*-azo)(dioxane) co-crystals in more detail, the laboratory laser setup was equipped with a high-speed laser beam shutter and a high-speed camera. A co-crystal was irradiated via a 532 nm laser pulses between 40 and 143 ms in length, at a constant power output of 10 mW, and with a recording rate of 1000 frames per second (fps). Crystals showed different response to light depending on the irradiation duration of the crystal. Even at short irradiation times (40 ms), the crystals were observed to emit a visibly opaque fog of outgassing (**Supplementary Figures 2.20–2.23**). At longer irradiation times (143 ms), larger holes are formed, with more opaque fog emanating from the crystal. The fog was tentatively assigned to condensation of dioxane expelled from the co-crystal, and we envision its formation as being analogous of the explosive boiling phenomenon observed in high-energy machining of organic polymers.[43]

2.3.2 Irradiation and attempted photo-carving of pure *trans*-azo solid

As a control, attempts to machine a single crystal of pure *trans*-azo **I** using the confocal microscopy system revealed no significant changes upon irradiation with the 532 nm laser at low power (<10 mW). Laser power above 15 mW, however, led to a machining effect, but accompanied by crystal cracking and/or visible displacement of material from the center towards the edge of the irradiated area (**Supplementary Figures 2.24a, 2.25**). Confocal Raman spectroscopy surface mapping revealed height differences of up to 10 μm in the vicinity of the irradiated crystal area, but without any indication of chemical changes. The Raman signals were identical across all surface features of the irradiated crystal, with the exception of the laser-induced hole that was readily detected by the disappearance of Raman bands (**Supplementary Figures 2.24b and c**). The mapping studies

indicate that the laser-induced displacement of the material is non-destructive, and analogous to the light-induced surface fluidization observed in azobenzene-containing polymer films.[55–57]

SEM analysis of features made on a crystal of *trans*-azo **I** by irradiation with laser power of 10 mW are consistent with the observations made by Raman spectroscopy and optical microscopy, revealing only partial penetration of the crystal leading to form a well, rather than a hole, accompanied by cracking and significant surface distortion. (**Figure 2.4b, Supplementary Figure 2.45**). Similar observation was observed by irradiation at 5 mW power where partial hole formation was observed with significant build-up of material around the irradiation side. Overall, these observations indicate that the ability to cleanly 'machine' (*trans*-azo)(dioxane) using low-power visible light is an emergent property of the co-crystal formation.

2.3.3 Laser photo-carving of the (*trans*-azo)(pyrazine) co-crystals

To investigate a similar system exhibiting photo-carving potential, we designed a second co-crystal based on *trans*-azo as a halogen bond donor, with pyrazine (volatile solid) as the halogen bond acceptor.[58] We expected the two pyridine-like nitrogen atoms of pyrazine to be much stronger XB acceptors than the ether oxygen atoms in dioxane, therefore increasing the overall stability of the resulting co-crystal. The co-crystal (*trans*-azo)(pyrazine) consists of anticipated linear chains of alternating XB donors and acceptors held *via* I···N interactions (d(I···N) = 2.840(3) Å, R_{XB} = 0.805) (Figure 5a). As expected from such a structure, (*trans*-azo)(pyrazine) also exhibits strong dichroism in plane-polarized light, changing the colour from dark red to light yellow depending on the orientation relative to the plane of polarization (**Supplementary Figure 2.26**).

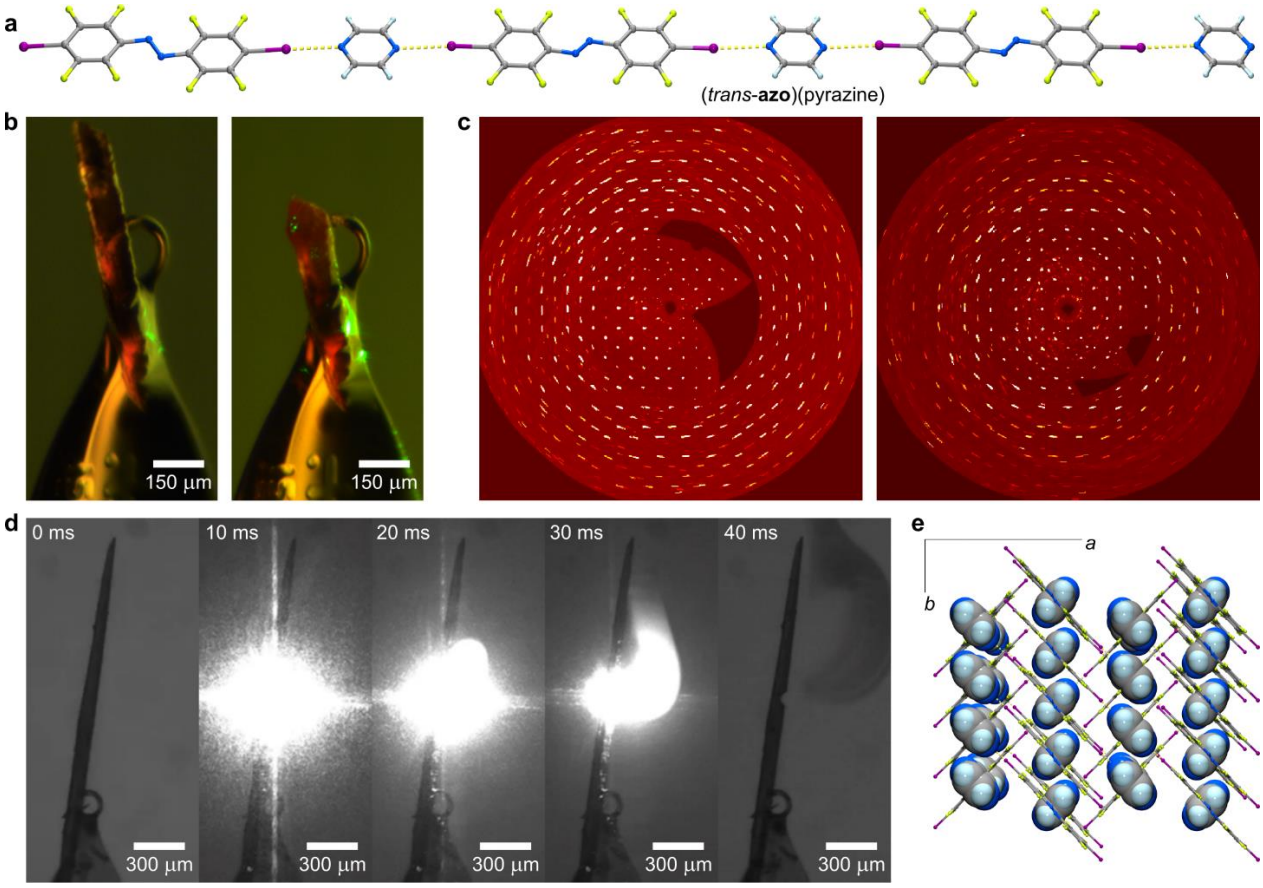

Figure 2.5. Illustration of cold photo-carving of (*trans*-azo)(pyrazine) co-crystal. a) Halogen-bonded chains in the crystal structure of (*trans*-azo)(pyrazine), with halogen bonds shows as dotted lines (Atom labels: F, green; N, blue, I, purple). **b)**, a crystal of (*trans*-azo)(pyrazine) before (left) and after (right) cutting using a 532 nm laser (power = 15 mW). **c**) Precession X-ray diffraction image showing the crystallographic 0kl plane for the co-crystal in part **b**) before (left) and after (right) irradiation, with the data after irradiation being collected as close as possible to the cut surface. **d**) Images of cold photo-carving of (*trans*-azo)(pyrazine) co-crystal using a 40 ms pulse of the 532 nm laser light obtained by monitoring the process by a high-speed (1000 fps) camera. **e**) Packing of molecules in the crystal structure of (*trans*-azo)(pyrazine), viewed along the [001] direction, with *trans*-azo molecules shown in stick and pyrazine molecules in the space-filling mode.

A single crystal of (*trans*-azo)(pyrazine) was readily machined or cut *via* low-powered light, while retaining crystallinity (**Figure 2.5b,c**). To investigate the retention of co-crystal structure for both (*trans*-azo)(pyrazine) and (*trans*-azo)(dioxane) upon machining, a full X-ray diffraction dataset was collected for a sample of each co-crystal, after which the crystals were cut in half using a 532 nm 15 mW laser, and the full dataset recorded again for the resulting bottom half of each crystal (**Figure 2.5b,c, Supplementary Figures 2.27 and 2.28**). In both cases, the diffraction data collected on the daughter crystals consisted predominantly of respective co-crystal phases, demonstrating that cold photo-carving is a localized phenomenon which does not change the extended structure of the irradiated crystal as a whole.

Analogous to the (*trans*-azo)(dioxane) co-crystal, Raman microscopy was used to study the machining of the (*trans*-azo)(pyrazine) co-crystal. Based on the calculated gas-phase spectra of *trans*-azo and pyrazine, we assigned the characteristic Raman band at 1023 cm^{-1} in the spectrum of the (*trans*-azo)(pyrazine) co-crystal to a *ν*(ring breathing) vibration of pyrazine (**Supplementary Figure 2.29, Supplementary Table 2.3**). Irradiation of the co-crystal with a 532 nm laser at a power of 37 mW led to the disappearance of this characteristic band (**Supplementary Figure 2.30**), indicating co-crystal disassembly by loss of pyrazine. Notably, the 1023 cm^{-1} band was still present in the Raman spectrum recorded from the very edge of the hole created by co-crystal irradiation, indicating that the loss of pyrazine is restricted to the irradiated site and does not significantly propagate through the crystal (**Supplementary Figure 2.31**). Investigation of the cut and punctured crystal of (*trans*-azo)(pyrazine) by SEM confirmed the micrometer precision of the process, and suggests cuts equivalent to those observed with (*trans*-azo)(dioxane) (**Figure 2.4c**).

Next, the photo-stability of the (*trans*-azo)(pyrazine) co-crystal was studied in comparison to its dioxane counterpart by monitoring the time-dependent evolution of the PXRD patterns of the respective microcrystalline powder samples upon continuous irradiation by a dispersed 532 nm LED source with a power output of 37 mW. A sample of (*trans*-azo)(pyrazine) revealed the transformation to *trans*-azo **II** upon prolonged irradiation (**Supplementary Figure 2.32**), with traces of the starting (*trans*-azo)(pyrazine) co-crystal still present even after 18 hours of irradiation. This demonstrated the higher photo-stability of (*trans*-azo)(pyrazine) compared to (*trans*-azo)(dioxane) which started converting to *trans*-azo **II** within 10 mins of irradiation and only trace quantities of the co-crystal could be detected after 2 hours (**Supplementary Figure 2.16**).

Thermogravimetric analysis and differential scanning calorimetry (TGA/DSC) was performed on a sample of (*trans*-azo)(pyrazine) (**Supplementary Figure 2.33**). The DSC trace revealed two endothermic peaks, the first of which was coupled with a mass loss of 11.9% occurring between 80 and 135 °C. The mass loss corresponds to the loss of pyrazine in the sample (calculated for pyrazine: 12.2%) and the conversion of (*trans*-azo)(pyrazine) to solid *trans*-azo **II**. The second endothermic peak at 196 °C was assigned to the melting point of *trans*-azo **I**. Unlike (*trans*-azo)(dioxane), this system does not exhibit a clear exothermic signal corresponding to the conversion of *trans*-azo **II** to *trans*-azo **I**. This is presumably due to the endothermic loss of the halogen bond acceptor in (*trans*-azo)(pyrazine) taking place at a higher temperature than in (*trans*-azo)(dioxane), obscuring the signal corresponding to the interconversion of *trans*-azo polymorphs. The interpretation of DSC data was validated by variable-temperature PXRD analysis (**Supplementary Figure 2.34**). A PXRD pattern collected at 25 °C was an excellent match to that simulated for (*trans*-azo)(pyrazine). Upon heating to 125 °C, the pattern showed a mixture of phases dominated by *trans*-azo **II** which, upon heating to 180 °C, fully converted to *trans*-azo **I**.

A single crystal of (*trans*-azo)(pyrazine) was investigated by hot-stage microscopy (Supplementary Figure 35), revealing no major changes in crystal shape before melting.

The cold photo-carving of (*trans*-azo)(pyrazine) was also investigated using a laboratory laser system equipped with a high-speed shutter and a high-speed camera (**Figure 2.5d**). Similar to the dioxane-based system, (*trans*-azo)(pyrazine) showed a differential response to irradiation by different laser power (**Supplementary Figures 2.36–2.38**). Irradiating a crystal of ~15 μm thickness at 5 mW for 40 ms produced no response, while irradiating with a pulse of the same length but at a power of 15 mW led to fog emission. Formation of a hole by irradiating for 40 ms required a power of 20 mW for (*trans*-azo)(pyrazine), which is higher than 10 mW required in the case of (*trans*-azo)(dioxane) under analogous conditions. This suggests that, for the same length of irradiation pulse, each co-crystal exhibits a different power threshold required for cold photo-carving. However, CPC can also be achieved at lower power levels simply by prolonged irradiation: hole formation in a crystal of (*trans*-azo)(pyrazine) of comparable thickness (~15 μm) was also achieved at a power of 15 mW by irradiating for 1 second.

2.3.4 Mechanistic studies

Additional studies were performed to better understand the mechanistic process occurring under irradiation, including gravimetric analysis by monitoring the change in weight of a sample of (*trans*-azo)(dioxane) placed on a Metler Toledo X3105 Dual range microbalence and continuously irradiated by a 532 nm 37 $mW \cdot cm^{-2}$ LED (**Supplementary Figure 2.46**). The sample weight prior to irradiation was 28.79 mg, and the final weight was 25.19 mg. This 12.5% weight loss is very close to that expected for the removal of dioxane from the co-crystal (calculated as 13.2%). At the same time, PXRD analysis of the irradiated sample revealed complete disappearance of X-ray

reflections associated with (*trans*-azo)(dioxane), and the appearance of signals of *trans*-azo **II**. To further investigate the possibility of sublimation of *trans*-azo occurring alongside dioxane loss upon irradiation, a sample of (*trans*-azo)(dioxane) was irradiated with a 532 nm 37 $mW \cdot cm^{-2}$ LED covered with a glass slide placed ca. 2 mm from the surface of the powder sample (**Supplementary Figure 2.47**). Visual inspection of the glass slide after 3 hours of irradiation revealed no evidence of sublimation, while the PXRD analysis of irradiated sample showed only X-ray reflections of solid *trans*-azo **II**. These experiments all clearly show the loss of dioxane upon irradiation of (*trans*-azo)(dioxane), but show no evidence for any noticeable loss of *trans*-azo. Additionally since the X-ray reflections are predominately *trans*-azo **II** reinforces the notion of cold photo-carving, as temperatures induced by the laser would have to be greater then 130 °C to cause the formation of the more stable *trans*-azo **I** polymorph.

These mechanistic studies, combined with the previously described Raman spectroscopy, PXRD, and high-speed camera experiments indicate that the photo-carving behaviour is related to the loss of a volatile coformer upon irradiation of a co-crystal containing an azo dye, with SEM additionally indicating that the non-volatile dye after loss of volatile coformer is sufficiently mobile to relocate and form nanocrystals in the vicinity of the irradiated area.

2.4 Conclusions

We presented a technique for gentle photo-carving of azo-volatile co-crystals (PAC): the ability to use visible (532 nm) laser light, with power as low as 0.5 mW, for micrometer-precision machining and imprinting of images onto organic molecular co-crystals. The low laser power needed for the cold photo-carving CPC process enables precise and automated shaping and engraving of co-

crystals using a commercial confocal Raman microscopy setup, and is explained by the general co-crystal design comprising a *trans*-azo chromophore halogen-bonded to a volatile co-crystal former such as dioxane or pyrazine. This supramolecular design, in which the light-absorbing and volatilized components are segregated and held together by non-covalent interactions, provides an opportunity to achieve micrometer control of the machining process and avoid the use of significantly higher beam power commonly used in the conventional machining of organic polymers. While the present work presents two examples of such behaviour, we believe that this supramolecular design can be generally applicable to generate diverse co-crystal materials amenable to cold photo-carving. The critical importance of co-crystallization for enabling CPC is evident from the herein attempted machining of the pure *trans*-azo solid, which requires higher power that also causes significant surface disruption and loss of machining precision. In contrast, the herein explored co-crystals based on the same *trans*-azo component are readily cut, machined, and embossed using low-power laser light. Although cold photo-carving is based on co-crystal formation, we note that the observed retention of crystal shape upon thermal removal of the volatile coformer suggests a potential route to obtain micrometer-precision machined crystals of the pure azo dye. This is a possibility that will be explored in the future. This proof-of-principle work presents a two-fold advance in materials science: it introduces co-crystals of a photo-reversible dye with a volatile coformer as a class of materials that can be designed to be shaped and machined with micrometer precision using low-power visible light, and introduces small-molecule organic solids as a class of materials that can be machined using light, in addition to much more common polymers, ceramics and metals.

2.5 Methods

2.5.1 Synthesis

The compound trans-4,4'-diiodooctafluoroazobenzene (trans-azo) was synthesized in one step by treatment of 4-iodo-2,3,5,6-tetrafluoroaniline (1.0 g, 3.4 mmol) with N-chlorosuccinimide (NCS) (918 mg, 6.8 mmol) and 1,8-diazabicyclo[5.4.0]undec-7-ene (DBU) (1.04 g 6.8 mmol), stirred in 50 mL CH2Cl2 at -78 ^{0}C for 10 minutes.[59] The resultant crude product was recrystallized with boiling hexanes (isolated yield: 30%). All reagents and solvents were purchased from Sigma Aldrich.

Synthesis of (*trans*-azo)(dioxane) co-crystal. In a typical experiment, 6 mg of *trans*-azo (0.010 mmol) were dissolved in a minimal volume of (1,4-)dioxane (2 mL). The solution was left to evaporate at room temperature, yielding long, orange, lath-shaped crystals.

Synthesis of (trans-azo)(pyrazine) co-crystal. In a typical experiment, 6 mg of *trans*-azo (0.010 mmol) and 6 mg of pyrazine (0.075 mmol) were mixed with hexanes (5 mL) with methylene chloride added dropwise until all material fully dissolved. The solution was left to evaporate at room temperature, yielding prismatic red crystals.

2.5.2 Powder X-ray diffraction

Powder X-ray diffraction experiments were performed on a Bruker D8 Advance diffractometer, using CuKα radiation (λ = 1.54184 Å) source operating at 40 mA and 40 kV, equipped with a Lynxeye XE linear position-sensitive detector, in the 2θ range of 4–40° with step size of 0.019° or, alternatively, on a Bruker D2 Phaser diffractometer using nickel-filtered CuKα radiation (λ = 1.54184 Å) source operating at 10 mA and 30 kV, equipped with a Lynxeye linear position-sensitive detector, in the 2θ-range of 4–40°.

2.5.3 Single-crystal X-ray diffraction

Data for (*trans*-azo)(dioxane), (*trans*-azo)(pyrazine), and trans-azo II were collected on a Bruker D8 Venture dual-source diffractometer equipped with a PHOTON II detector and an Oxford Cryostream 800 cooling system, using mirror-monochromated MoKα ($\lambda = 0.71073$ Å) or CuKα radiation ($\lambda = 1.54184$ Å) from respective microfocus sources. Data were collected in a series of φ- and ω-scans. APEX3 software was used for data collection, integration, and reduction.[60] Numerical absorption corrections were applied using SADABS-2016/2.[61] Structures were solved by dual-space iterative methods using SHELXT[62] and refined by full-matrix least-squares on F^2 using all data with SHELXL[63] within the OLEX2[64] and/or WinGX[65] environment.

2.5.4 UV-Vis absorbance spectroscopy

Absorbance measurements were collected on an Agilent Cary 300 Bio UV-Visible spectrometer. A 55 mg/L solution of *trans*-azo was made up in THF, the absorbance spectrum was acquired using instrument default conditions. The spectrum of the corresponding cis-azo isomer was taken following 30 min of irradiation by a 532 nm LED (37 mW).

2.5.5 Raman spectroscopy

Raman microscopy experiments were performed on confocal Raman Witec 300 R microscope setup using two separate probe wavelengths of 785 and 532 nm. Integration time, number of accumulations and laser power were varied depending on experiment. Simulated Raman shifts were calculated by DFT using Gaussian16,[66] employing the B3LYP density functional.[67,68] Basis set 6-311G(d,p) was used for all atoms.[69] The basis set for iodine[70] was obtained from the Basis Set Exchange.[71]

2.5.6 Thermal analysis

Thermogravimetric analysis (TGA) and differential scanning calorimetry (DSC) measurements were performed simultaneously using a Mettler-Toledo TGA/DSC 1 Star system thermobalance. The samples were placed in alumina crucibles and measurements conducted in a stream of nitrogen (50 cm^3 min^{-1}) gas, at a heating rate of 5 °C min^{-1}. Data collection and analysis were performed using the Mettler-Toledo STARe Software 16.20 program package. Alternatively, DSC measurements were performed on a TA Instruments LTD DSC2500 at a heating rate of 1 °C min^{-1}, under a stream of nitrogen (50 cm^3 min^{-1}) gas, using a hermetically closed aluminium pan.

Hot-stage microscopy was performed using a Mettler Toledo FP90 Central Processor, equipped with a Mettler FP84 HT TA Microscopy Cell. Images were obtained on an Infinity 1 Lumenera camera attached to a Leica DM2500 optical microscope, using the Studio Capture software suite. Heating was performed from 20 to 200 °C at a rate of 20 °C min^{-1}.

2.5.7 Scanning electron microscopy

Single crystals of (*trans*-azo)(dioxane) , (*trans*-azo)(pyrazine), and trans-azo I were sputter-coated with Pd, and placed into an FEI Helios Nanolab 660 DualBeam (Focused Ion Beam-Extreme High-Resolution Scanning Electron Microscope) for imaging.

2.5.8 General microscopy

Handling of crystals, for example for dichroism observation and sample selection for machining or diffraction experiments, was done using a Nikon SMZ1500 stereomicroscope with zoom capabilities (from 0.75x to 11x), the microscope was equipped with a Omax A35140U camera, and Toupview was the acquisition software used.

2.5.9 Detailed machining procedure A

Using the confocal Raman Witec 300 R 532 nm solid state laser with a range of power settings (0.1–20 mW), and multiple objectives (10, 20, 50, and 100× Zeiss objectives with NA = 0.25, 0.5, 0.8, and 0.9, respectively), a series of detailed drawings were engraved into the crystals using a pre-made input files with listed coordinates.

2.5.10 Detailed machining procedure B

Confocal machining experiments on crystals were conducted on a Zeiss710 Multiphoton Microscope. The images were taken with a 20× PLAN APOCHROMAT, NA = 0.8, DIC objective, and the bleaching module were performed with the aid of the Zeiss ZEN software, utilizing two-photon excitation at 750 nm provided by a direct-coupled Chameleon laser.

2.5.11 Laboratory laser system including a high-speed camera

A Redlake MotionPro Y4 (Tallahassee, FL, USA) high-speed charge-coupled device camera was used to capture machining events at 1000 frames/s. MGL-III-532 Green DPSS Laser and Lasos lasertechnik 633nm Helium-Neon laser was coupled with a tunable neutral density filter, Melles Griot electronic controlled shutter, and a Melles Griot convex lens with a focal length of 75 mm, aligned onto a crystal mount with a 150 μm loop (**Supplementary Figure 2.6**).

2.6 References

1. Mir, N. A., Dubey, R. & Desiraju, G. R. Strategy and Methodology in the Synthesis of Multicomponent Molecular Solids: The Quest for Higher Cocrystals. *Acc. Chem. Res.* **52**, 2210–2220 (2019).
2. Aitipamula, S. *et al.* Polymorphs, Salts, and Cocrystals: What's in a Name? *Cryst. Growth Des.* **12**, 2147–2152 (2012).
3. Desiraju, G. R. Crystal Engineering: From Molecule to Crystal. *J. Am. Chem. Soc.* **135**, 9952–9967 (2013).
4. Kavanagh, O. N., Croker, D. M., Walker, G. M. & Zaworotko, M. J. Pharmaceutical Cocrystals: from Serendipity to Design to Application. *Drug Discov. Today* **24**, 796–804 (2019).
5. MacGillivray, L. R. Papaefstathiou, G., Friščić, T., Hamilton, T. D., Bucar, D.-K., Chu, Q., Varshney, D. B., & Georgiev, I. G. Supramolecular Control of Reactivity in the Solid State: From Templates to Ladderanes to Metal–Organic Frameworks. *Acc. Chem. Res.* **41**, 280–291 (2008).
6. Bushuyev, O. S., Corkery, T. C., Barrett, C. J. & Friščić, T. Photo-mechanical Azobenzene Cocrystals and *in situ* X-ray Diffraction Monitoring of their Optically-Induced Crystal-to-Crystal Isomerisation. *Chem. Sci.* **5**, 3158–3164 (2014).
7. Zaworotko, M. J. Molecules to Crystals, Crystals to Molecules … and Back Again? *Cryst. Growth Des.* **7**, 4–9 (2007).
8. Lu, B., Fang, X. & Yan, D. Luminescent Polymorphic Co-crystals: A Promising Way to the Diversity of Molecular Assembly, Fluorescence Polarization, and Optical Waveguide. *ACS Appl. Mater. Interfaces* **12**, 31940–31951 (2020).
9. Christopherson, J.-C., Topić, F., Barrett, C. J. & Friščić, T. Halogen-Bonded Cocrystals as Optical Materials: Next-Generation Control over Light–Matter Interactions. *Cryst. Growth Des.* **18**, 1245–1259 (2018).
10. Liu, C.-H., Niazi, M.R. & Perepichka, D. F. Strong Enhancement of π-Electron Donor/Acceptor Ability by Complementary DD/AA Hydrogen Bonding. *Angew. Chem. Int. Ed.* **58**, 17312–17321 (2019).
11. Aakeroy, C. B., Wijethunga, T. K., Benton, J. & Desper, J. Stabilizing Volatile Liquid Chemicals using Co-Crystalization. *Chem. Commun.* **51**, 2425-2428 (2015).
12. Cavallo, G. *et al*. The Halogen Bond. *Chem. Rev.* **116**, 2478–2601 (2016).
13. Mukherjee, A., Tothadi, S. & Desiraju, G. R. Halogen Bonds in Crystal Engineering: Like Hydrogen Bonds yet Different. *Acc. Chem. Res.* **47**, 2514–2524 (2014).

14. Raatikainen, K. & Rissanen, K. Breathing Molecular Crystals: Halogen- and Hydrogen-Bonded Porous Molecular Crystals with Solvent Induced Adaptation of the Nanosized Channels. *Chem. Sci.* **3**, 1235–1239 (2012).
15. Metrangolo, P. *et al*. Nonporous Organic Solids Capable of Dynamically Resolving Mixtures of Diiodoperfluoroalkanes. *Science* **323**, 1461–1464 (2009).
16. Catalano, L. *et al*. Dynamic Characterization of Crystalline Supramolecular Rotors Assembled through Halogen Bonding. *J. Am. Chem. Soc.* **137**, 15386–15389 (2015).
17. Szell, P. M. J., Zablotny, S. & Bryce, D. L. Halogen Bonding as a Supramolecular Dynamics Catalyst. *Nat. Commun.* **10**, 916 (2019).
18. Cavallo, G. *et al*. Superfluorinated Ionic Liquid Crystals Based on Supramolecular, Halogen-Bonded Anions. *Angew. Chem. Int. Ed.* **55**, 6300–6304 (2016).
19. Sinnwell, M. A. & MacGillivray, L. R. Halogen-Bond-Templated [2+2] Photodimerization in the Solid State: Directed Synthesis and Rare Self-Inclusion of a Halogenated Product. *Angew. Chem. Int. Ed.* **55**, 3477–3480 (2016).
20. Priimagi, A., Cavallo, G., Metrangolo, P. & Resnati, G. The Halogen Bond in the Design of Functional Supramolecular Materials: Recent Advances. *Acc. Chem. Res.* **46**, 2686–2695 (2013).
21. Saccone, M. & Catalano, L. Halogen Bonding beyond Crystals in Materials Science. *J. Phys. Chem. B*, **123**, 9281–9290 (2019).
22. Naumov, P., Chizhik, S., Panda. M. K., Nath, N. K. & Boldyreva, E. Mechanically Responsive Molecular Crystals. *Chem. Rev.* **115**, 12440–12490 (2015).
23. Bushuyev, O. S., Tomberg, A., Friščić, T. & Barrett, C. J. Shaping Crystals with Light: Crystal-to-Crystal Isomerization and Photomechanical Effect in Fluorinated Azobenzenes. *J. Am. Chem. Soc.* **135**, 12556–12559 (2013).
24. Natarajan, A. *et al*. The Photoarrangement of α-Santonin is a Single-Crystal-to-Single-Crystal Reaction: A Long Kept Secret in Solid-State Organic Chemistry Revealed. *J. Am. Chem. Soc.* **129**, 9846–9847 (2007).
25. Chu, Q., Swenson, D. C. & MacGillivray, L. R. A Single-Crystal-to-Single-Crystal Transformation Mediated by Argentophilic Forces Converts a Finite Metal Complex into an Infinite Coordination Network. *Angew. Chem. Int. Ed.* **44**, 3569–3572 (2005).
26. Toh, N. L., Nagarathinam, M. & Vittal, J. J. Topochemical Photodimerization in the Coordination Polymer $[\{(CF_3CO_2)(\mu\text{-}O_2CCH_3)Zn\}_2(\mu\text{-bpe})_2]_n$ through Single-Crystal to Single-Crystal Transformation. *Angew. Chem. Int. Ed.* **117**, 2277–2281 (2005).
27. Biradha, K. & Santra, R. Crystal Engineering of Topochemical Solid State Reactions. *Chem. Soc. Rev.* **42**, 950–967 (2013).
28. Sun, A., Lauher, J. W. & Goroff, N. S. Preparation of Poly(Diiododiacetylene), an Ordered Conjugated Polymer of Carbon and Iodine. *Science* **312**, 1030–1034 (2006).

29. Kitagawa, D. *et al*. Control of Photomechanical Crystal Twisting by Illumination Direction. *J. Am. Chem. Soc.* **140**, 4208–4212 (2018).
30. Tong, F., Al-Haidar, M., Zhu, L., Al-Kaysi, R. O. & Bardeen, C. J. Photoinduced Peeling of Molecular Crystals. *Chem. Commun.* **55**, 3709–3712 (2019).
31. Halabi, J. M., Ahmed, E., Sofela, S. & Naumov, P. Performance of Molecular Crystals in Conversion of Light to Mechanical Work. *Proc. Natl. Acad. Sci. U.S.A.* **118**, e2020604118 (2021).
32. Irie, M., Fukaminato, T., Matsuda, K. & Kobatake, S. Photochromism of Diarylethene Molecules and Crystals: Memories, Switches, and Actuators. *Chem. Rev.* **114**, 12174–12277 (2014).
33. Halabi, J. M. *et al*. Spatial Photocontrol of the Optical Output from an Organic Crystal Waveguide. *J. Am. Chem. Soc.* **141**, 14966–14970 (2019).
34. Karothu, D. P. *et al*. Mechanically Robust Amino Acid Crystals as Fiber-Optic Transducers and Wide Bandpass Filters for Optical Communication in the Near-Infrared. *Nat. Commun.* **12**, 1326 (2021).
35. Duggirala, N. K., Perry, M. L., Almarsson, O. & Zaworotko, M. J. Pharmaceutical Cocrystal: Along the Path to Improved Medicines. *Chem. Commun.* **52**, 640–655 (2016)
36. Grobelny, A. L., Verdu, F. A., & Groeneman, R. H. Solvent-free Synthesis and Purification of a Photoproduct *via* Sublimation of a Tetrahalogenated Template. *CrystEngComm* **19**, 3562–3565 (2017)
37. Yao, Y., Zhang, L., Leydecker, T. & Samorì, P. Direct Photolithography on Molecular Crystals for High Performance Organic Optoelectronic Devices. *J. Am. Chem. Soc.* **140**, 6984–6990 (2018).
38. Sun, J. & Litchinitser, N. M. Toward Practical, Subwavelength, Visible-Light Photolithography with Hyperlens. *ACS Nano* **12**, 542–548 (2018).
39. Desbiolles, B. X. E., Bertsch, A. & Renaud, P. Ion Beam Etching Redeposition for 3D Multimaterial Nanostructure Manufacturing. *Microsyst. Nanoeng.* **5**, 11 (2019).
40. Wang, Z. *et al*. Patterning Organic/Inorganic Hybrid Bragg Stacks by Integrating One-Dimensional Photonic Crystals and Macrocavities through Photolithography: Toward Tunable Colorful Patterns as Highly Selective Sensors. *ACS Appl. Mater. Interfaces* **4**, 1397–1403 (2012).
41. Ghorai, S. *et al*. From Co-crystals to Functional Thin Films: Photolithography using [2+2] Photodimerization. *Chem. Sci.* **4**, 4304–4308 (2013).
42. Li, W. *et al*. Shaping Organic Microcrystals Using Focused Ion Beam Milling. *Cryst. Growth Des.* **20**, 1583–1589 (2020).
43. Wood, M. J. *et al*. Femtosecond Laser Micromachining of Co-polymeric Urethane Materials. *Appl. Surf. Sci.* **483**, 633–641 (2019).

44. Kandidov, V.P., Dormidonov, A. E., Kosareva, O. G., Chin, S. L. & Liu, W. in *self-focusing: Past and Present: Fundamentals and Prospects* (eds Robert W. Boyd, Sventiana G. Lukisova, & Y. R. Shen) 371–298 (springer New York, 2009).
45. Guan, L., Peng, K., Yang, Y., Qiu, X. & Wang, C. The Nanofabrication of Polydimethylsiloxane using a Focused Ion Beam. *Nanotechnology* **20**, 145301 (2009).
46. Alias, M. S., *et al*. Enhanced Etching, Surface Damage Recovery, and Submicron Patterning of Hybrid Perovskites using a Chemically Gas-Assisted Focused-Ion Beam for Subwavelength Grating Photonic Applications. *J. Phys. Chem. Lett.* **7**, 137–142 (2016).
47. Bei, H., Shim, S., Miller, M. K., Pharr, G. M. & George, E. P. Effects of Focused Ion Beam Milling on the Nanomechanical Behavior of a Molybdenum-alloy Single Crystal. *Appl. Phys. Lett.* **91**, 111915 (2007).
48. Vesseur, E. J. R. *et al*. Surface Plasmon Polariton Modes in a Single-Crystal Au Nanoresonator Fabricated using Focused-ion-beam Milling. *Appl. Phys. Lett.* **92**, 083110 (2008).
49. Yager, K. G., Barrett, C. J. Temperature Modeling of Laser-Irradiated Azo-Polymer Thin Films. *J. Chem. Phys.* **120**(2), 1089–1096 (2004)
50. Vainauskas, J., Topić, F., Bushuyev, O. S., Barrett, C. J. & Friščić, T. Halogen Bonding to the Azulene π-system: Cocrystal Design of Pleochroism. *Chem. Commun.* **56**, 15145–15148 (2020).
51. Lommerse, J. P. M., Stone, A. J., Taylor, R. & Allen, F. H. The Nature and Geometry of Intermolecular Interactions between Halogens and Oxygen or Nitrogen. *J. Am. Chem. Soc.* **118**, 3108–3116 (1996).
52. Mantina, M., Chamberlin, A. C., Valero, R., Cramer, C. J. & Truhlar, D. G. Consistent van der Waals Radii for the Whole Main Group. *J. Phys. Chem. A* **113**, 5806–5812 (2009).
53. Bushuyev, O. S., Singleton, T. A. & Barrett, C. J. Fast, Reversible, and General Photomechanical Motion in Single Crystals of Various Azo Compounds Using Visible Light. *Adv. Mater.* **25**, 1796–1800 (2013).
54. Salzillo, T. & Brillante, A. Commenting on the Photoreactions of Anthracene Derivatives in the Solid State. *CrystEngComm* **21**, 3127–3136 (2019).
55. Kim, K. *et al*. Light-Directed Soft Mass Migration for Micro/Nanophotonics. *Adv. Opt. Mater.* **7**, 1900074 (2019).
56. Kitamura, I., Oishi, K., Hara, M., Nagano, S. & Seki, T. Photoinitiated Marangoni Flow Morphing in a Liquid Crystalline Polymer Film Directed by Super-Inkjet Printing Patterns. *Sci. Rep.* **9**, 2556 (2019).
57. Cheng, Y.-C., Lu, H.-C., Lee, X., Zeng, H. & Priimagi, A. Kirigami-Based Light-Induced Shape-Morphing and Locomotion. *Adv. Mater.* **32**, 1906233 (2020).

58. Braga, D., Grepioni, F. & Lampronti, G. I. Supramolecular Metathesis: Co-former Exchange in Co-crystals of Pyrazine with (*R*,*R*)-, (*S*,*S*)-, (*R*,*S*)- and (*S*,*S*/*R*,*R*)-tartaric acid. *CrystEngComm* **13**, 3122–3124 (2011).
59. Antoine, J. A. & Lin, Q. Synthesis of Azobenzenes Using *N*-Chlorosuccinimide and 1,8-Diazabicyclo[5.4.0]undec-7-ene (DBU). *J. Org. Chem.* **82**, 9873–9876 (2017).
60. Bruker, APEX3, Bruker AXS Inc., Madison, Wisconsin, USA, 2012.
61. Krause, L., Herbst-Irmer, R., Sheldrick, G. M. & Stalke, D. Comparison of Silver and Molybdenum Microfocus X-ray Sources for Single-crystal Structure Determination. *J. Appl. Cryst.* **48**, 3–10 (2015).
62. Sheldrick, G. M. SHELXT - Integrated Space-Group and Crystal-Structure Determination. *Acta Cryst.* **A71**, 3–8 (2015).
63. Sheldrick, G. M. Crystal Structure Refinement with SHELXL. *Acta Cryst.* **C71**, 3–8 (2015).
64. Dolomanov, O. V., Bourhis, L. J., Gildea, R. J., Howard, J. A. K. & Puschmann, H. OLEX2: A Complete Structure Solution, Refinement and Analysis Program. *J. Appl. Cryst.* **42**, 339–341 (2009).
65. Farrugia, L. J. WinGX and ORTEP for Windows: an Update. *J. Appl. Cryst.* **45**, 849–854 (2012).
66. Frisch, M. J. *et al*. Gaussian 16, Revision C.01, Gaussian, Inc., Wallingford, CT, 2016.
67. Becke, A. D. Density-functional Thermochemistry. III. The Role of Exact Exchange. *J. Chem. Phys.* **98**, 5648–5652 (1993).
68. Lee, C., Yang, W. & Parr, R. G. Development of the Colle-Salvetti Correlation-Energy Formula into a Functional of the Electron Density. *Phys. Rev. B* **37**, 785–789 (1998).
69. Ditchfield, R., Hehre, W. J. & Pople, J. A. Self-Consistent Molecular-Orbital Methods. IX. An Extended Gaussian-Type Basis for Molecular-Orbital Studies of Organic Molecules. *J. Chem. Phys.* **54**, 724–728 (1971).
70. Glukhovtsev, M. N., Pross, A., McGrath, M. P. & Radom, L. Extension of Gaussian-2 (G2) Theory to Bromine- and Iodine-containing Molecules: Use of Effective Core Potentials. *J. Chem. Phys.* **103**, 1878–1885 (1995).
71. Pritchard, B. P., Altarawy, D., Didier, B., Gibson, T. D. & Windus, T. L. New Basis Set Exchange: An Open, Up-to-Date Resource for the Molecular Sciences Community. *J. Chem. Inf. Model.* **59**, 4814–4820 (2019).

2.7 Appendix 1: Supporting information for Chapter 2

2.7.1 Experimental data

2.7.1.1 UV-Vis spectra

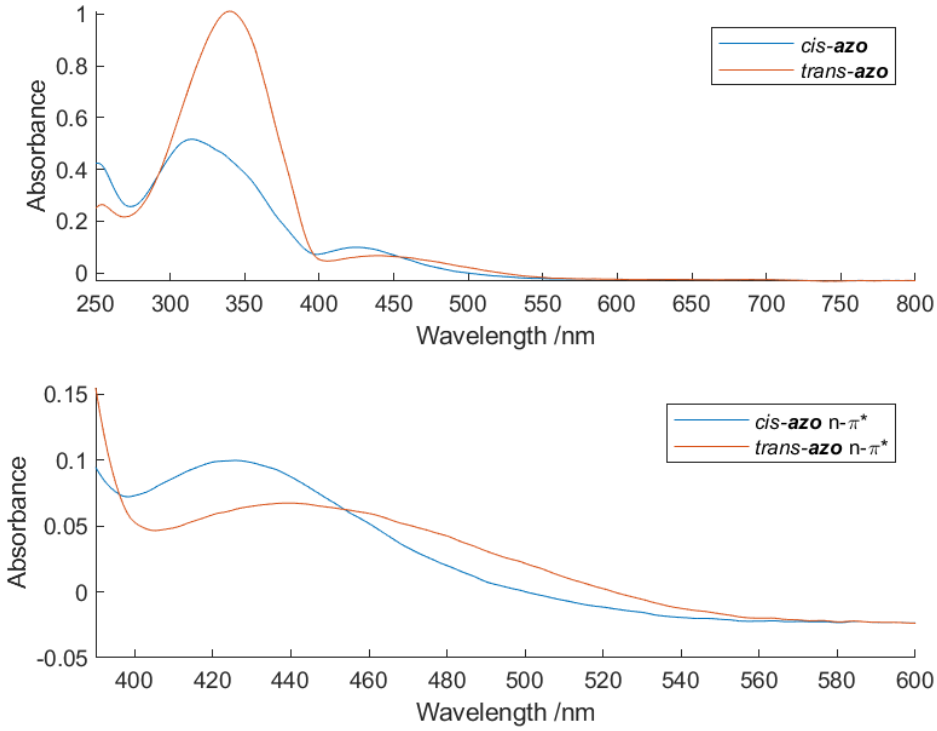

Supplementary Figure 2.1. UV-Vis absorbance spectra of *trans*- and *cis*-azo in THF solutions.

2.7.1.2 Single-crystal X-ray diffraction

The X-ray data for (*trans*-azo)(dioxane), (*trans*-azo)(pyrazine) and *trans*-azo **II** were collected on a Bruker D8 Venture dual-source diffractometer equipped with a PHOTON II detector and an Oxford Cryostream 800 cooling system, using mirror-monochromated Mo*K*α ($\lambda = 0.71073$ Å) or Cu*K*α radiation ($\lambda = 1.54184$ Å) from respective microfocus sources. Data were collected in a series of φ- and ω-scans. APEX3 software was used for data collection, integration and reduction.[1] Numerical absorption corrections were applied using SADABS-2016/2.[2]

Structures were solved by dual-space iterative methods using SHELXT[3] and refined by full-matrix least-squares on F^2 using all data with SHELXL[4] within the OLEX2[5] and/or WinGX[6] environment. In all cases, some reflections were found to have been obscured by the beam stop and were omitted from the refinement. Extinction correction was applied in all cases. Hydrogen atoms were placed in calculated positions and treated as riding on the parent carbon atoms with isotropic displacement parameters 1.2 times larger than the respective parent atoms. Planarity restrains and geometrical restraints for equivalent 1,2- and 1,3-distances were applied to *trans*-azo molecules in all structures. Rigid bond and proximity restraints were applied to the anisotropic displacement parameters (ADPs) of all the atoms belonging to disordered moieties. Constraints were applied to the anisotropic displacement parameters (ADPs) of all equivalent atoms in two disorder components in *trans*-azo **II**.

In (*trans*-azo)(dioxane), *trans*-azo molecule (except the iodine atoms) was modelled as disordered over two components whose relative occupancies were freely refined, converging to 81.1(10) and 18.9(10)%, respectively.

In (*trans*-azo)(pyrazine), *trans*-azo was disordered over two components, around a two-fold axis and a mirror plane (and thus an inversion centre, too), with only one half of a *trans*-azo molecule modelled explicitly, and its other half, as well as the whole other disorder component, generated by symmetry elements. Relative occupancies of the two disorder components were fixed at 50%, as required by the symmetry.

In *trans*-azo **II**, non-merohedric twinning was found with a two-fold axis around the reciprocal axis *c** as the operator. The data was therefore indexed by two orientation matrices and processed accordingly. Similarly to (*trans*-azo)(dioxane), *trans*-azo molecule (except the iodine atoms) was modelled as disordered over two components whose relative occupancies were freely refined, converging to 51.6(15) and 48.4(15)%, respectively. The batch scale factor refined to 23.5(5)%.

Crystal structure figures were generated using Mercury[7] and POV-Ray.[8]

CCDC 2068925–2068927 contain the supplementary crystallographic data for this paper. The data can be obtained free of charge from The Cambridge Crystallographic Data Centre via www.ccdc.cam.ac.uk/structures.

Supplementary Table 2.1. Crystallographic data for the reported crystal structures of (*trans*-azo)(dioxane), (*trans*-azo)(pyrazine) and *trans*-azo **II**.

Compound	(*trans*-azo)(dioxane)	(*trans*-azo)(pyrazine)	*trans*-azo **II**
CCDC Number	2068925	2068926	2068927
T (K)	253.0(1)	298(2)	203.0(1)
Formula	$C_{16}H_8F_8I_2N_2O_2$	$C_{16}H_4F_8I_2N_4$	$C_{12}F_8I_2N_2$
M_r	666.04	658.03	577.94
Crystal system	Triclinic	Orthorhombic	monoclinic
Space group	$P\bar{1}$	*Pnnm*	$P2_1/n$
a (Å)	6.2861(7)	15.7552(3)	5.8516(2)
b (Å)	7.6127(7)	5.00220(10)	5.9043(2)
c (Å)	10.8138(11)	12.0214(2)	20.9411(8)
α (°)	86.737(3)	90	90
β (°)	81.911(4)	90	92.6120(10)
γ (°)	70.447(2)	90	90
V (Å^3)	482.77(9)	947.41(3)	722.75(4)
Z	1	2	2
ρ_{calc} (g cm^{-3})	2.291	2.307	2.656
λ (Å)	0.71073	1.54184	1.54184
μ (mm^{-1})	3.348	26.919	35.090
F(000)	312	612	528
Crystal size (mm^3)	0.747×0.350×0.296	0.268×0.188×0.148	0.434×0.283×0.046
Data collection θ range (°)	3.686–30.577	4.627–72.414	4.227–72.368
Reflections collected [R_{int}]	19492 [0.0483]	13631 [0.0518]	2936 [0.1060]
Reflections [$I > 2\sigma(I)$]	2805 [2668]	975 [960]	2936 [2856]
Data completeness (%)	94.9 to θ = 30.50°	98.5 to θ = 72.00°	97.4 to θ = 67.75°
Data/parameters/restraints	2805/237/628	975/117/166	2936/145/634
Goodness-of-fit on F^2	1.203	1.099	1.056
Final R, data with $I > 2\sigma(I)$	R_1 = 0.0353 wR_2 = 0.0873	R_1 = 0.0217 wR_2 = 0.0546	R_1 = 0.1282 wR_2 = 0.3625
Final R for all data	R_1 = 0.0370 wR_2 = 0.0881	R_1 = 0.0218 wR_2 = 0.0547	R_1 = 0.1295 wR_2 = 0.3682
Largest diff. peak/hole (e Å^{-3})	1.107/−0.873	0.521/−0.594	2.755/−2.054
Extinction coefficient	0.119(15)	0.0038(4)	0.011(4)

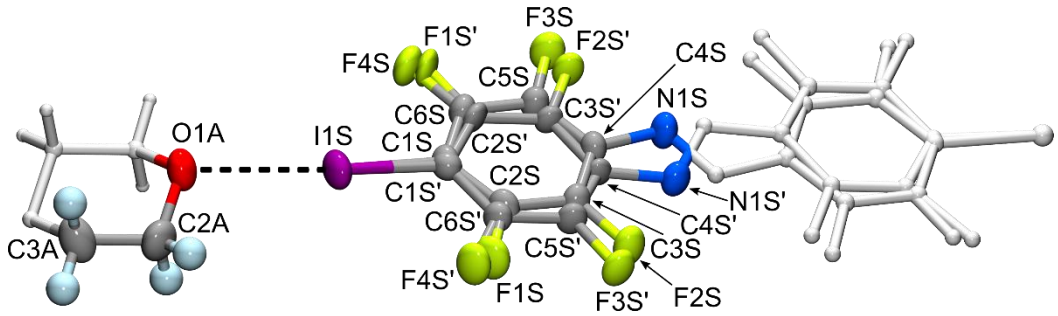

Supplementary Figure 2.2. Asymmetric unit of (*trans*-azo)(dioxane), collected at 253 K, showing the atom labelling scheme. Displacement ellipsoids are drawn at the 50 % probability level and the hydrogen atoms are shown as small spheres of arbitrary radius. The symmetry-dependent parts of *trans*-azo and dioxane molecules are shown in ball-and-stick model in light grey. Halogen bond is shown as a dashed black line.

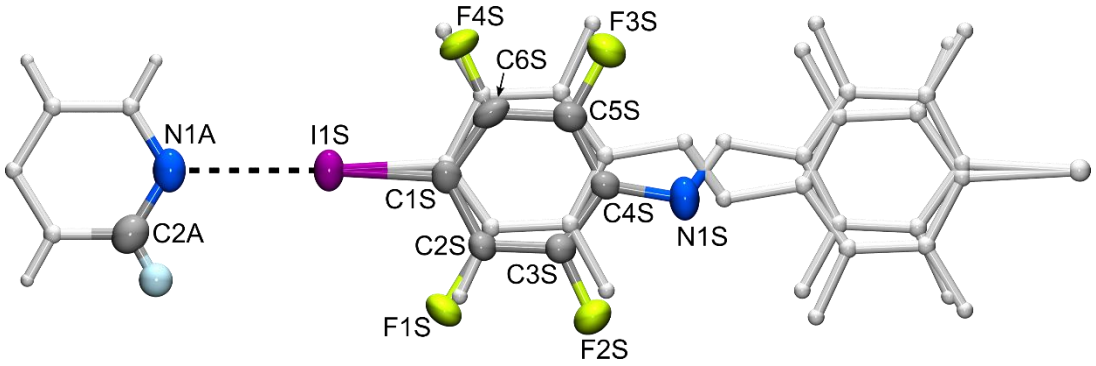

Supplementary Figure 2.3. Asymmetric unit of (*trans*-azo)(pyrazine), collected at 298 K, showing the atom labelling scheme. Displacement ellipsoids are drawn at the 50 % probability level and the hydrogen atoms are shown as small spheres of arbitrary radius. The symmetry-dependent parts of *trans*-azo and pyrazine molecules are shown in ball-and-stick model in light grey. Halogen bond is shown as a dashed black line.

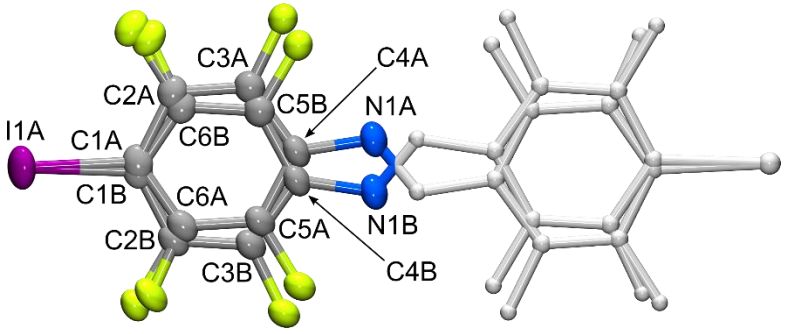

Supplementary Figure 2.4. Asymmetric unit of *trans*-azo **II**, collected at 203 K, showing the atom labelling scheme. Displacement ellipsoids are drawn at the 50 % probability level. The symmetry-dependent part of *trans*-azo molecule are shown in ball-and-stick model in light grey.

The structure of the newly observed polymorph *trans*-azo-II was found to be very similar to the previously reported structure of *trans*-azo-I, with layers of *trans*-azo molecules parallel to the respective *ab*-planes in either structure and short I···F contacts between the layers (Supplementary Figure 5a,b). However, the asymmetric unit in *trans*-azo-II was found to contain half a molecule of *trans*-azo unlike the whole molecule of *trans*-azo in the asymmetric unit of *trans*-azo-I, reflected in the approximate halving of unit cell volume from 1462.3(2) $Å^3$ in *trans*-azo-I to 722.75(4) $Å^3$ in *trans*-azo-II despite the same space group ($P2_1/n$). Besides that, the difference in packing of *trans*-azo molecules in the two structures gives rise to markedly different the centroid-centroid distances between neighbouring molecules in columns: while in *trans*-azo-I, there are two distinct distances of 4.733 and 5.789 Å along the *a*-axis (Supplementary Figure 5c) and a single 5.968 Å distance along the *b*-axis (Supplementary Figure 5e), in *trans*-azo-II the corresponding distances are 5.852 Å along the *a*-axis (Supplementary Figure 5d) and 5.904 Å along the *b*-axis (Supplementary Figure 5f). Although the structures of the two polymorphs are very similar, the two can be readily distinguished by PXRD even in a mixture (e.g. as in Supplementary Figure 18).

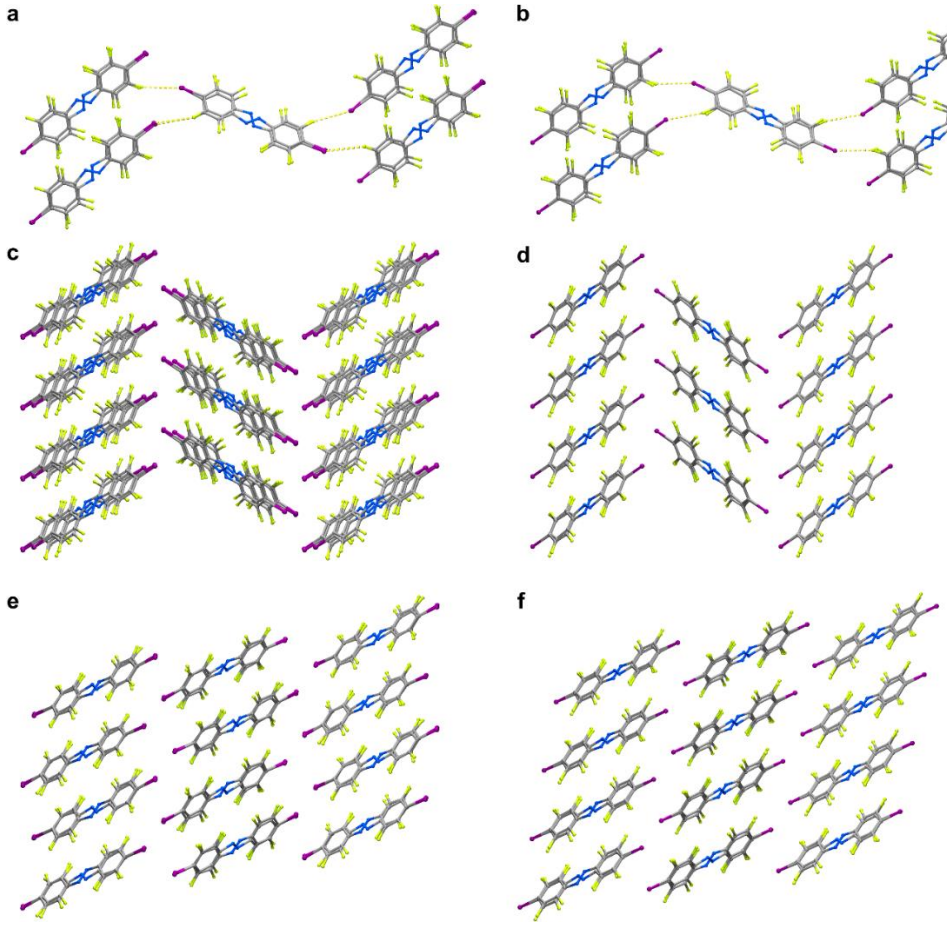

Supplementary Figure 2.5. Comparison of the crystal structures of two polymorphs of *trans*-azo. Short I···F contacts in the structure of: **a** *trans*-azo-I; and **b** *trans*-azo-II. Projections along the crystallographic *a*-axes of the structures of: **c** *trans*-azo-I; and **d** *trans*-azo-II. Projections along the crystallographic *b*-axes of the structures of: **e** *trans*-azo-I; and **f** *trans*-azo-II.

2.7.1.3 Laboratory laser setup

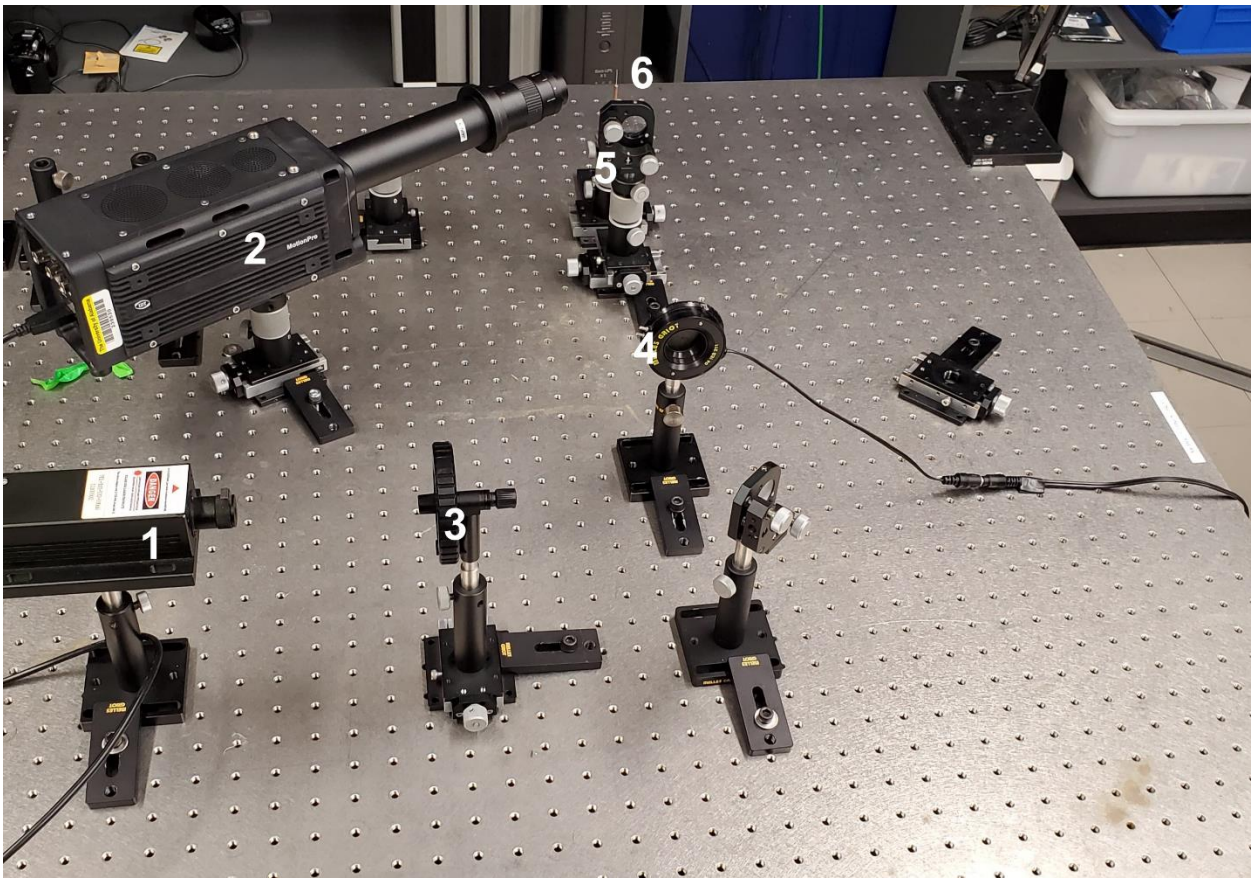

Supplementary Figure 2.6. Laboratory laser setup with high-speed camera and shutter: **(1)** 532 nm Laser, **(2)** Redlake MotionPro Y4, **(3)** Tunable neutral density filter, **(4)** Melles Griot tuneable shutter, **(5)** Melles Griot convex lens, **(6)** Crystal mount with a 150 μm loop.

2.7.1.4 Beam intensity profiles

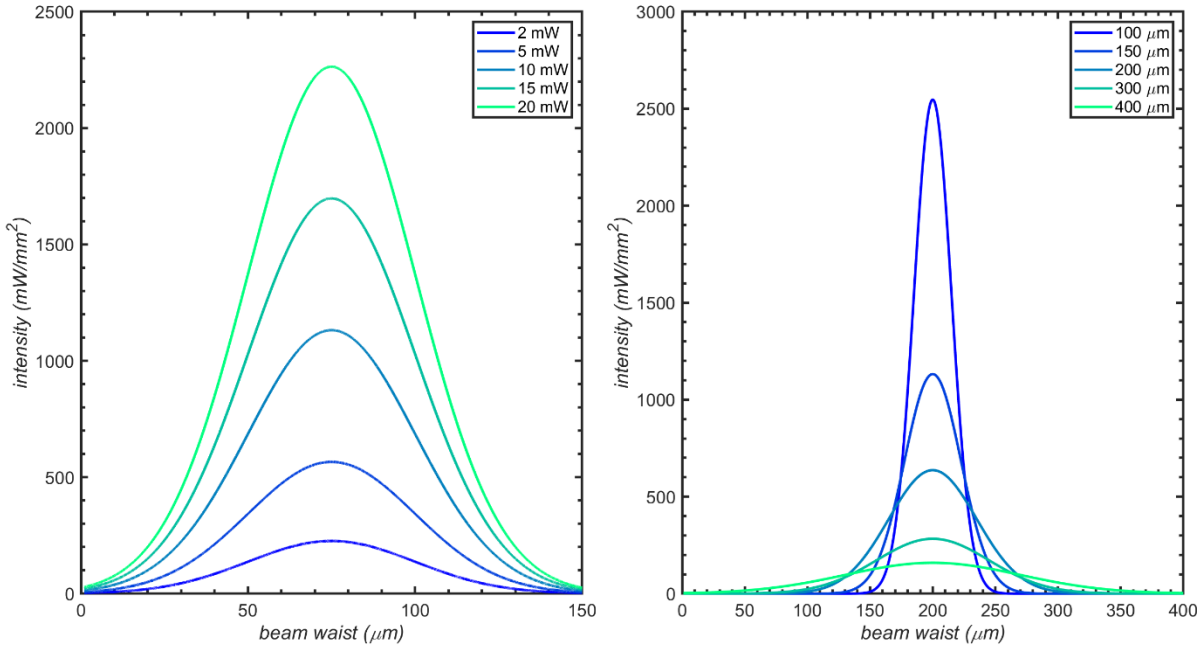

Supplementary Figure 2.7. (Left) a Gaussian beam profile of a 150 μm size beam of differing powers (of 2, 5, 10, 15, and 20 mW) discussed in this manuscript.. (Right) a Gaussian beam profile at differing beam sizes (100, 150, 200, 300, 400 μm) at a 10 mW output power, described by the equation

$$f(x) = a \cdot e^{-(x-b)^2/2c^2}$$

Supplementary Formula 2.1. The Gaussian function used to simulate the beam intensity profile where the variable *a* represents the intensity at the centre of the beam waist.

$$I_0 = \frac{2 \cdot P_0}{\pi \cdot {w_0}^2}$$

Supplementary Formula 2.2. Intensity profile of a beam profile at the centre of the beam waist; where P_0 = total power of the beam, and w_0 = the beam waist radius.

2.7.2 Photo-carving of (*trans*-azo)(dioxane)

2.7.2.1 Optical properties and photo-carving of single crystals

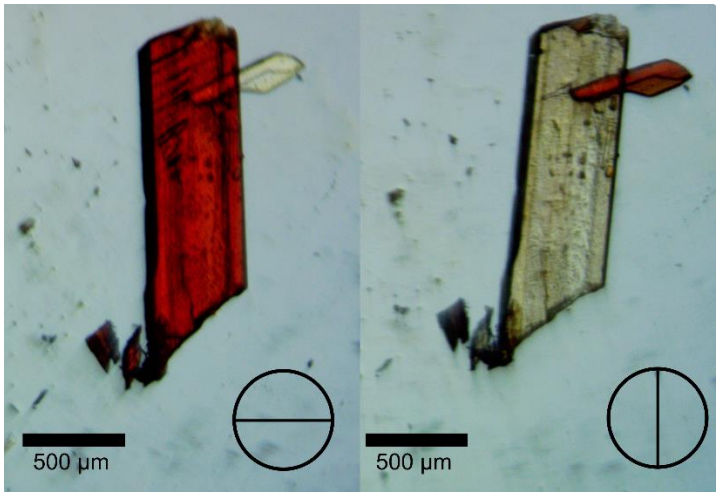

Supplementary Figure 2.8. Dichroism of the (*trans*-azo)(dioxane) crystals at different orientations to plane-polarized light.

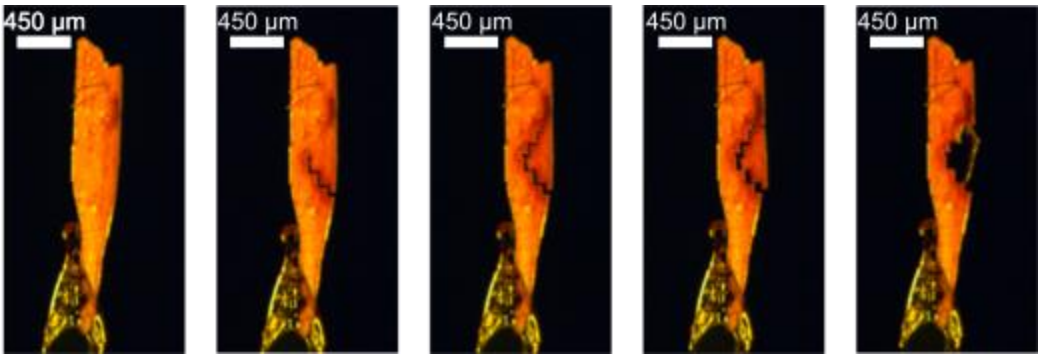

Supplementary Figure 2.9. A sequence of pictures, left to right, showing fine manual carving of the crystal of (*trans*-azo)(dioxane) performed using the laboratory laser setup. Crystal was cut in a zig-zag fashion using 10 mw 532 nm laser light.

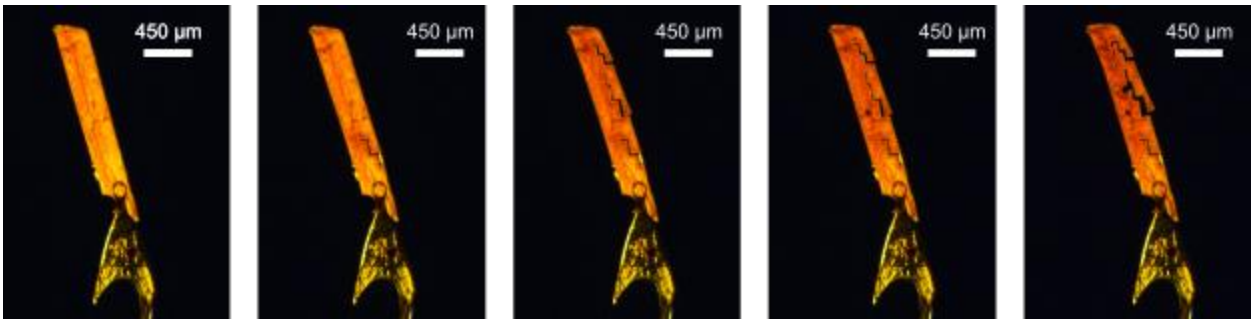

Supplementary Figure 2.10. A sequence of pictures, left to right, showing fine manual carving of the crystal of (*trans*-azo)(dioxane) performed using the laboratory laser setup. Crystal was cut in a zig-zag fashion or punctured to create holes using 10 mw 532 nm laser light.

2.7.2.2 Thickness dependence

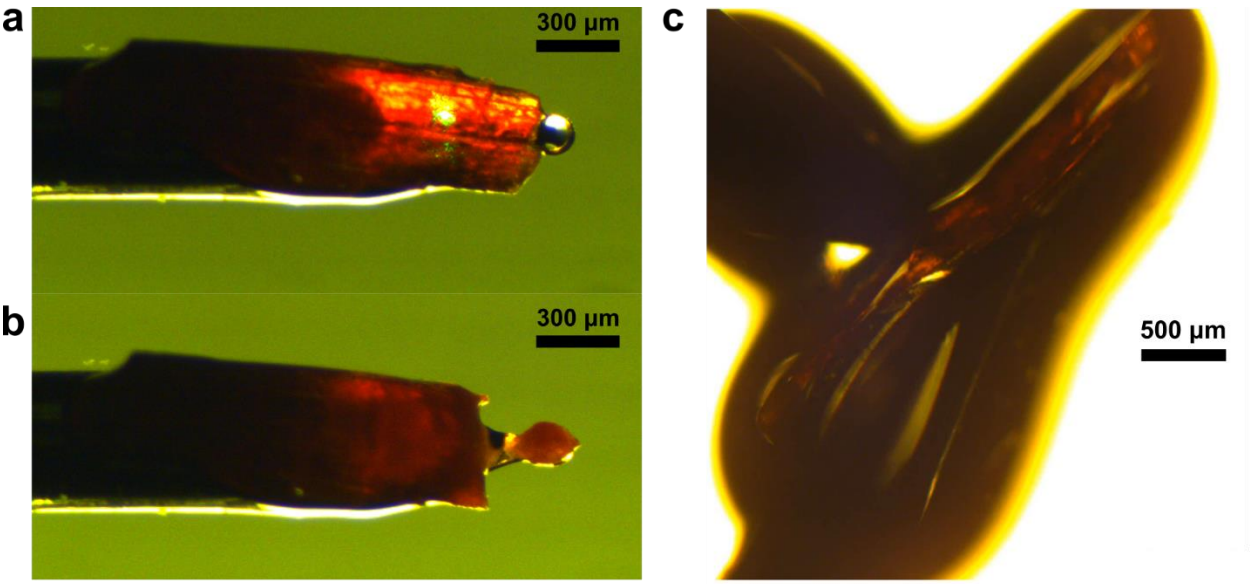

Supplementary Figure 2.11. Laser cutting of a large (*trans*-azo)(dioxane) crystal (thickness ca. 250 µm): **a**, prior to irradiation with 15 mW 532 nm light, **b**, after irradiation, **c**, side view of the crystal, displaying its thickness.

2.7.2.3 Raman spectroscopy

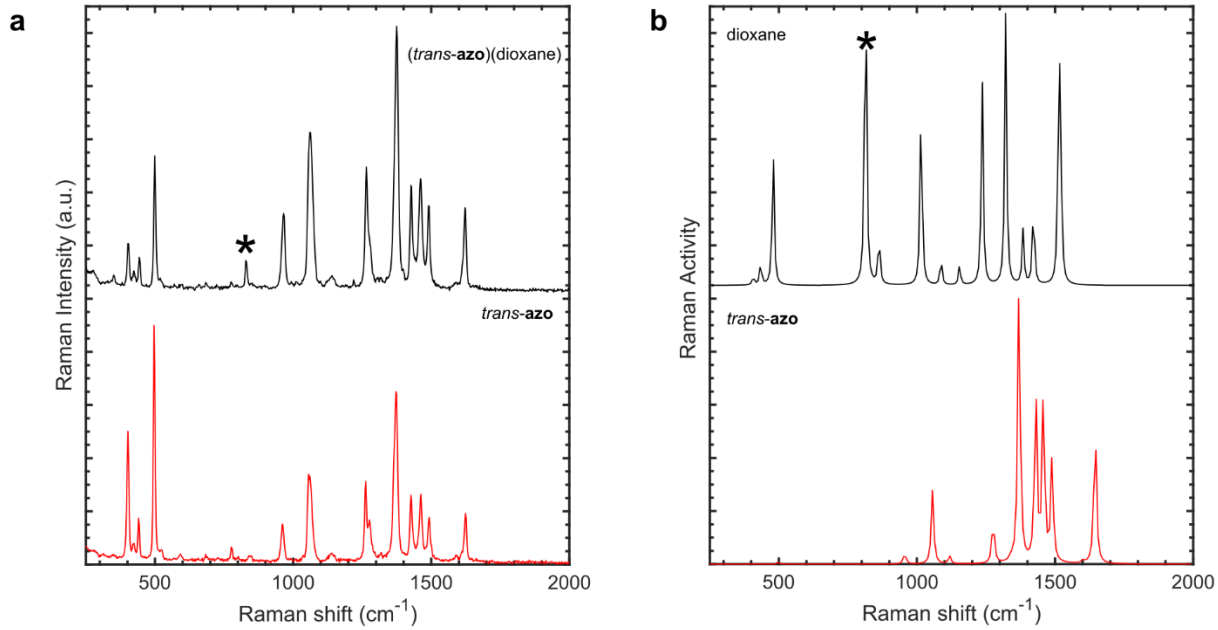

Supplementary Figure 2.12. a, Experimental Raman spectra of (*trans*-azo)(dioxane) and *trans*-azo **II**. Acquired with the 785 nm probe, 25 mW power, 2.5 s integration, 10 accumulations. **b**, Simulated gas-phase Raman spectra of dioxane and *trans*-azo. Asterisk (*) indicates the position of the dioxane *ν*(ring breathing) Raman band.

Supplementary Table 2.2. Assigned Raman shifts for (*trans*-azo)(dioxane) co-crystal.

(*trans*-azo)(dioxane) experimental shifts (cm^{-1})	*trans*-azo experimental shifts (cm^{-1})	dioxane simulated shifts (cm^{-1})	*trans*-azo simulated (cm^{-1})	assignment
350	N/A	N/A	N/A	
402	402	N/A	N/A	
423	423	N/A	413	*ν*(Aromatic)
443	440	N/A	444	*ν*(Aromatic)
499	497	N/A	491	*ν*(Aromatic)
778	776	N/A	N/A	
830	N/A	810	N/A	*ν*(ring breathing), dioxane
966	961	N/A	950	*ν*(Aromatic)
1061	1056	N/A	1050	*ν*(C−N)
1265	1263	N/A	1270	*ν*(C−N)
N/A	1276 Sh	N/A	N/A	
1375	1373	N/A	1364	*ν*(N=N)
1426	1426	N/A	1424	*ν*(N=N)
1461	1463	N/A	1452	*ν*(N=N)
1492	1492	N/A	1484	*ν*(N=N), *ν*(Aromatic)
1622	1624	N/A	1640	*ν*(Aromatic)

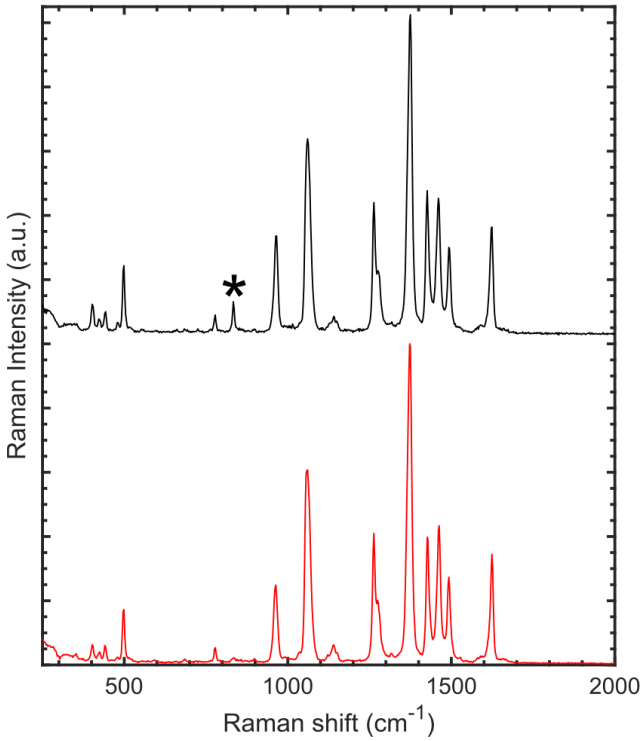

Supplementary Figure 2.13. Experimental Raman spectra of a (*trans*-azo)(dioxane) crystal before (top) and after (bottom) irradiation for 1 s with a 532 nm laser at 1 mW power setting. Acquired with the 785 nm probe, 25 mW power, 2.5 s integration, 10 accumulations. Asterisk (*) indicates the position of the dioxane *v*(ring breathing) Raman band that disappears upon irradiation, indicating loss of dioxane.

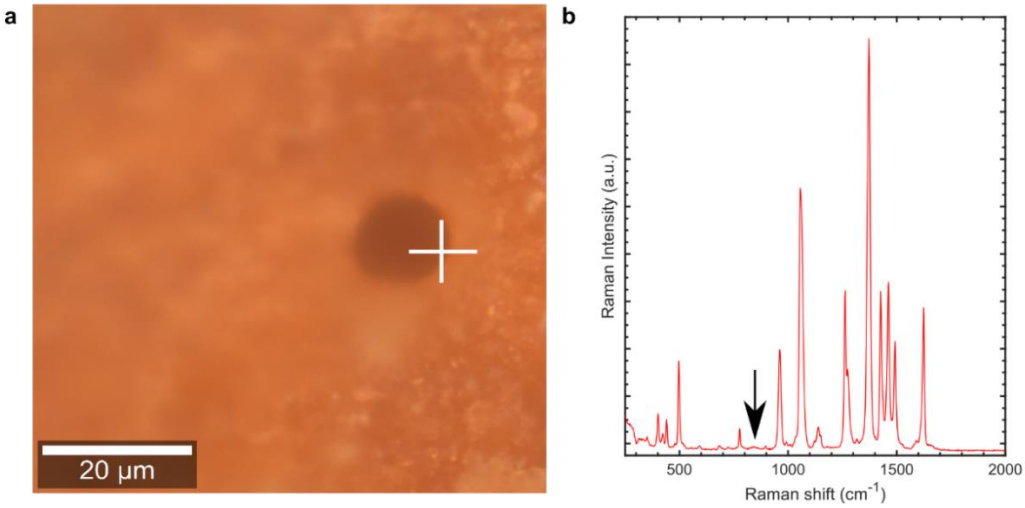

Supplementary Figure 2.14. Raman spectroscopy investigation of a hole created in a (*trans*-azo)(dioxane) crystal by irradiation with a 532 nm laser. **a,** Micrograph of the hole and **b,** the spectrum collected at the spot marked by the cross with the 785 nm probe, 25 mW power, 2.5 s integration, 10 accumulations. Arrow indicates the expected position of the (absent) dioxane *v*(ring breathing) Raman band.

2.7.2.4 Stability study

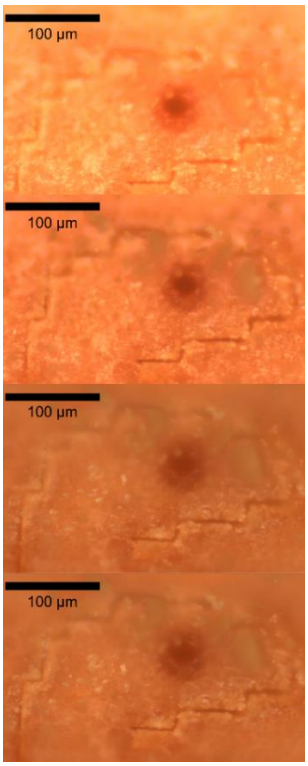

Supplementary Figure 2.15. Aging of a zig-zag lines of photo-engraved (*trans*-azo)(dioxane) co-crystal, from top to bottom: directly after irradiation, 1, 2, and 3 days after irradiation.

2.7.2.5 Powder X-ray diffraction studies under irradiation

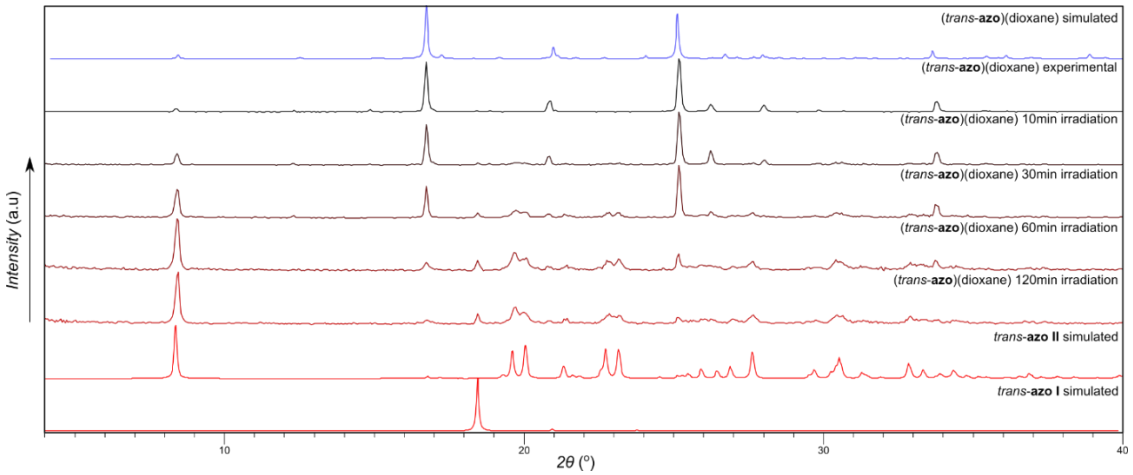

Supplementary Figure 2.16. Time evolution of **p**owder X-ray diffraction pattern of a bulk sample of (*trans*-azo)(dioxane) upon irradiation with dispersed 532 nm light (37 mW LED). Simulated (*trans*-azo)(dioxane) pattern was created with preferred orientation of the 001 crystallographic plane, and March-Dollase parameter of 0.4. Simulated *trans*-azo **I** was created with preferred orientation of the 013 crystallographic plane, and March-Dollase parameter of 0.2.

2.7.2.6 Thermal analysis

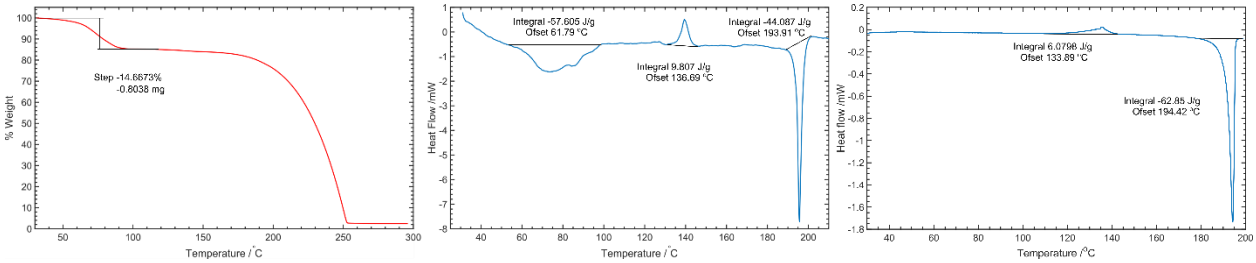

Supplementary Figure 2.17. TGA (red) and DSC (blue) traces of (*trans*-azo)(dioxane) (left/center), and DSC trace of *trans*-azo **II** (right) performed on a Mettler-Toledo TGA/DSC 1 Star system thermobalance. Measurements were done under a stream of nitrogen (50 cm^3 min^{-1}) gas, at a heating rate of 5 °C min^{-1}. As seen from the DSC plots, the compound *trans*-azo **I** melts with an onset at 194 °C, while *trans*-azo **II** undergoes a polymorphic transformation with an onset in the range 134–137 °C.

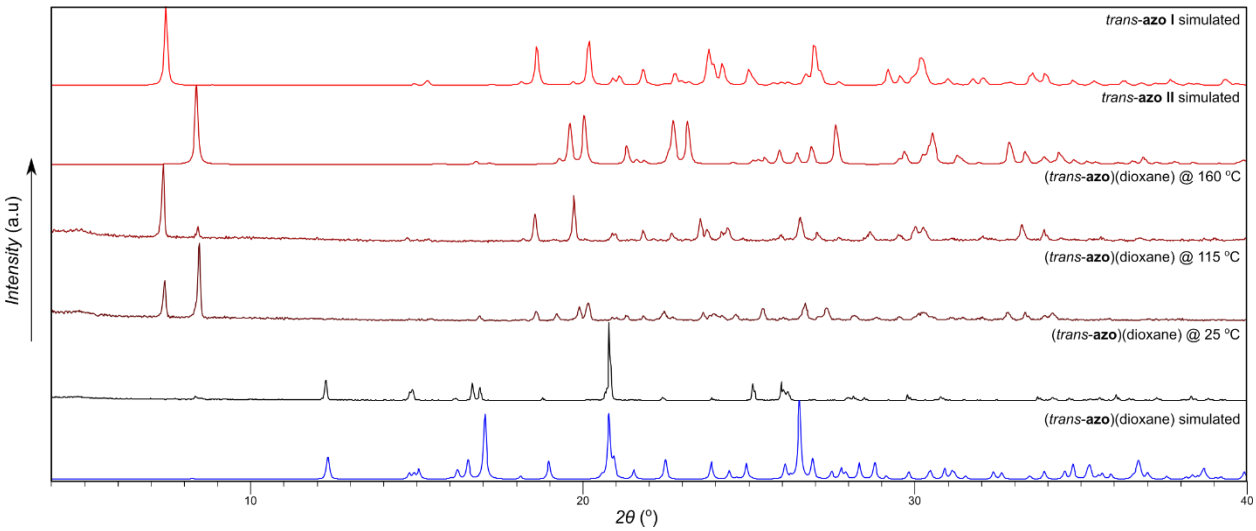

Supplementary Figure 2.18. Hot-stage powder X-ray diffraction patterns of a bulk sample of (*trans*-azo)(dioxane) at 25 °C and after heating to 115 and 160 °C.

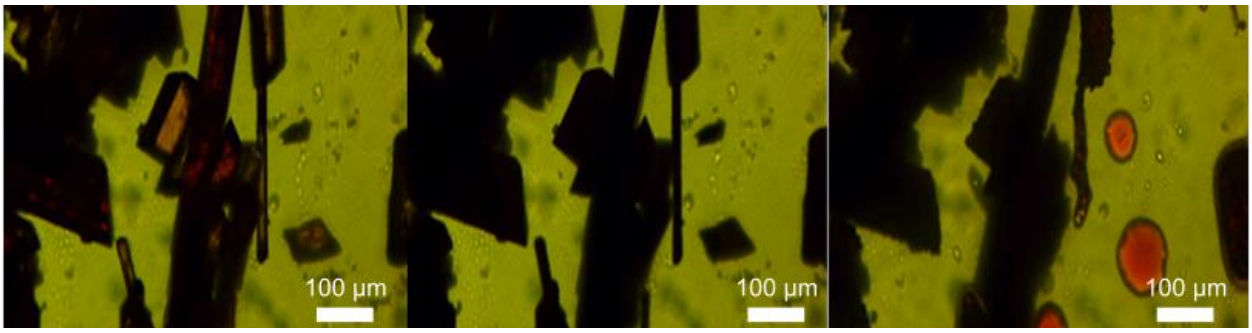

Supplementary Figure 2.19. Hot-stage microscopy of (*trans*-azo)(dioxane). The observed crystal (left) becomes opaque yet largely maintains its shape upon heating to 100 °C (center) before melting upon heating to 200 °C (right).

2.7.2.7 High-speed camera studies

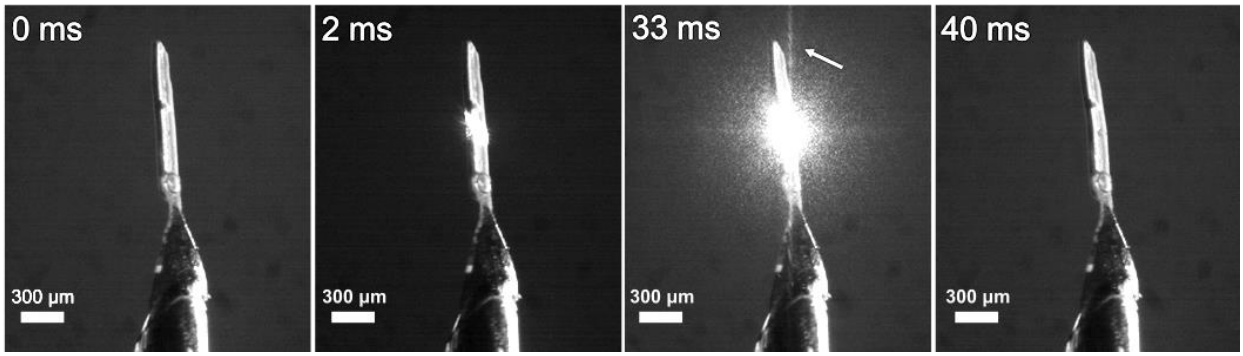

Supplementary Figure 2.20. Co-crystal (*trans*-azo)(dioxane) irradiated with a 40 ms laser pulse with a 10 mW 532 nm laser. White arrow indicates the fog released from the crystal.

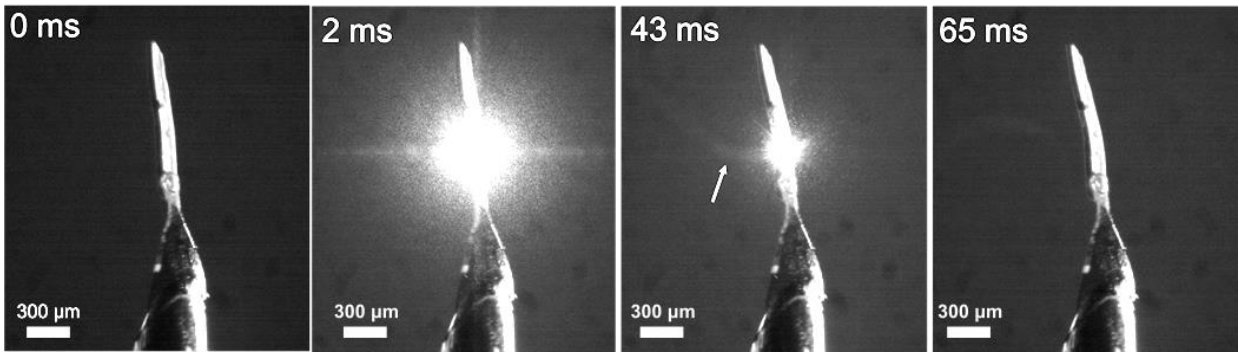

Supplementary Figure 2.21. Co-crystal (*trans*-azo)(dioxane) irradiated with a 65 ms pulse of a 10 mW 532 nm laser. White arrow indicates the fog released from the crystal.

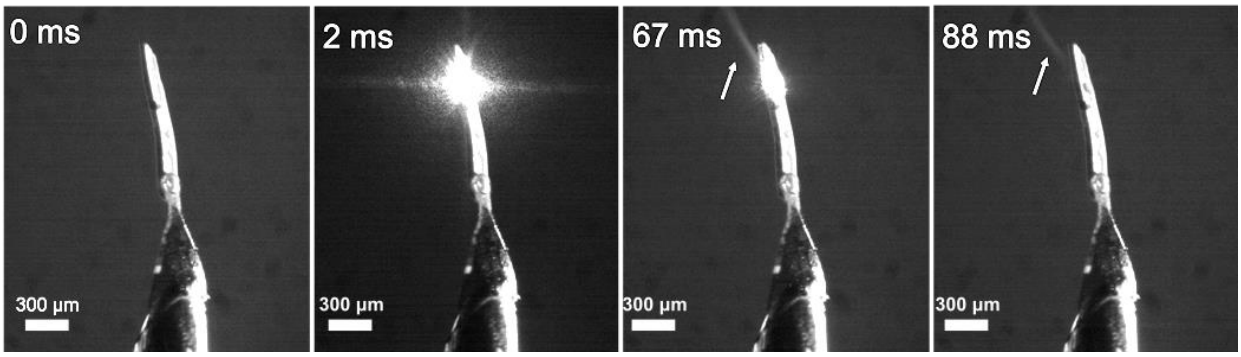

Supplementary Figure 2.22. Co-crystal (*trans*-azo)(dioxane) irradiated with a 88 ms pulse of a 10 mW 532 nm laser. White arrow indicates the fog released from the crystal.

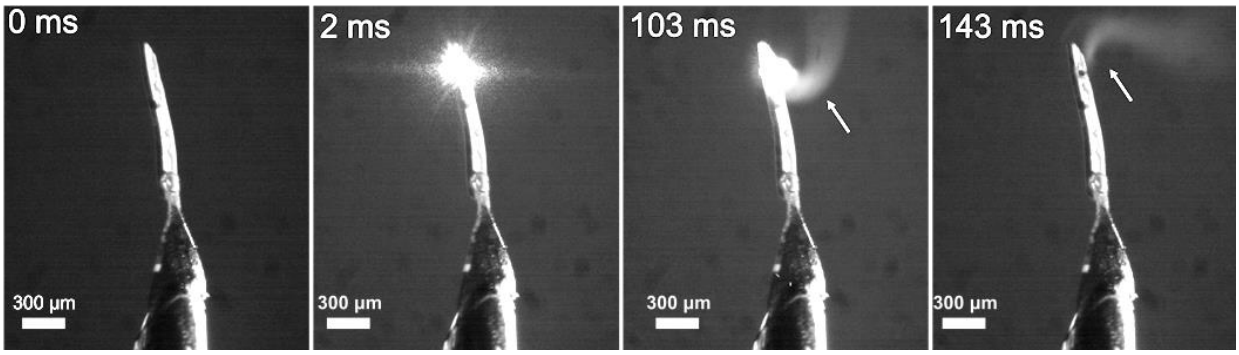

Supplementary Figure 2.23. Co-crystal (*trans*-azo)(dioxane) irradiated with a 140 ms pulse of a 10 mW 532 nm laser. White arrow indicates the 'foggy vapour' released from the crystal.

2.7.3 Attempted photo-carving of *trans*-azo I

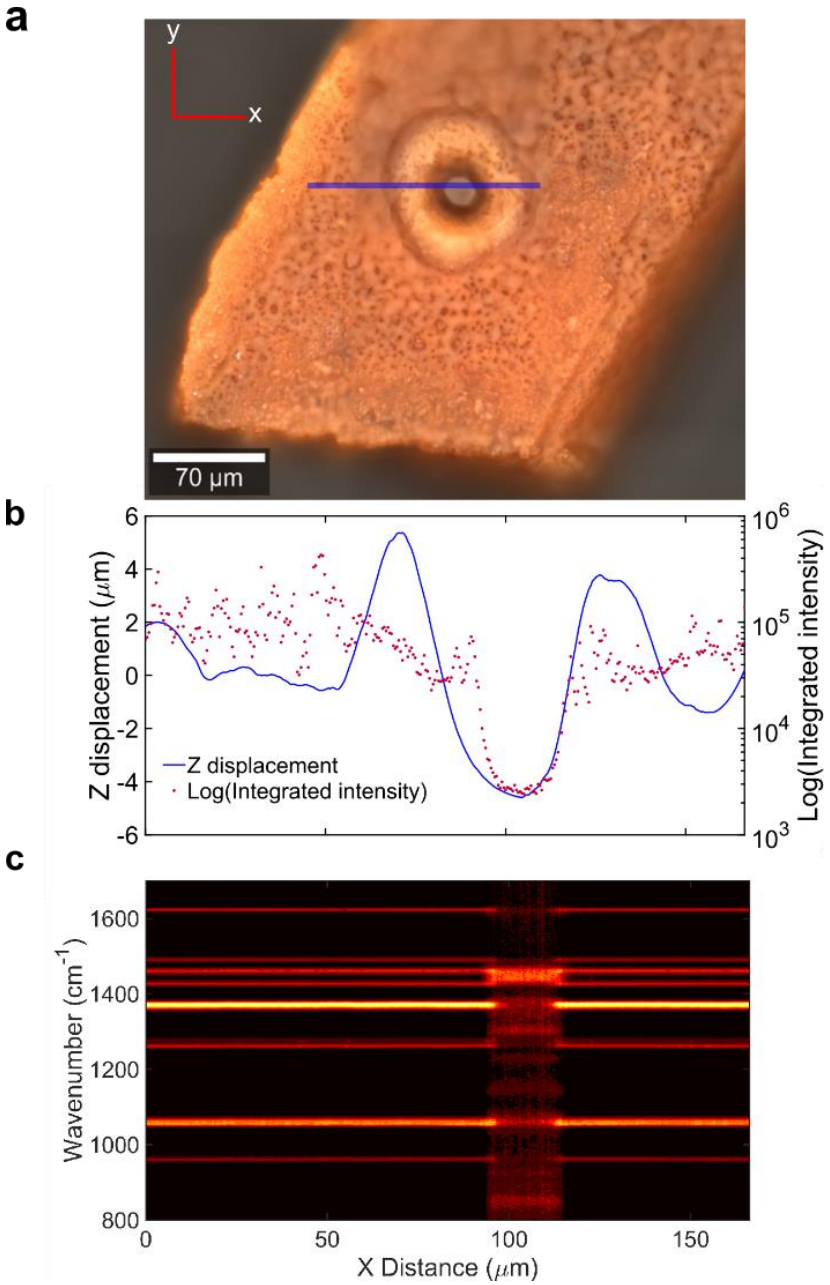

Supplementary Figure 2.24. "Fluidization" effect of a *trans*-azo crystal mapped by confocal Raman spectroscopy surface mapping. **a**, Microscopy image of crystal, with the mapping along the blue line. **b**, Logarithm of the integrated Raman intensity, and changes in the distance between the crystal surface and the objective, monitored by changes in the focal length of Raman signal (smoothed *z*-displacement). **c**, Contour plots of normalized Raman spectra over mapping distance.

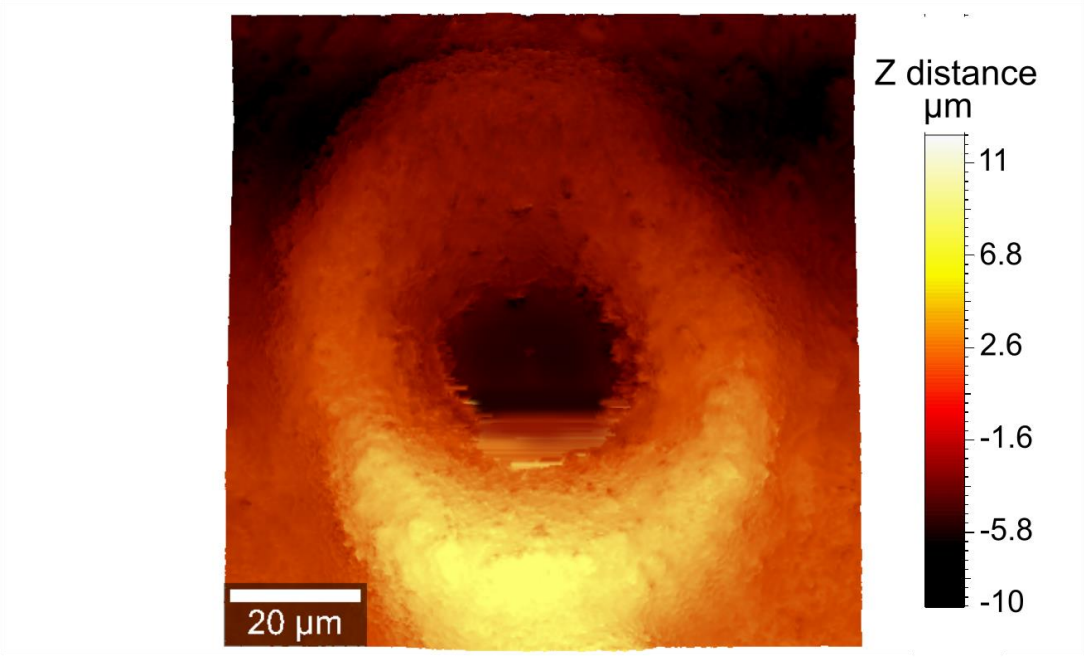

Supplementary Figure 2.25. Confocal mapping of the surface of a *trans*-azo crystal upon irradiation by a 20 mW, 532 nm laser beam.

2.7.4 Photo-carving of (*trans*-azo)(pyrazine)

2.7.4.1 Optical properties

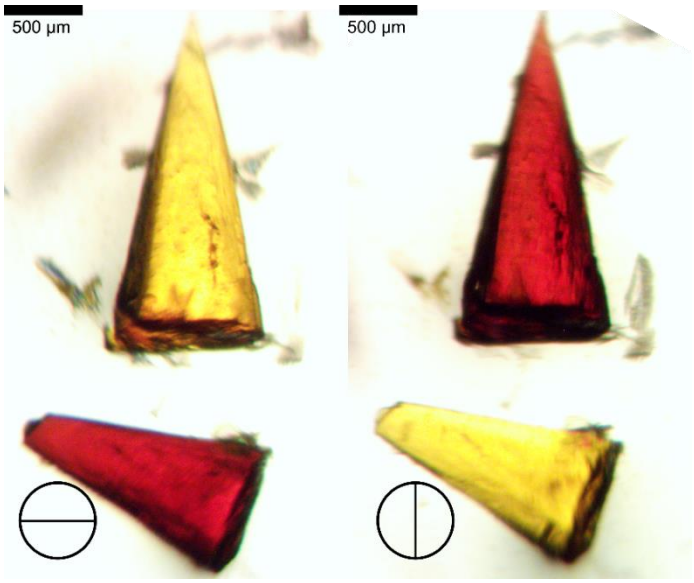

Supplementary Figure 2.26. Dichroism of the (*trans*-azo)(pyrazine) crystals at different orientations to plane-polarized light.

2.7.4.2 Crystallographic studies of photo-carving of single crystals

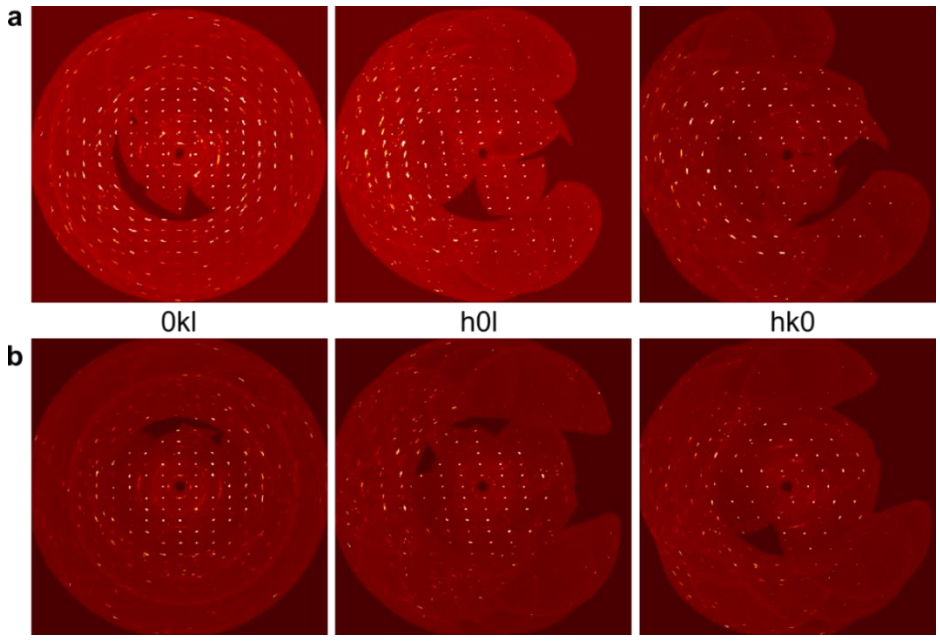

Supplementary Figure 2.27. Precession images of (*trans*-azo)(dioxane) showing the 0kl, h0l and hk0 layers: **a**, before and **b**, after photo-carving by a 532 nm laser at 20 mW power. A portion of the crystal was fully removed by laser light.

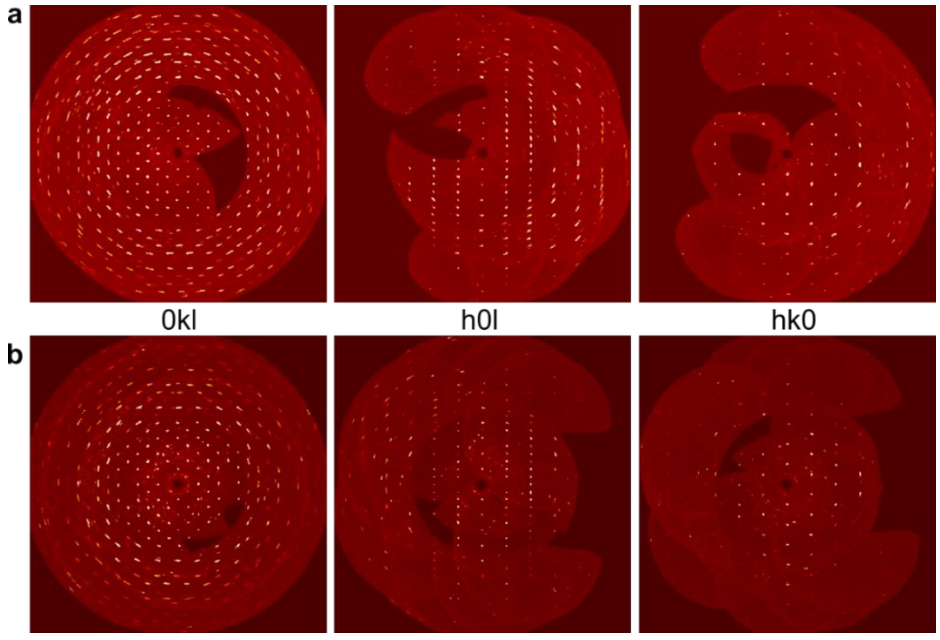

Supplementary Figure 2.28. Precession images of (*trans*-azo)(pyrazine) showing the 0kl, h0l and hk0 layers: **a**, before and **b**, after photocarving by a 532 nm laser at 20 mW power. A portion of the crystal was fully removed by laser light.

2.7.4.3 Raman spectroscopy

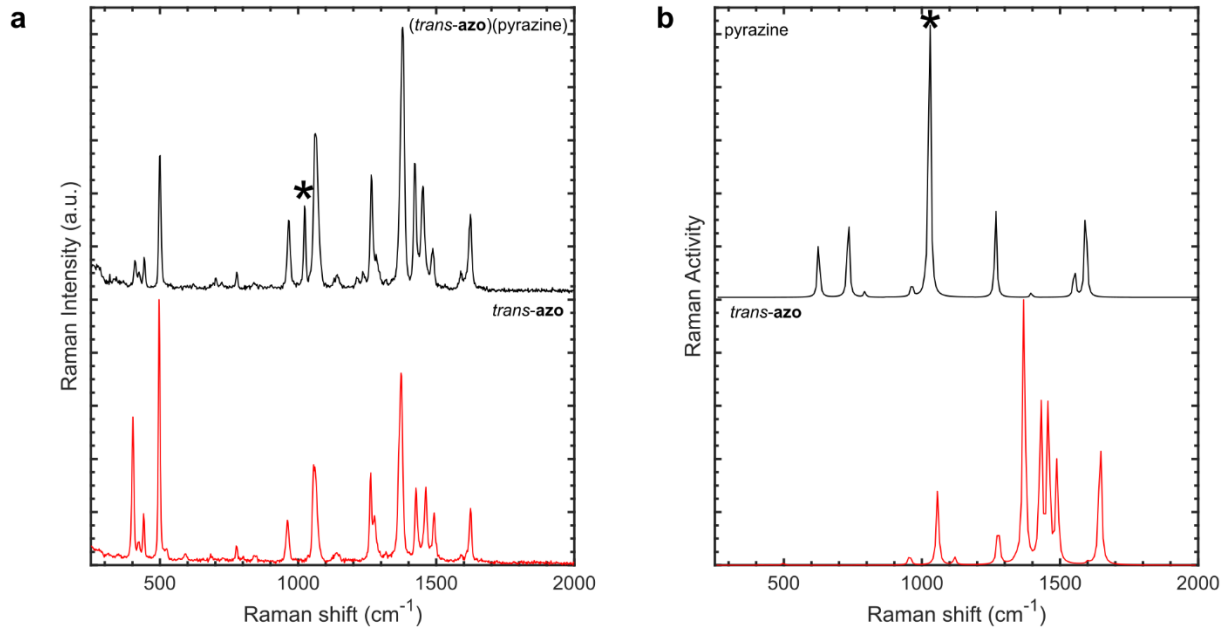

Supplementary Figure 2.29. a, Experimental Raman spectra of (*trans*-azo)(pyrazine) and *trans*-azo **II**. Acquired with the 785 nm probe, 25 mW power, 2.5 s integration, 10 accumulations. **b**, Simulated gas-phase Raman spectra of pyrazine and *trans*-azo. Asterisk (*) indicates the position of the pyrazine *ν*(ring breathing) Raman band.

Supplementary Table 2.3. Assigned Raman shifts for (*trans*-azo)(pyrazine) co-crystal.

(*trans*-azo)(pyrazine) experimental shifts (cm^{-1}) on	*trans*-azo experimental shifts (cm^{-1})	pyrazine simulated shifts (cm^{-1})	*trans*-azo simulated (cm^{-1})	assignment
409	402	N/A	N/A	*v*(Aromatic)
424 sh	423	N/A	413	*v*(Aromatic)
442	440	N/A	444	*v*(Aromatic)
501	497	N/A	491	*v*(Aromatic)
778	776	N/A	N/A	
965	961	N/A	950	*v*(Aromatic)
1023	N/A	1020	N/A	*v*(ring breathing) pyrazine
1065	1056	N/A	1050	*v*(C−N)
1265	1263	N/A	1270	*v*(C−N)
1285 sh	1276 sh	N/A	N/A	
1379	1373	N/A	1364	*v*(N=N)
1422	1426	N/A	1424	*v*(N=N)
1454	1463	N/A	1452	*v*(N=N)
1488	1492	N/A	1484	*v*(N=N), *v*(Aromatic)
1624	1624	N/A	1640	*v*(Aromatic)

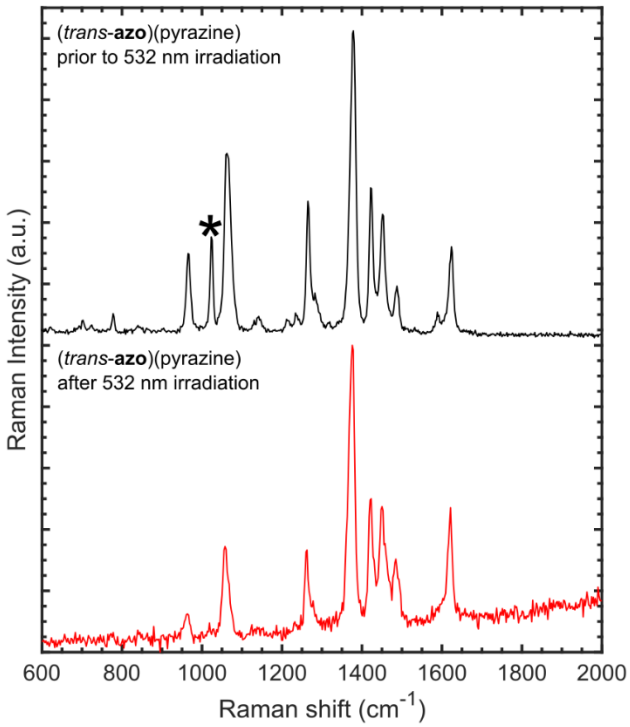

Supplementary Figure 2.30. Experimental Raman spectra of a (*trans*-azo)(pyrazine) crystal before (top) and after (bottom) irradiation for 1 s with a 532 nm laser at 3 mW power setting. Acquired with the 785 nm probe, 25 mW power, 2.5 s integration, 10 accumulations. Asterisk (*) indicates the position of the pyrazine *ν*(ring breathing) Raman band that disappears upon irradiation, indicating loss of pyrazine.

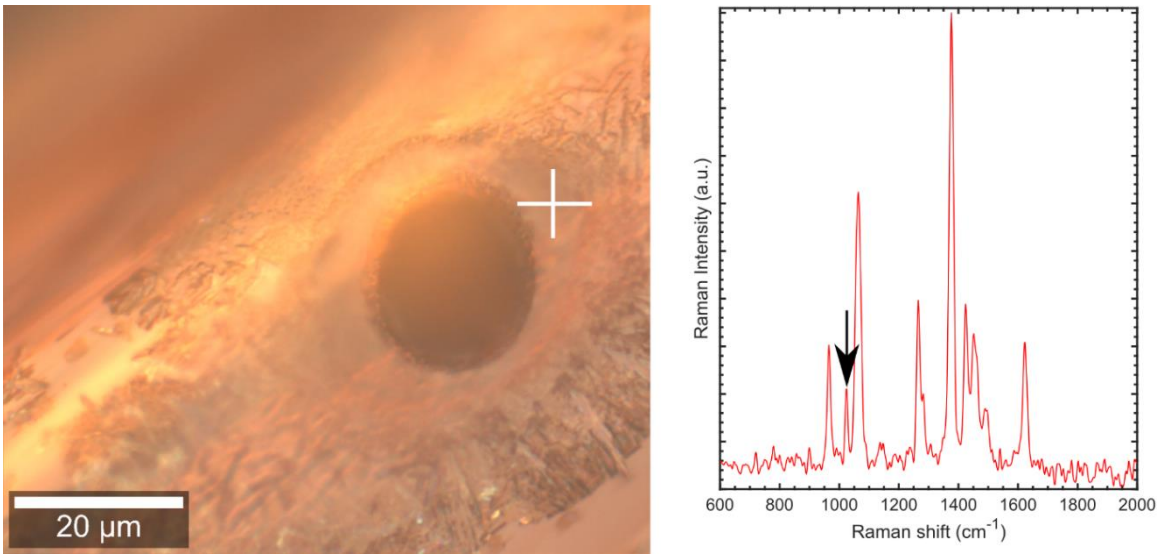

Supplementary Figure 2.31. Raman spectroscopy investigation of a hole created in a (*trans*-azo)(pyrazine) crystal by irradiation with a 532 nm laser. Micrograph of the hole (left) and the corresponding Raman spectrum (right) collected at the spot marked by the cross. Acquired with the 785 nm probe, 25 mW power, 2.5 s integration, 10 accumulations. Arrow indicates the expected position of the pyrazine *ν*(ring breathing) Raman band.

2.7.4.4 Powder X-ray diffraction studies under irradiation

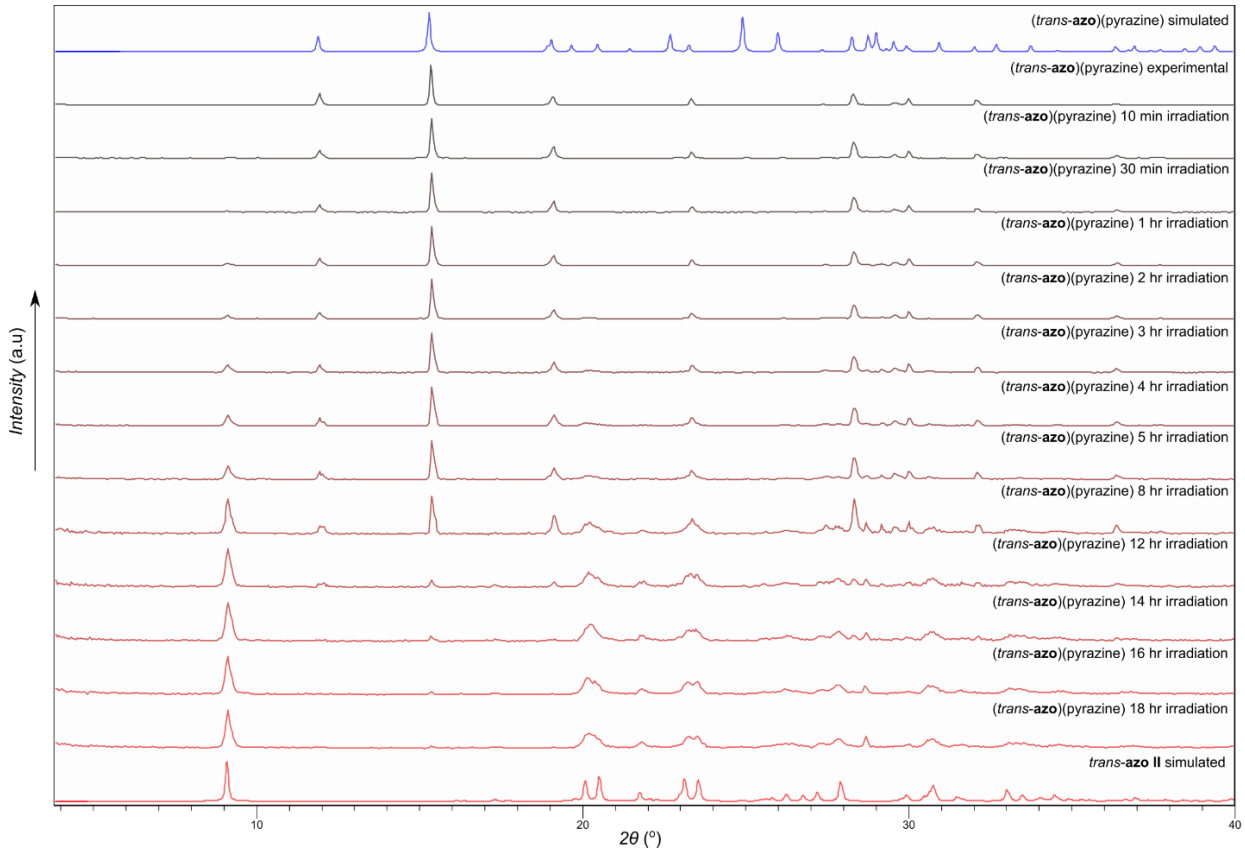

Supplementary Figure 2.32. Time evolution of the powder X-ray diffraction pattern of a bulk sample of (*trans*-azo)(pyrazine) upon irradiation with dispersed 532 nm light (37 mW LED).

2.7.4.5 Thermal analysis

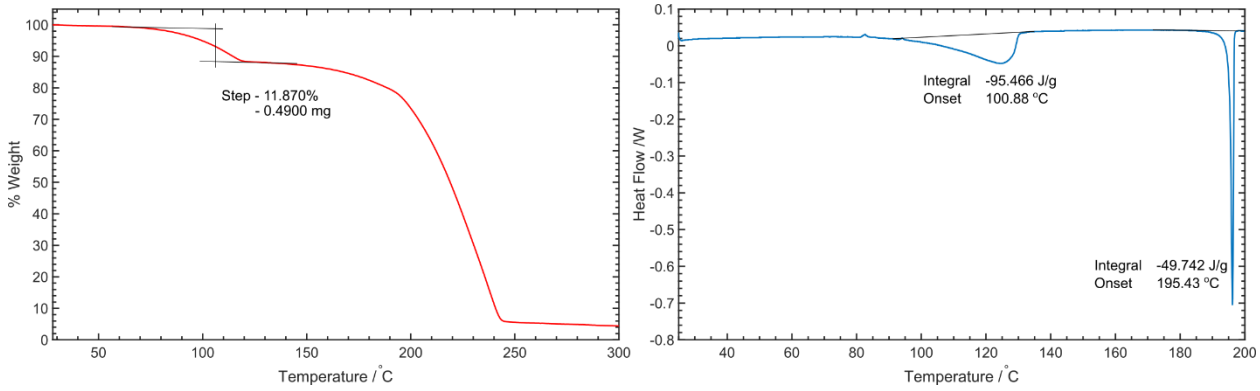

Supplementary Figure 2.33. TGA (red) and DSC (blue) traces of (*trans*-azo)(pyrazine), TGA was performed on a Mettler-Toledo TGA/DSC 1 Star system thermobalance. DSC was performed on a TA instruments LTD DSC2500 both were performed under a stream of nitrogen (50 cm^3 min^{-1}) gas, at a heating rate of 1 °C min^{-1}.

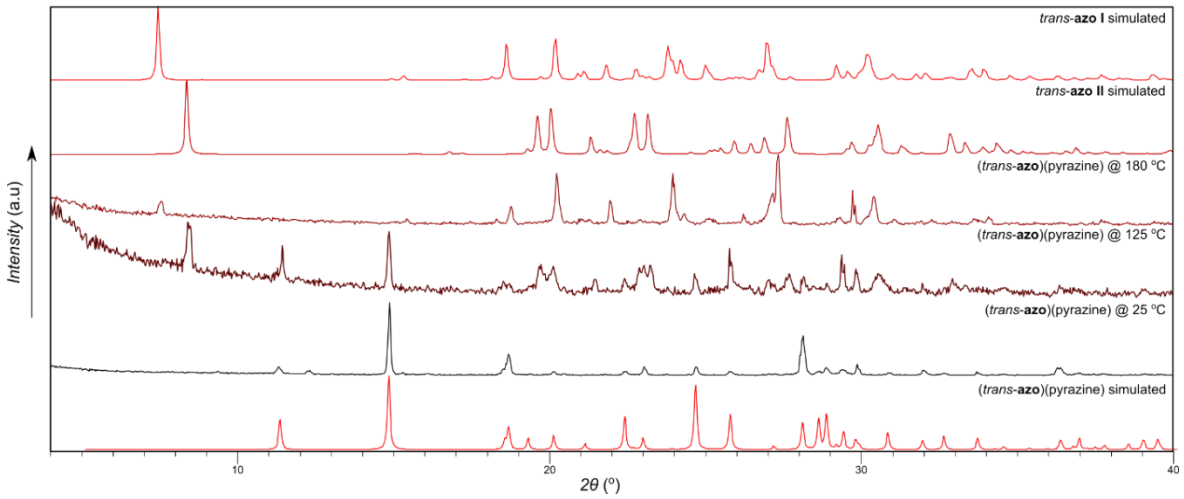

Supplementary Figure 2.34. Hot-stage powder X-ray diffraction pattern of a bulk sample of (*trans*-azo)(pyrazine) at 25 °C and after heating to 135 and 180 °C.

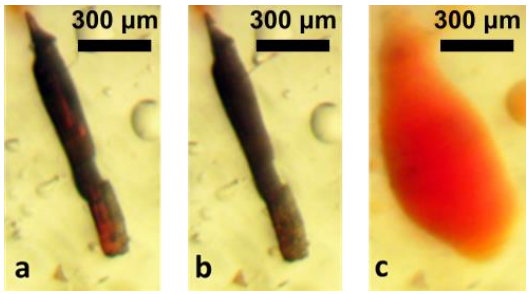

Supplementary Figure 2.35. Hot-stage microscopy of a (*trans*-azo)(pyrazine) co-crystal. **a**, Crystal before heating. **b**, Crystal upon heating to 100 °C, demonstrating darkening and loss of transparency, while maintaining shape. **c**, Melting upon heating to 200 °C.

2.7.4.6 High-speed camera studies

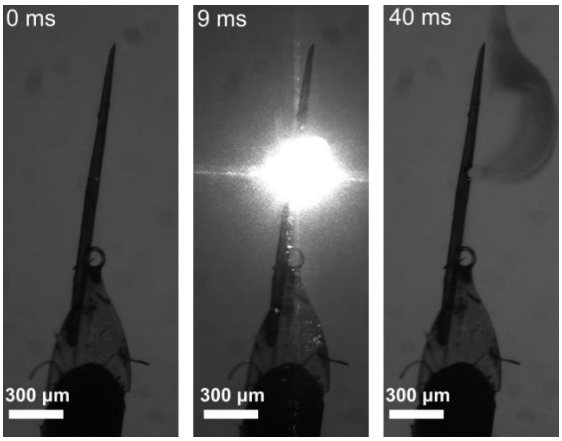

Supplementary Figure 2.36. Co-crystal (*trans*-azo)(pyrazine) irradiated with a 40 ms laser pulse (20 mW, 532 nm). Formation of a cut, and emission of 'foggy vapour' is visible.

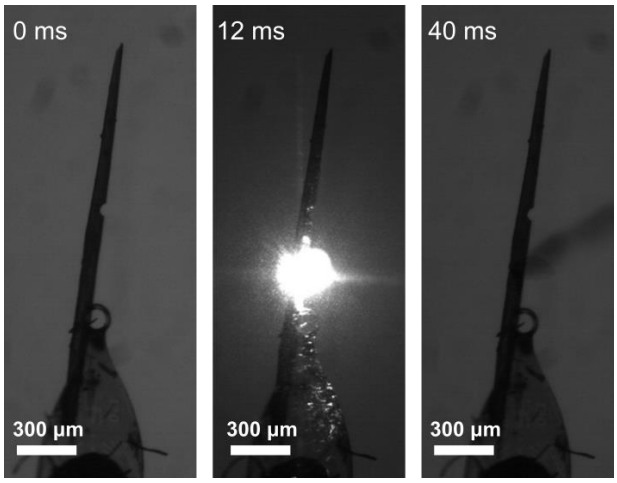

Supplementary Figure 2.37. Co-crystal (*trans*-azo)(pyrazine) irradiated with a 40 ms laser pulse (15 mW, 532 nm). In contrast to analogous experiment at 20 mW (Supplementary Figure 33), only the emission of 'foggy vapour' is visible, with no crystal cutting.

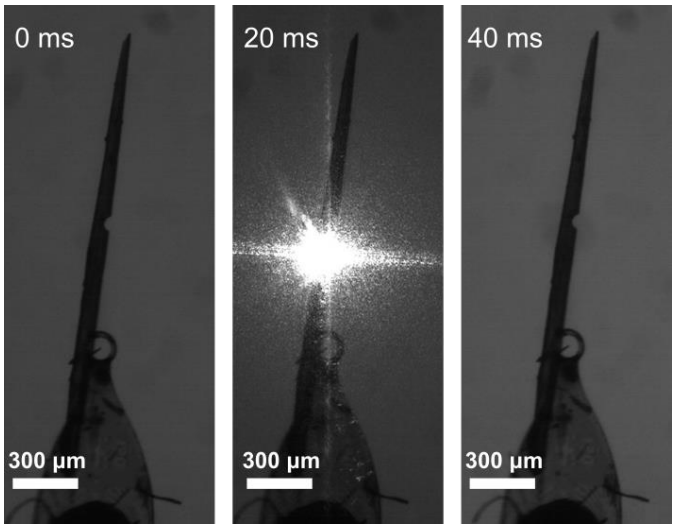

Supplementary Figure 2.38. Co-crystal (*trans*-azo)(pyrazine) irradiated with a 40 ms laser pulse (5 mW, 532 nm). In contrast to analogous experiments at 20 mW and 15 mW (Supplementary Figures 33, 34), no crystal cutting or fog emission is visible.

2.7.5 Additional photo-carving images and videos

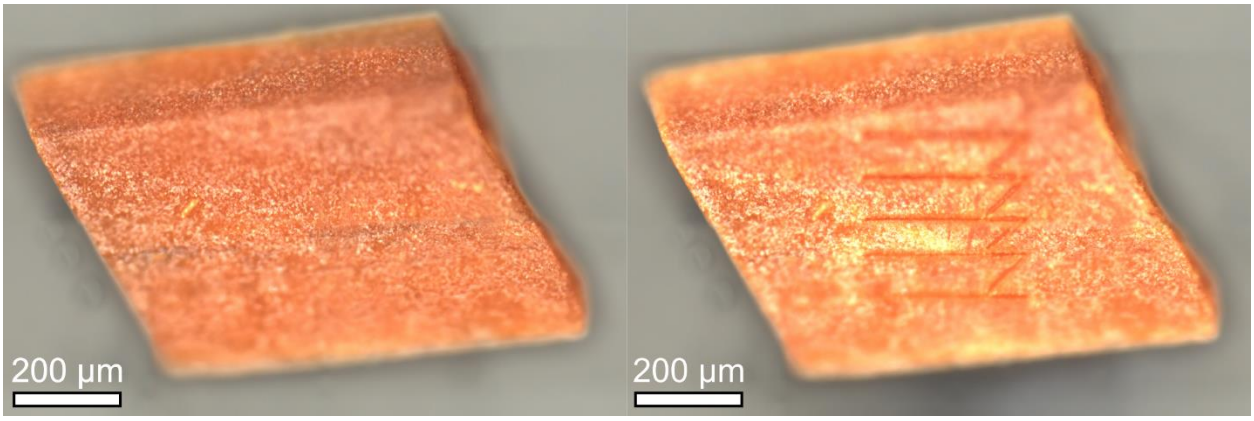

Supplementary Figure 2.39. A (*trans*-azo)(dioxane) (left), and the same crystal with a number of parallel lines carved using 1 mw 532 nm laser light from a confocal Raman microscope using a 10× objective.

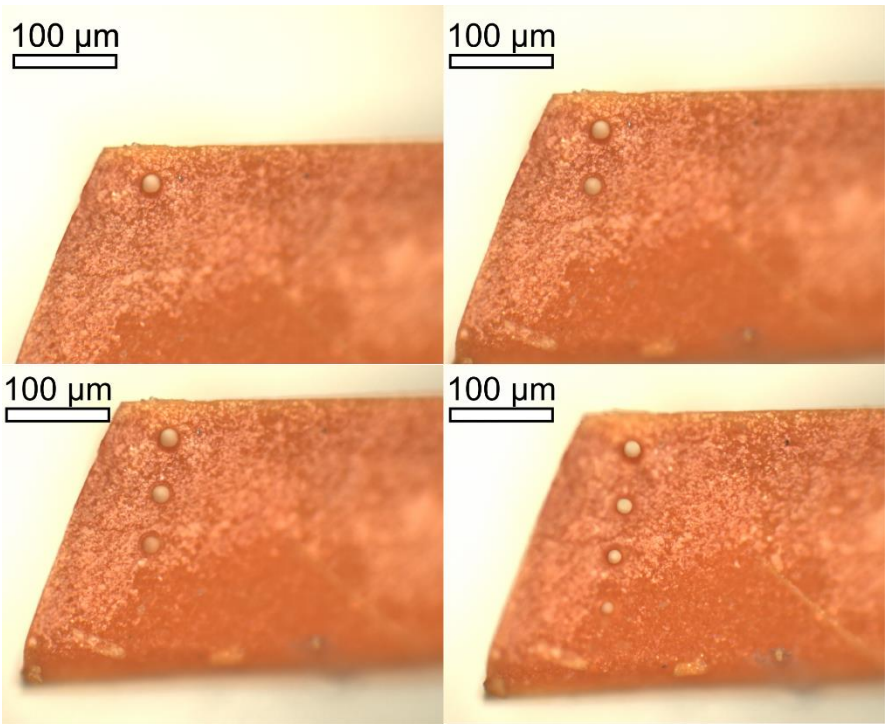

Supplementary Figure 2.40. A sequence of pictures, from upper left to lower right corner, showing a crystal of (*trans*-azo)(dioxane) with holes pierced using low-power 532 nm laser light from a confocal Raman microscope at different powers 15, 10, 5, 2 mW using a 20× objective.

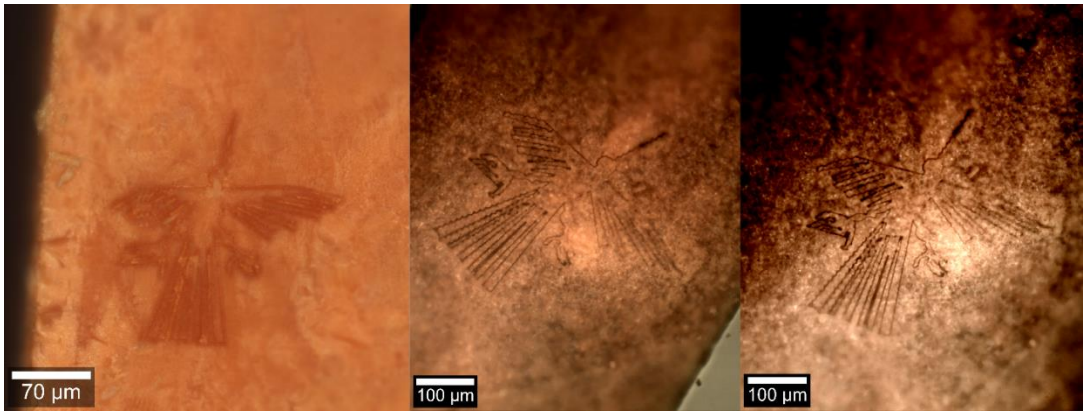

Supplementary Figure 2.41. A selection of pictures, showing the image of a Nazca Condor carved into the crystal of (*trans*-azo)(dioxane) at different scales using a 1 mW 532 nm laser light from a confocal Raman microscope with a 50× objective.

2.7.5.1 Supplementary video and data files information

All videos were acquired on the laboratory laser setup, using either a Redlake MotionPro Y4 high-speed camera or an Infinity Analyze microscope camera equipped with 4x lens.

Video 1: Photo-carving of (*trans*-azo)(pyrazine), performed using a 532 nm 15 mW laser.
Video 2: Photo-carving of (*trans*-azo)(dioxane), performed using a 532 nm 10 mW laser.
Video 3: Detailed photo-carving of (*trans*-azo)(dioxane) co-crystal independent of crystal face, performed using a 532 nm 10 mW laser.
Video 4: Precision photo-carving of (*trans*-azo)(dioxane). A series of ~200 µm steps are carved through the crystal using a 532 nm 10 mW laser.
Video 5: Slow motion video of (*trans*-azo)(dioxane) irradiated with a 140 ms pulse of a 10 mW 532 nm laser.
Video 6: Slow motion photo-carving of (*trans*-azo)(dioxane) crystal, performed using a 532 nm 10 mW laser.
Data File 1: Source file containing the data points with respect to figure 2a (532 nm laser).
Data File 2: Source file containing the data points with respect to figure 2a (785 nm laser).
Data File 3: Source file containing the data points with respect to figure 2b.
Data File 4: Source file containing the data points with respect to figure 2b.

2.7.6 Selected SEM images

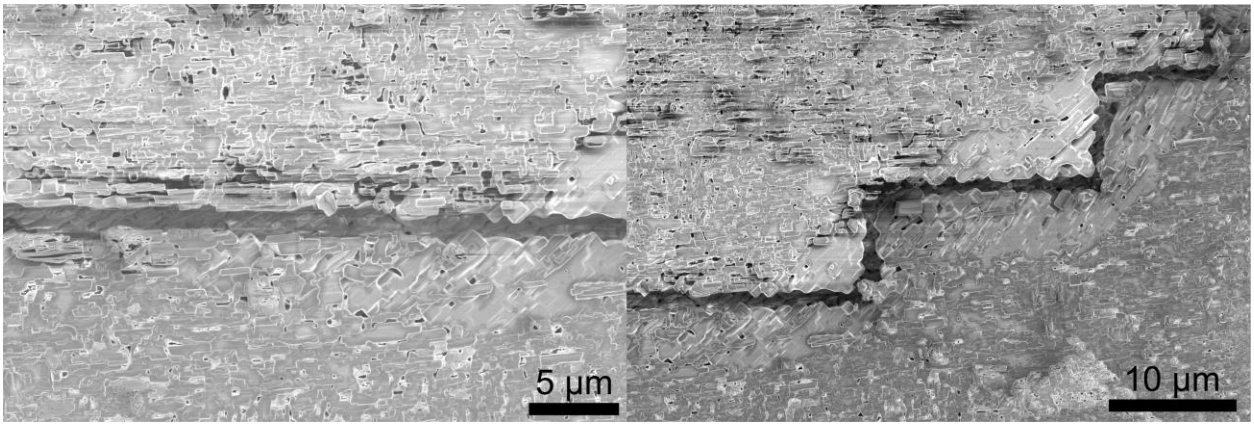

Supplementary Figure 2.42. SEM images of micrometer sized cuts into the surface of a (*trans*-azo)(dioxane) co-crystal produced by a 1 mW 532 nm confocal laser beam.

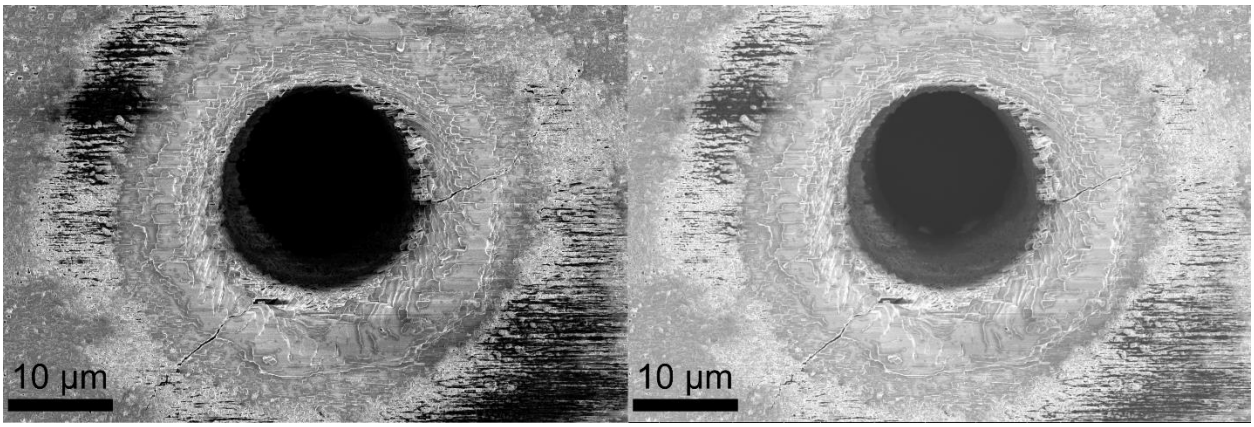

Supplementary Figure 2.43. SEM images of a hole produced by a 532 nm, 5 mW confocal beam in a (*trans*-azo)(dioxane) co-crystal: (left) focused on the surface of the crystal and (right) focused into the hole.

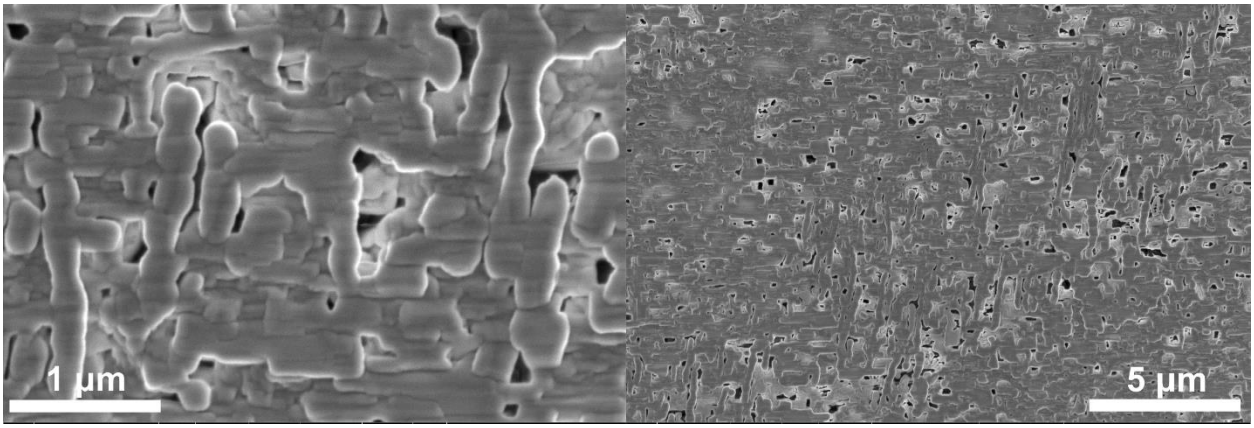

Supplementary Figure 2.44. SEM images of an unmodified surface of (*trans*-azo)(dioxane) crystal.

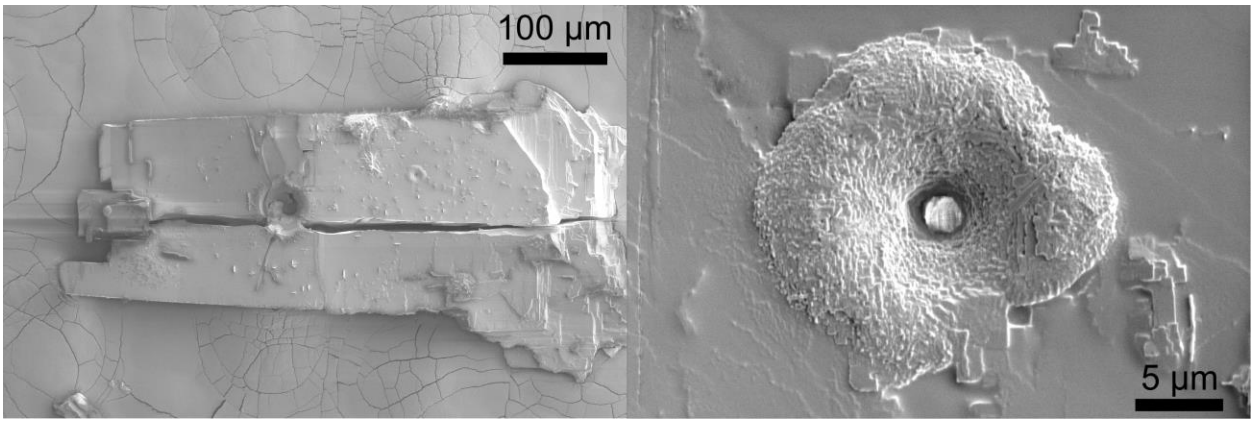

Supplementary Figure 2.45. SEM images of the surface of *trans*-azo **I**, after attempted photo-carving using a 20 mW 532 nm confocal beam (right), leading to cracking and breaking of the crystal, or 5 mW 532 nm confocal beam (left).

2.7.7 Mechanistic investigation

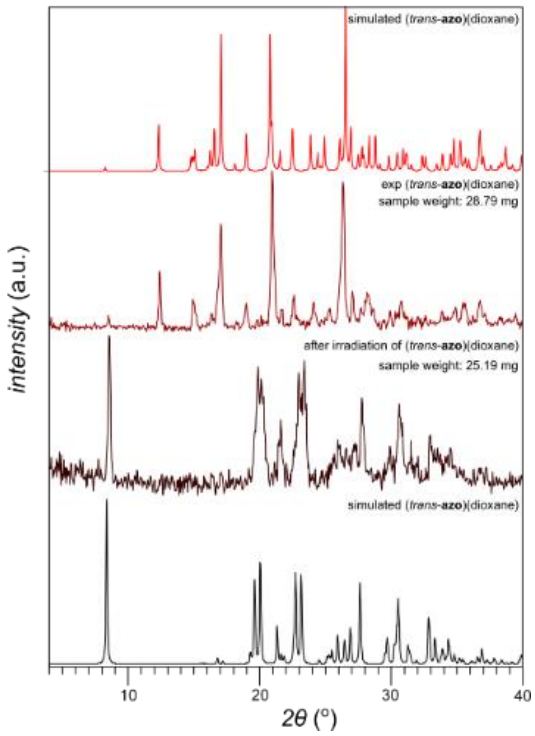

Supplementary Figure 2.46. Gravimetric analysis of sample under irradiation by a 532 nm 37 $mW \cdot cm^{-2}$ LED and their corresponding PXRD. Weight was monitored by Mettler Toledo XS105 DualRange (beginning weight: 28.79 mg, final weight: 25.19 mg, weight loss %: 12.5%)

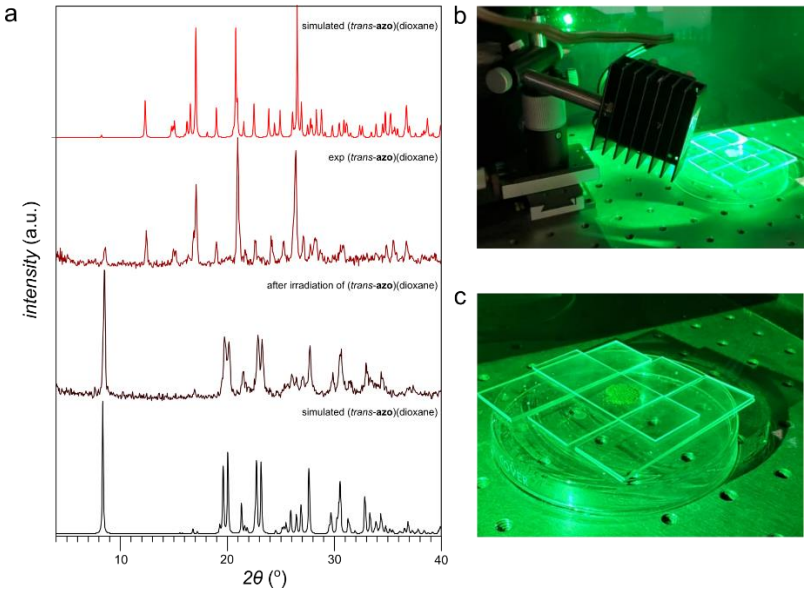

Supplementary Figure 2.47. Sublimation test of (*trans*-azo)(dioxane) and their corresponding PXRDs revealing no visible sublimation of *trans*-azo crystals.

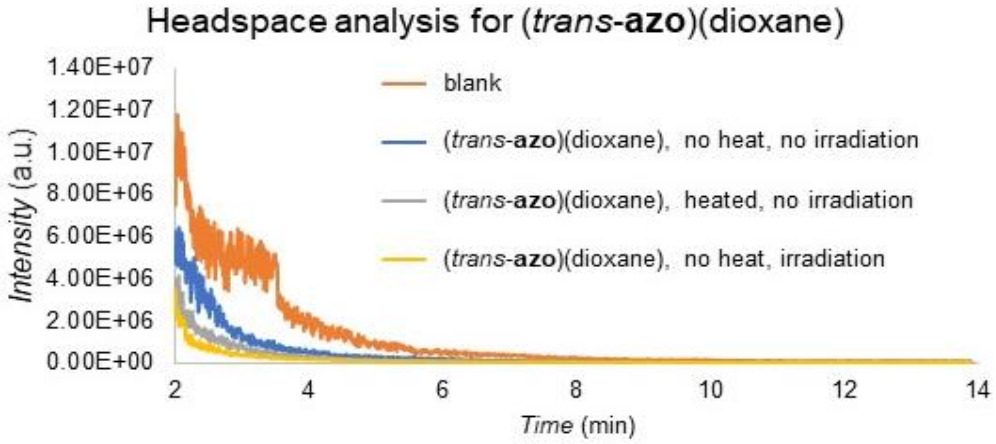

Supplementary Figure 2.48. Results of GC-MS head space analysis for a (*trans*-azo)(dioxane) co-crystal under different conditions, showing no signal associated with mass of either *trans*-azo or dioxane throughout the experiment.

2.7.8 References

1. Bruker, APEX3, Bruker AXS Inc., Madison, Wisconsin, USA, 2012.

2. Krause, L., Herbst-Irmer, R., Sheldrick, G. M. & Stalke, D. Comparison of Silver and Molybdenum Microfocus X-ray Sources for Single-crystal Structure Determination. *J. Appl. Cryst.* **48**, 3–10 (2015).

3. Sheldrick, G. M. SHELXT - Integrated Space-Group and Crystal-Structure Determination. *Acta Cryst.* **A71**, 3–8 (2015).

4. Sheldrick, G. M. Crystal Structure Refinement with SHELXL. *Acta Cryst.* **C71**, 3–8 (2015).

5. Dolomanov, O. V., Bourhis, L. J., Gildea, R. J., Howard, J. A. K. & Puschmann, H. OLEX2: A Complete Structure Solution, Refinement and Analysis Program. *J. Appl. Cryst.* **42**, 339–341 (2009).

6. Farrugia, L. J. WinGX and ORTEP for Windows: an Update. *J. Appl. Cryst.* **45**, 849–854 (2012).

7. C. F. Macrae *et al*. Mercury 4.0: from visualization to analysis, design and prediction. *J. Appl. Cryst.*, **53**, 226–235 (2020).

8. Persistence of Vision Pty. Ltd., Persistence of Vision Raytracer, Persistence of Vision Pty. Ltd., Williamstown, Victoria, Australia, (2018).

Rationale for Chapter 3

In Chapter 3, we sought to further investigate the process of Cold Photo-Carving (CPC), by replacing the stable halogen-bond donating component *trans*-azo (seen in Chapter 2), with its less stable isomer *cis*-azo, while the halogen-bond acceptors remained the same (dioxane, and pyrazine). This was done with a two-fold reasoning, firstly to investigate if CPC is reliant on *trans*-azo, and secondly to see if the potentially more favourable isomerization from *cis* to *trans* would have an impact on the precision of the photo-carving. Additionally *cis*-azo had previously been shown to undergo large photo-mechanical bending associated with *cis* to *trans* isomerization, so therefore we sought to develop a material which might undergo both a photo-mechanical and photo-carving response.

Chapter 3 was reproduced with permission from ChemRxiv pre-print server Cambridge University press.

Citation: Borchers, T. H., Topić F., Arhangelskis, M., Vainauskas, J., Titi, H. M., Bushuyev, O. S., Barrett, C. J., & Friščić., T. Three-in-one: dye-volatile co-crystals exhibiting intensity-dependent photo-chromic, photo-mechanical and photo-carving response. *ChemRxiv*, (2022).

Three-In-One: Dye-Volatile Co-Crystals Exhibiting Intensity-Dependent Photo-Chromic, Photo-Mechanical and Photo-Carving Response

Tristan H. Borchers,[1] Filip Topić,[1] Mihails Arhangelskis,[2] Jogirdas Vainauskas,[1] Hatem M. Titi,[1] Oleksandr S. Bushuyev,[1] Christopher J. Barrett,[1] Tomislav Friščić.[1,3]**

[1]Department of Chemistry, McGill University, Montreal, Canada.
[2]Faculty of Chemistry, University of Warsaw, Warsaw, Poland.
[3]School of Chemistry, University of Birmingham, Birmingham, United Kingdom.

3.1 Abstract

Co-crystallization of a *cis*-azobenzene dye with volatile co-crystal former molecules, such as pyrazine and dioxane, leads to materials that exhibit at least three different light intensity-dependent responses upon irradiation with low-energy visible light. Specifically, the halogen bond-driven assembly of *cis*-(*p*-iodoperfluorophenyl)azobenzene with volatile halogen bond acceptors produces co-crystals whose light-induced behaviour varies significantly depending on the intensity of the light applied. Low-intensity (<1 $mW \cdot cm^{-2}$) light irradiation leads to a colour change due to low levels of *cis*→*trans* isomerization. Irradiation at higher intensities (150 $mW \cdot mm^{-2}$) produces photo-mechanical bending, caused by more extensive azo dye isomerization. At still higher irradiation intensities (2.25 $W \cdot mm^{-2}$) the co-crystals undergo photo-carving, *i.e.* they are readily shaped, punctured, and cut with micrometer precision using laser light. This work demonstrates how the recently reported photo-carving behaviour can be combined with different types of photo-responses, providing a design for multi-responsive materials that can respond to different levels of irradiation with optical colour change, photo-mechanical bending, or photo-carving, as laser power is increased.

3.2 Introduction

Modulating the optical or photo-responsive properties of solid state materials by light, *i.e.* inducing changes in shape,[1] photo-mechanical motion,[2–4] or optical properties,[5] is of great interest for applications including molecular robotics,[6] nano-actuators,[7] and light harvesting.[8] Particular interest has been given to crystalline materials, which can exhibit unique properties when used as organic semiconductors,[9] OLEDs,[10] or waveguides,[11,12] and a variety of transformations have been used to elicit active photo-responsive properties in organic solids such as isomerizations,[13,14] polymerizations,[15,16] and dimerizations.[17–20] Formation of multi-component crystals (co-crystals) is a powerful crystal engineering and supramolecular strategy to tune the solid state physicochemical properties of organic molecules, or even to develop materials with entirely new emergent properties,[21] through molecular self-assembly rather than covalent derivatization.[22] Notable applications of co-crystallization include pharmaceutical materials development,[23,24] the design of mechano-, photo- or thermo-responsive materials,[25,26] organic semiconducting solids,[27] optical materials,[28] and luminescent crystals.[29] The formation of co-crystals has provided a successful route to develop materials that can exhibit complex solid state behaviour, including different types of response to different types of stimuli, as illustrated by Liu *et al*. in which authors showed control of emissive properties of organic co-crystals based on different external stimuli.[30]

The use of azobenzene-based (azo) dye molecules as co-crystal components was shown to produce materials with unique photo-mechanical or enhanced optical behaviour, such as dichroism or pleochroism.[31,32] We have recently shown that co-crystallization of a *trans*-azo dye with a volatile co-crystal former leads to a new class of organic solids: dye:volatile co-crystals which can undergo ‘cold photo-carving’ (CPC), *i.e.* micrometer-precision cutting, shaping, or embossing upon irradiation with low-energy visible light.[33] Cold photo-carving offers a mild, low-energy

approach compared to machining and photolithography, based on light and not heat. While machining and photolithography techniques have previously been used to cut or introduce micrometer engravings into polymers,[34] polymeric resins,[35] co-crystal thin films,[36] photonic crystals,[37] hyperbolic metamaterials,[38] and nanostructures,[39] such processes typically require laser powers on the order of kiloWatts per mm^2 to gigaWatts per mm^2, or the use of other types of high energy beams, as in focused ion beam milling.[40,41] In contrast, cold photo-carving is not based on high-temperature disruption of strong intramolecular covalent bonds, but on gentle, low-temperature and localized cleavage of non-covalent interactions, such as halogen bonds (XB).[42] As a result, CPC can achieve micrometer-precision surface and volume effects, using laser beams with only a small fraction of the intensity compared to those used for traditional laser beam machining (LBM).[33]

We now report that the use of *cis*-(*p*-iodoperfluorophenyl)azobenzene (*cis*-azo) dye (**Figure 3.1a**) as a component of dye:volatile co-crystals provides access to a new class of photo-responsive molecular crystals that can undergo at least three distinct types of photo-induced response upon visible light irradiation. Combining a fluorinated *cis*-azo XB donor with volatile XB acceptors dioxane or pyrazine (**Figure 3.1a**) produces structurally well-defined co-crystals (*cis*-azo)(dioxane) and (*cis*-azo)(pyrazine) which selectively, and depending on the irradiation light intensity, undergo optical colour change, photo-mechanical bending, or photo-carving. Each of these optical responses, which result from using the photo-switchable *cis*-azo unit as a co-crystal component, can be achieved in the same crystal by careful control of laser irradiation parameters, including power and beam diameter.

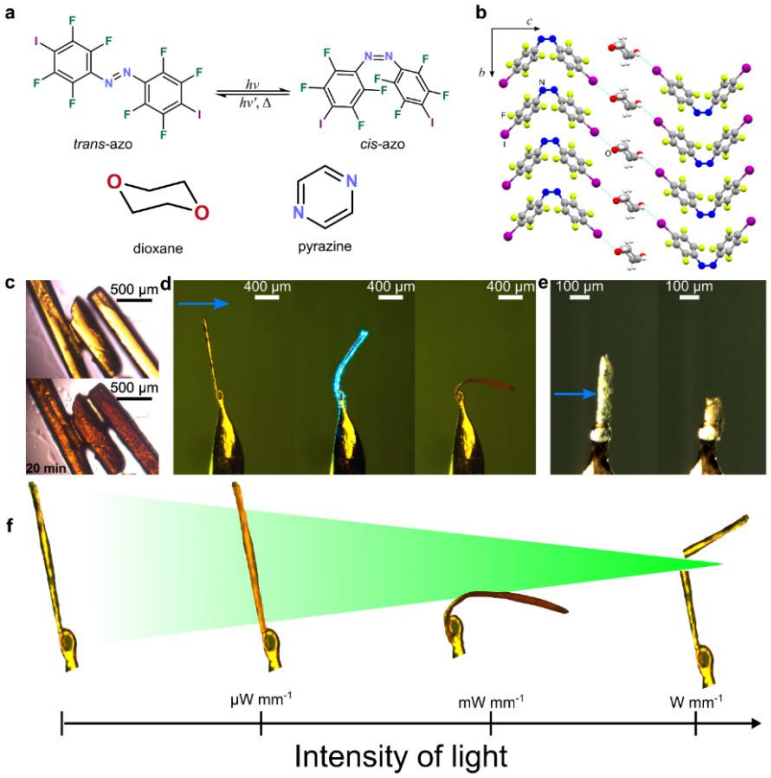

Figure 3.1. Illustration of 3-way responsive *cis*-azobenzene co-crystals a) Schematic representation of azo isomerization, molecular structures of XB donor (*cis*-azo) and acceptors (dioxane and pyrazine) used in this work. **b)** Fragment of the crystal structure of (*cis*-azo)(dioxane) co-crystal, viewed along the [100] crystallographic direction. **c)** Images illustrating the optical colour change occurring when (*cis*-azo)(dioxane) co-crystals are irradiated with a dispersed 532 nm LED. **d)** Images illustrating the observed photo-mechanical bending of the (*cis*-azo)(dioxane) co-crystal upon irradiation by 488 nm light of power density 150 $mW \cdot mm^{-2}$ for different lengths of time. **e)** Images illustrating the photo-carving of a single (cis-azo)(dioxane) co-crystal upon exposure to a laser beam of 532 nm wavelength and light intensity of 2.25 $W \cdot mm^{-2}$). **f)** Schematic illustration of the multi-responsive behaviour of the (*cis*-azo)(dioxane) and (*cis*-azo)(pyrazine) co-crystals upon irradiation with light of different intensities, controlled through modification of the beam diameter. In **c)** and **d)**, the direction of the incident beam is indicated by the blue arrow.

3.3 Results and discussion

3.3.1 Triple photo-response in (*cis*-azo)(dioxane) co-crystals

Yellow needle-shaped single crystals of (*cis*-azo)(dioxane) were obtained by slow evaporation of a solution of *cis*-azo in dioxane (**Figure 3.1d**). Structural analysis by single crystal X-ray diffraction revealed a structure consisting of zigzag chains held together by I···O halogen bonds. The I···O distances were found to be significantly shorter (2.854(2) Å, which corresponds to the RXB parameter,[43] *i.e.* the ratio of the I···O distance to the sum of the van der Waals radii[44] of O and I atoms, of 0.815) than those previously reported for the analogous (*trans*-azo)(dioxane) co-crystal ($d_{I\cdots O}$ = 2.981(3) Å, RXB = 0.852).[33] The irradiation of a (*cis*-azo)(dioxane) crystal was carried out with either blue or green light at 488, 515, or 532 nm. Irradiation at the lowest light intensity was achieved by using a 532 nm light-emitting diode (LED) of output power of 37 mW cm^{-2}, placed 10 cm away from the crystal. Experiments at higher light intensities were performed using an in-house laser system (**Supplementary Figure 3.4**) which included one or two separate laser beams. In a typical experiment, the laser beam was passed through a 50:50 beam splitter, with the transmitted beam passing through a series of optical elements to increase and collimate the size of the beam prior to reaching the sample. The reflected beam, on the other hand, was passed through a different series of optical elements, including a neutral density filter and a convex lens, which reduced the diameter and thus increased the intensity of the beam reaching the sample orthogonal to the transmitted beam. The use of this system enabled simple, shutter-controlled switching between a laser beam of higher light intensity with a lower diameter, and a beam of lower light intensity with a larger diameter. The reflected beam diameter was measured using the 'knife edge' technique, and was determined to be 78 μm while the transmited beam was determined to be 2 mm in diameter (**Supplementary Figures 3.5 and 3.6**).

The single crystals of (*cis*-azo)(dioxane) were found to exhibit three fundamentally different types of photo-response upon irradiation, dependent on the light intensity employed. Notably, using laser beams with wavelengths of 488, 515, or 532 nm revealed that the type of photo-response was not noticeably dependent on the wavelength of incident irradiation, as long as either green or blue light was used, as both excite well within the n-π* absorption band (**Supplementary Figure 3.1**). At low power intensities (below 1 mW cm^{-2}) generated using the LED light source, irradiation resulted only in colour change (**Figure 3.1c**) to the single crystal, which was assignable to isomerization of *cis*- to *trans*-azo taking place uniformly across the near-surface region of the crystal. The extent of isomerization for a single crystal was estimated by ^{19}F nuclear magnetic resonance spectroscopy (NMR) of a solution made by dissolving in $CDCl_3$ a single crystal of (*cis*-azo)(dioxane) that was irradiated for 20 mins using a dispersed 532 nm LED source. After overnight data collection, integration of the NMR spectrum revealed that irradiation of the crystal produced only a small amount of *trans*-azo, with a ratio of *cis* to *trans* isomers of 92:8 (**Supplementary Figure 3.7**), as opposed to a non-irradiated (*cis*-azo)(dioxane) crystal which showed no signal associated to the *trans*-isomer (**Supplementary Figure 3.8**). Increasing the irradiation light intensity to 150 mW mm^{-2}, by switching to a laser light source with a beam diameter of 2 mm, produced not only a change in crystal colour, but also a strong photo-mechanical effect as the single crystals were observed to bend rapidly and significantly (within seconds) in a direction perpendicular to the long needle axis. The initial bending motion was towards the incident beam, followed by significant deflection in the opposite direction. The resulting curve-shaped crystal was orange-red in colour, suggesting that the bending is also related to photo-induced *cis*→*trans* isomerization, specifically the rapid build-up of *trans*-azo on the irradiated crystal surface.[13] The extent of the isomerization of the bent crystal was similarly studied by ^{19}F

NMR, where it was found that the resultant bent crystal exhibited larger amounts of isomerization with the ratio between *cis* and *trans* isomers being 83:17 (**Supplementary Figure 3.8**). The larger amount of isomerization could be a requirement to induce a photo-mechanical response.

Finally, switching to a laser beam of a 78 μm diameter, increasing light intensity to 2.25 W mm^{-2}, resulted in photo-carving that was evident by clean cutting of the crystal. In contrast to irradiation at lower power densities, which led to a change in colour throughout the crystal, in this case the colour change from yellow to red was only observed on the irradiated spot, suggesting that only the directly irradiated part of the crystal undergoes isomerization. Consequently, single crystals of (*cis*-azo)(dioxane) were found to undergo three distinct types of photo-response: photo-chemical colour change, photo-mechanical bending, and photo-carving, each achievable through manipulating the intensity of the incident light. Moreover, eliciting a photo-response at a lower light intensity did not prevent the co-crystal from also exhibiting a different response at a higher light intensity. This was evident by using a beam of 78 μm diameter to irradiate a single crystal that was already bent through irradiation with a beam 2 mm wide: irradiation with the 78 μm diameter beam led to photo-carving, independent of whether or not the crystal was previously irradiated.

3.3.2 Photo-chromic response at low light intensity

The mechanism of the observed transformations was investigated by irradiating a polycrystalline powder of (*cis*-azo)(dioxane) with a 532 nm LED source of 37 mW cm^{-2} light intensity. Structural changes to the material were then monitored through powder X-ray diffraction (PXRD) after different durations of irradiation, revealing the formation of the previously reported *trans*-azo polymorph **II** (**Figure 3.2a**). The PXRD pattern of a sample after 2 h irradiation showed complete disappearance of Bragg reflections of (*cis*-azo)(dioxane), along with the appearance of new

reflections corresponding to the metastable and thermodynamically preferred polymorphs *trans*-azo **II** and *trans*-azo **I**, respectively, along with small amount of solid *cis*-azo (Figure 2a). The PXRD analysis was also performed on a single crystal of (*cis*-azo)(dioxane) that was first cut using the higher light intensity (78 μm beam diameter) 532 nm laser beam, and then placed on a zero-background Si sample holder. The resulting PXRD pattern (**Figure 3.2c,d**) again clearly demonstrated the formation of *trans*-azo **I** and **II** polymorphs, as well as residual (*cis*-azo)(dioxane). Overall, PXRD analyses of the photo-responsive behaviour of (*cis*-azo)(dioxane) in the form of either bulk microcrystalline powder, or a single crystal, all revealed only the formation of *trans*-azo **I** and **II**, with no indication of intermediate phases.

3.3.3 Raman spectroscopy reveals an intermediate co-crystal

Next, the photo-responsive behaviour of a single crystal of (*cis*-azo)(dioxane) was investigated by Raman spectroscopy (**Figure 3.2b, Supplementary Figure 3.9**). Both the isomerization and dioxane loss from the crystal were probed on a confocal Raman microscope using a sequence of two rapid pulses (0.1 s each) of laser light of 532 nm wavelength and 0.1 mW power. After each pulse, the Raman spectrum of the irradiated spot on the crystal was immediately recorded using a red laser at 785 nm, which was previously verified not to elicit a photo-response. After the first 532 nm pulse, the Raman signals associated with the *cis*-azo component disappeared completely, concomitant with the appearance of new Raman bands associated with *trans*-azo. Importantly, the characteristic ν(C-O-C) Raman band for dioxane at 830 cm^{-1} remained, suggesting that irradiation induced a rapid transformation of (*cis*-azo)(dioxane) to the corresponding (*trans*-azo)(dioxane) co-crystal. Raman spectroscopy analysis of the irradiated spot following the second 532 nm laser pulse then revealed the complete disappearance of the ν(C-O-C) Raman band, with the overall spectrum exhibiting only the Raman shifts of pure *trans*-azo. This band disappearance suggests

the complete loss of dioxane, consistent with the results of PXRD analyses. Overall, the Raman spectroscopy analyses on the single crystal indicate that the laser light-induced desolvation of (*cis*-azo)(dioxane) proceeds through a *cis*→*trans* photo-isomerization, giving rise first to a transient appearance of (*trans*-azo)(dioxane), which subsequently converts to pure solid *trans*-azo. Although the short-lived (*trans*-azo)(dioxane) phase was not observed by PXRD, such behaviour is consistent with our previous *in situ* investigation of the irradiation of a *cis*-azo co-crystal with a non-volatile coformer, which revealed a topotactic transformation to a corresponding *trans*-azo co-crystal.[31]

3.3.4 Micrometer-precision photo-carving

Next, we explored whether cutting and engraving of (*cis*-azo)(dioxane) could be achieved with the same micrometer-level precision that was observed for (*trans*-azo)(dioxane). Single crystals of (*cis*-azo)(dioxane) were irradiated with 532 nm laser light using a confocal microscope system which enabled numerically-controlled precision photo-carving of the crystal surface. The changes to the co-crystal surface upon irradiation with the same confocal microscope laser system were characterized by scanning electron microscopy.

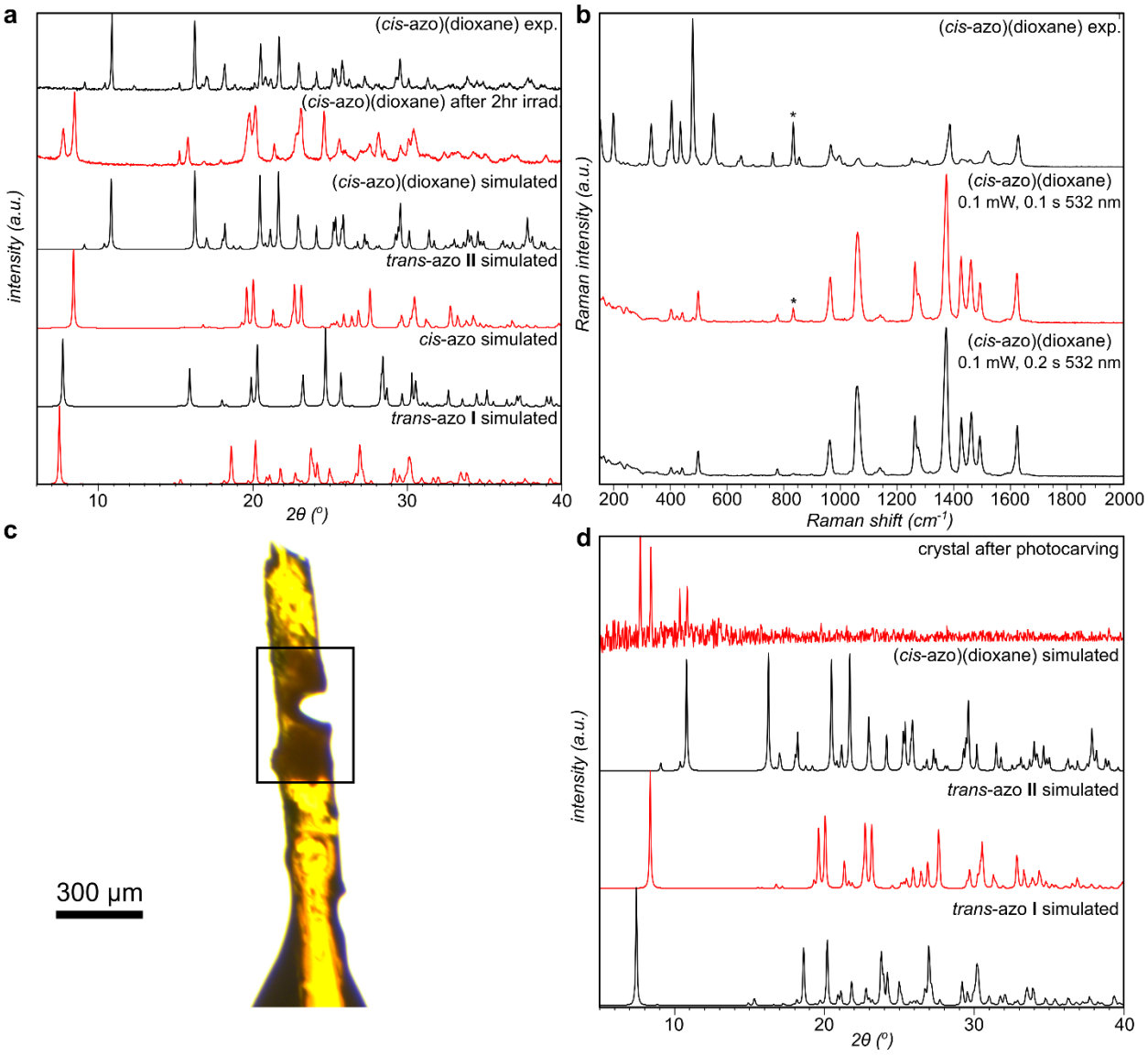

Figure 3.2. Photo-response of (*cis*-azo)(dioxane) co-crystal studied by various methods a) PXRD analysis of bulk (*cis*-azo)(dioxane). **b)** Raman analysis of a single crystal of (*cis*-azo)(dioxane). **c)** Optical image of a single crystal of (*cis*-azo)(dioxane) after a photo-carving experiment using a 2.25 $W \cdot mm^{-2}$ 532 nm laser, the square box indicates the area over which PXRD analysis was performed . **d)** Resultant PXRD pattern of the single crystal in part **c)**, square box indicates the area studied.

microscopy (SEM) (**Figure 3.3, Supplementary Figure 3.10**), with micrometer analysis of the precision cuts and holes. Upon irradiation with laser light of higher power (>5 mW, which corresponds to a light intensity of approximately 5W mm^{-2}), larger holes of approximately 20 μm diameter were carved into the crystal surface, with SEM imaging revealing significant buildup of material, most likely trans-azo **II**, with ridges over 1 μm in height forming around the area of the hole.

The use of a lower power (1 mW) laser beam in the confocal microscope photo-carving experiment was found to decrease the cut diameter to approximately 1 μm, with SEM imaging revealing the appearance of small plate-like crystals aligned perpendicular to the cut and lying parallel to the crystal surface. The appearance and orientation of the crystallites indicate a high mobility of *trans*-azo molecules, and crystalization of *trans*-azo **II**, constrained in the direction of the laser movement. The demonstrated control of the cuts/holes produced by the confocal laser system suggests that despite being based on a process that involves both molecular- (*cis*→*trans*) and supramolecular-level (loss of volatile coformer) transformations, the photo-carving of (*cis*-azo)(dioxane) can achieve a similar level of precision as reported for the analogous *trans*-azo co-crystal.[33]

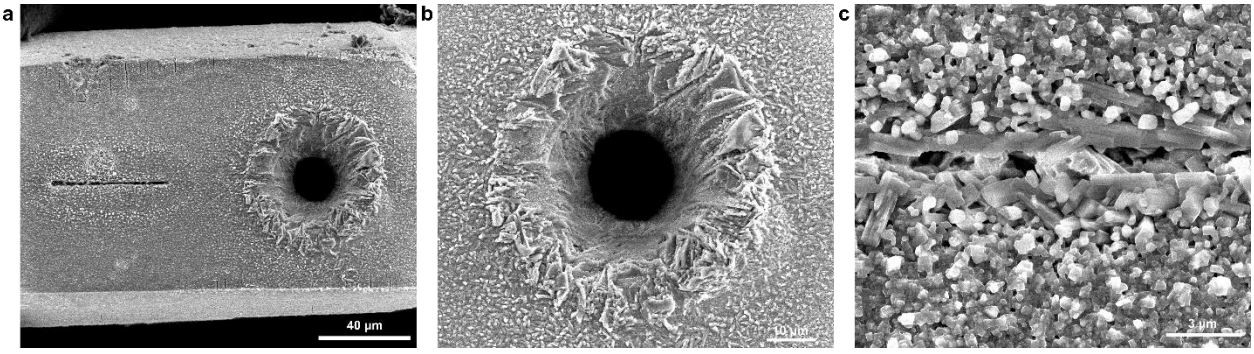

Figure 3.3. Selected SEM images of a hole and a cut created on the surface of a (*cis*-azo)(dioxane) co-crystal by photo-carving using the confocal laser setup. a) SEM image of resulting (*cis*-azo)(dioxane) crystal, showing controled size of CPC using varying laser powers. **b)** A large hole obtained by a 5 mW 5s duration 532 nmirradiation. **c)** A linear cut created by a dragging a 1 mW 532 nm beam across the surface.

3.3.5 High-speed optical monitoring of the photo-carving process

Photo-carving was also studied visually, using a 78 µm beam diameter laser at powers of 5–15 mW and a high-speed camera operating at 1000 frames per second (fps) (**Supplementary Figures 3.11–3.13**). While irradiation at the low power setting of 5 mW did not result in a hole, the higher irradiation powers of 10 and 15 mW both resulted in photo-carving, evident by the formation of a hole in the crystal surface. In both cases a change in colour was observed at the hole edges, consistent with *cis*→*trans* isomerization.

3.3.6 Photo-responsive behaviour of the (*cis*-azo)(pyrazine) co-crystal

Crystals of (*cis*-azo)(pyrazine) were readily obtained by crystallization of a pre-ground equimolar mixture of *trans*-azo and pyrazine. The sample was then dissolved in hexanes with dropwise addition of DCM to fully solubilize the sample. The resultant solution was irradiated by a 532 nm LED, and left to crystalize by slow evaporation. In contrast to needle-shaped crystals of (*cis*-

azo)(dioxane), the crystals of (*cis*-azo)(pyrazine) adopted the form of large (typical dimensions of 1000 × 250 × 50 μm) plates (**Figures 3.4c,d**). Single crystal X-ray diffraction analysis revealed a structure analogous to that of (*cis*-azo)(dioxane), with zigzag chains of alternating molecules of pyrazine and *cis*-azo molecules connected through I···N halogen bonds. The I···N halogen-bonding distances were found to be longer ($d_{I\cdots N}$RB = 2.896(5) Å, RXB = 0.820) than those in the previously reported (*trans*-azo)(pyrazine) co-crystal ($d_{I\cdots N}$ = 2.840(3) Å, RXB = 0.805).[33]

The (*cis*-azo)(pyrazine) co-crystal also exhibited three distinct types of responses upon irradiation with green or blue light of different light intensities. Irradiation with low light intensity 532 LED light led to a change in colour from bright yellow to dark orange (Figure 4c), which was accompanied by minor cracking seen on the crystal, indicating strain caused by *cis*-*trans* isomerization. After dissolving the irradiated co-crystal in $CDCl_3$ solvent ^{19}F NMR analysis revealed that *cis*- to *trans*-azo conversion took place to an extent of ca. 8% (Supplementary Figure 14). Notably, such conversion was achieved after 2 hours of irradiation, indicating greater photo-stability of (*cis*-azo)(pyrazine) compared to (*cis*-azo)(dioxane) which showed conversion after only 20 minutes of irradiation.

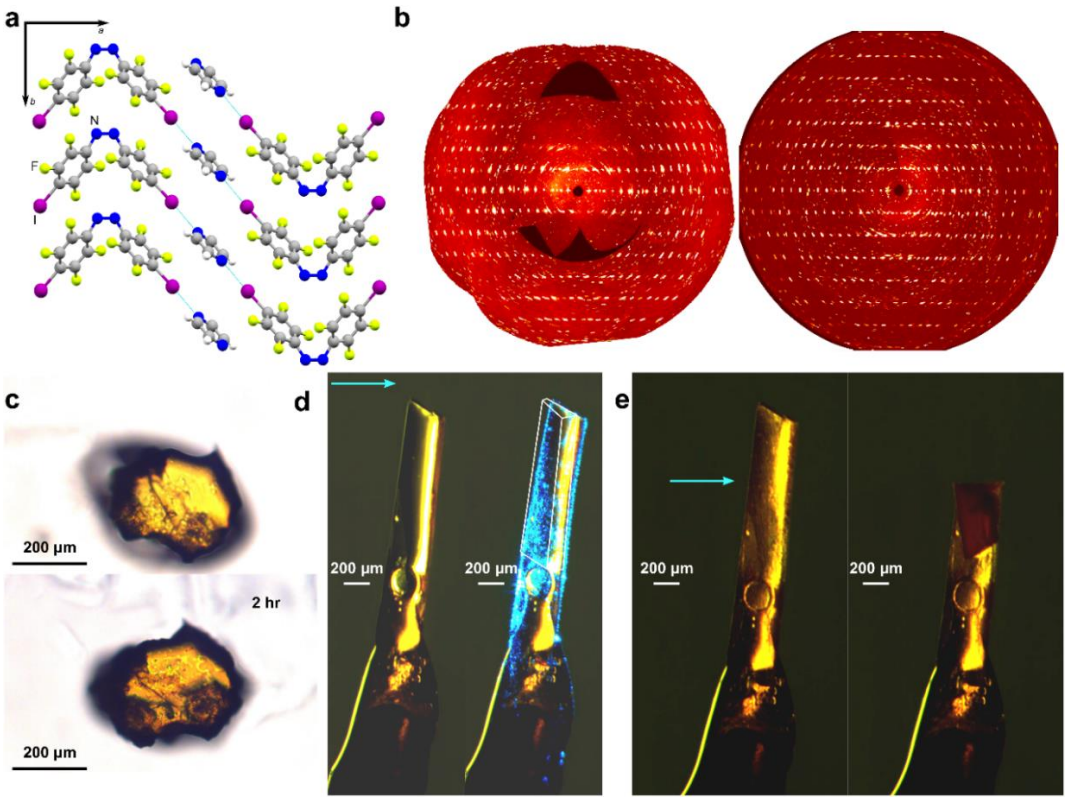

Figure 3.4. An overview of the photo-responsive behaviour of the (*cis*-azo)(pyrazine) co-crystal. **a)** Fragment of the crystal structure of the (*cis*-azo)(pyrazine) co-crystal, viewed along the crystallographic [001] direction; **b)** composite diffraction images for the crystallographic *h*0*l* plane for a (*cis*-azo)(pyrazine) single crystal before (left) and after (right) photo-carving using a 532 nm 2.25 W·mm^{-2} laser, the crystal was cut in half and the resultant bottom half was recovered and re-run. **c)** Optical images of (*cis*-azo)(pyrazine) irradiated by a dispersed 532 nm LED. **d)** Photographic images of a (*cis*-azo)(pyrazine) co-crystal that was irradiated with a 488 nm laser 150 mW·mm^{-2}, demonstrating photo-mechanical behaviour with the first panel being the crystal prior to irradiation, the 2nd after a minute of irradiation. The blue arrow represents the direction of the laser beam, and the white outline represents the location of the original crystal prior to irradiation. **e)** Photographic images of a (*cis*-azo)(pyrazine) crystal before (left) and after (right) being irradiated with a 2.25 W·mm^{-2} 532 nm laser.

The (*cis*-azo)(pyrazine) crystals also exhibited a photo-mechanical response, albeit less pronounced than for (*cis*-azo)(dioxane) (**Figure 3.4C**). Upon irradiation by dispersed laser light of 488 nm wavelength and intensity of 150 $mW \cdot mm^{-2}$, a crystal of (*cis*-azo)(pyrazine) was observed to bend away from the source of irradiation over a course of a minute, with the irradiated section changing colour from yellow to red, consistent with *cis* → *trans* isomerization in the solid. Similar results were obtained when using 532 nm radiation of the same light intensity.

Photo-induced carving was demonstrated by either green/blue light, and can be demonstrated on both fresh or prevoiusly irradiated crystals. Using a sample of (*cis*-azo)(pyrazine) the sample was exposed to 532 nm laser radiation, showing the ability to readily carve through the crystal with ease using the smaller diameter higher light intensity beam (2.25 $W \cdot mm^{-2}$, **Figure 3.4d**). In contrast to its dioxane counterpart, crystals of (*cis*-azo)(pyrazine) were found to retain crystallinity after cutting with a 532 nm laser beam, which was evident from full X-ray diffraction data that was collected from a parent (*cis*-azo)(pyrazine) single crystal before irradiation, and on the daughter crystal resulting from cutting (**Figure 3.4b, supplementary Figure 3.15–3.16**). The freshly laser-cut crystal exhibited only X-ray diffraction signals of (*cis*-azo)(pyrazine), with the only indication of *cis*→*trans* isomerization being a slight change in the colour of the cut crystal surface from yellow to red.

Changes to (*cis*-azo)(pyrazine) upon irradiation were also followed by PXRD (Supplementary Figure S16), by irradiating a bulk crystalline powder of the co-crystal with dispersed green (532 nm wavelength) LED light of light intensity 37 $mW \cdot cm^{-2}$. Visual inspection of the PXRD patterns of the material before and after irradiation indicated the complete transformation of (*cis*-azo)(pyrazine) to a physical mixture of *trans*-azo **I** and *trans*-azo **II** solids over a period of 20 hours, demonstrating improved photo-stability compared to (*cis*-

azo)(dioxane). Similiarly to (*cis*-azo)(dioxane), analysis of the PXRD patterns did not reveal any sign of (*trans*-azo)(pyrazine) or solid *cis*-azo, suggesting that *cis* → *trans* isomerization and loss of co-former upon irradiation of the (*cis*-azo)(pyrazine) co-crystal are either simultaneous or occur through intermediates that are too minute to be observed *via* PXRD. Attempts to follow the irradiation of (*cis*-azo)(pyrazine) by single crystal Raman spectroscopy were not successful due to co-crystals exhibiting significant fluoresence upon irradiation with the 785 nm laser probe.

Analysis by SEM revealed similar precision cuts compared to the analogous dioxane co-crystal (**Supplementary Figure 3.17**). Using a higher power green laser (>15 mW) irradiating a single point for 5s, the resultant crystal exhibited the presence of hole at the spot of irradiation, with significant material buildup around the hole. Reducing the power of the laser line (~3 mW) and automating a linear cutting process revealed plate-like crystallites forming on the edge of the cut similar to the analogous dioxane co-crystal suggesting the same crystallization of *trans*-azo **II** near the edges of the cut, due to material displacement from the irradiated area.

3.3.7 Theoretical modelling

The stability of *cis*-azo co-crystals was also evaluated and compared to that of the corresponding previously reported *trans*-azo systems through calculations based on periodic density-functional theory (DFT) with semi-empirical dispersion correction (SEDC). Specifically, periodic DFT was used to calculate the energy difference ($\Delta E_{\text{isomerization}}$, **Table 3.1**) between (*cis*-azo)(dioxane) or (*cis*-azo)(pyrazine) and their *trans*-azo analogs,[31] as well as the energy of co-crystal decomposition (ΔE_{decomp}, **Table 3.2**) into the crystalline solid azo and the gaseous coformer. The ΔE_{decomp} values were calculated for two possible outcomes of co-crystal decomposition, specifically the formation of the azo component as either the solid *cis*-azo or the *trans*-azo polymorph **II**. Finally, the strength

of halogen bonding in each co-crystal was evaluated by calculating the interaction strength for a pair of azo and coformer molecules (**Table 3.2**).

Calculations indicated that the isomerization of the *cis*- to the respective *trans*-azo co-crystal should be enthalpically favourable in all cases, with $\Delta E_{\text{isomerization}}$ values of -34.25 and -43.68 kJ·mol^{-1} for the (*cis*-azo)(dioxane) and (*cis*-azo)(pyrazine) co-crystal, respectively. These energy differences are also in good agreement with those calculated for individual crystalline azo-compounds, *e.g.* isomerization of *cis*-azo to either *trans*-azo **I** (-37.67 kJ mol^{-1}) or *trans*-azo **II** (-36.97 kJ mol^{-1}), and with previously reported gas-phase calculations[13] (-36.99 kJ·mol^{-1}). The significant stabilization calculated for the process of *cis*→*trans* isomerization is in agreement with the observations based on Raman spectroscopy which indicated that the isomerization takes place prior to evaporation of the coformers. The calculated values indicate that the *cis*→*trans* isomerization in the (*cis*-azo)(pyrazine) co-crystal is ca 10 kJ mol^{-1} more favourable compared to (*cis*-azo)(dioxane).

Table 3.1. Calculated energy of *cis*→*trans* isomerization for the co-crystals and azo component.

Co-crystal isomerization process	$\Delta E_{\text{isomerization}}$ **/kJ mol^{-1}**
(*cis*-azo)(dioxane) → (*trans*-azo)(dioxane)	-34.25
(*cis*-azo)(pyrazine) → (*trans*-azo)(pyrazine)	-43.68
cis-azo → *trans*-azo **I**	-37.67
cis-azo → *trans*-azo **II**	-36.97
cis-azo → *trans*-azo (g)[13]	-36.99

Table 3.2. Calculated energies (in kJ mol^{-1}) associated with the loss of volatile coformer from the crystal structures of (*cis*-azo)(dioxane), (*cis*-azo)(pyrazine), (*trans*-azo)(dioxane) and (*trans*-azo)(pyrazine) co-crystals, and energy of halogen bond (XB) interactions, obtained through periodic DFT analysis.

Model	**ΔE_{decomp}(*cis*) /kJ mol^{-1}**	**ΔE_{decomp}(*trans* II) /kJ mol^{-1}**	**XB interaction energy /kJ mol^{-1}**
(*cis*-azo)(dioxane)	86.86	49.74	-18.55
(*cis*-azo)(pyrazine)	100.18	63.07	-28.11
(*trans*-azo)(dioxane)	N/A	84.13	-19.05
(*trans*-azo)(pyrazine)	N/A	106.86	-27.15

Decomposition energies for the co-crystals were calculated considering two potential decomposition pathways: the *cis*-azo co-crystals converting into either a mixture of crystalline *cis*-azo and the gaseous coformer, or into a mixture of crystalline *trans*-azo **II** and gaseous coformer. The calculated values suggest that both decompostion pathways should be enthalpically unfavourable, which is consistent with the required input of energy in the form of light or heat. Independent of the decomposition pathway, calculations indicate that the pyrazine-based co-crystals should be more stable against decomposition than their dioxane counterparts, which is in agreement with the results of irradiation experiments. The calculated halogen-bonding energies additionally highlight the stability of the pyrazine co-crystals compared to their dioxane

counterparts, and suggest that the increase in halogen-bonding strength upon switching from an oxygen-based to a nitrogen-based acceptor contributes to the overall stability of the co-crystal.

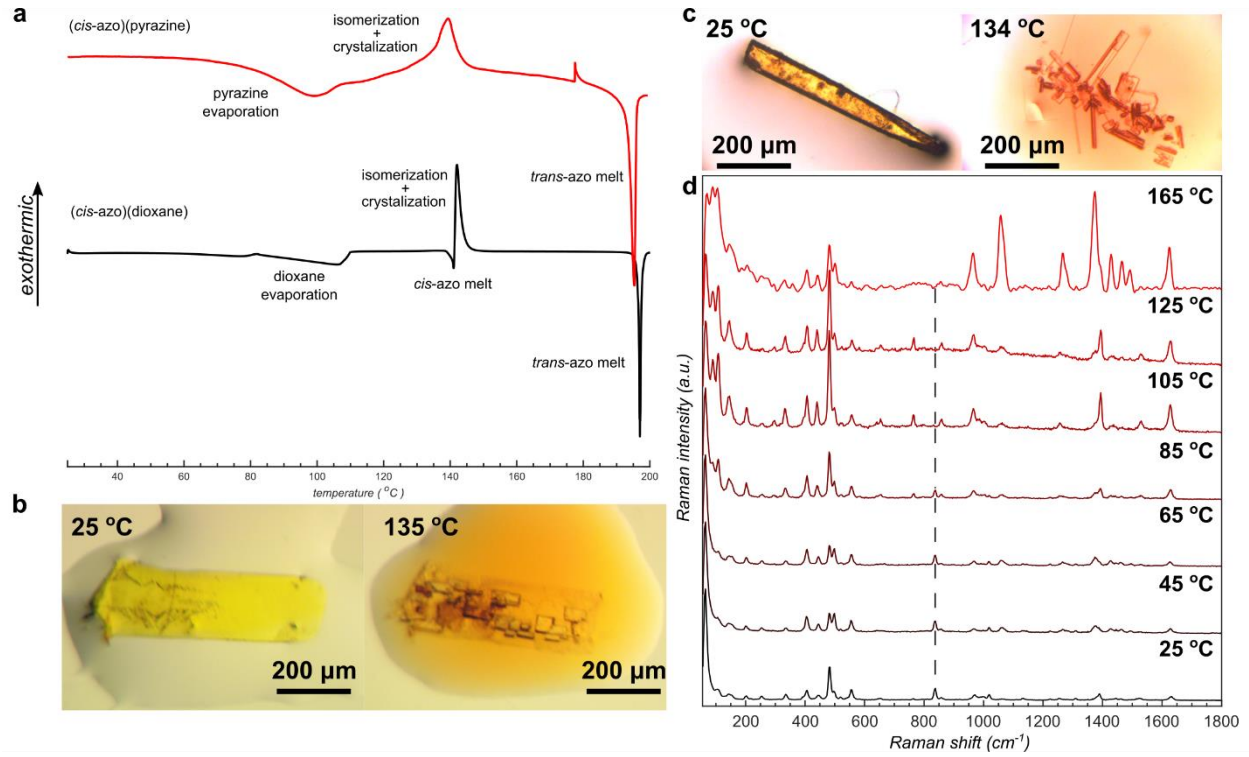

Figure 3.5. Thermal studies of the *cis*-azo co-crystals. a) Overlay of DSC thermograms for the (*cis*-azo)(pyrazine) (red) and (*cis*-azo)(dioxane) (black) co-crystals. **b)** Hot-stage optical microscopy images of a (*cis*-azo)(pyrazine) crystal in paraffin oil, before and after recrystalization into *trans*-azo. **c)** Hot-stage optical microscopy images of a (*cis*-azo)(dioxane) in paraffin oil, before and after recrystalization into *trans*-azo. **d)** Overlay of Raman spectra collected from a single crystal of (*cis*-azo)(dioxane) at different temperatures demonstrating the desolvation of the dioxane prior to isomerization into *trans*-azo, the dashed line representing the location of the Raman band for the ring-breathing vibration of dioxane.

3.3.8 Thermal analysis

The observed mechanism of light-driven isomerization and loss of coformer from (*cis*-azo)(dioxane) is different from the analogous heat-driven process, as evidenced by differential scanning calorimetry (DSC) and thermogravimetric analysis (TGA) on a bulk sample of (*cis*-azo)(dioxane). The DSC thermogram for (*cis*-azo)(dioxane) heated at a rate of 5 °C min^{-1} shows an endothermic process in the 80 – 110 °C range, attributed to dioxane loss. This assignment was supported by TGA, which revealed a 14.2% loss of weight in the same thermal range, consistent with the theoretically calculated content of dioxane (13.2%) in (*cis*-azo)(dioxane) (**Supplementary Figure 3.19**). Further heating leads to another endothermic event at 141 °C, immediately followed by an exothermic process, which have been interpreted as the melting of *cis*-azo followed by thermally-induced isomerization and crystallization into solid *trans*-azo.[31] Upon further heating, the DSC thermogram exhibits a sharp endothermic process at 197 °C, consistent with the melting of *trans*-azo. The interpretation of DSC data was verified by hot-stage optical microscopy (**Figure 3.5c, Supplementary Figure 3.23**). Heating of a yellow (*cis*-azo)(dioxane) crystal did not produce visible changes in shape or colour until 104 °C, when the crystal begins to darken and crack, which was interpreted as due to the loss of dioxane coformer. Indeed, if the heating is conducted with a (*cis*-azo)(dioxane) co-crystal submerged in oil, the darkening of the crystal is associated with the appearance of bubbles on the crystal surface, consistent with removal of gaseous dioxane. Further heating leads to liquefaction at ca. 121 °C, followed by recrystallization at ca. 139 °C to form crystallites of *trans*-azo that subsequently melt at the expected melting point temperature of 185 °C. Thermal decomposition of (*cis*-azo)(dioxane) was also studied *in situ* through variable-temperature Raman spectroscopy (**Figure 3.5d**) on a single crystal of (*cis*-azo)(dioxane). While the initial Raman spectrum (25 °C) revealed only bands

of *cis*-azo and dioxane (ν(C-O-C) at 830 cm^{-1}), increasing the temperature to 105 °C led to the appearance of new low-frequency bands (<150 cm^{-1}), indicating changes in intermolecular vibrations, and the disappearance of the dioxane Raman band at 830 cm^{-1}. Further heating to 165 °C leads also to the appearance of new Raman bands which were consistent with *trans*-azo. These observations are consistent with thermal decomposition of (*cis*-azo)(dioxane) proceeding first through the loss of dioxane, followed by *cis*→*trans* isomerization.

Overall, the sequence of heat-induced events that transform (*cis*-azo)(dioxane) into *trans*-azo is clearly different from the analogous light-driven process. The DSC, TGA and hot-stage microscopy show that the first step in the heat-driven process is desolvation of the co-crystal to form solid *cis*-azo which subsequently melts and then undergoes isomerization and crystallization to form solid *trans*-azo. In contrast, irradiation of (*cis*-azo)(dioxane) proceeds through a qualitatively distinct process of *cis*→*trans* isomerization to first yield solid (*trans*-azo)(dioxane) which subsequently loses dioxane to form solid *trans*-azo.

DSC analysis of bulk (*cis*-azo)(pyrazine) (**Figure 3.5a**) revealed two distinct endothermic events, the first between 80 – 120 °C, which was identified as loss of pyrazine coformer (confirmed by TGA, which revealed a mass loss of ca. 12.5%, **Supplementary Figure 3.20**), and the second at 196 °C, which was assigned to the melting of *trans*-azo. An exothermic process was also observed between ca. 129 – 148 °C, which was identified as a combination of recrystallization and *cis*→*trans* isomerization. The interpretation of DSC measurements was again validated by variable temperature optical microscopy on a single crystal of (*cis*-azo)(pyrazine), conducted either with a neat crystal (Supplementary Figure 23) or a crystal submerged in oil (**Figure 3.5b**). The two experiments yielded very similar results, with the crystal retaining the overall appearance until ca. 90 °C, followed by darkening and appearance of bubbles (in case of the crystal submerged in oil)

at higher temperatures. These observations are consistent with *cis*→*trans* isomerization and thermal loss of pyrazine. After ca. 140 °C the sample consists of solid *trans*-azo, which was identified by PXRD, and subsequently either melts or dissolves in oil around 200 °C.

3.4 Conclusions

We presented new materials which exhibit multiple different optical, mechanical, and structural responses to visible green or blue light. Using a high-intensity light beam, the herein presented halogen-bonded co-crystals can be readily carved, machined or engraved. Upon reducing light intensity, however, the photo-response can be switched from photo-carving to photo-mechanical bending. Further reduction in the light intensity enables the photo-response to be further modified, leading only to a change in crystal colour. These various responses in a single material are enabled by the general co-crystal design which pairs a *cis*-azo chromophore halogen-bonded to a volatile co-crystal former (dioxane, pyrazine). The light-induced colour change and photo-mechanical bending occur due to different extents of the dye *cis*→*trans* isomerization taking place at different irradiation intensities, while the photo-carving effect is due the combination of the volatility of the co-crystal former and the photochromic nature of the azobenzene. Mechanistic studies by *in situ* Raman spectroscopy on a single crystal show that light-driven desolvation of the (*cis*-azo)(dioxane) co-crystal occurs through an intermediate of (*trans*-azo)(dioxane), *i.e*. that light absorption leads first to isomerization, followed by loss of volatile co-crystal component. By conducting analogous thermal analysis and hot-stage microscopy experiments, this mechanism is shown to be different from the analogous heat-induced process, in which co-crystal decomposition is observed prior to the isomerization of the azo component. Overall, this work demonstrates the ability to design multi-response organic crystals, by combining light-responsive behaviour at the molecular (*cis*→*trans*) and supramolecular (light-induced loss of volatile coformer) level. We

believe that this simple design for dye-volatile co-crystals provides an exciting new opportunity to rationally design materials that not only respond to an external stimulus, but can also adapt their response to finer properties of the stimulus.

3.5 Materials and methods

3.5.1 Synthesis

Trans-azo was synthesized in one step by treatment of 4-iodo-2,3,5,6-tetrafluoroaniline with *N*-chlorosuccinimide (NCS) and 1,8-diazabicyclo[5.4.0]undec-7-ene (DBU).[45] All reagents and solvents were purchased from Sigma Aldrich. For co-crystallization of (*trans*-azo)(dioxane) approx. 6 mg of *trans*-azo (0.010 mmol) was dissolved in a minimal volume of (1,4-)dioxane (ca. 2 mL). The solution was then irradiated for 30 mins *via* a 532 nm 37 $mW \cdot cm^{-2}$ LED and left to evaporate at room temperature, yielding long, yellow, needle-shaped crystals. For co-crystallization of (*cis*-azo)(pyrazine), approx. 6 mg of *trans*-azo (0.010 mmol) and 6 mg of pyrazine (0.075 mmol) were mixed in hexanes (ca. 5 mL) with methylene chloride added dropwise until all material fully dissolved. The solution was then irradiated with a 532 nm 37 $mW \cdot cm^{-2}$ LED. The solution was left to evaporate at room temperature, yielding lath-shaped yellow crystals.

3.5.2 Powder X-ray diffraction

Powder X-ray diffraction experiments were performed on a Bruker D8 Advance diffractometer, using Cu*K*α radiation (λ = 1.54184 Å) source operating at 40 mA and 40 kV, equipped with a Lynxeye XE linear position-sensitive detector, in the 2θ range of 4–40° with step size of 0.019° or, alternatively, on a Bruker D2 Phaser diffractometer using nickel-filtered Cu*K*α radiation (λ = 1.54184 Å) source operating at 10 mA and 30 kV, equipped with a Lynxeye linear position-sensitive detector, in the 2θ-range of 4–40°.

3.5.3 Single-crystal X-ray diffraction

Data for (*cis*-azo)(dioxane), and (*cis*-azo)(pyrazine), were collected on a Bruker D8 Venture dual-source diffractometer equipped with a PHOTON II detector and an Oxford Cryostream 800 cooling system, using mirror-monochromated Mo*K*α ($\lambda = 0.71073$ Å) or Cu*K*α radiation ($\lambda = 1.54184$ Å) from respective microfocus sources. Data were collected in a series of φ- and ω-scans. APEX3 software was used for data collection, integration, and reduction.[46] Numerical absorption corrections were applied using SADABS-2016/2.[47] Structures were solved by dual-space iterative methods using SHELXT,[48] and refined by full-matrix least-squares on F^2 using all data with SHELXL,[49] within the OLEX2,[50] and/or WinGX[51] environments.

3.5.4 UV-Vis absorbance spectroscopy

Absorbance measurements were collected on an Agilent Cary 300 Bio UV-Visible spectrometer. A 55 mg/L solution of *trans*-azo was prepared in THF, and the absorbance spectrum was acquired using instrument default conditions. The spectrum of the corresponding *cis*-**azo** isomer was collected following 30 min of irradiation by a 532 nm LED (37 mW).

3.5.5 Raman spectroscopy

Raman microscopy experiments were performed on a confocal Raman Witec 300 R microscope setup using two separate probe wavelengths of 785 and 532 nm. Integration time, number of accumulations and laser power were varied depending on experiment. Simulated Raman shifts were calculated by DFT using Gaussian16,[52] employing the B3LYP density functional.[53,54] Basis sets 6-311G(d,p) were used for all atoms.[55] The basis set for iodine[56] was obtained from the *Basis Set Exchange*.[57]

3.5.6 Thermal analysis

Thermogravimetric analysis (TGA) and differential scanning calorimetry (DSC) measurements were performed simultaneously using a Mettler-Toledo TGA/DSC 1 Star system thermobalance. The samples were placed in alumina crucibles and measurements conducted under a stream of nitrogen (50 cm^3 min^{-1}) gas, at a heating rate of 5 C° min^{-1}. Data collection and analysis were performed using the Mettler-Toledo STAR^e Software 16.20 program package. Alternatively, DSC measurements were performed on a TA Instruments LTD DSC2500 at a heating rate of 5 C° min^{-1}, under a stream of nitrogen (50 cm^3 min^{-1}) gas, using a hermetically closed aluminum pan. Hot-stage microscopy was performed using a Mettler Toledo FP90 Central Processor, equipped with a Mettler FP84 HT TA Microscopy Cell. Images were obtained on an Infinity 1 Lumenera camera attached to a Leica DM2500 optical microscope, using the Studio Capture software suite. Heating was performed from 20 to 200 °C at a rate of 20 C° min^{-1}.

3.5.7 Scanning electron microscopy

Single crystals of (*cis*-azo)(dioxane) and (*cis*-azo)(pyrazine) were sputter-coated with Pt, and placed into an FEI Helios Nanolab 660 DualBeam (Focused Ion Beam-Extreme High-Resolution Scanning Electron Microscope) for imaging.

3.5.8 Detailed machining procedure

A confocal Raman Witec 300 R 532 nm solid state laser was used with a range of power settings (0.1–20 mW), and multiple objectives (10, 20, 50, and 100× Zeiss objectives with NA = 0.25, 0.5, 0.8, and 0.9, respectively). A series of detailed drawings were copied and then engraved into the crystals using a pre-made input files with listed coordinates.

3.5.9 Laboratory laser system including a high-speed camera

A Redlake MotionPro Y4 (Tallahassee, FL, USA) high-speed charge-coupled device camera was used to capture machining events at 1000 frames/s. A MGL-III-532 Green DPSS Laser and Lasos lasertechnik 633nm Helium-Neon laser was coupled with a tunable neutral density filter, a Melles Griot electronic controlled shutter, and a Melles Griot convex lens with a focal length of 75 mm, aligned onto a crystal mount with a 150 μm loop (**Supplementary Figure 3.6**).

3.5.10 Periodic DFT calculations

Periodic DFT calculations were performed using the plane-wave DFT code CASTEP 20.[58] The input files were prepared from the CIFs of the experimentally-determined crystal structures using the program cif2cell.[59] Crystal structures of all materials were geometry-optimized with respect to atom positions and unit cell parameters, subject to the space group symmetry constraints. The calculations were performed with PBE[60] functionals combined with a Grimme D3 semiempirical dispersion correction scheme.[61] The plane-wave basis set was truncated at 750 eV cutoff and the 1st electronic Brillouin zone was sampled with the $2\pi \times 0.07$ Å^{-1} Monkhorst-Pack grid k-point spacing.[62] Tight convergence criteria were used in the optimization, namely: 5×10^{-6} eV atom^{-1} for total energy; 0.01 eV Å^{-1} for atomic forces; 5×10^{-4} Å for atomic displacement and 0.02 GPa for residual stress.

Calculations for the gas-phase molecules were performed by placing one molecule in a cubic simulation cell of 20 Å dimension and performing a fixed cell geometry optimization. In that case a single Γ k-point was used for electronic Brillouin zone sampling, all other settings were kept the same as for the optimization of the crystal structures. For dimer interaction energies, two molecules were placed in the same 30 × 30 × 30 Å simulation box, with their geometries extracted

from the optimized crystal structures. In that case only single-point calculations were performed, rather than geometry optimizations, since the aim was to calculate interaction energies for the in-crystal intermolecular orientation. The dimer interaction energies were computed by subtracting the total energies of individual molecules from the total energy of the dimer. The energies of individual crystal structures and gas-phase molecules were used to compute decomposition energies.

3.6 References

1. Shields, D. J., Karothu, D.-P., Sambath K., Ranaweera, R. A. A. U., Schramm, S., Duncan, A., Duncan, B., Krause, J. A., Gudmundsdottir, A. D. & Naumov, P. Cracking under Internal Pressure: Photodynamic Behavior of Vinyl Azide Crystals through N2 Release. *J. Am. Chem. Soc.* **142**, 18565–18575 (2020).

2. Taniguchi, T., Kubota, A., Moritoki, T., Asahi, T. & Koshima, H. Two-step photomechanical motion of a dibenzobarrelene crystal. *RSC. Adv.* **8**, 34314–34320 (2018).

3. Bartholomew, A. K., Stone, I. B., Stiegerwald, M. L., Lambert, T. H., Roy, X. Highly twisted azobenzene ligand causes crystals to continuously roll in sunlight. *J. Am. Chem. Soc.* **144**, 37, 16773-16777 (2022).

4. Yue, Y., Shu, Y., Ye, K., Sun, J., Liu, C., Dai, S., Jin, L., Ding, C., Lu, R. Molecular twisting affects the solid-state photochemical reactions of unsaturated ketones and the photomechnical effects of molecular crystals. *Chem. Eur. J.* e202203178, (2022)

5. Kitagawa, D., Kawasaki, K., Tanaka, R. & Kobatake, S. Mechanical Behavior of Molecular Crystals Induced by Combination of Photochromic Reaction and Reversible Single-Crystal-to-Single-Crystal Phase Transition. *Chem. Mat.* **29**, 7524–7532 (2017).

6. Xu, T., Gao, W., Xu, L.-P., Zhang, X. & Wang, S. Fuel-Free Synthetic Micro-/Nanomachines. *Adv. Mater.* **29**, 1603250 (2017).

7. Xu, L., Mou, F., Gong, H., Luo, M. & Guan, J. Light-driven micro/nanomotors: from fundamentals to applications. *Chem. Soc. Rev.* **46**, 6905–6926 (2017).

8. So, M. C., Wiederrecht, G. P., Mondloch, J. E., Hupp, J. T. & Farha, O. K. Metal–organic framework materials for light-harvesting and energy transfer. *Chem. Commun.* **51**, 3501–3510 (2015).

9. Black, H. T. & Perepichka, D. F. Crystal Engineering of Dual Channel p/n Organic Semiconductors by Complementary Hydrogen Bonding. *Angew. Chem. Int. Ed.* **53**, 2138–2142 (2014).

10. Hayashi, S. & Koizumi, T. Elastic Organic Crystals of a Fluorescent π-Conjugated Molecule. *Angew. Chem. Int. Ed.* **55**, 2701–2704 (2016).

11. Halabi, J. M., Ahmed, E., Catalano, L., Karothu, D. P., Rezgui, R., & Naumov, P. Spatial Photocontrol of the Optical Output from an Organic Crystal Waveguide. *J. Am. Chem. Soc.* **141**, 14966–14970 (2019).

12. Karothu, D. P., Dushaq, G. Ahmed, E., Catalano, L., Polavaram, S., Fereira, R., Li, L., Mohamed, S., Rasras, M., Naumov, P. Mechanically robust amino acid crystals as fiber-optic transducers and wide bandpass filters for optical communication in the near-infrared. *Nat. Commun.* **12**, 1326 (2021).

13. Bushuyev, O. S., Tomberg, A., Friščić, T. & Barrett, C. J. Shaping Crystals with Light: Crystal-to-Crystal Isomerization and Photomechanical Effect in Fluorinated Azobenzenes. *J. Am. Chem. Soc.* **135**, 12556–12559 (2013).

14. Natarajan, A., Tsai, C. K., Khan, S. I., McCarren, P., Houk, K. N. & Farcia-Garibay, M. A. The Photoarrangement of α-Santonin is a Single-Crystal-to-Single-Crystal Reaction: A Long Kept Secret in Solid-State Organic Chemistry Revealed. *J. Am. Chem. Soc.* **129**, 9846–9847 (2007).

15. Biradha, K. & Santra, R. Crystal engineering of topochemical solid state reactions. *Chem. Soc. Rev.* **42**, 950–967 (2013).

16. Sun, A., Lauher, J. W. & Goroff, N. S. Preparation of poly(diiododiacetylene), an ordered conjugated polymer of carbon and iodine. *Science* **312**, 1030–1034 (2006).

17. Campillo-Alvarado, G., Li, C., Feng, Z., Hutchins, K. M., Swenson, D. C., Hopfl, H., Morales-Rojas, H. & MacGillivray, L. R. Single-Crystal-to-Single-Crystal [2 + 2] Photodimerization Involving B←N Coordination with Generation of a Thiophene Host. *Organometallics* **39**, 2197–2201 (2020).

18. Chu, Q., Swenson, D. C. & MacGillivray, L. R. A single-crystal-to-single-crystal transformation mediated by argentophilic forces converts a finite metal complex into an infinite coordination network. *Angew. Chem. Int. Ed.* **44**, 3569–3572 (2005).

19. Xu, T.-Y., Tong, F., Xu, H., Wang, M.-Q., Tian, H., Qu, D.-H. Energineering Photomechanical Molecular Crystals to Achieve Extraordinary Expansion Based on Solid-State [2+2] Photocycloaddition. *J. Am. Chem. Soc.* **144**, 14, 6278–6290 (2022).

20 Morimoto, K., Kitagawa, D., Tong, F., Chalek, K., Mueller, L. J., Bardeen, C. J., & Kobatake, S. Correlating Reaction Dynamics and Size Change during the Photomechanical Transformation of 9-Methylanthracene Single Crystals *Angew. Chem. Int. Ed.* **61**, e202114089 (2022).

21. Sinnwell, M. A. & MacGillivray, L. R. Halogen-Bond-Templated [2+2] Photodimerization in the Solid State: Directed Synthesis and Rare Self-Inclusion of a Halogenated Product. *Angew. Chem. Int. Ed.* **55**, 3477–3480 (2016).

22. Anthony, J. E., Brooks, J. S., Eaton, D. L. & Parkin, S. R. Functionalized Petacene: Imporved Elctronic Properties from Control of Solid-State Order. *J. Am. Chem. Soc.* **123**, 9482–9483 (2001).

23. Trask, A. V., Motherwell, W. D. S. & Jones, W. Pharmaceutical Cocrystallization: Engineering a Remedy for Caffeine Hydration. *Cryst. Growth. Des.* **5**, 1013–1021 (2005).

24. Kavanagh, O. N., Croker, D. M., Walker, G. M. & Zaworotko, M. J. Pharmaceutical cocrystals: from serendipity to design to application. *Drug. Discov.* **24**, 796–804 (2019).

25. MacGillivray, L. R., Papaefstathiou, G. S., Friščić, T., Hamilton, T. D., Bucar, D.-K., Chu, Q., Varshney, D. B., & Georgiev I. G. Supramolecular Control of Reactivity in the Solid State: From Templates to Ladderanes to Metal−Organic Frameworks. *Acc. Chem. Res.* **41**, 280–291 (2008).

26. Zaworotko, M. J. Molecules to Crystals, Crystals to Molecules ... and Back Again? *Cryst. Growth. Des.* **7**, 4–9 (2007).

27. Gao, G., Chen, M., Roberts, J., Feng, M., Xiao, C., Zhang, G., Parkin, S., Risko, C., & Zhang, L. Rational Functionalization of a C_{70} Buckybowl to Enable a C_{70}:Buckybowl Cocrystal for Organic Semiconductor Applications. *J. Am. Chem. Soc.* **142**, 5, 2460–2470 (2020).

28. Wang, J., Zhang, S. T., Xu, S. P., Li, A. S., Li, B., Ye, L., Geng, Y. J., Tian, Y., & Xu, W. Q. Morphology-Dependent Luminescence and Optical Waveguide Property in Large-Size Organic Charge Transfer Cocrystals with Anisotropic Spatial Distibution of Transition Dipole Moment. *Adv. Optical. Mater.* **8**, 1901280 (2020).

29. Lu, B., Fang, X. & Yan, D. Luminescent Polymorphic Co-crystals: A Promising Way to the Diversity of Molecular Assembly, Fluorescence Polarization, and Optical Waveguide. *ACS. Appl. Mater. Interfaces* **12**, 31940–31951 (2020).

30. Liu, Y. *et al.* Reversible Luminescent Switching in an Organic Cocrystal: Multi-Stimuli-Induced Crystal-to-Crystal Phase Transformation. *Angew. Chem. Int. Ed.* **59**, 15098–15103 (2020).

31. Bushuyev, O. S., Corkery, T. C., Barrett, C. J. & Friščić, T. Photo-mechanical azobenzene cocrystals and in situ X-ray diffraction monitoring of their optically-induced crystal-to-crystal isomerisation. *Chem. Sci.* **5**, 3158–3164 (2014).

32. Vainauskas, J., Topić, F., Bushuyev, O. S., Barrett, C. J. & Friščić, T. Halogen bonding to the azulene π-system: cocrystal design of pleochroism. *Chem. Commun.* **56**, 15145–15148 (2020).

33. Borchers, T.H., Topić, F., Christopherson, JC, Bushuyev, O. S., Vainauskas, J., Titi, H. M., Friščić, T. & Barrett, C. J. Cold photo-carving of halogen-bonded co-crystals of a dye and a volatile co-former using visible light. *Nat. Chem.* **14**, 574–581 (2022).

34. Wood, M. J., Coady, M. J., Aristizabal, F., Nielsen, K., Ragogna, P. J. & Krietzig, A.-M. Femtosecond laser micromachining of co-polymeric urethane materials. *Appl. Surf. Sci.* **483**, 633–641 (2019).

35. Yao, Y., Zhang, L., Leydecker, T. & Samorì, P. Direct Photolithography on Molecular Crystals for High Performance Organic Optoelectronic Devices. *J. Am. Chem. Soc.* **140**, 6984–6990 (2018).

36. Ghorai, S. . Sumrak, J. C., Hutchins, K. M., Bucar, D.-K., Tivanski, A. V. & MacGillivray, L. R. From co-crystals to functional thin films: photolithography using [2+2] photodimerization. *Chem. Sci.* **4**, 4304–4308 (2013).

37. Wang, Z. Zhang, J., Xie, J., Yin, Y., Wang, Z., Shen, H., Li, Y., Li, J., Liang, S., Cui, L., Zhang, L., Zhang, H. & Yang, B. Patterning Organic/Inorganic Hybrid Bragg Stacks by Integrating One-Dimensional Photonic Crystals and Macrocavities through Photolithography: Toward Tunable Colorful Patterns as Highly Selective Sensors. *ACS. Appl. Mater. Interfaces* **4**, 1397–1403 (2012).

38. Sun, J. & Litchinitser, N. M. Toward Practical, Subwavelength, Visible-Light Photolithography with Hyperlens. *ACS Nano* **12**, 542–548 (2018).

39. Desbiolles, B. X. E., Bertsch, A. & Renaud, P. Ion beam etching redeposition for 3D multimaterial nanostructure manufacturing. *Microsyst. Nanoeng.* **5**, 11 (2019).

40. Kandidov, V. P., Dormidonov, A. E., Kosareva, O. G., Chin, S. L. & Liu, W. in *Self-focusing: Past and Present: Fundamentals and Prospects* (eds Robert W. Boyd, Svetlana G. Lukishova, & Y. R. Shen) 371–398 (Springer New York, 2009).

41. Li, W. van Baren, J., Berges, A., Bekyarova, E., Lui, C. H., & Bardeen C. J. Shaping Organic Microcrystals Using Focused Ion Beam Milling. *Cryst. Growth. Des.* **20**, 1583–1589 (2020).

42. Cavallo, G., Metrangolo, P., Milani, R., Pilati, T., Priimagi, A., Resnati, G. & Terraneo G. The Halogen Bond. *Chem. Rev.* **116**, 2445–2601 (2016).

43. Lommerse, J. P. M., Stone, A. J., Taylor, R. & Allen, F. H. The Nature and Geometry of Intermolecular Interactions between Halogens and Oxygen or Nitrogen. *J. Am. Chem. Soc.* **118**, 3108–3116 (1996).

44. Mantina, M., Chamberlin, A. C., Valero, R., Cramer, C. J. & Truhlar, D. G. Consistent van der Waals Radii for the Whole Main Group. *J. Phys. Chem. A* **113**, 5806–5812 (2009).

45. Antoine, J. A. & Lin, Q. Synthesis of azobenzenes using N-chlorosuccinimide and 1,8-diazabicyclo[5.4.0]undec-7-ene (DBU*). J. Org. Chem.* **82**, 9873–9876 (2017).

46. APEX3 (Bruker AXS Inc., 2012).

47. Krause, L., Herbst-Irmer, R., Sheldrick, G. M. & Stalke, D. Comparison of silver and molybdenum microfocus X-ray sources for single-crystal structure determination. *J. Appl. Cryst.* **48**, 3–10 (2015).

48. Sheldrick, G. M. SHELXT—integrated space-group and crystal-structure determination. *Acta Cryst.* **A71**, 3–8 (2015).

49. Sheldrick, G. M. Crystal structure refinement with SHELXL. *Acta Cryst.* **C71**, 3–8 (2015).

50. Dolomanov, O. V., Bourhis, L. J., Gildea, R. J., Howard, J. A. K. & Puschmann, H. OLEX2: a complete structure solution, refinement and analysis program. *J. Appl. Cryst.* **42**, 339–341 (2009).

51. Farrugia, L. J. WinGX and ORTEP for Windows: an update. *J. Appl. Cryst.* **45**, 849–854 (2012).

52. Frisch, M. J. *et al*. Gaussian 16, Revision C.01 (Gaussian, Inc., 2016).

53. Becke, A. D. Density-functional thermochemistry. III. The role of exact exchange. *J. Chem. Phys.* **98**, 5648–5652 (1993).

54. Lee, C., Yang, W. & Parr, R. G. Development of the Colle–Salvetti correlation-energy formula into a functional of the electron density. *Phys. Rev. B* **37**, 785–789 (1998).

55. Ditchfield, R., Hehre, W. J. & Pople, J. A. Self-consistent molecular-orbital methods. IX. An extended Gaussian-type basis for molecular-orbital studies of organic molecules. *J. Chem. Phys.* **54**, 724–728 (1971).

56. Glukhovtsev, M. N., Pross, A., McGrath, M. P. & Radom, L. Extension of Gaussian-2 (G2) theory to bromine- and iodine-containing molecules: use of effective core potentials. *J. Chem. Phys.* **103**, 1878–1885 (1995).

57. Pritchard, B. P., Altarawy, D., Didier, B., Gibson, T. D. & Windus, T. L. New basis set exchange: an open, up-to-date resource for the molecular sciences community. *J. Chem. Inf. Model*. **59**, 4814–4820 (2019).

58. Clark, S. J., Segall, M. D., Pickard, C. J., Hasnip, P. J., Probert, M. I. J., Refson, K., & Payne, M. C. First principles methods using CASTEP. *Z. Kristallogr. Cryst. Mater.* **220**, 5/6, 567–570 (2005).

59. Bjorkman, T. Generating geometries for electronic structure programs. *Comput. Phys. Commun.* **182**, 5, 1183–1186 (2011).

60. Perdew, J. P., Burke, K., & Ernzerhof, M. Generalized gradiet approximation made simple. *Phys. Rev. Lett.* **77**, 3865 (1996).

61. Grimme, S., Antony, J., Ehrlich, S., & Krieg, H. A consistent and accurate *ab initio* parametrization of density functional dispersion correction (DFT-D) for the 94 elements H-Pu. *J. Chem. Phys.* **132**, 154104 (2010).

62. Monkhorst, H. J., Pack, J. D. Special points for the brillouin-zone integrations. *Phys. Rev. B.* **13**, 5188 (1976).

3.7 Appendix 2: Supporting information for Chapter 3

3.7.1 Experimental data

3.7.1.1 UV-Vis absorbance

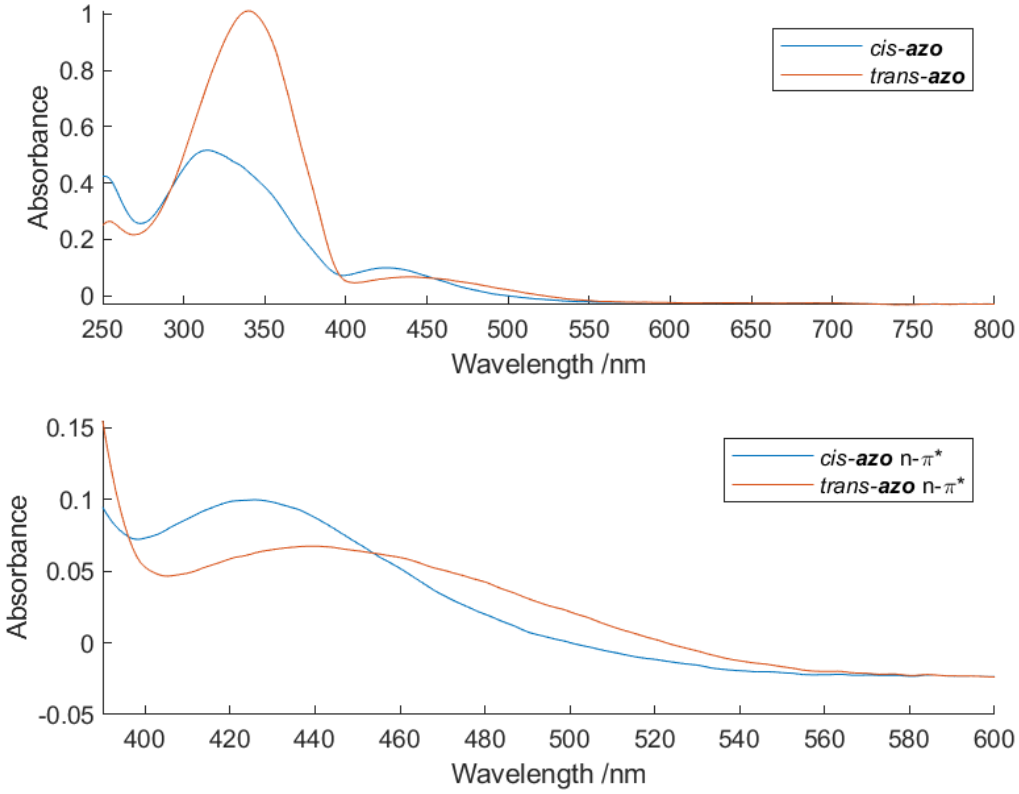

Supplementary Figure 3.1. UV/Vis absorbance spectra of *trans*- and *cis*-azo in THF solutions.

3.7.1.2 Single crystal X-ray diffraction

The X-ray data for (*cis*-azo)(dioxane), (*cis*-azo)(pyrazine) were collected on a Bruker D8 Venture dual-source diffractometer equipped with a PHOTON II detector and an Oxford Cryostream 800 cooling system, using mirror-monochromated Mo*K*α ($\lambda = 0.71073$ Å) or Cu*K*α radiation ($\lambda = 1.54184$ Å) from respective microfocus sources. Data were collected in a series of φ- and ω-scans. APEX3 software was used for data collection, integration and reduction.[1] Numerical absorption corrections were applied using SADABS-2016/2.[2]

Structures were solved by dual-space iterative methods using SHELXT[3] and refined by full-matrix least-squares on F^2 using all data with SHELXL[4] within the OLEX2[5] and/or WinGX[6] environment. For both structure models, some reflections were found to have been obscured by the beam stop and were omitted from the refinement. Hydrogen atoms were placed in calculated positions and treated as riding on the parent carbon atoms with isotropic displacement parameters 1.2 times larger than the respective parent atoms. Equivalent 1,2- and 1,3-distances were restrained to be of the same length for dioxane molecules in (*cis*-azo)(dioxane), with rigid bond and proximity restraints also applied to their anisotropic displacement parameters. The dioxane molecules were modelled as disordered around the inversion centre over two components, with their occupancies refining to 0.675(10) and 0.325(10), respective.

Crystal structure figures were generated using Mercury,[7] and POV-Ray methods.[8]

CCDC 2162225 and 2162226 contain the supplementary crystallographic data for this paper. The data can be obtained free of charge from The Cambridge Crystallographic Data Centre *via* www.ccdc.cam.ac.uk/structures.

Supplementary Table 3.1. Crystallographic data for the reported crystal structures of (*cis*-**azo**)(dioxane) and (*cis*-azo)(pyrazine).

Compound	(*cis*-**azo**)(dioxane)	(*cis*-**azo**)(pyrazine)
CCDC Number	2162225	2162226
T (K)	253.0(1)	298(2)
Formula	$C_{16}H_8F_8I_2N_2O_2$	$C_{16}H_4F_8I_2N_4$
M_r	666.04	658.03
Crystal system	Monoclinic	Monoclinic
Space group	*C*2/*c*	*C*2/*c*
a (Å)	21.1357(14)	29.0978(6)
b (Å)	5.4973(4)	5.72450(10)
c (Å)	18.4971(12)	11.5731(3)
α (°)	90	90
β (°)	112.909(2)	95.6637(11)
γ (°)	90	90
V (Å^3)	1979.6(2)	1918.32(7)
Z	4	4
ρ_{calc} (g cm^{-3})	2.235	2.278
λ (Å)	0.71073	1.54184
μ (mm^{-1})	3.266	26.589
F(000)	1248.0	1224
Crystal size (mm^3)	0.522 × 0.120 × 0.075	0.456 × 0.214 × 0.096
Data collection θ range (°)	3.852–32.629	3.052–72.433
Reflections collected [R_{int}]	28174	14995
Reflections [$I > 2\sigma(I)$]	2915	1556
Data completeness (%)	98.9	99.4
Data/parameters/restraints	3596/164/103	1875/136/0
Goodness-of-fit on F^2	1.065	1.092
Final R, data with $I > 2\sigma(I)$	R_1 = 0.0313 wR_2 = 0.0737	R_1 = 0.0346 wR_2 = 0.0771
Final R for all data	R_1 = 0.0420 wR_2 = 0.0817	R_1 = 0.0460 wR_2 = 0.0882
Largest diff. peak/hole (e Å^{-3})	1.196/−1.015	0.856/−0.864

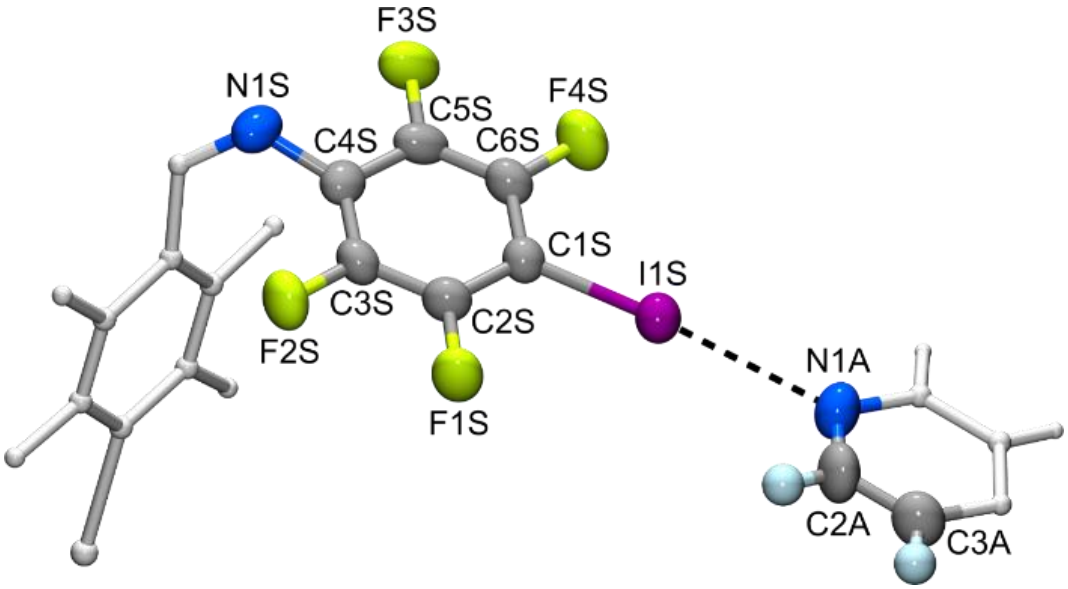

Supplementary Figure 3.2. ORTEP view of the asymmetric unit of (*cis*-azo)(pyrazine), collected at 298 k. showing the atom labelling scheme (CCDC code). Hydrogen atoms are shown as small spheres of arbitrary radius. The symmetry-dependent parts of *cis*-azo and pyrazine molecules are shown in ball-and-stick model in light grey. The halogen bond is shown as a dashed black line.

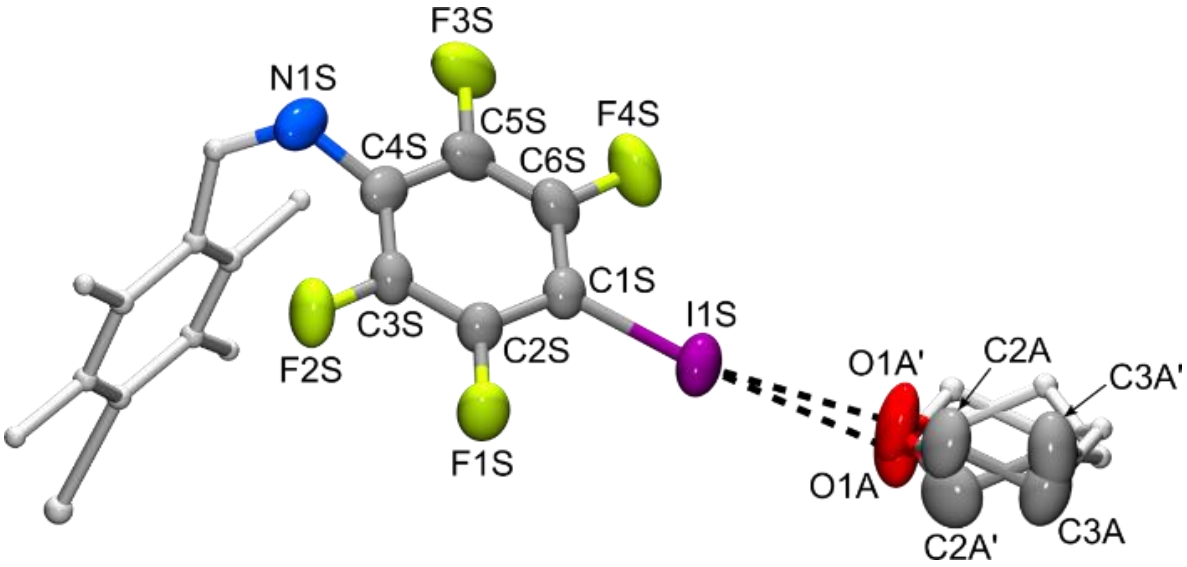

Supplementary Figure 3.3. ORTEP view of the asymmetric unit of (*cis*-azo)(dioxane), collected at 253 k. showing the atom labelling scheme (CDC code). Displacement ellipsoids are drawn at a 50 % probability level. The symmetry-dependent parts of *cis*-azo and dioxane molecules are shown in ball-and-stick model in light grey. Halogen bonds are shown as a dashed black line.

3.7.1.3 Laboratory laser setup

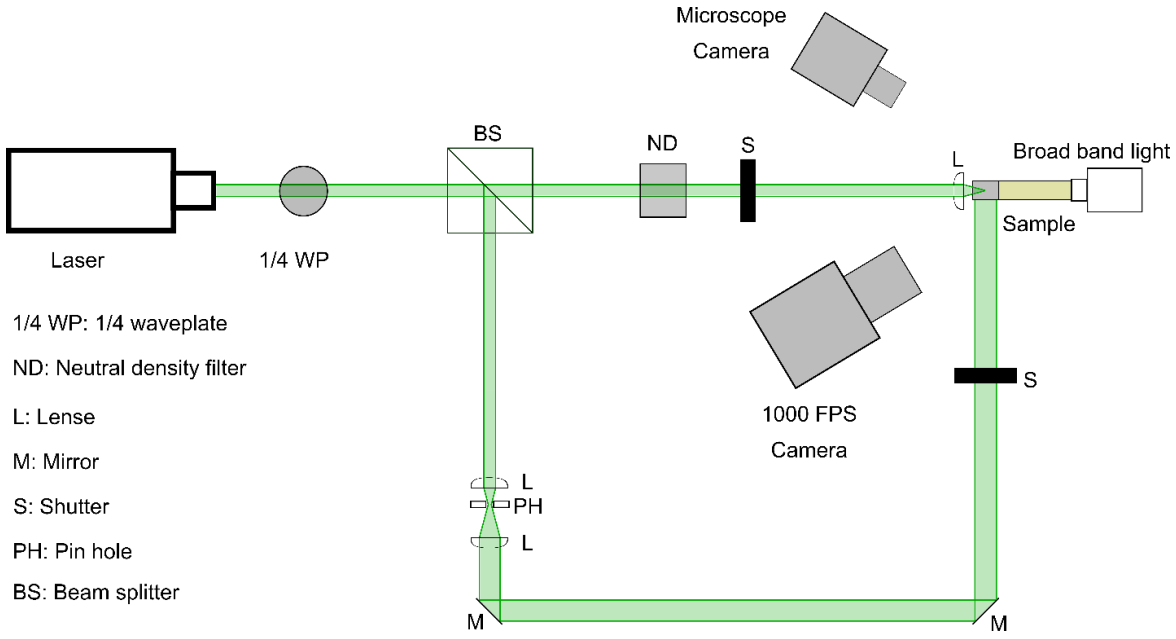

Supplementary Figure 3.4. Schematic of the laboratory laser setup including the various optical components and equipment and multiple cameras.

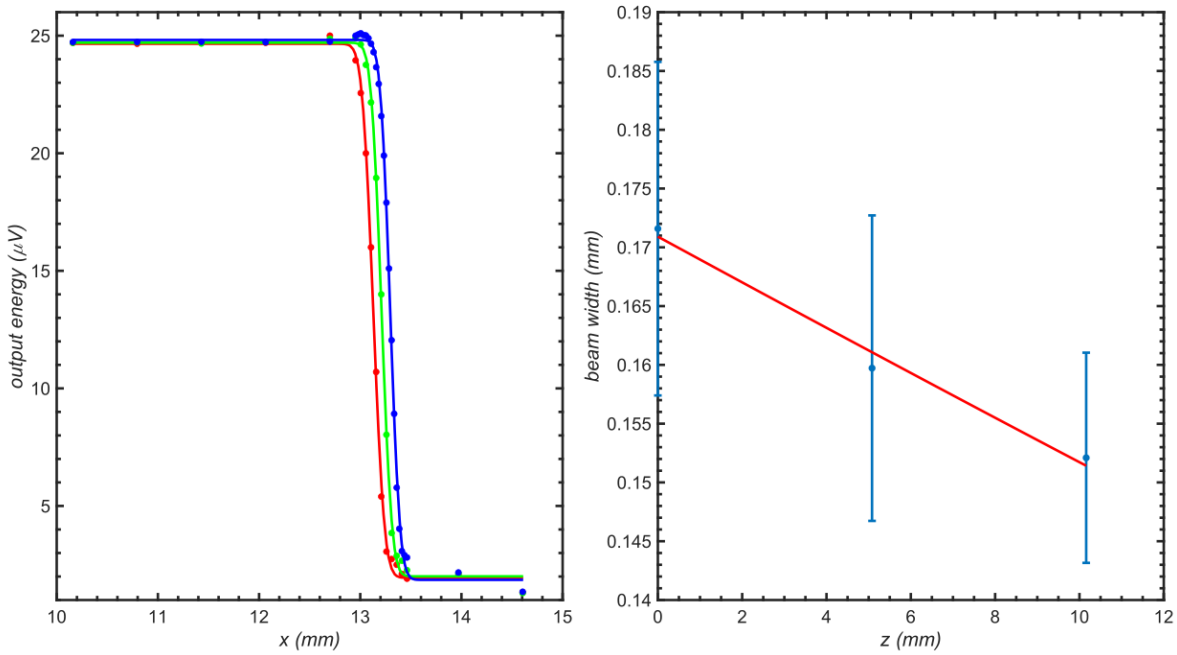

Supplementary Figure 3.5. Determination of beam diameter at the irradiation surface of the photo-carving beam *via* a knife edge experiment. Left) output energy with respect to knife position. Right) beam width at various positions of sampling.

$$P = P_0 + \frac{P_{max}}{2}(1 - \mathrm{erf}\left(\frac{\sqrt{2}(x - x_0)}{w}\right))$$

Supplementary Formula 3.1. Fit for measured data, P_0 is background power, P_{max} is maximum power, x_0 is the position of shift at half of the real power, erf is a standard error function, and w is the beam radius.

$$f(x) = a \cdot e^{-(x-b)^2/2c^2}$$

Supplementary Formula 3.2. Gaussian function used to simulate the beam intensity profile where the variable a is the intensity at the centre of the beam diameter.

$$I_0 = \frac{2 \cdot P_0}{\pi \cdot {w_0}^2}$$

Supplementary Formula 3.3. intensity of a beam profile at the centre of the beam diameter; P_0 = total power of the beam, and w_0 = beam radius.

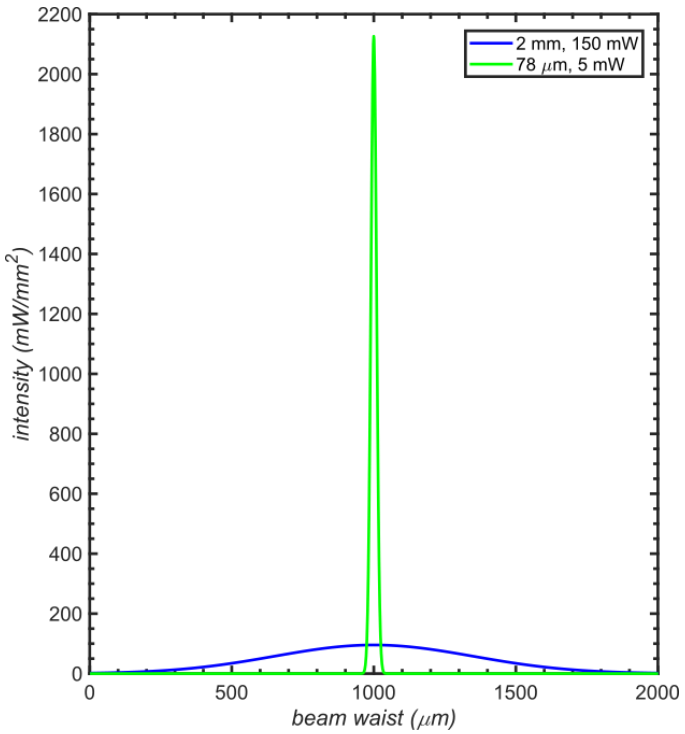

Supplementary Figure 3.6. A Gaussian beam profile, to show the intensity distribution of the two beams used throughout this study; a photo-carving beam (green), and a photo-actuating beam (blue). The beam size of the photo-carving beam was calculated *via* a knife-edge experiment.

3.7.2 (*cis*-azo)(dioxane) co-crystals

3.7.2.1 NMR analysis

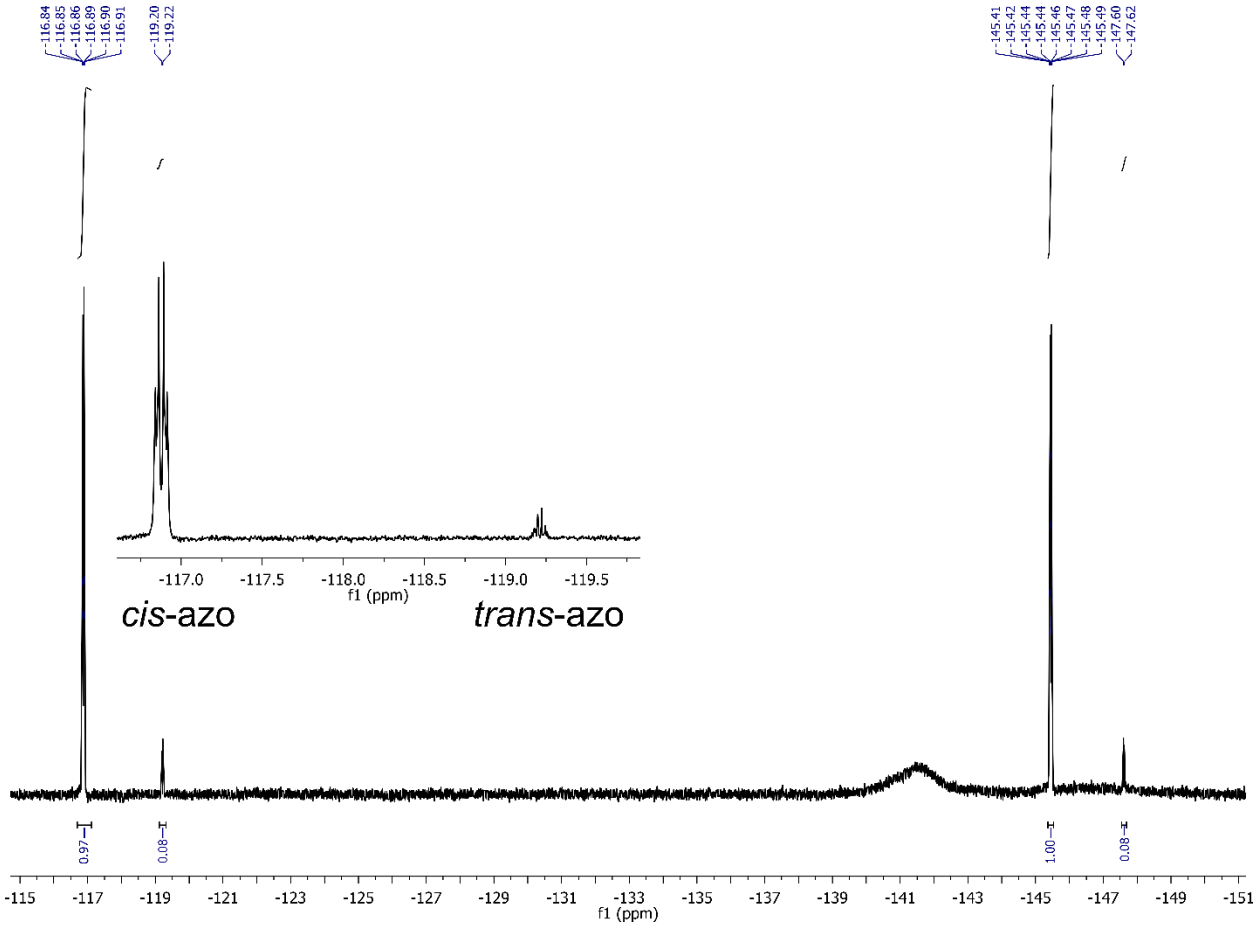

Supplementary Figure 3.7. F19 NMR spectra of a dissolved (*cis*-azo)(dioxane) single crystal after 20 min of irradiation by a dispersed LED.

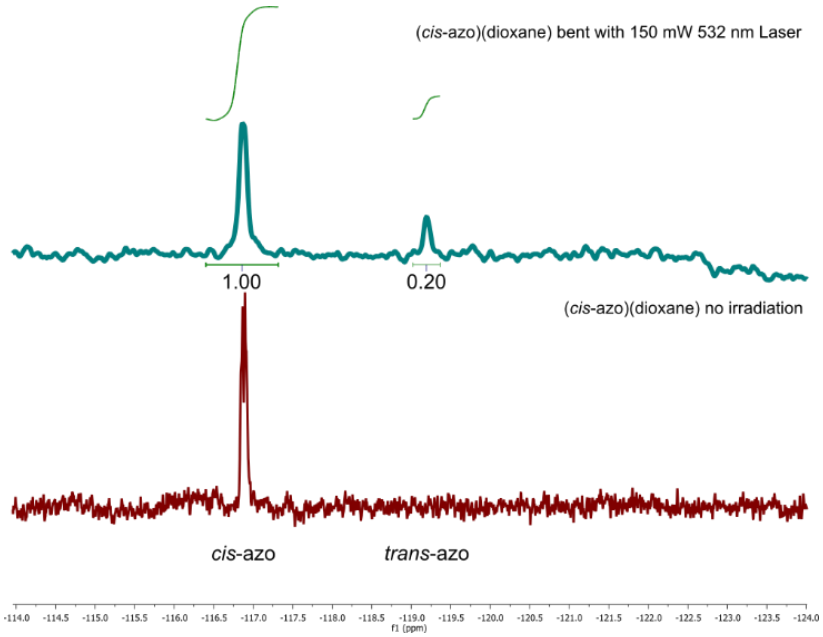

Supplementary Figure 3.8. F19 NMR spectra of a dissolved (*cis*-azo)(dioxane) single crystal after approximately 1 min irradiation by a 532 nm 150 mW laser (Top). F19 NMR spectra of a dissolved (*cis*-azo)(dioxane) single crystal before any irradiation.

3.7.2.2 Raman spectroscopy

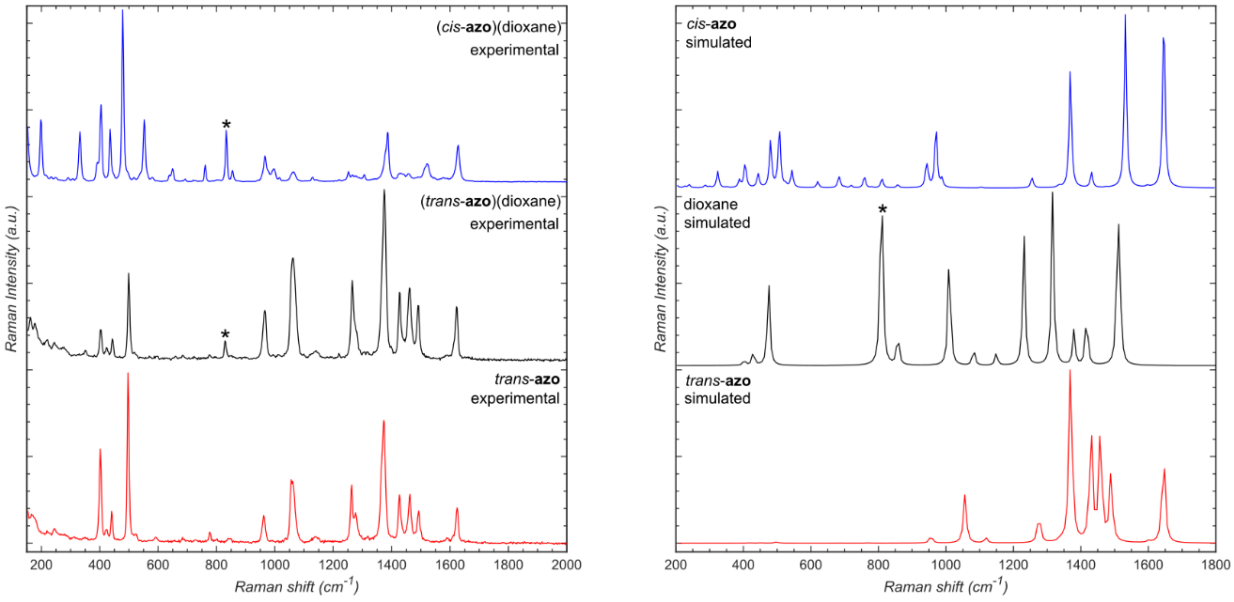

Supplementary Figure 3.9. Right) Experimental Raman spectra of (*cis*-azo)(dioxane), (*trans*-azo)(dioxane) and *trans*-azo **II** acquired with a 785 nm probe, at 25 mW power, 2.5 s integration, over 10 accumulations. Left) Simulated gas-phase Raman spectra of dioxane, *cis*-**azo** and *trans*-**azo**. The asterisk (*) indicates the position of the dioxane *v*(ring breathing) Raman band.

Supplementary Table 3.2. Assigned Raman shifts.

(*cis*-**azo**)(dioxane) experimental shifts (cm^{-1})	(*trans*-**azo**)(dioxane) experimental shifts (cm^{-1})	*trans*-**azo** experimental shifts (cm^{-1})	*cis*-**azo** simulated shifts (cm^{-1})	dioxane simulated shifts (cm^{-1})	*trans*-**azo** simulated shifts (cm^{-1})	assignment
336	N/A	N/A	324	N/A	N/A	*ν*(Aromatic)
N/A	350	N/A	N/A	N/A	N/A	
N/A	402	402	N/A	N/A	N/A	
410	N/A	N/A	405	N/A	N/A	*ν*(Aromatic)
N/A	423	423	N/A	N/A	413	*ν*(Aromatic)
437	443	440	443	N/A	444	*ν*(Aromatic)
501	499	497	506	N/A	491	*ν*(Aromatic), *ν*(N=N)
557	N/A	N/A	544	N/A	N/A	*ν*(Aromatic), *ν*(N=N)
N/A	778	776	N/A	N/A	N/A	
833	830	N/A	N/A	810	N/A	*ν*(ring breathing), dioxane
970	966	961	971	N/A	950	*ν*(Aromatic)
N/A	1061	1056	N/A	N/A	1050	*ν*(C−N)
N/A	1265	1263	N/A	N/A	1270	*ν*(C−N)
N/A	N/A	1276 Sh	N/A	N/A	N/A	
N/A	1375	1373	N/A	N/A	1364	*ν*(N=N)
1368	N/A	N/A	1387	N/A	N/A	*ν*(Aromatic)
N/A	1426	1426	N/A	N/A	1424	*ν*(N=N)
N/A	1461	1463	N/A	N/A	1452	*ν*(N=N)
N/A	1492	1492	N/A	N/A	1484	*ν*(N=N), *ν*(Aromatic)
1525	N/A	N/A	1532	N/A	N/A	*ν*(N=N)
1634	1622	1624	1648	N/A	1640	*ν*(Aromatic)

3.7.2.3 Scanning electron microscopy

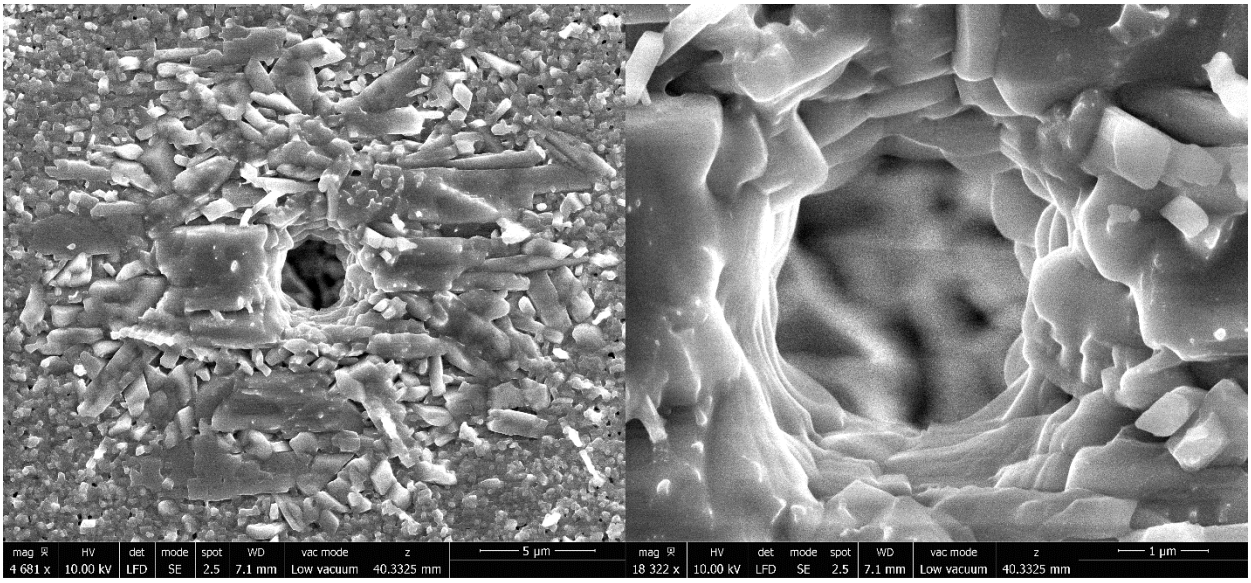

Supplementary Figure 3.10. SEM images of (*cis*-azo)(dioxane) after carving showing precision hole formation, *via* a 532 nm 1 mW confocal laser system.

3.7.2.4 High speed camera studies

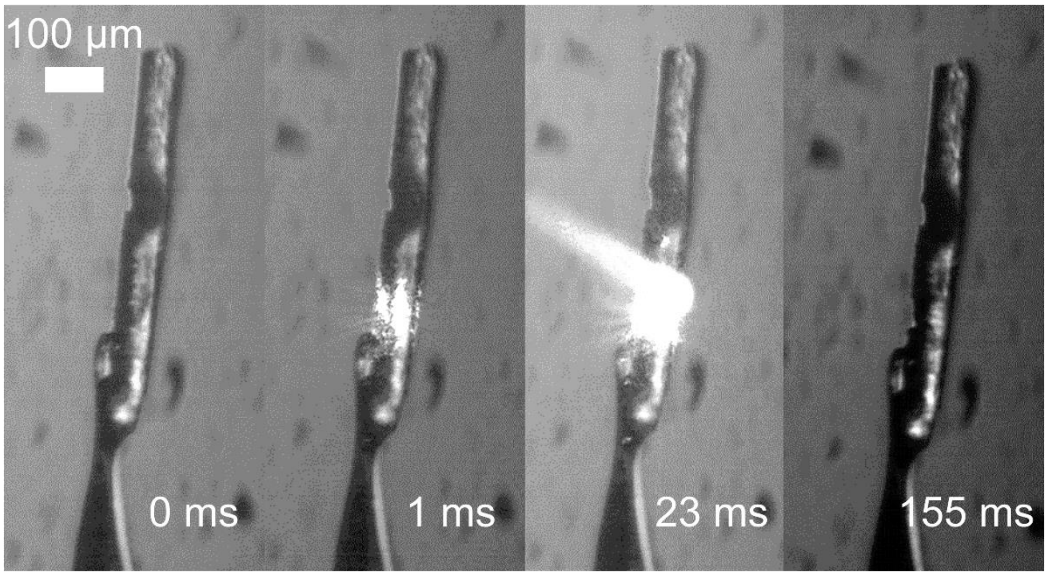

Supplementary Figure 3.11. Images of a machining process of (*cis*-azo)(dioxane) captured *via* a high speed camera using a 532 nm 5 mW laser.

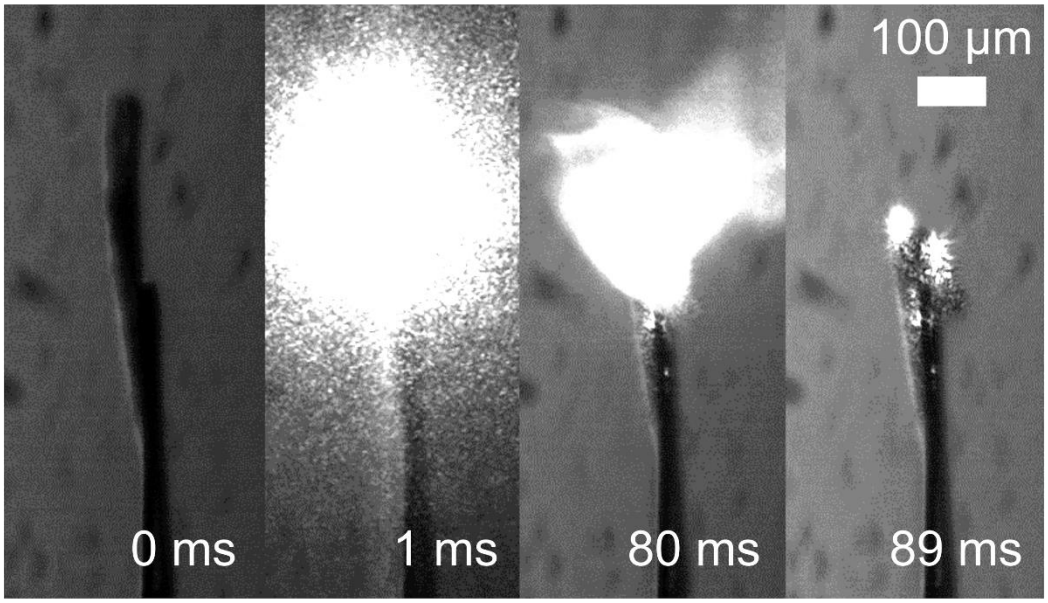

Supplementary Figure 3.12. Images of a machining process of (*cis*-azo)(dioxane) captured *via* a high speed camera using a 532 nm 15 mW laser.

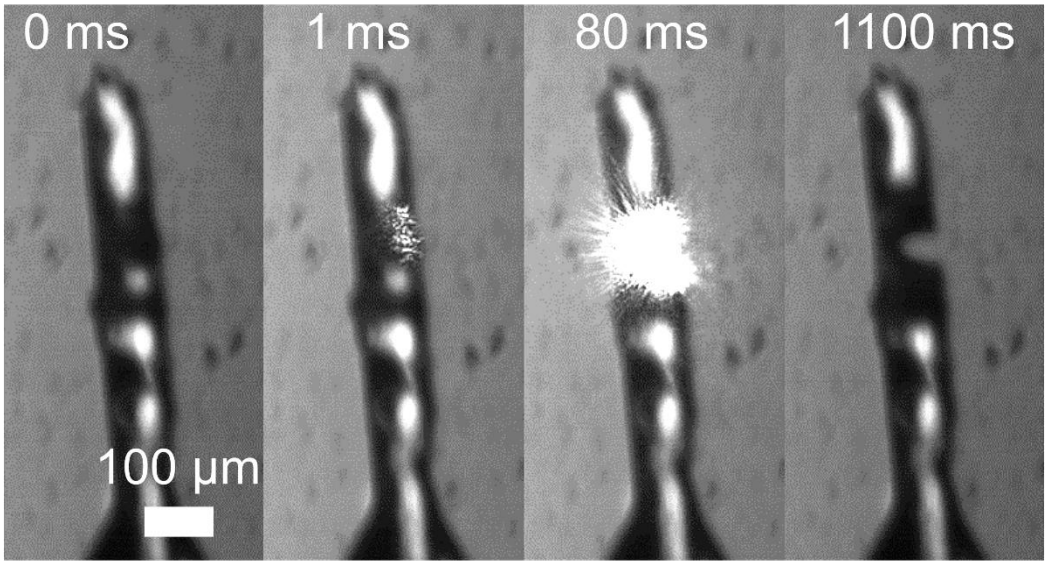

Supplementary Figure 3.13. Images of a machining process of (*cis*-azo)(dioxane) captured *via* a high speed camera using a 532 nm 10 mW laser.

3.7.3 (*cis*-azo)(pyrazine) co-crystals

3.7.3.1 NMR analysis

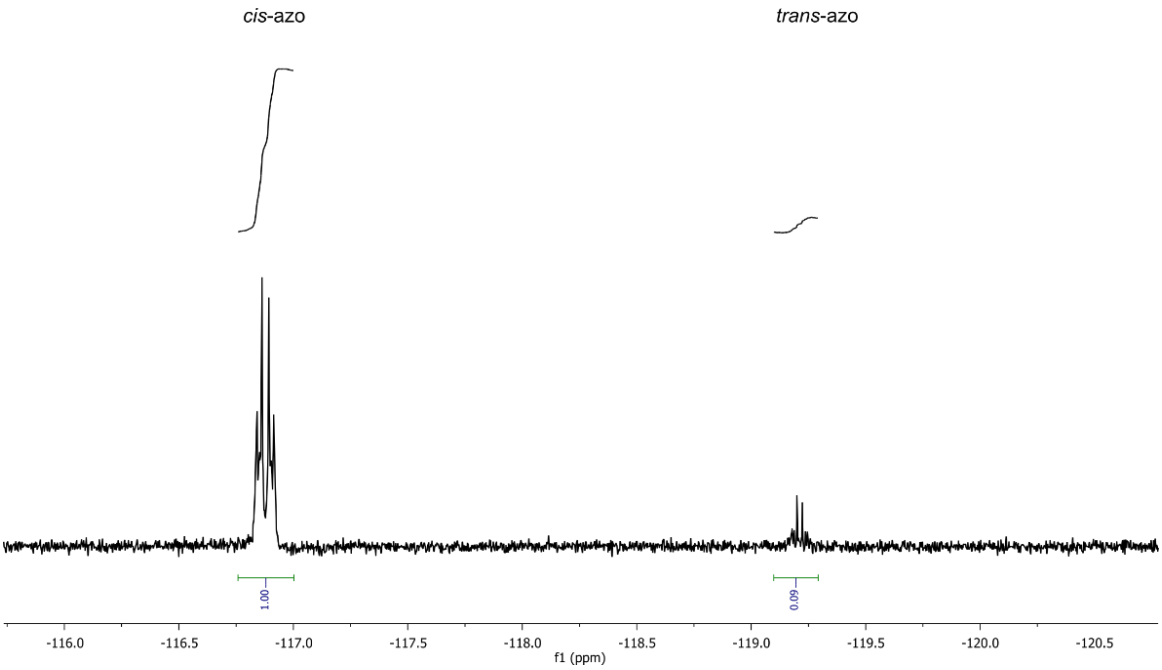

Supplementary Figure 3.14. F19 NMR spectrum of a dissolved (*cis*-azo)(pyrazine) single crystal after 2 hrs of irradiation.

3.7.3.2 Crystallographic studies of photo-carving of single crystals

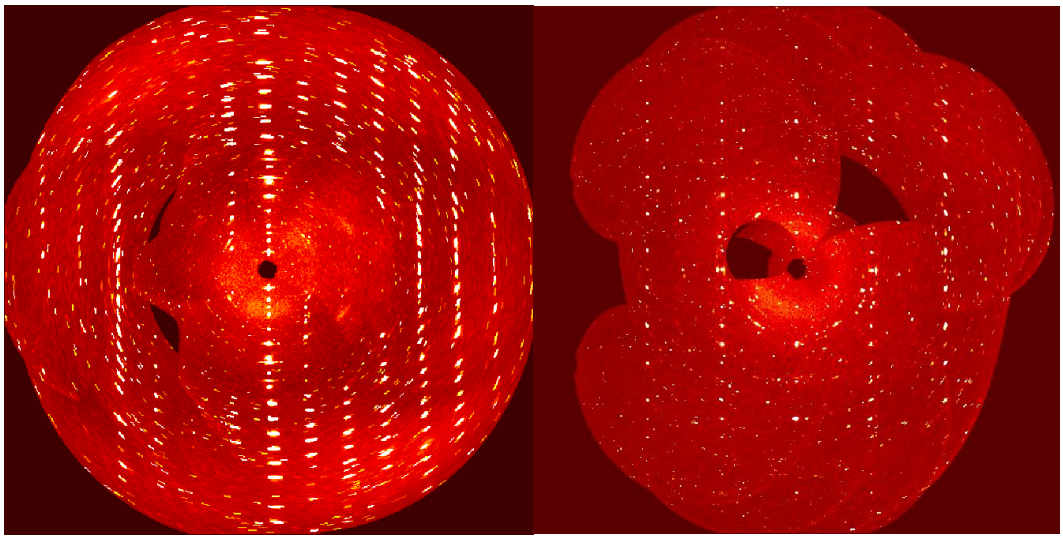

Supplementary Figure 3.15. Precision images of (*cis*-azo)(pyrazine) showing the 0kl layers: (left) before and after (right) photo-carving by a 532 nm laser at 20 mW power. A portion of the crystal was fully removed by laser light.

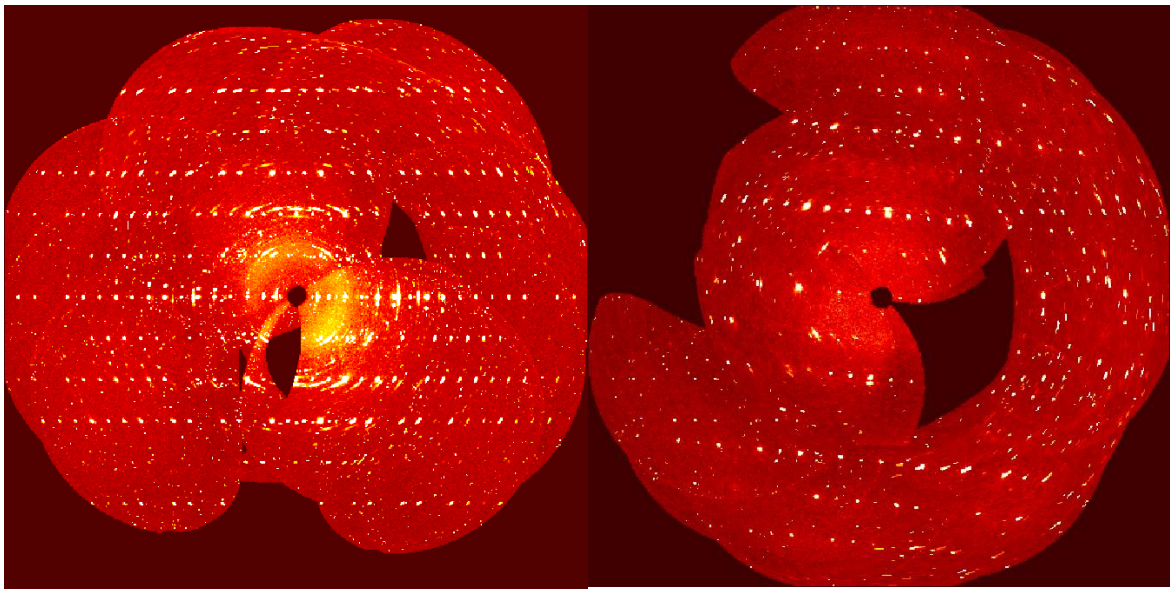

Supplementary Figure 3.16. Precision images of (*cis*-azo)(pyrazine) showing the hk0 layers: (left) before and after (right) photo-carving by a 532 nm laser at 20 mW power. A portion of the crystal was fully removed by laser light.

3.7.3.3 X-ray diffraction analysis

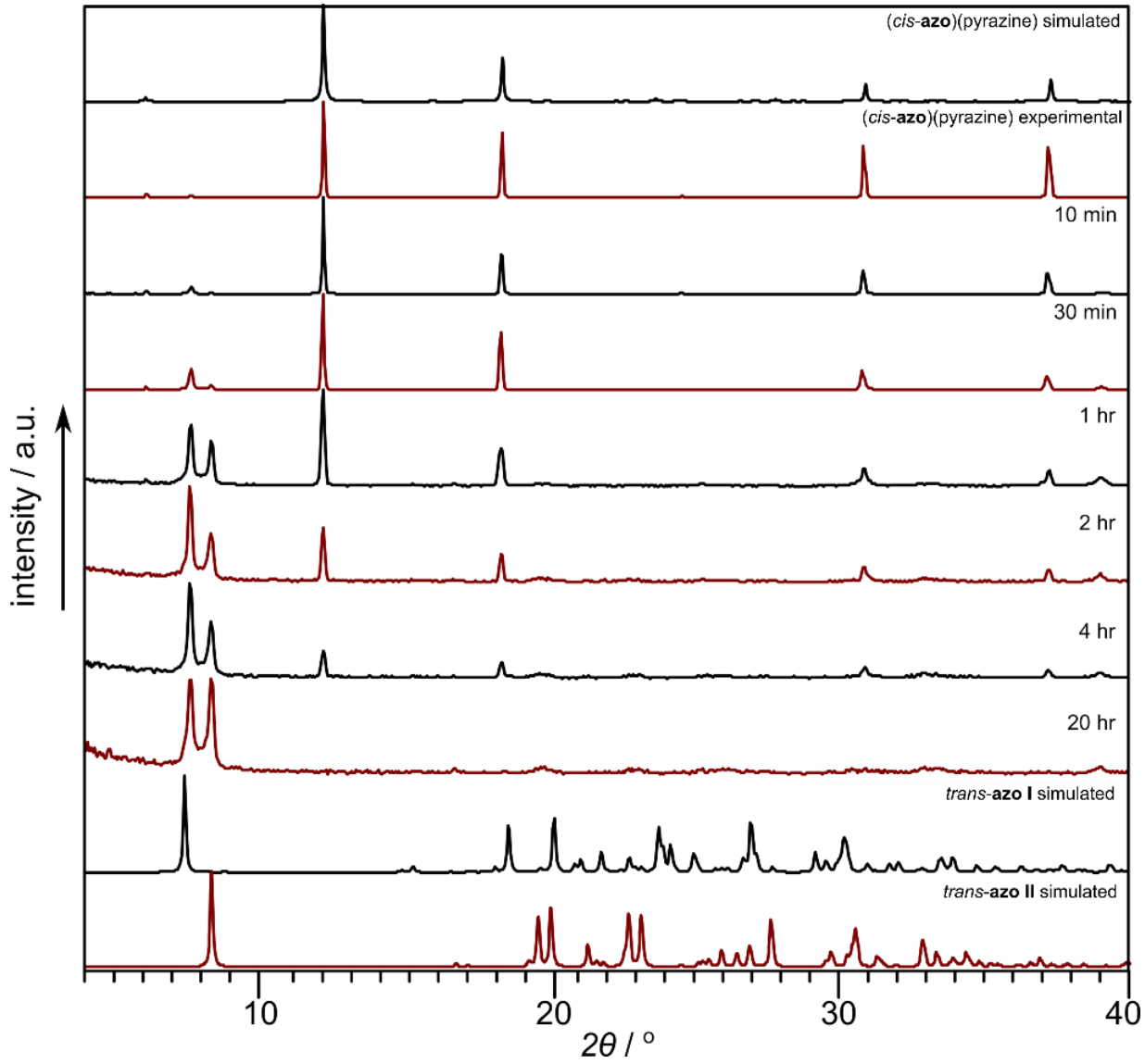

Supplementary Figure 3.17. Time evolution of powder X-ray diffraction patterns of a bulk sample of (*cis*-azo)(pyrazine) under irradiation by a 532 nm 37 mW·cm^{-2} LED.

3.7.3.4 Scanning electron microscopy analysis

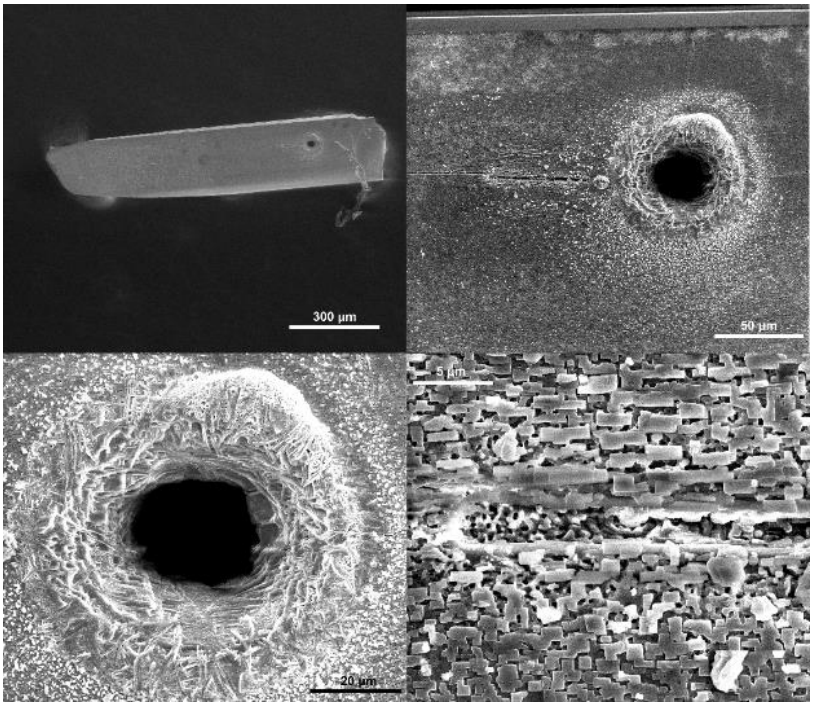

Supplementary Figure 3.18. SEM images of (*cis*-azo)(pyrazine) after photo-induced carving by a 532 nm 15 mW confocal laser system (top right/bottom left), and photo-induced carving by a 532 nm 3 mW confocal laser system (bottom right).

3.7.3.5 Computational analysis of co-crystals

Supplementary Table 3.3. Periodic density functional theory results of models discussed in this study.

Model	**Energy per unit cell /eV**	**# of Molecules in the cell**	**Energy per formula unit /eV**
(*trans*-azo)(dioxane)	-10963.46	2 (1 *trans*, 1 dioxane)	-10963.46
(*cis*-azo)(dioxane)	-21926.21	4 (2 *trans*, 2 dioxane)	-10963.11
(trans-azo)(pyrazine) (model reduced sym to P21/n (parallel azos))	-21147.07	4 (2 trans, 2 pyrazine)	-10573.54
(*cis*-azo)(pyrazine)	-21146.16	4 (2 cis, 2 pyrazine)	-10573.08
Pyrazine (crystal)	-2496.19	2	-1248.10
Pyrazine (g)	-1247.02	1	-1247.02
Dioxane (g)	-1637.18	1	-1637.18
trans-azo **I**	-37301.68	4	-9325.42
trans-azo **II**	-18650.83	2	-9325.415
cis-azo	-18650.06	2	-9325.03

Supplementary Table 3.4. Formation energy calculations of various models discussed in this study.

Formation energies	Energy /eV	Energy /kJ/mol
(*cis-azo*) + pyrazine to (*cis-azo*)(pyrazine)	0.040685	3.92553291
(*trans-azo* I) + pyrazine to (*trans-azo*)(pyrazine)	-0.02099	-2.02524114
(*trans-azo* II) + pyrazine to (*trans-azo*)(pyrazine)	-0.028265	-2.72717679

3.7.4 Thermodynamic studies

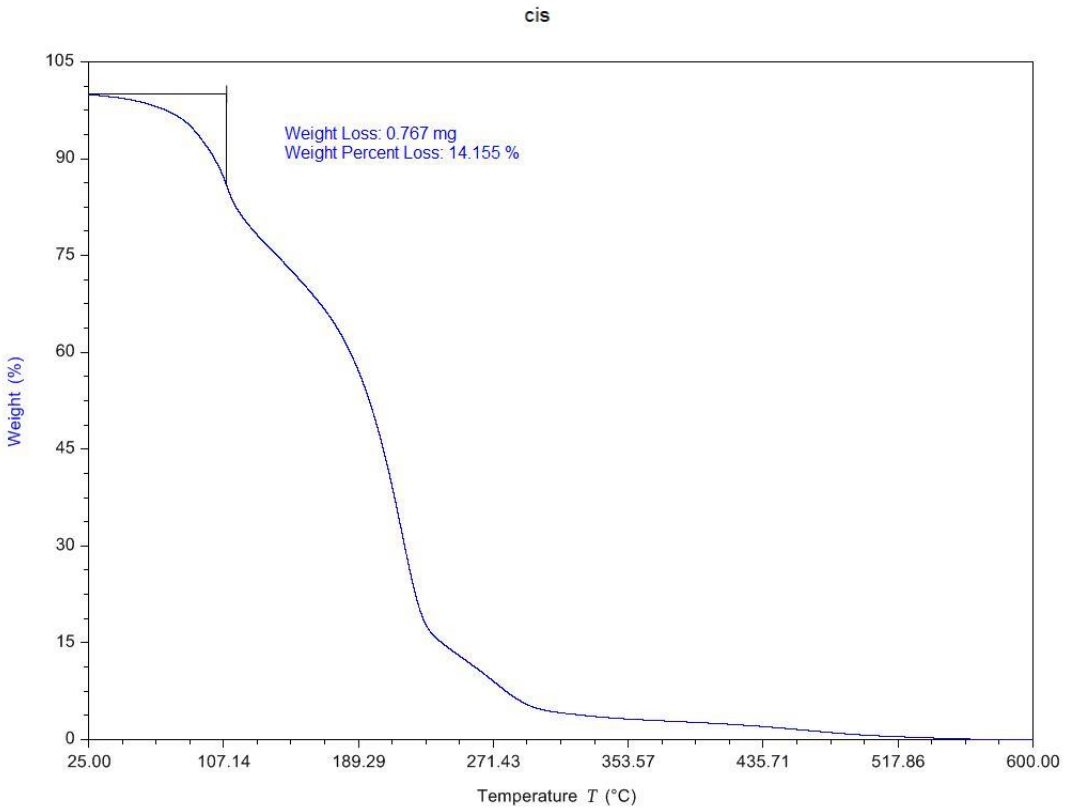

Supplementary Figure 3.19. Thermogravimetric analysis of (*cis*-azo)(dioxane).

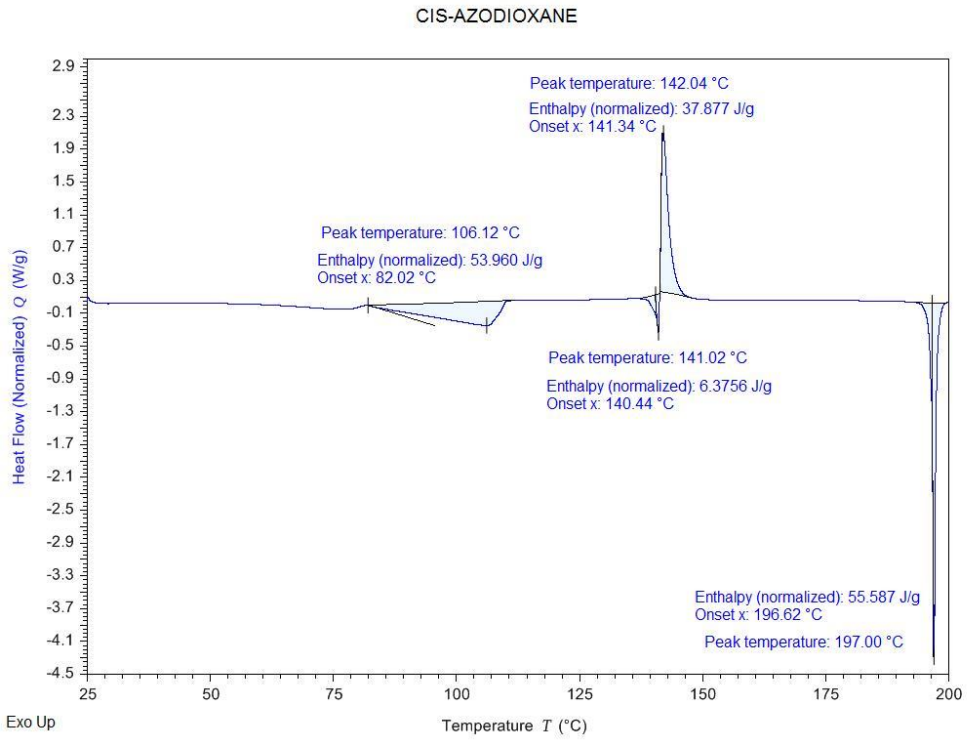

Supplementary Figure 3.20. Differential scanning calorimetry analysis of (*cis*-azo)(dioxane).

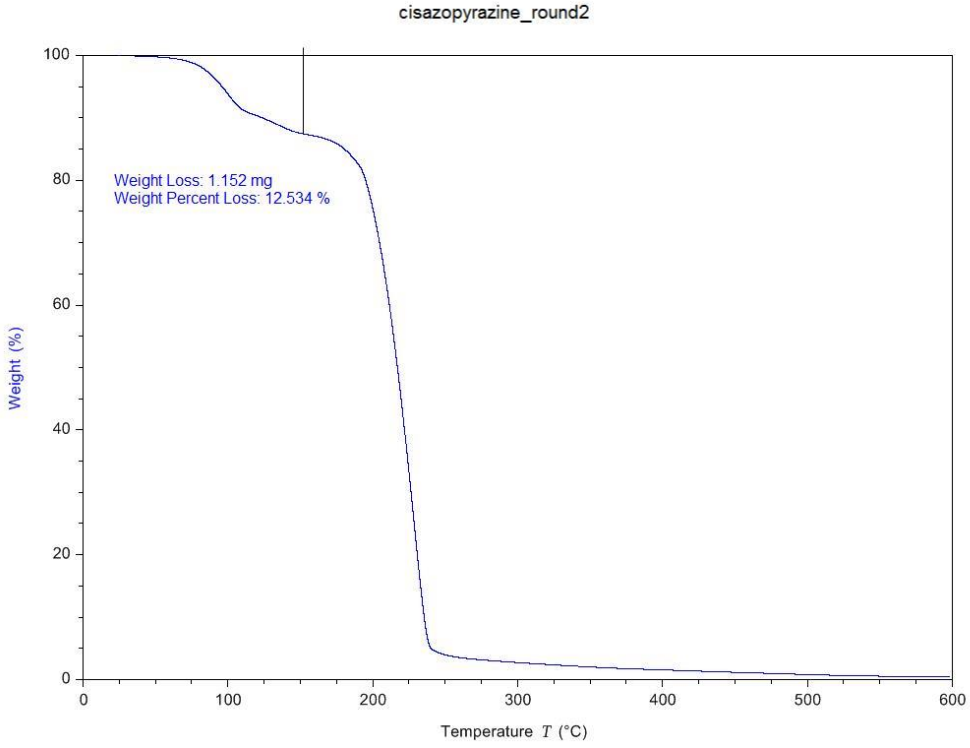

Supplementary Figure 3.21. Thermogravimetric analysis of (*cis*-azo)(pyrazine).

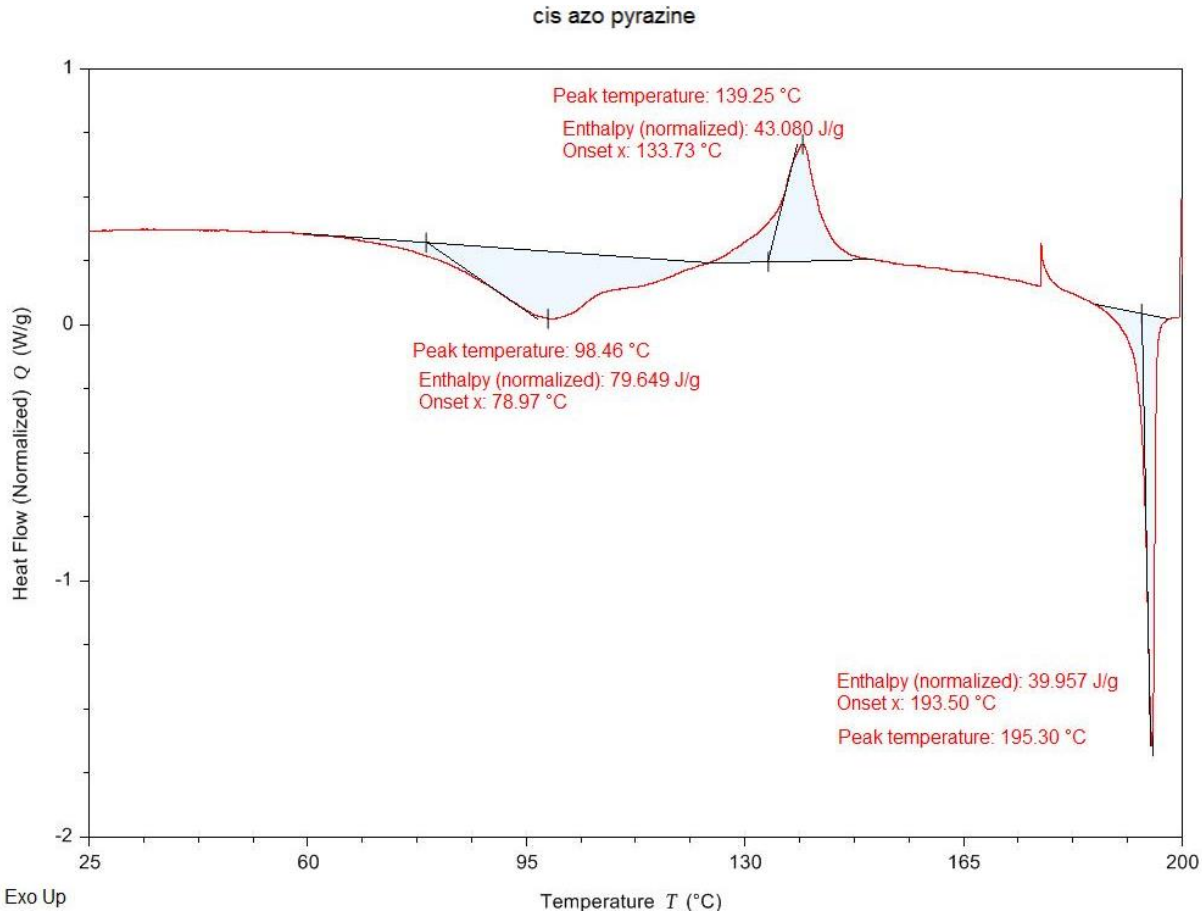

Supplementary Figure 3.22. Differential scanning calorimetry analysis of (*cis*-azo)(pyrazine).

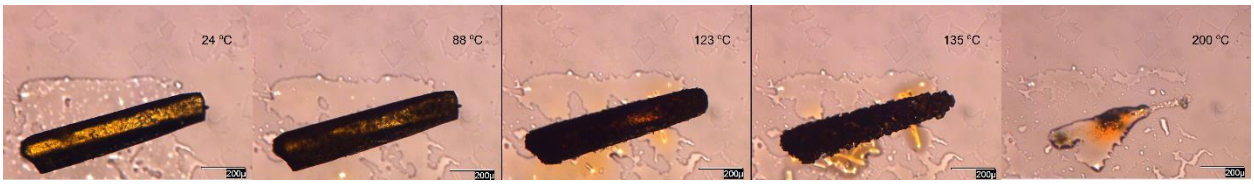

Supplementary Figure 3.23. Hot-stage microscopy images of (*cis*-azo)(dioxane).

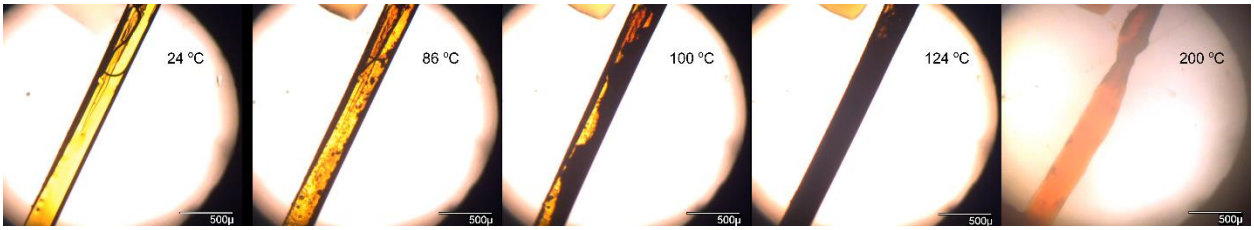

Supplementary Figure 3.24. Hot-stage microscopy images of (*cis*-azo)(pyrazine).

3.7.5 Additional photo-carving images and movies of *cis*-azo co-crystals

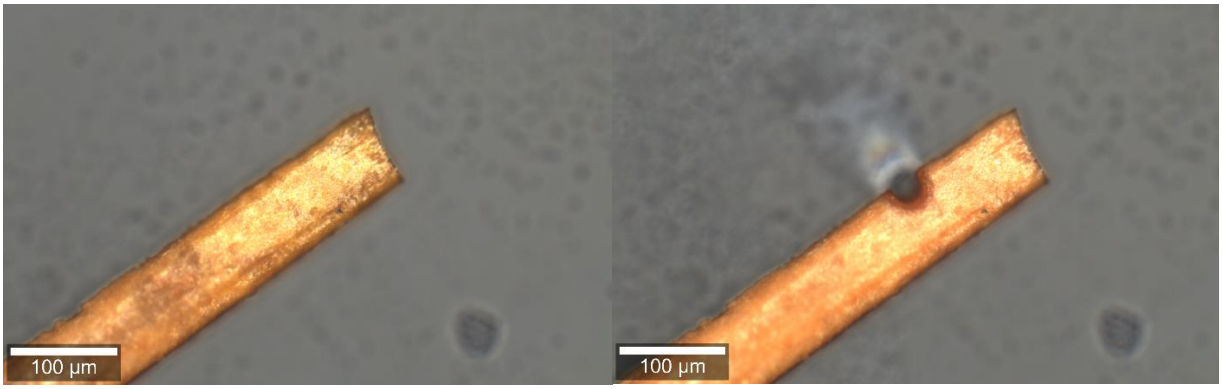

Supplementary Figure 3.25. (*cis*-azo)(dioxane) before (left) and after (right) photo-irradiation using a confocal Raman 532 nm at 10 mW laser power for 1s duration.

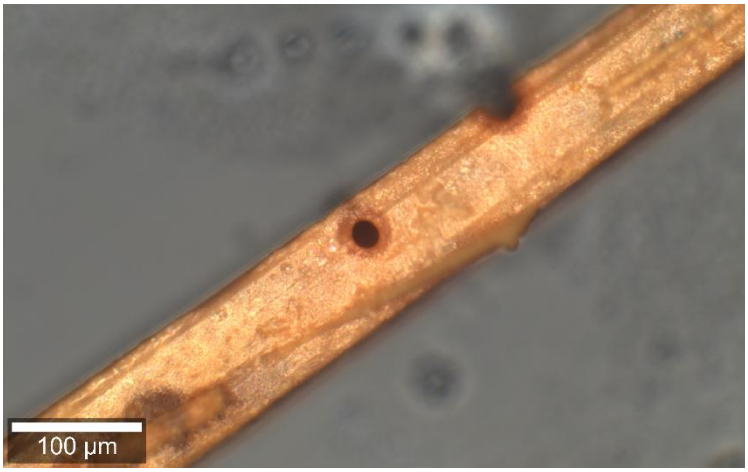

Supplementary Figure 3.26. (*cis*-azo)(dioxane) after photo-irradiation using a confocal Raman 532 nm at 5 mW laser power for 1s duration.

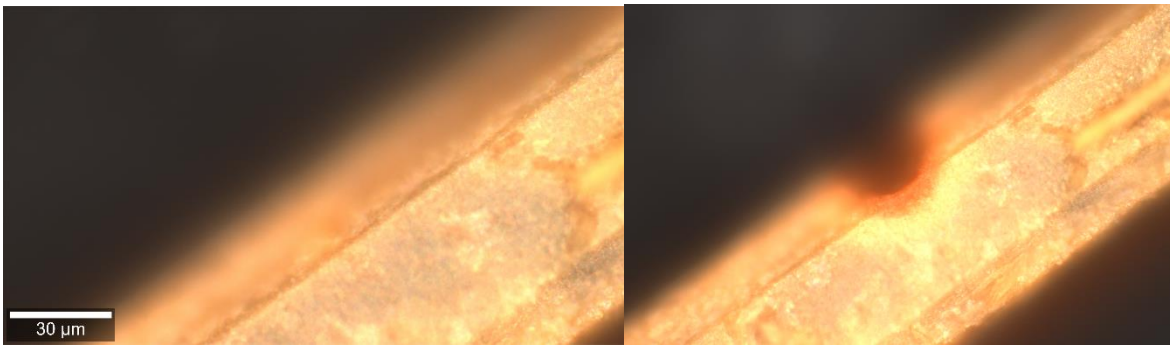

Supplementary Figure 3.27. (*cis*-azo)(dioxane) after photo-irradiation using a confocal Raman 532 nm at 2.5 mW laser power for 1s duration.

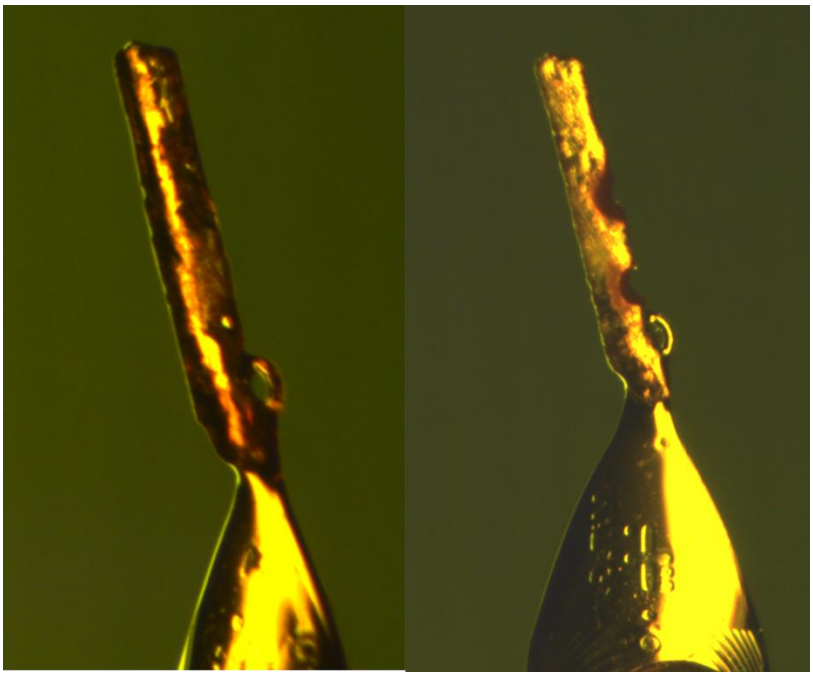

Supplementary Figure 3.28. (*cis*-azo)(dioxane) before (left) and after (right) photo-irradiation using the laboratory laser system (SI Figure 4) at 2.25 W cm^{-2} laser power.

3.7.5.1 Supplementary video and data file information

Video 1. Photo-mechanical bending of (*cis*-azo)(dioxane).

Video 2. Photo-mechanical bending of (*cis*-azo)(pyrazine).

Video 3. Photo-carving of (*cis*-azo)(dioxane).

Video 4. Photo-carving of (*cis*-azo)(pyrazine).

Video 5. High-speed camera video of (*cis*)(dioxane) photo-carving 15 mW 532 nm irradiation.

Video 6. High-speed camera video of (*cis*)(dioxane) photo-carving 10 mW 532 nm irradiation.

Video 7. High-speed camera video of (*cis*)(dioxane) photo-carving 5 mW 532 nm irradiation.

3.7.6 References

1. Bruker, APEX3, Bruker AXS Inc., Madison, Wisconsin, USA, 2012.

2. Krause, L., Herbst-Irmer, R., Sheldrick, G. M. & Stalke, D. Comparison of Silver and Molybdenum Microfocus X-ray Sources for Single-crystal Structure Determination. *J. Appl. Cryst.* **48**, 3–10 (2015).

3. Sheldrick, G. M. SHELXT - Integrated Space-Group and Crystal-Structure Determination. *Acta Cryst.* **A71**, 3–8 (2015).

4. Sheldrick, G. M. Crystal Structure Refinement with SHELXL. *Acta Cryst.* **C71**, 3–8 (2015).

5. Dolomanov, O. V., Bourhis, L. J., Gildea, R. J., Howard, J. A. K. & Puschmann, H. OLEX2: A Complete Structure Solution, Refinement and Analysis Program. *J. Appl. Cryst.* **42**, 339–341 (2009).

6. Farrugia, L. J. WinGX and ORTEP for Windows: an Update. *J. Appl. Cryst.* **45**, 849–854 (2012).

7. C. F. Macrae *et al*. Mercury 4.0: from Visualization to Analysis, Design and Prediction. *J. Appl. Cryst.*, **53**, 226–235 (2020).

8. Persistence of Vision Pty. Ltd., Persistence of Vision Raytracer, Persistence of Vision Pty. Ltd., Williamstown, Victoria, Australia, (2018).

Rationale for Chapter 4

In the previous two Chapters 2 and 3, the new phenomenon of 'Cold Photo-carving' (CPC) was described in detail with a series of azo dye and volatile conformer co-crystals. This CPC technique demonstrated dye-volatile co-crystals that could be readily cut, carved, or machined with micrometer precession using low-intensity visible light. This Chapter 4 builds upon these photo-carving and photo-mechanical effects by expanding CPC to a new class of co-crystals, combining two distinct chromophores into a photo-responsive co-crystal. We report here the successful synthesis and investigation of the photo-responsive behaviour of materials based on a co-crystallization of a *trans* azo dye as halogen bonding donor, with both a deeply coloured aromatic conformer azulene, and also its structural yet colourless isomer naphthalene, as halogen bonding acceptors. These azulene co-crystals displayed two separate responses upon irradiation with low-powered green visible, and high-powered infrared (IR) light, both CPC similar to previously described co-crystals in Chapters 2 and 3, but, when irradiated by a high-powered IR laser source, these azulene co-crystals also displayed a re-formation at the spot of irradiation, with the growth of a new crystalline phase. This provides a single material that can produce two distinct photo-responses, selected by the wavelength of irradiation to target either of the 2 dye coformers separately.

Chapter 4 is being prepared as a manuscript for submission, after this Thesis submission. Citation: Borchers, T. H., Vainauskas, J., Titi, H. M., Barrett, C. J., & Friščić., T. "Multi-Component Crystals with Wavelength-Dependent Mechanical Response to Visible and Infrared Light" manuscript in preparation (2022).

Multi-Component Crystals with Wavelength-Dependent Mechanical Response to Visible and Infrared Light

T. H. Borchers, J. Vainauskas, H. M. Titi, C. J. Barrett, and T. Friščić**

Department of Chemistry, McGill University, Montreal, QC, Canada

4.1 Abstract

'Cold Photo-carving' (CPC) is a phenomenon recently observed in azobenzene co-crystals, in which a new material is synthesized through co-crystallization of a chromophore (dye) with a volatile co-crystal former. The resulting dye-volatile co-crystals are found to be readily cut, carved, or punctured with micrometer precession using low-intensity visible light, providing a unique opportunity to design materials that are inherently machinable. This Chapter outlines the synthesis and investigation of the behaviour of materials based on a related design, involving co-crystallization of two distinct chromophores into a photo-responsive co-crystal. Specifically, the herein described materials are based on co-crystallization of an azo dye (*trans*-azo) with a deeply coloured aromatic component (azulene). The co-crystals are found to exhibit two separate responses upon irradiation with low-powered green and high-powered infrared (IR) light. Co-crystals of azulene and *trans*-azo will undergo CPC when irradiated by a green laser but, when irradiated by a high-powered IR laser source, these co-crystals undergo a large change in the surface at the spot of irradiation, including the growth of a new crystalline phase. These effects appear dependent on the wavelength of radiation, and therefore these multi-chromophore co-crystals act as a material that can selectively display either of two separate responses triggered simply by the wavelength of the excitation laser.

4.2 Introduction

Molecules that exhibit light-responsive behaviour, also known as photo-switching, have been key to the development of advanced molecular materials[1] such as organic semiconductors,[2,3] energy transduction and storage materials,[4] as well as polymeric molecular machines.[5] Azobenzene-based (azo) dyes are a well-established class of molecular photo-switches that undergo photo-induced isomerization reversibly between a stable *trans*- and a metastable *cis*-form (**Figure 4.1a**). Typically, the *cis*-form will readily transform back to the *trans*-isomer either through photo-isomerization driven by visible light, or *via* thermal relaxation at room temperature.[6] Tailoring the functional groups on the azo unit allows for tuning of the optical properties of the molecules, and the resulting solid state materials,[7] including the *cis*→*trans* relaxation rate. A notable example of such behaviour is the introduction of fluorine substituents which provides sufficient stabilization for the *cis*-isomers to be isolated in the form of crystalline solids.[7] More broadly, the covalent modification of the azo moiety has led to optimizing the synthesis of a broad class of azobenzene-based dyes that have been developed into various functional materials applications, including as components of photo-responsive thin-films,[8,9] liquid crystals,[10] and crystalline solids.[11]

Designing crystalline solids is an effective way to produce materials that exhibit unique responses to light,[12–14] specifically when the molecular building blocks of the crystal contain a chromophore in either a single- or a multi-component crystal (a co-crystal).[16,17] Since the pioneering work of Etter,[18] co-crystallization has been recognized as a powerful crystal engineering method to control the molecular assembly of molecules, and is now central to the production of pharmaceuticals,[17–20] materials that undergo photo-dimerization reactions,[21–23] waveguides,[24] and for tuning of photo-luminescent properties.[25,26] The design of co-crystals relies on carefully combining supramolecular synthons,[27] and a good understanding of various

intermolecular interactions, including hydrogen-bonding, π-π stacking, and halogen bonding.[28] Halogen bonding (XB) occurs through polarization of a large halogen atom (I, Br, Cl) bonded to a highly-electron-withdrawing group, leading to the formation of an σ-hole; an area of positive potential on the halogen atom opposite the σ-bond.[29] These polarized atoms can now form XBs with heteroatoms (N, O, S, F) which possess concentrated electron density, held together by the electrostatic interactions between the halogen atom as the XB donor, and the heteroatom as the XB acceptor.[29–31] The highly directional nature of the XB supramolecular interactions has been exploited in the formation of azobenzene-based co-crystals as a way to control various optical properties of the crystals, as well as the photo-mechanical properties.[15,32,33] Halogen bonds to π-systems of arene molecules have also been explored,[33,35] yet are considered to be weaker in interaction compared to traditional XBs with heteroatoms as acceptors.[36]

Recent studies (Chapters 2 and 3) reported halogen bonding co-crystals that can be cut, carved, or punctured with low-powered visible light. Such behaviour was termed 'cold photo-carving' (CPC) due to the low power (non-heating, room Temperature) laser light able to produce such cutting or surface patterning.[37] The CPC phenomenon is enabled through the co-crystal design of a light-absorbing dye and a volatile co-crystal former (coformer),[28] and it is speculated that the geometric isomerization of the azo dye is key to photo-carving.

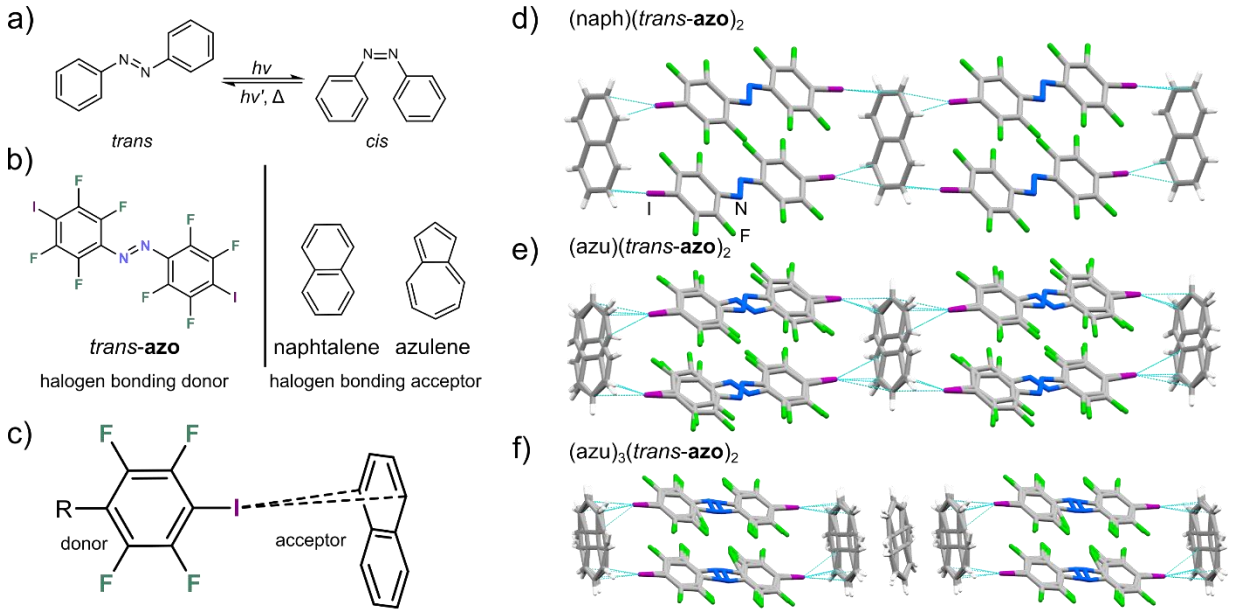

Figure 4.1. Schematic representation of molecules used in this study: a) schematic of azo isomerization, **b)** molecular structures, and **c)** a general I···π bonding motif. Linear (Step-ladder motif) arrangements of supramolecular chains of the co-crystals studied: **d)** (naph)(*trans*-azo)$_2$, **e)** (azu)(*trans*-azo)$_2$, **f)** (azu)$_3$(*trans*-azo)$_2$.

This Chapter investigates the behaviour of photo-responsive co-crystals combining two distinctly absorbing chromophores: an azobenzene dye (*trans*-4,4'-diiodooctafluoroazobenzene, *trans*-azo, **Figure 4.1b**) and a second volatile chromophore azulene (azu, **Figure 4.1b**), a strongly-coloured dark blue dye. Co-crystallization of azu and *trans*-azo leads to two distinct co-crystals with different compositions (stoichiomorphs): (azu)$_3$(*trans*-azo)$_2$ and (azu)(*trans*-azo)$_2$ (**Figure 4.1d,e**). These previously reported co-crystals form through a step-ladder motif, held together by unique I···π halogen bonds (**Figure 4.1c**). The shortest I···C contact distances of each stiochomorph were found to be 3.245 Å and 3.543 Å for (azu)$_3$(*trans*-azo)$_2$, while (azu)(*trans*-azo)$_2$ had contact distances of 3.323 Å and 3.378 Å.[38] Both co-crystals exhibit strong pleochromism under polarized light, changing colour from red to blue (**Figure 2b**) upon rotation with respect to the polarization

of the light source. The pleochroic behaviour is a result of the crystal structures of both materials, exhibiting mutually orthogonal alignment of the transition dipole moments of the two molecules (**Figure 2a**).

The *trans*-azo dye was also co-crystallized with naphthalene (naph) (**Supplementary Figure 4.1**), which is a structural isomer of azulene, yet colourless, non-absorbing at the visible and IR wavelengths used to address the azu. This co-crystallization results in the (naph)(*trans*-azo)$_2$ co-crystal, containing naph and *trans*-azo in a respective 1:2 stoichiometric ratio.[38] The (naph)(*trans*-azo)$_2$ co-crystal is isostructural to the (azu)(*trans*-azo)$_2$ co-crystal (**Figure 4.1d,e**), and the underlying crystal structure exhibits similar I···π contact distances to those found in azulene co-crystals, with lengths of 3.366(7) Å, and 3.343(7) Å. Despite several attempts, a co-crystal of (naph)$_3$(*trans*-azo)$_2$ composition, which would be analogous to the known co-crystal (azu)$_3$(*trans*-azo)$_2$, has never been observed (**Supplementary Figure 4.2**). Instead, the powder X-ray diffraction (PXRD) patterns of the resulting materials indicated only the presence of crystalline (naph)(*trans*-azo)$_2$ co-crystal and solid naph. However, mixing varying proportions of naphthalene and azulene successfully formed solid solutions in a 3:2 stoichiometry; ((naph)(azu)$_2$(*trans*-azo)$_2$, (naph)$_2$(azu)(*trans*-azo)$_2$) (**Supplementary Figure 4.3**). However, when using equivalent amounts of azulene and naphthalene (1:1), the PXRD pattern of the resulting material revealed X-ray diffraction signals that are interpreted as a combination of (naph)(azu)$_2$(*trans*-azo)$_2$ and (naph)$_2$(azu)(*trans*-azo)$_2$, suggesting that some distinctive order may exist in the solid solutions. Unlike azu, solid naph appears colourless, yet the (naph)(*trans*-azo)$_2$ co-crystal retains strong dichroism under polarized light ranging from red to transparent (**Figure 4.2C**). As naphthalene has near-zero absorbance in the visible region, it was used it as a control throughout this study, as we expected low frequency (red/IR) light to have no effect on the molecule.

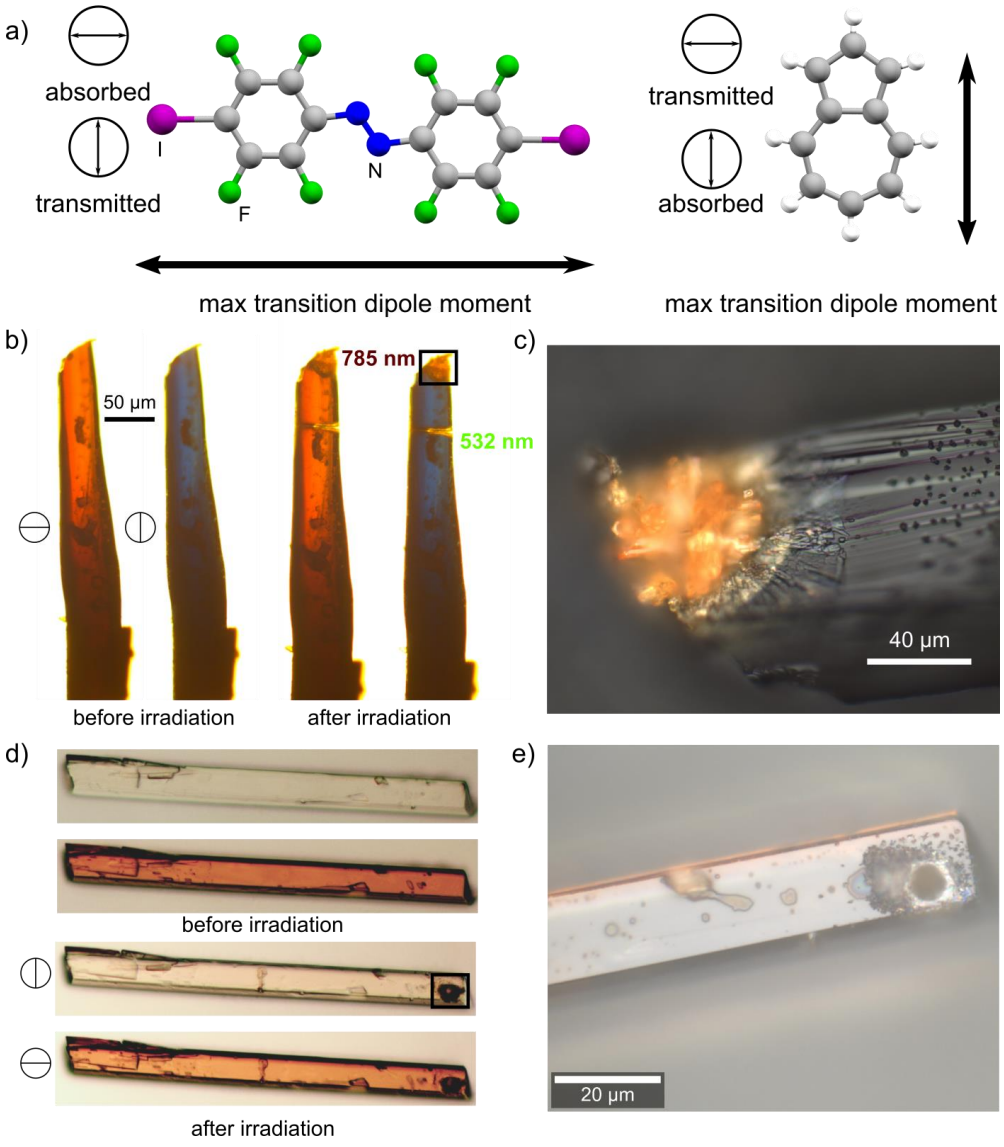

Figure 4.2. Photo and optical response of co-crystals studied. a) Schematic representation of a *trans*-azo and an azulene molecule, with the direction of the maximum transition dipole moments shown for both molecules. **b)** Optical images of a (azu)(*trans*-azo)$_2$ crystal under polarized light before and after irradiation with 532 nm and 785 nm lasers. **c)** Optical microscopy image of the surface of a (azu)(*trans*-azo)$_2$ co-crystal following irradiation with a 785 nm laser. **d)** Optical microscopy images of (naph)(*trans*-azo)$_2$ under polarized light before and after irradiation with a 532 nm laser. **e)** Example of CPC successfully performed on a (naph)(*trans*-azo)$_2$ co-crystal.

4.3 Results and Discussion

4.3.1 CPC of (azu)$_3$(*trans*-azo)$_2$ and (azu)(*trans*-azo)$_2$ co-crystals

Upon irradiation with low-power green light (532 nm, ≈ 0.5 mW), single crystals of (azu)(*trans*-azo)$_2$ were found to undergo CPC (**Figure 4.2b**). Clean lines can be seen cut into the crystals, with the edges of the cuts undergoing a large optical colour change (blue to orange/red), suggesting evaporation of azu and recrystallization of *trans*-azo near the rea of the surface being irradiated. Similar CPC behaviour is observed on the surfaces of the isostructural (naph)(*trans*-azo)$_2$ co-crystals when irradiated with a 532 nm laser of 0.5 mW power (**Figure 4.2d,e**). Lines or holes can be seen on the crystals at the areas of irradiation, indicating that the two co-crystals ((azu)(*trans*-azo)$_2$, and (naph)(*trans*-azo)$_2$) exhibit identical behaviour upon irradiation by green light. Next, we studied the response of the isostructural crystals to light of lower frequency. Specifically, upon irradiation by low-powered infrared (IR, 785 nm) light, the co-crystal (azu)(*trans*-azo)$_2$ did not exhibit any surface modification. However, increasing the power of the IR laser to > 20 mW led to the appearance of changes on the co-crystal surface. The surface disruption induced by IR laser appears different to that achieved upon irradiation by green laser. Rather than clean cuts and holes in the crystal, yellow/orange single crystals were observed to grow from the location of irradiation (**Figure 4.2b,c**). The (naph)(*trans*-azo)$_2$ co-crystals were irradiated under identical conditions and showed no response to the IR laser light, even when irradiated by a 785 nm IR laser at maximum power (70 mW). These findings indicate that the photo-response to irradiation by IR light directly relates to the absorbance profile of the azu and not the naph co-crystal components.

Next we explored the photo-responsive nature of the second stoichiomorph, $(azu)_3(trans\text{-}azo)_2$, by irradiating polycrystalline samples using a green 532 nm laser. The resultant polycrystalline powder was removed at the point of irradiation, allowing for detailed lines to be drawn into a polycrystalline sample (**Supplementary Figure 4.4**). Similar to the single crystal studies, the area in the vicinity of the laser irradiation showed a large change in colour, from dark blue to bright orange. Optical microscopy, however, could not be performed with sufficient resolution to observe any other differences between the resulting crystallites. However, using the higher power 785 nm IR laser line, the resulting powder was observed to produce micrometer-sized yellow/red crystallites growing from the surface (**Supplementary Figure 4.5**).

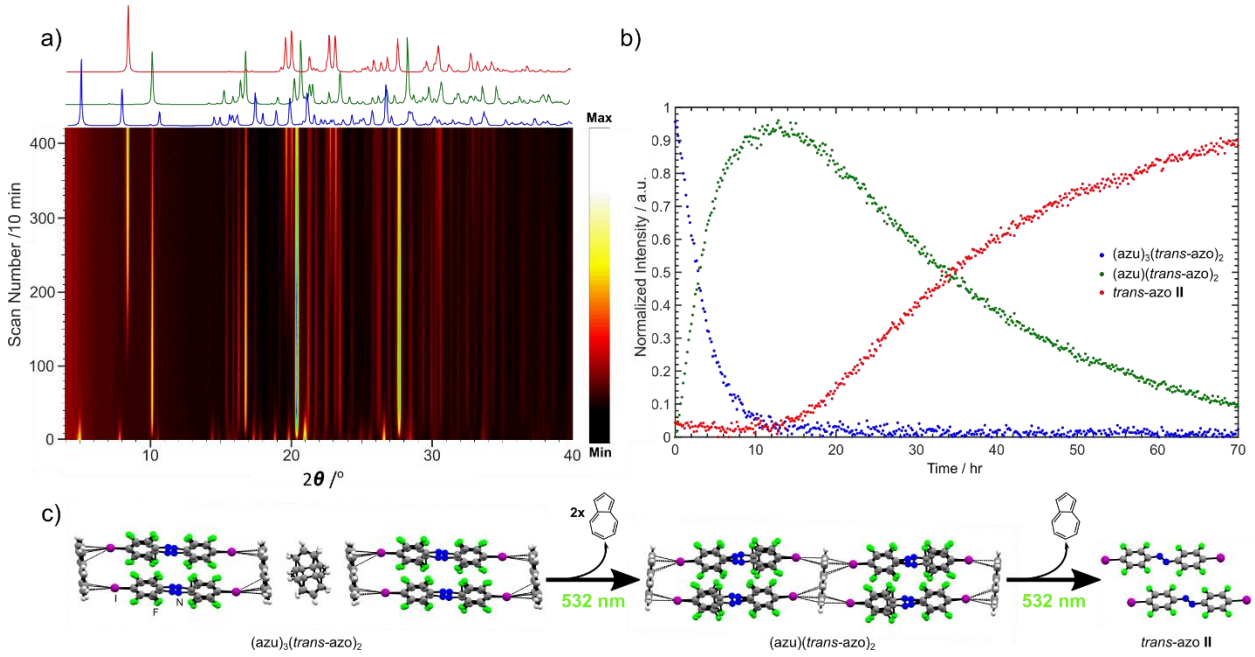

Figure 4.3. Time-resolved monitoring of $(azu)_3(trans\text{-}azo)_2$ under continuous irradiation by a 532 nm LED. a) Time-resolved *in situ* powder X-ray diffractogram. **b)** Normalized intensity of various components. **c)** The proposed mechanism of light-induced transformation of $(azu)_3(trans\text{-}azo)_2$ to $(azu)(trans\text{-}azo)_2$, and finally to *trans*-azo **II**.

The photo-stability and mechanism of the photo-evaporation of the two azulene co-crystals was studied by time-resolved PXRD monitoring of (azu)$_3$(*trans*-azo)$_2$ under constant irradiation by a LED of 37 mW·cm^{-2} intensity and 532 nm wavelength (**Figure 4.3**). The (azu)$_3$(*trans*-azo)$_2$ co-crystal was found to rapidly convert into (azu)(*trans*-azo)$_2$, with full conversion occurring within 10 hours of irradiation. The (azu)(*trans*-azo)$_2$ co-crystal eventually converted to the kinetically favoured *trans*-azo polymorph (*trans*-azo **II**). Such conversion however, took significantly longer, and trace amounts of (azu)(*trans*-azo)$_2$ could be detected in the powder X-ray diffraction pattern even after 70 hours of irradiation. Based on these results, the (azu)(*trans*-azo)$_2$ appears to be the more photo-stable co-crystal. These observations can be rationalized through the molecular packing in the co-crystal structure, as for every azulene unit in (azu)(*trans*-azo)$_2$ there are four halogen bonds to neighbouring XB donors. In contrast, the structure of the second stoichiomorph, (azu)$_3$(*trans*-azo)$_2$, exhibits two azulene molecules that are symmetrically equivalent, each participating in two halogen bonds, as well as a third azulene molecule that is not engaging in any I···π halogen-bonding contacts. The comparison between the two co-crystal structures suggests that the observed instability of (azu)$_3$(*trans*-azo)$_2$ is related to the overall smaller number of halogen bonds to azulene molecules. In addition, the polycrystalline powder optically changed throughout the experiment progression. The powder colour changed from dark blue to green and, ultimately, to a yellow-orange powder, consistent with the experimentally measured bandgaps (**See Supplementary Information**).

To test if the photo-responsive behaviour of (azu)$_3$(*trans*-azo)$_2$ is dependent on the wavelength of light, another polycrystalline sample of (azu)$_3$(*trans*-azo)$_2$ was irradiated with a 633 nm 37 mW·cm^{-2} LED and the process was continuously monitored by PXRD (**Supplementary Figure 4.6**). Analysis of the observed changes in the PXRD pattern of the irradiated material

revealed that the complete conversion of $(azu)_3$(*trans*-azo)$_2$ to the (azu)(*trans*-azo)$_2$ co-crystal took over 20 hours, and after a period of 65 hours the X-ray reflections corresponding to (azu)(*trans*-azo)$_2$ remained dominant in the powder X-ray diffractogram. Despite the 532 and 633 nm LEDs operating at the same power levels, these results indicate that irradiation with the 532 nm LED converts the starting co-crystal to the final photo-product more quickly, suggesting that green light is more effective as a tool for CPC. Additionally, as a control $(azu)_3$(*trans*-azo)$_2$ was monitored by PXRD over a period of 24 hours under no irradiation (**Supplementary Figures 4.7, 4.8**). While conversion of $(azu)_3$(*trans*-azo)$_2$ to (azu)(*trans*-azo)$_2$ was observable in this case also, the conversion is minor in comparison to that of the samples irradiated by either the 532 nm or 633 nm LED.

Thermal analysis of the $(azu)_3$(*trans*-azo)$_2$ co-crystal was performed *via* variable temperature PXRD (VT-PXRD) ranging from 25–150 ^{0}C (**Supplementary Figure 4.9**) and showed a conversion similar to that observed in the photo-irradiation studies, in which the $(azu)_3$(*trans*-azo)$_2$ was found to convert to the (azu)(*trans*-azo)$_2$ co-crystal, with full conversion occurring at ca. 65 ^{0}C. The resulting co-crystal appears stable until ca. 90 ^{0}C, when new X-ray reflections appeared that were consistent with the formation of crystalline *trans*-azo **II**. In contrast to the photo-irradiation studies, thermal analysis revealed an additional process in which *trans*-azo **II** converts to *trans*-azo **I**, with the polymorphic transition occurring between 115–135 ^{0}C. The temperature observed to be required for the polymorphic conversion and the lack of *trans*-azo **I** observed in the resultant photo-studies are consistent with CPC being a low temperature phenomenon. Differential scanning calorimetry (DSC) and thermogravometric analysis (TGA) were used to confirm the stoichiomorphic and polymorphic transitions occurring throughout the study (**Supplementary Figure 4.10**). The DSC traces consisted of three distinct endothermic

events at 74 ^{0}C, 110 ^{0}C, and 141 ^{0}C. The first event was identified as the transition from (azu)$_3$(*trans*-azo)$_2$ to (azu)(*trans*-azo)$_2$ with the additional formation of amorphous azulene. The temperature of the second endotherm is consistent with the transition from (azu)(*trans*-azo)$_2$ to *trans*-azo **II**, while the final endotherm at 141 ^{0}C is in agreement with the TGA results showing a mass loss of 24.5% (theoretical expectation 24.6 % of 3 parts azulene) occurring between 125–175 ^{0}C. Although several transitions were observed, the evaporation of the azulene appeared to occur through a single step rather than in multiple steps. The TGA observations suggest that the transition from (azu)$_3$(*trans*-azo)$_2$ to (azu)(*trans*-azo)$_2$, or from (azu)(*trans*-azo)$_2$ co-crystal to pure solid *trans*-azo **II**, occurs with the appearance of additional azulene in amorphous form, which is in agreement with the endothermic events observed in the DSC.

4.3.2 CPC of (naph)(*trans*-azo)$_2$ co-crystals

Photo-stability of the (naph)(*trans*-azo)$_2$ was studied *via* continuous irradiation of a polycrystalline sample of (naph)(*trans*-azo)$_2$ by a 532 nm 37 mW·cm^{-2} LED, and the monitoring occurred *via* PXRD in the same fashion as for the azulene co-crystals (**Supplementary Figure 4.11**). Similar to (azu)(*trans*-azo)$_2$, a conversion to *trans*-azo **II** was observed. The conversion begins steadily and an increase of *trans*-azo **II** reflections is observed rapidly with 50% of the polymorph forming after 17 hours. The rate steadily slows down and near conversion is reached after 90 hours of irradiation. The slowing in rate could be explained by the thickness of the sample, as the upper surface of the sample converted first and the sample near the far side required longer to convert. No additional species were seen in the X-ray powder diffractogram.

Analysis by VT-PXRD of the (naph)(*trans*-azo)$_2$ crystals showed the same solid form transformation pathway as for the photo-irradiated sample (**Supplementary Figure 4.12**). The (naph)(*trans*-azo)$_2$ co-crystal begins to convert to the solid *trans*-azo **II** at 80 ^{0}C, and the resulting

crystalline phase underwent an additional transition with new Bragg reflections assigned to *trans*-azo **I** beginning at 95 ^{0}C. While the thermodynamically favourable *trans*-azo **I** polymorph is not visible when irradiation is conducted using a low-powered LED ($mW \cdot cm^{-2}$), it is present when the sample is heated, again suggesting that CPC is a low temperature phenomenon. Analysis by thermal methods, specifically by DSC and TGA measurements on the same sample, showed agreement with the VT-PXRD (**Supplementary Figure 4.13**). The DSC thermogram exhibited two distinct endothermic events at 117 ^{0}C and 192 ^{0}C. The first event was also found to be associated with a mass loss of ca. 10.5 %, as established by TGA, and was interpreted as the loss of naph (theoretically calculated content of naph is ca. 10 %). The second endotherm was interpreted as the melting of *trans*-azo **I**.

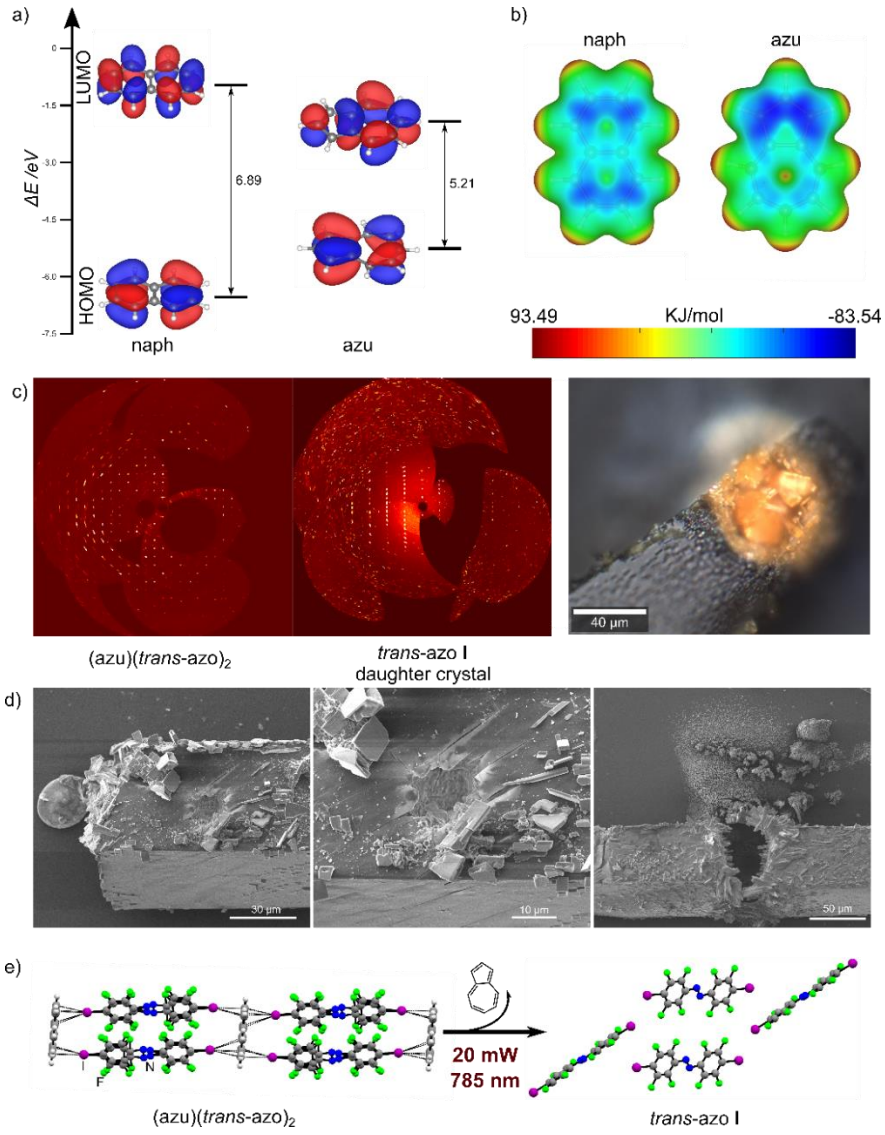

Figure 4.4. Irradiation of the (azu)(*trans*-azo)$_2$ with IR light. a) Calculated molecular orbitals of naph and azu, highlighting the respective HOMO-LUMO gap in the gas phase. **b)** Calculated electrostatic potential maps of naphthalene and azulene. **c)** Precession X-ray images (left to right) for a single crystal of (azu)(*trans*-azo)$_2$ prior to irradiation by IR light, and for a resulting daughter crystal after irradiation of IR light. **d)** Optical image of a (azu)(*trans*-azo)$_2$ crystal after irradiation with a 785 nm IR laser. **e)** SEM images of an (azu)(*trans*-azo)$_2$ co-crystal after 785 nm IR irradiation. **f)** Schematic representation of the light-driven transformation of (azu)(*trans*-azo)$_2$ to *trans*-azo **I**.

4.3.3 Response of (azu)(*trans*-azo)$_2$ and (naph)(*trans*-azo)$_2$ co-crystals to IR irradiation

As previously noted, exposure of a single crystal of (azu)(*trans*-azo)$_2$ to IR light leads to the appearance of X-ray diffraction-quality yellow-orange crystals growing from the surface of the irradiated area of the crystal (**Figure 4.4 d-e)**. One of such resulting crystals was carefully removed and diffraction spectra collected using a single crystal X-ray diffractometer (**Figure 4.4c, Supplementary Figure 4.14**). The crystal structure was solved in a $P2_1/n$ space group, in which *trans*-azo molecules arrange in a herringbone fashion. The structure was assigned as the previously reported thermodynamically favourable polymorph *trans*-azo **I**, rather than the kinetic polymorph *trans*-azo **II** which is the photo-product in previously reported co-crystals that undergo CPC. The discrepancies between the photo-product upon IR irradiation and green light irradiation, is potentially due to the IR laser being operated at a higher power then the green laser. The high-powered laser would induce more heat on the surface of crystal, and therefore cause the crystallization of the higher temperature polymorph *trans*-azo **I**. As for the mechanism of the evaporation of azulene and recrystallization to *trans*-azo **I**, we suggest that the high-powered IR laser has a larger beam width than the low-powered green laser, therefore causing the evaporation of a larger amount of azu. The removal of larger quantities of azu also makes available a larger amount of *trans*-azo for crystallization into *trans*-azo **I** crystals that can now grow to sizes of tens of microns, as observed by scanning electron microscopy (**Figure 4.4e**, **Supplementary Figure 4.15**).

In contrast to the (azu)(*trans*-azo)$_2$ co-crystals, irradiation by IR light appeared to have no effect on the co-crystals of (naph)(*trans*-azo)$_2$. We speculate that this is directly due to the electronic structure differences of azulene compared to naphthalene, which could be related to different absorbance profiles of the two molecules. The gas phase HOMO-LUMO energy gaps of

the individual molecules were calculated using the program package Gaussian16,[39] using PBEO functionals at a cc-pvtz level of theory.[41,42] Azulene had a lower calculated energy gap (**Figure 4.4a**) than its structural isomer naphthalene (5.21 eV to 6.89 eV respectively). This difference is proposed to be due to the strong electronic polarization of the azulene molecule, compared to the naphthalene molecule (**Figure 4.4b**). Optical properties of the three separate co-crystals were also studied by solution UV-Vis absorbance spectroscopy (**Supplementary Figure 4.16**) and solid state UV-Vis reflection spectroscopy (**Supplementary Figure 4.17-4.18**). In the solution studies, the three co-crystals were prepared prior to desolvation in THF through mechano-chemical methods. All three co-crystals exhibited major absorbance bands in the UV region between 200–400 nm, and minor bands in the visible region ranging from 400 nm to 800 nm. The co-crystal (naph)(*trans*-azo)$_2$ displayed a minor absorbance band located in the 400–600 nm range, which was assigned to the n-π^* transitions associated with the azo molecule. The two azulene co-crystals exhibited significantly wider bands in the visible region, ranging from 400–750 nm, and from 400–800 nm, for the (azu)(*trans*-azo)$_2$ and (azu)$_3$(*trans*-azo)$_2$ co-crystals, respectively. The increased broadness of the bands in comparison to the naphthalene co-crystal is due to the azulene bandgap. In addition, the absorbance band was found to trail off at the laser line wavelength of 785 nm, suggesting that azulene molecules absorb the IR laser while naphthalene molecules don not. Solid state reflectance measurements were acquired to calculate band-gaps within the solids *via* tauc plots, where the 3 co-crystals and their individual components were measured. The measured bandgaps for the individual components were found to be 3.55 eV, 1.57 eV, and 1.89 eV for naphthalene, azulene, and *trans*-azo respectively. The co-crystals all exhibited red-shifted bandgap values compared to those of the individual components, notably 1.63 eV, 1.39 eV, and 1.31 eV, for (naph)(*trans*-azo)$_2$, (azu)$_3$(*trans*-azo)$_2$, and (azu)(*trans*-azo)$_2$ respectively. Both azulene co-

crystals were found to have a smaller bandgap than the naphthalene co-crystals, and fall within the wavelength of the IR laser (785 nm, 891 nm, and 946 nm for $(azu)_3(trans\text{-}azo)_2$, and $(azu)(trans\text{-}azo)_2$ respectively). The bandgap of the $(naph)(trans\text{-}azo)_2$ co-crystal appeared slightly higher in energy at 760 nm. As the bandgaps of the two azulene co-crystals are within excitation of the IR laser (785 nm), the solid would be expected to absorb the laser light, and produce heat. The naphthalene co-crystal bandgap is higher in energy than the IR laser, and therefore would not be expected to produce the same heat as would the azulene co-crystals. This could explain why we see the photo-response to IR light with the azulene co-crystals and not with the naphthalene co-crystals.

4.4 Conclusions

Here we have further investigated the process of CPC, by studying the photo-responsive properties of three new co-crystals; $(azu)_3(trans\text{-}azo)_2$, $(azu)(trans\text{-}azo)_2$, and $(naph)(trans\text{-}azo)_2$. All three co-crystals exhibited successful CPC properties when irradiated with low power green light, yet the two azulene crystals also exhibited a second photo-response to a high-powered IR irradiation. We speculate that this is due to the stronger absorption of the azulene co-crystals compared to the naphthalene co-crystal. The second photo-response differed greatly from CPC; while CPC can be used to cut detailed patterns into the crystal with micrometer precision, the response to IR light by the azulene co-crystals led to a much larger surface change in which micron size diffraction quality single crystals was seen growing from the surface of the mother crystal. The second response also produced a different photo-product, with the resultant crystals being characterized as *trans*-azo **I** rather than the kinetic polymorph *trans*-azo **II** seen in traditional CPC. This leads to a material that

follows two separate transformation pathways, allowing control over the co-crystal surface properties simply by varying the excitation laser wavelength. This work provides a better understanding of the low heat requirements of CPC and introduces a new form of photo-carving with higher powered laser light.

4.5 Materials and Methods

4.5.1 Synthesis

Trans-azo was synthesized in one step by treatment of 4-iodo-2,3,5,6-tetrafluoroaniline with *N*-chlorosuccinimide (NCS) and 1,8-diazabicyclo[5.4.0]undec-7-ene (DBU).[42] All reagents and solvents were purchased from Sigma Aldrich. Co-crystallization of (azu)(*trans*-azo)$_2$, (azu)$_3$(*trans*-azo)$_2$, and (naph)(*trans*-azo)$_2$ were all prepared mechano-chemically at a 50 mg scale using 5 mL stainless steel jars with a 2 mg ball. In a typical experiment the reactants would be placed in the jar at the appropriate molar ratio with the addition of 10 µl of nitromethane, and the resultant mixture would be milled for 15 mins at 30 Hz using a Retsch MM 400 mixer mill. If the objective was to grow single crystals of the material then the resultant mixtures would be recrystallized through slow evaporation in hexanes.

4.5.2 Powder X-ray diffraction

Powder X-ray diffraction experiments were performed on a Bruker D8 Advance diffractometer, using a Cu*K*α radiation (λ = 1.54184 Å) source operating at 40 mA and 40 kV, equipped with a Lynxeye XE linear position-sensitive detector, in the 2θ range of 4–40° with step size of 0.019° or, alternatively, on a Bruker D2 Phaser diffractometer using nickel-filtered Cu*K*α radiation (λ =

1.54184 Å) source operating at 10 mA and 30 kV, equipped with a Lynxeye linear position-sensitive detector, in the 2θ-range of 4–40°.

4.5.3 Single-crystal X-ray diffraction

Data for (naph)(*trans*-azo)$_2$, were collected on a Bruker D8 Venture dual-source diffractometer equipped with a PHOTON II detector and an Oxford Cryostream 800 cooling system, using mirror-monochromated Mo*K*α ($\lambda = 0.71073$ Å) or Cu*K*α radiation ($\lambda = 1.54184$ Å) from respective microfocus sources. Data were collected in a series of φ- and ω-scans. APEX3 software was used for data collection, integration, and reduction.[43] Numerical absorption corrections were applied using SADABS-2016/2.[44] Structures were solved by dual-space iterative methods using SHELXT[45] and refined by full-matrix least-squares on F^2 using all data with SHELXL[46] within the OLEX2[47] and/or WinGX[48] environment.

4.5.4 Thermal analysis

Thermogravimetric analysis (TGA) and differential scanning calorimetry (DSC) measurements were performed simultaneously using a Mettler-Toledo TGA/DSC 1 Star system thermobalance. The samples were placed in alumina crucibles and measurements conducted under a stream of nitrogen (50 cm^3 min^{-1}) gas, at a heating rate of 5 C° min^{-1}. Data collection and analysis were performed using the Mettler-Toledo STAR^e Software 16.20 program package. Alternatively, DSC measurements were performed on a TA Instruments LTD DSC2500 at a heating rate of 1 C° min^{-1}, under a stream of nitrogen (50 cm^3 min^{-1}) gas, using a hermetically closed aluminum pan.

4.5.5 Scanning electron microscopy

Single crystals of (azu)(*trans*-azo)$_2$ were sputter-coated with Pt, and placed into an FEI Helios Nanolab 660 DualBeam (Focused Ion Beam-Extreme High-Resolution Scanning Electron Microscope) for imaging.

4.5.6 General microscopy

Assessment of crystals, for example for dichroism observation and sample selection for machining or diffraction experiments, was performed using a Nikon SMZ1500 stereomicroscope with zoom capabilities (from 0.75× to 11×). The microscope was equipped with a Omax A35140U camera, and Toupview acquisition software was used.

4.5.7 Detailed machining procedure

Using a confocal Raman Witec 300 R 532 nm and 785 nm solid state lasers with a range of power settings (0.1–20 mW, 532 nm and 0.1–70 mW 785 nm), and multiple objectives (10, 20, 50, and 100× Zeiss objectives with NA = 0.25, 0.5, 0.8, and 0.9, respectively), a series of photo-experiments are undertaken.

4.5.8 UV-Vis absorbance spectroscopy

Absorbance measurements were collected on an Agilent Cary 300 Bio UV-Visible spectrometer. A 55 mg/L solution was prepared from dissolving one of the three co-crystals; (azu)(*trans*-azo)$_2$, (azu)$_3$(*trans*-azo)$_2$, and (naph)(*trans*-azo)$_2$ in acetonitrile. The absorbance spectrum was acquired using instrument default conditions.

4.5.9 Raman spectroscopy

Raman microscopy experiments were performed on confocal Raman Witec 300 R microscope setup using two separate probe wavelengths of 785 nm and 532 nm. Integration time, number of accumulations and laser power were varied depending on experiment.

4.5.10 Gaussian calculations

Molecular orbitals and electrostatic potential maps (ESP) were calculated by DFT using Gaussian16,[39] with PBEO functionals[40] at a cc-pvtz[41] level of theory.

4.5.11 UV-Vis reflectance spectroscopy

% R *vs* wavelength spectra were acquired on a Lambda 750 UV/Vis/NIR spectrometer from Perkin-Elmer. $BaSO_4$ (ACS) was used as a standard for instrumental calibration (autozero corrections). Samples were filled into a 1 cm quartz cuvette. Full spectra were recorded in reflectance in the range of 2500–300 nm with 5 nm intervals and between 620–300 nm with 0.5 nm intervals.

4.6 References

1. Russew, M.-M. & Hecht, S. Photoswitches: From Molecules to Materials. *Adv. Mater.* **22**, 3348–3360, (2010).

2. Black, H. T. & Perepichka, D. F. Crystal Engineering of Dual Channel p/n Organic Semiconductors by Complementary Hydrogen Bonding. *Angew. Chem. Int. Ed.* **53**, 2138–2142, (2014).

3. Hamzehpoor, E. & Perepichka, D. F. Crystal Engineering of Room Temperature Phosphorescence in Organic Solids. *Angew. Chem. Int. Ed.* **59**, 9977–9981, (2020).

4. Ikeda, T. & Tsutsumi, O. Optical switching and image storage by means of azobenzene liquid-crystal films. *Science* **268**, 1873–1875 (1995).

5. Yamada, M., Kondo, M., Mamiya, J.-I., Yu, Y., Kinoshita, M., Barrett, C. J., Photomobile Polymer Materials: Towards Light-Driven Plastic Motors. *Angew. Chem. Int. Ed.* **47**, 4986-4988, (2008).

6. Zhao, Y. & Ikeda, T. *Smart light-responsive materials: azobenzene-containing polymers and liquid crystals*. (John Wiley & Sons, 2009).

7. Bléger, D., Schwarz, J., Brouwer, A. M. & Hecht, S. o-Fluoroazobenzenes as Readily Synthesized Photoswitches Offering Nearly Quantitative Two-Way Isomerization with Visible Light. *J. Am. Chem. Soc.* **134**, 20597–20600, (2012).

8. Yager, K. G. & Barrett, C. J. All-optical patterning of azo polymer films. *Current Opinion in Solid State and Materials Science* **5**, 487–494, (2001).

9. Tanchak, O. M. & Barrett, C. J. Light-Induced Reversible Volume Changes in Thin Films of Azo Polymers: The Photomechanical Effect. *Macromolecules* **38**, 10566–(2005).

10. Thum, M. D., Ratchford, D. C., Casalini, R., Wynne, J. H. & Lundin, J. G. Azobenzene-Doped Liquid Crystals in Electrospun Nanofibrous Mats for Photochemical Phase Control. *ACS Appl.ied Nano Mater.* **4**, 297–304, doi:10.1021/acsanm.0c02654 (2021).

11. Taniguchi, T., Asahi, T. & Koshima, H. Photomechanical Azobenzene Crystals. *Crystals* **9**, 437 (2019).

12. Naumov, P., Sahoo, S. C., Zakharov, B. A. & Boldyreva, E. V. Dynamic Single Crystals: Kinematic Analysis of Photoinduced Crystal Jumping (The Photosalient Effect). *Angew. Chem. Int. Ed.***52**, 9990–9995, (2013).

13. Tong, F., Kitagawa, D., Bushnak, I., Al-Kaysi, R. O. & Bardeen, C. J. Light-Powered Autonomous Flagella-Like Motion of Molecular Crystal Microwires. *Angew. Chem. Int. Ed.* **60**, 2414–2423, (2021).

14. Medishetty, R. Husain, A., Bai, Z., Runceveski, T., Dinnebier, R. E., Naumov, P., Vittal, J. J., Single Crystals Popping Under UV Light: A Photosalient Effect Triggered by a [2+2] Cycloaddition Reaction. *Angew. Chem. Int. Ed.* **53**, 5907–5911, (2014).

15. Bushuyev, O. S., Corkery, T. C., Barrett, C. J. & Friščić, T. Photo-mechanical azobenzene cocrystals and in situ X-ray diffraction monitoring of their optically-induced crystal-to-crystal isomerisation. *Chem. Sci.* **5**, 3158–3164, (2014).

16. Bushuyev, O. S., Tomberg, A., Friščić, T. & Barrett, C. J. Shaping Crystals with Light: Crystal-to-Crystal Isomerization and Photomechanical Effect in Fluorinated Azobenzenes. *J. Am. Chem. Soc.* **135**, 12556–12559, (2013).

17. Trask, A. V., Motherwell, W. D. S. & Jones, W. Pharmaceutical Cocrystallization: Engineering a Remedy for Caffeine Hydration. *Cryst. Growth & Des.* **5**, 1013–1021, (2005).

18. Huang, K. S., Britton, D., Etter, M., C., & Byrn, S. R. A Novel Class of Phenol-Pyridine Co-crystals for Second Harmonic Generation. *J. Mater. Chem.* **5**, 713-720, (1997).

19. Duggirala, N. K., Perry, M. L., Almarsson, Ö. & Zaworotko, M. J. Pharmaceutical cocrystals: along the path to improved medicines. *Chem. Commun.* **52**, 640–655, (2016).

20. Kavanagh, O. N., Croker, D. M., Walker, G. M. & Zaworotko, M. J. Pharmaceutical cocrystals: from serendipity to design to application. *Drug Discov. Today* **24**, 796–804, (2019).

21. Quentin, J., Reinheimer, E. W. & MacGillivray, L. R. Halogen-Bond Mediated [2+2] Photodimerizations: À la Carte Access to Unsymmetrical Cyclobutanes in the Solid State. *Molecules* **27**, 1048 (2022).

22. Sinnwell, M. A. & MacGillivray, L. R. Halogen-Bond-Templated [2+2] Photodimerization in the Solid State: Directed Synthesis and Rare Self-Inclusion of a Halogenated Product. *Angew. Chem. Int. Ed.* **55**, 3477–3480, (2016).

23. MacGillivray, L. R., Reid, J. L. & Ripmeester, J. A. Supramolecular Control of Reactivity in the Solid State Using Linear Molecular Templates. *J. Am. Chem. Soc.* **122**, 7817–7818, (2000).

24. Du, S., Ma, S., Xu, B. & Tian, W. Optical Waveguide and Photoluminescent Polarization in Organic Cocrystal Polymorphs. *J. Phys. Chem. Lett.* **12**, 9233–9238, (2021).

25. Salunke, J. K. Durandin, N. A., Rouko, T-P., Candeias, N. R., Vivo, P., Vuorimaa-Laukkanene, E., Laaksonen, T., & Priimagi, A. Halogen-Bond-Assisted Photoluminescence Modulation in Carbazole-Based Emitter. *Sci. Rep.* **8**, 14431, (2018).

26. Lu, B., Fang, X. & Yan, D. Luminescent Polymorphic Co-crystals: A Promising Way to the Diversity of Molecular Assembly, Fluorescence Polarization, and Optical Waveguide. *ACS Appl. Mater. Interfaces* **12**, 31940–31951, (2020).

27. Desiraju, G. R. Supramolecular Synthons in Crystal Engineering—A New Organic Synthesis. *Angew. Chem. Int. Ed.* **34**, 2311-2327, (1995).

28. Desiraju, G. R. Crystal Engineering: From Molecule to Crystal. *J. Am. Chem. Soc.* **135**, 9952–9967, (2013).

29. Cavallo, G. Metrangolo, P., Milani, R., Pilati, T., Priimagi, A., Resenati, G., & Terraneo, G. The Halogen Bond. *Chem. Rev.* **116**, 2478–2601, (2016).

30. Priimagi, A., Cavallo, G., Metrangolo, P. & Resnati, G. The Halogen Bond in the Design of Functional Supramolecular Materials: Recent Advances. *Acc.Chem. Res.* **46**, 2686–2695, (2013).

31. Saccone, M. & Catalano, L. Halogen Bonding beyond Crystals in Materials Science. *The J.Phys. Chem. B* **123**, 9281–9290, (2019).

32. Christopherson, J.-C., Potts, K. P., Bushuyev, O. S., Topić, F., Huskić, I., Rissanen, K., Barrett, C. J., & Friščić, T. Assembly and dichroism of a four-component halogen-bonded metal–organic cocrystal salt solvate involving dicyanoaurate(I) acceptors. *Faraday Discuss.* **203**, 441–457, (2017).

33. Bushuyev, O. S., Friščić, T. & Barrett, C. J. Controlling Dichroism of Molecular Crystals by Cocrystallization. *Cryst. Growth & Des.* **16**, 541–545, (2016).

34. d'Agostino, S., Grepioni, F., Braga, D. & Ventura, B. Tipping the Balance with the Aid of Stoichiometry: Room Temperature Phosphorescence versus Fluorescence in Organic Cocrystals. *Cryst. Growth Des.* **15**, 2039–2045, doi:10.1021/acs.cgd.5b00226 (2015).

35. Shen, Q. J. Pang, X., Zhao, X. R., & Gao, H. Y. Phosphorescent cocrystals constructed by 1,4-diiodotetrafluorobenzene and polyaromatic hydrocarbons based on C–I···π halogen bonding and other assisting weak interactions. *CrystEngComm* **14**, 5027–5034, (2012).

36. Forni, A., Pieraccini, S., Rendine, S., Gabas, F. & Sironi, M. Halogen-Bonding Interactions with π Systems: CCSD(T), MP2, and DFT Calculations. *ChemPhysChem* **13**, 4224–4234 (2012)

37. Borchers, T. H. Topić, F., Christopherson, J-C., Bushuyev, O. S., Vainauskas, J., Titi, H. M., Friščić, T., Barrett, C. J. Cold photo-carving of halogen-bonded co-crystals of a dye and a volatile co-former using visible light. *Nat. Chem.* **14**, 574–581, (2022).

38. Vainauskas, J., Topić, F., Bushuyev, O. S., Barrett, C. J. & Friščić, T. Halogen bonding to the azulene π-system: cocrystal design of pleochroism. *Chem. Commun*. **56**, 15145–15148, (2020).

39. Frisch, M. J. *et al*. Gaussian 16, Revision C.01, Gaussian, Inc., Wallingford, CT, 2016.

40. Adamo, C. Toward Reliable Density Functional Methods without Adjustable Parameters: The PBEO Model. J. *Chem. Phys*. **110**, 6158 (1999).

41. Dunning, T. H. Gaussian Basis Sets for use in Correlated Molecular Calculations. 1. The Atoms Boron Through Neon and Hydrogen. *J. Chem. Phys.* **90**, 1007, (1989).

42. Antoine, J. A. & Lin, Q. Synthesis of Azobenzenes Using N-Chlorosuccinimide and 1,8-Diazabicyclo[5.4.0]undec-7-ene (DBU). *J. Org. Chem.* **82**, 9873–9876 (2017).

43. Bruker, APEX3, Bruker AXS Inc., Madison, Wisconsin, USA, 2012.

44. Krause, L., Herbst-Irmer, R., Sheldrick, G. M. & Stalke, D. Comparison of Silver and Molybdenum Microfocus X-ray Sources for Single-crystal Structure Determination. *J. Appl. Cryst.* **48**, 3–10 (2015).

45. Sheldrick, G. M. SHELXT - Integrated Space-Group and Crystal-Structure Determination. *Acta Cryst.* **A71**, 3–8 (2015).

46. Sheldrick, G. M. Crystal Structure Refinement with SHELXL. *Acta Cryst.* **C71**, 3–8 (2015).

47. Dolomanov, O. V., Bourhis, L. J., Gildea, R. J., Howard, J. A. K. & Puschmann, H. OLEX2: A Complete Structure Solution, Refinement and Analysis Program. *J. Appl. Cryst.* **42**, 339–341 (2009).

48. Farrugia, L. J. WinGX and ORTEP for Windows: an Update. *J. Appl. Cryst.* **45**, 849–854 (2012).

4.7 Appendix 3: Supporting information for Chapter 4

4.7.1 Single crystal X-ray diffraction data

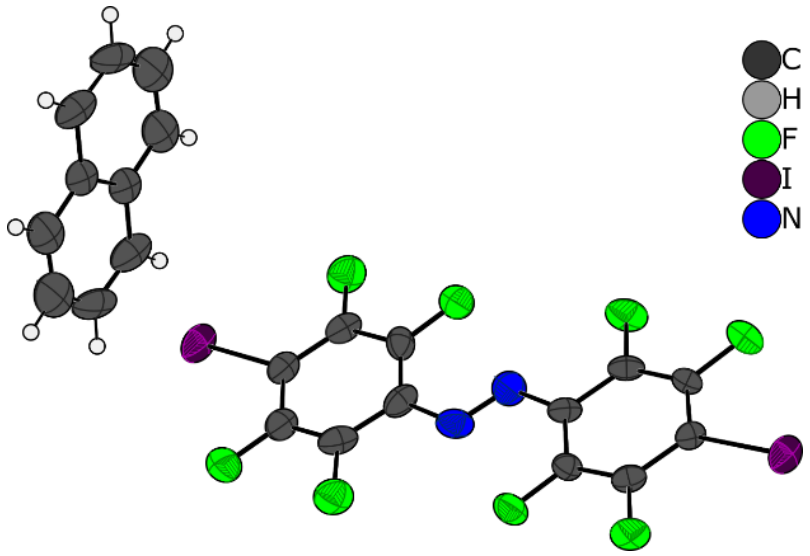

Supplementary Figure 4.1. ORTEP representation of (naph)(*trans*-azo)$_2$, showing ellipsoids at the 50% probability level.

Supplementary Table 4.1. Crystallographic data for the reported crystal structures of (naph)(*trans*-azo)$_2$.

Identification code	(naph)(azo)$_2$
Empirical formula	$C_{17}H_4F_8I_2N_2$
Formula weight	642.02
Temperature/K	273.15
Crystal system	triclinic
Space group	P-1
a/Å	5.98220(10)
b/Å	11.9530(2)
c/Å	12.9134(3)
α/°	90.1920(10)
β/°	98.7290(10)
γ/°	91.2400(10)
Volume/Å^3	912.45(3)
Z	2
ρ_{calc} g/cm^3	2.337
μ/mm^{-1}	27.894
F(000)	596.0
Crystal size/mm^3	0.040 × 0.005 × 0.005
Radiation	CuKα (λ = 1.54178)
2Θ range for data collection/°	6.926 to 144.958
Data completeness %	99.5
Index ranges	-7 ≤ h ≤ 7, -14 ≤ k ≤ 14, -15 ≤ l ≤ 15
Reflections collected	13528
Independent reflections	3601 [R_{int} = 0.0796, R_{sigma} = 0.0705]
Data/restraints/parameters	3601/0/263
Goodness-of-fit on F^2	1.043
Final R indexes [I>=2σ (I)]	R_1 = 0.0757, wR_2 = 0.1999
Final R indexes [all data]	R_1 = 0.0869, wR_2 = 0.2222
Largest diff. peak/hole / e Å^{-3}	2.80/-1.90

4.7.2 Powder X-ray Diffraction analysis of (naph)(*trans*-azo)$_2$ co-crystals

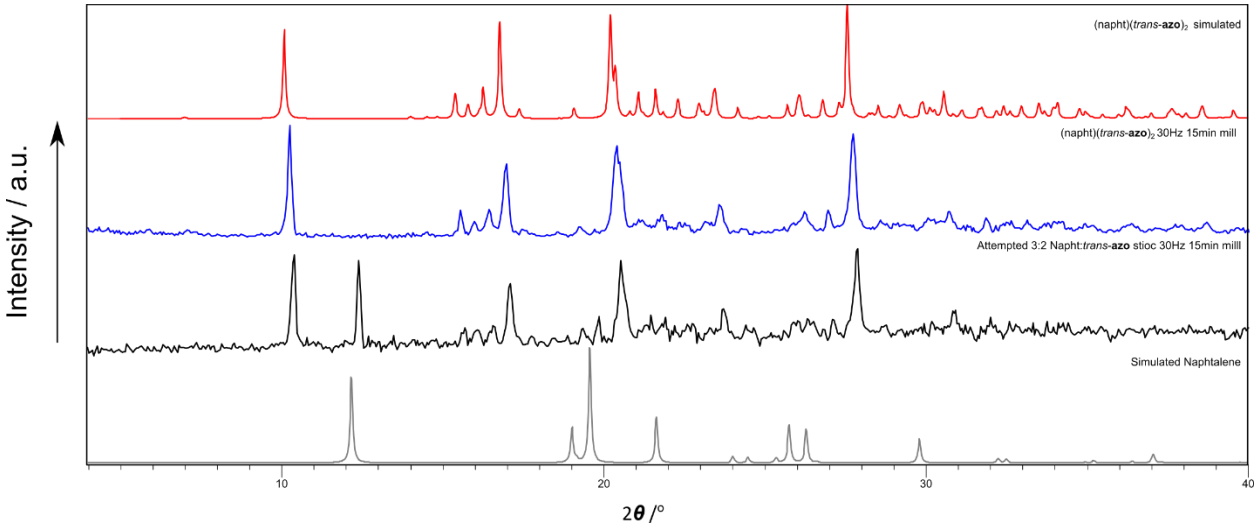

Supplementary Figure 4.2.PXRD of different stoichiometric equivalents of naphthalene, and *trans*-azo, formed through ball milling at 30 Hz for 15 mins using a 0.7 mg steel ball, on a 50 mg scale with 10 μL of Nitromethane added to the solution.

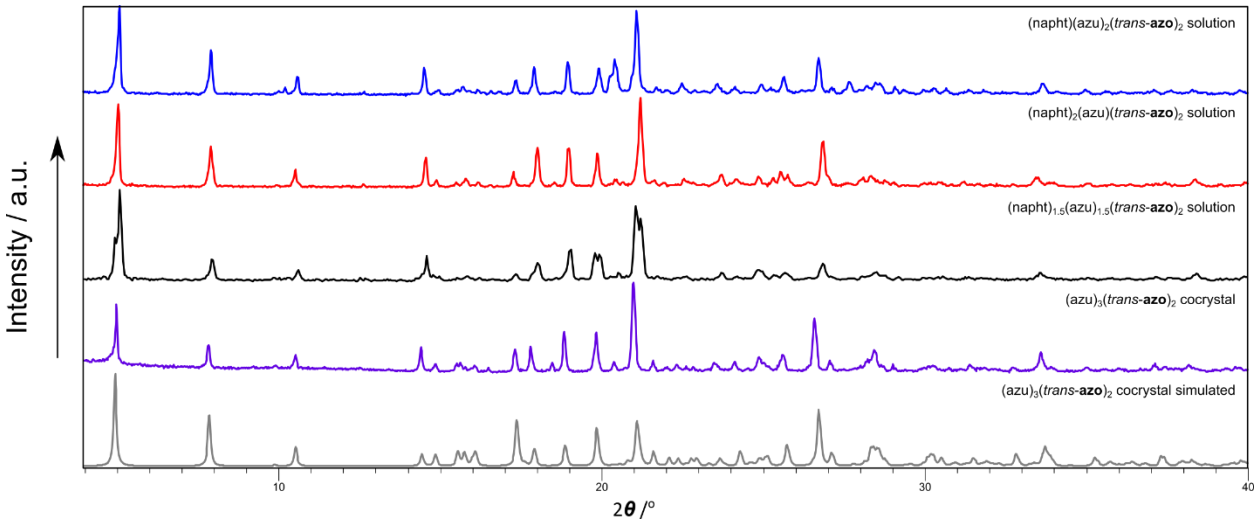

Supplementary Figure 4.3. PXRD of different stoichiometric equivalents of azulene, naphthalene, and *trans*-azo, formed through ball milling at 30 Hz for 15 mins using a 0.7 mg steel ball, on a 50 mg scale with 10 μL of Nitromethane added to the solution.

4.7.3 CPC of (azu)$_3$(*trans*-azo)$_2$ and (azu)(*trans*-azo)$_2$ co-crystals

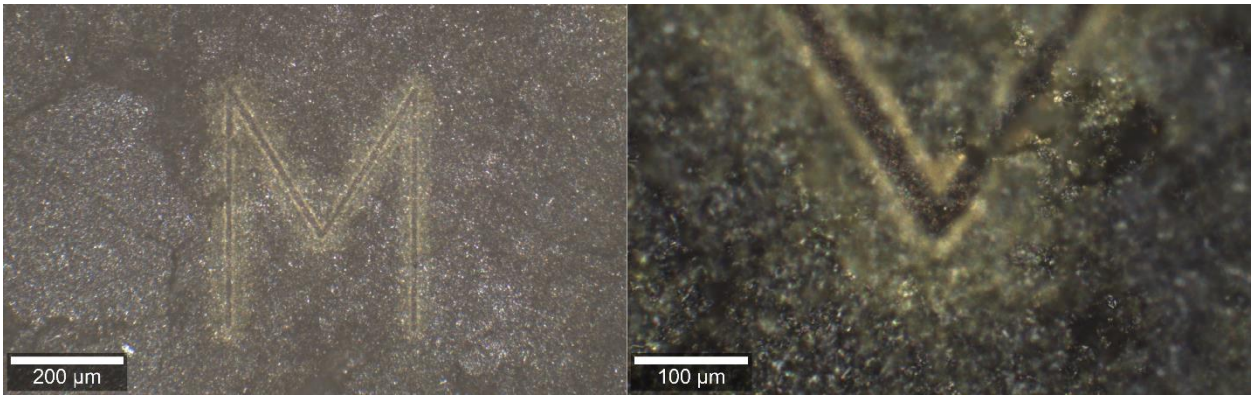

Supplementary Figure 4.4. Surface of a bulk sample of (azu)$_3$(*trans*-azo)$_2$ irradiated with a confocal system using a 1 mW 532 nm probe, to show CPC patterning achieved.

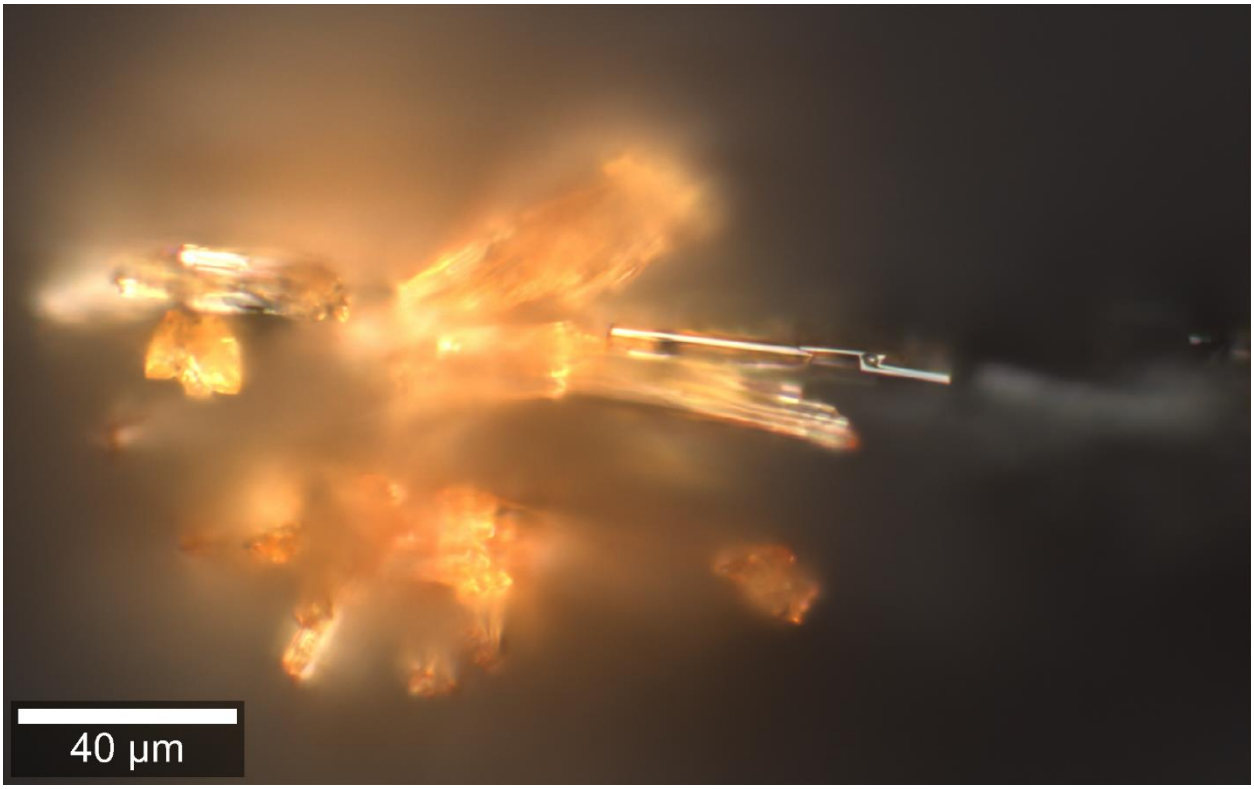

Supplementary Figure 4.5. Surface of a bulk sample of (azu)$_3$(*trans*-azo)$_2$ irradiated with a confocal system using a 20 mW 785 nm probe.

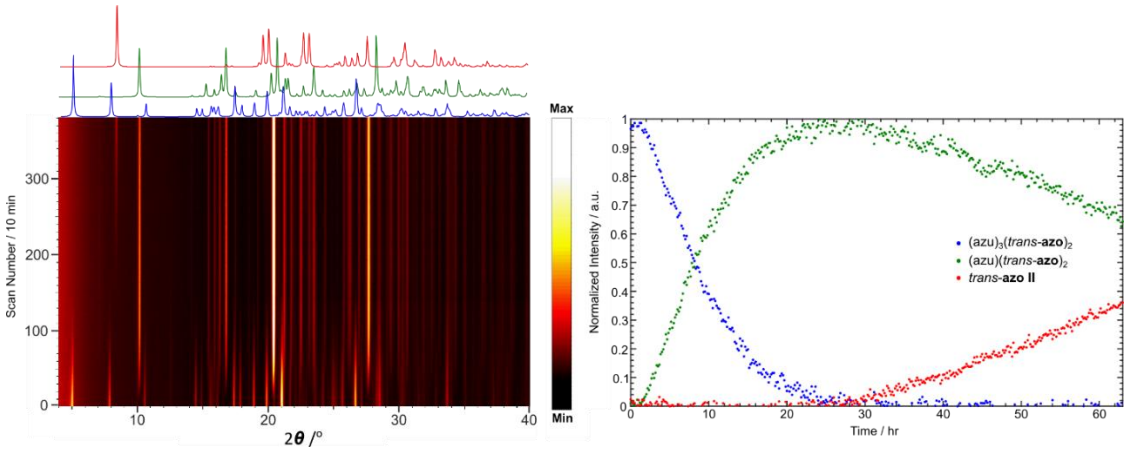

Supplementary Figure 4.6. Time-resolved monitoring of $(azu)_3(trans\text{-}azo)_2$ under continuous irradiation by a 633 nm 37 $mW \cdot cm^{-2}$ dispersed LED. The green trace represents the normalized integrated peak intensity of the 011 Bragg reflection of $(azu)(trans\text{-}azo)_2$ ($2\theta \approx 10.2$ °) throughout the reaction. The blue trace represents the normalized integrated peak intensity of the 001 Bragg reflection of $(azu)_3(trans\text{-}azo)_2$ ($2\theta \approx 4.8$ °). The red trace represents the normalized integrated peak intensity of the 002 Bragg reflection of *trans*-azo **II** ($2\theta \approx 8.4$ °) throughout the reaction.

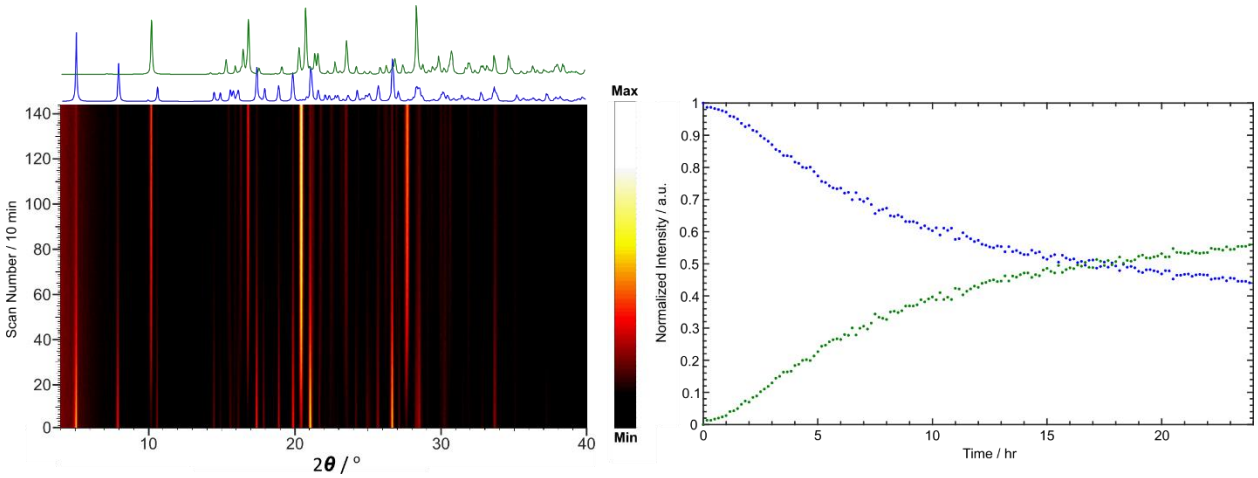

Supplementary Figure 4.7. Time-resolved monitoring of $(azu)_3(trans\text{-}azo)_2$ under no irradiation. The green trace represents the normalized integrated peak intensity of the 011 Bragg reflection of $(azu)(trans\text{-}azo)_2$ ($2\theta \approx 10.2$ °) throughout the reaction. The blue trace represents normalized integrated peak intensity of the 001 Bragg reflection of $(azu)_3(trans\text{-}azo)_2$ ($2\theta \approx 4.8$ °).

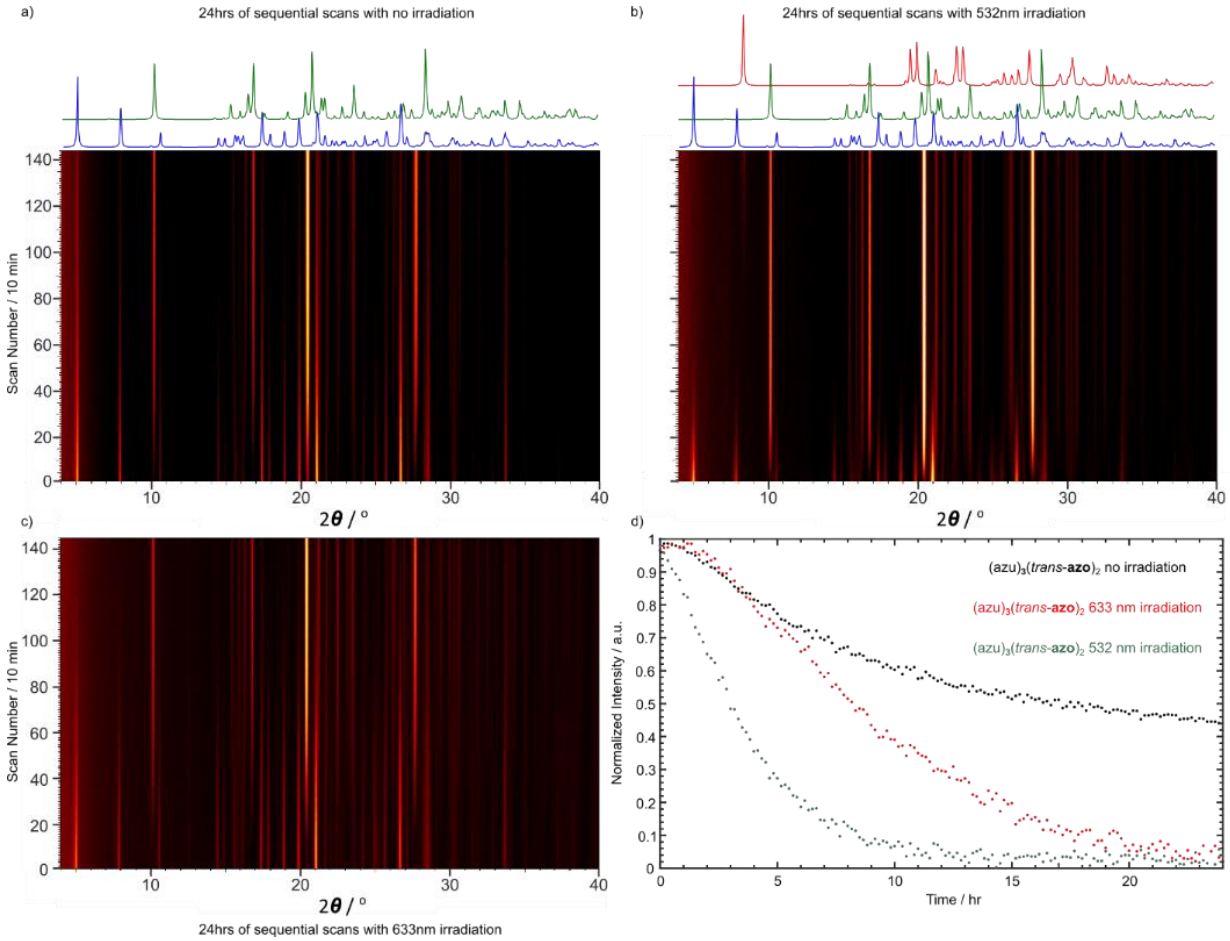

Supplementary Figure 4.8. a) Time-resolved monitoring of $(azu)_3(trans\text{-}azo)_2$ under no irradiation. **b)** Time-resolved monitoring of $(azu)_3(trans\text{-}azo)_2$ under continuous irradiation by a 532 nm 37 $mW \cdot cm^{-2}$ dispersed LED. **c)** Time-resolved monitoring of $(azu)_3(trans\text{-}azo)_2$ under continuous irradiation by a 633 nm dispersed 37 $mW \cdot cm^{-2}$ LED. **d)** overlaid normalized integrated peak intensities of the 001 Bragg reflections of $(azu)_3(trans\text{-}azo)_2$ ($2\theta \approx 4.8$ °). The black trace represents no irradiation, the red trace represents irradiation at 633 nm from a, and the green trace represents irradiation at 532 nm.

4.7.4 Thermal analysis of (azu)$_3$(*trans*-azo)$_2$

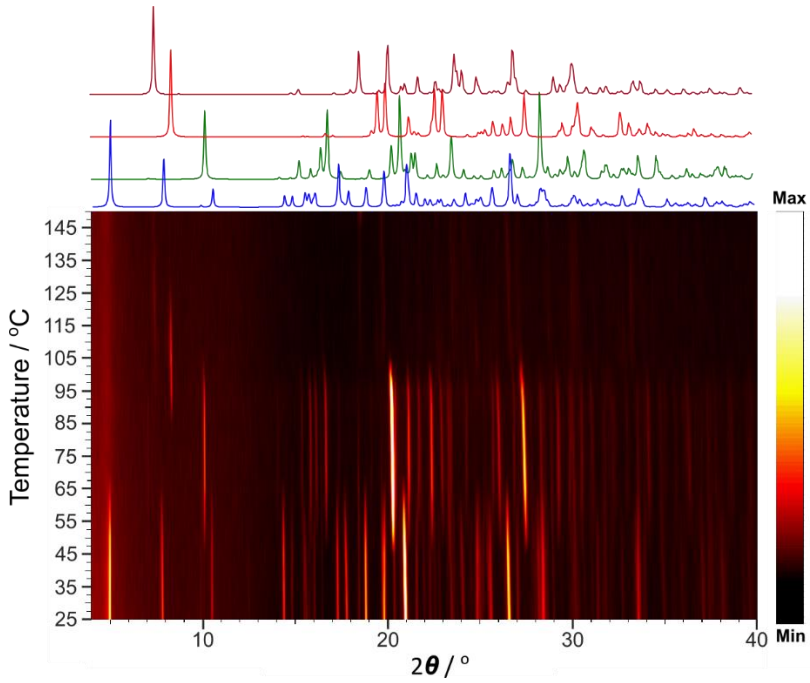

Supplementary Figure 4.9. Variable temperature PXRD taken of (azu)$_3$(*trans*-azo)$_2$ co-crystals with a ΔT of 5 C° per scan, taken over a temperature range of 25–150 °C. The blue trace is a simulated PXRD of (azu)$_3$(*trans*-azo)$_2$, the green trace is a simulated PXRD of (azu)(*trans*-azo)$_2$, the light red trace is a simulated PXRD of *trans*-azo **II**, and dark red trace is a simulated PXRD of *trans*-azo **I**.

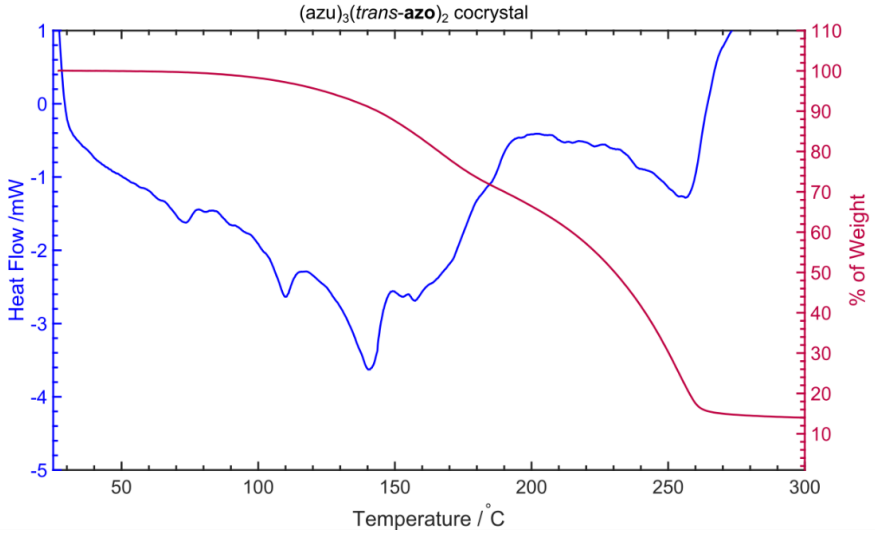

Supplementary Figure 4.10. TGA (red) and DSC (blue) traces of (azu)$_3$(*trans*-azo)$_2$, performed on a Mettler-Toledo TGA/DSC 1 Star system thermobalance. Both runs were performed under a stream of nitrogen (50 cm^3 min^{-1}) gas, at a heating rate of 1 C° min^{-1}.

4.7.5 CPC of (naph)(*trans*-azo)$_2$ co-crystals

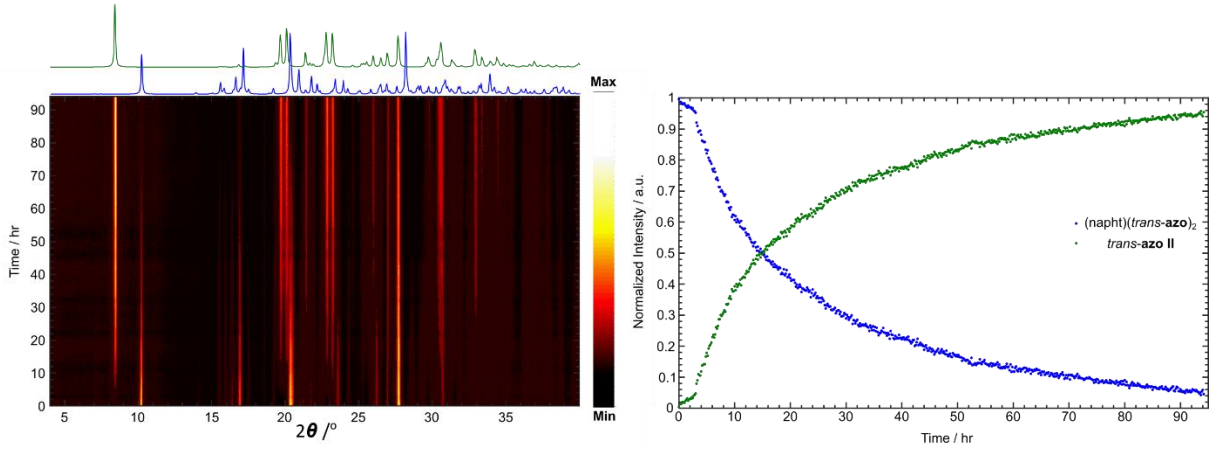

Supplementary Figure 4.11. Time-resolved monitoring of (naph)(*trans*-azo)$_2$ under continuous irradiation by a 532 nm dispersed LED, powered at 750 mA, 5V. The green trace represents the normalized integrated peak intensity of the 002 Bragg reflection of *trans*-azo **II** ($2\theta \approx 8.4$ º) throughout the reaction. The blue trace represents the normalized integrated peak intensity of the 011 Bragg reflection of (naph)(*trans*-azo)$_2$ ($2\theta \approx 10.2$ º).

4.7.6 Thermal analysis of (naph)(*trans*-azo)$_2$

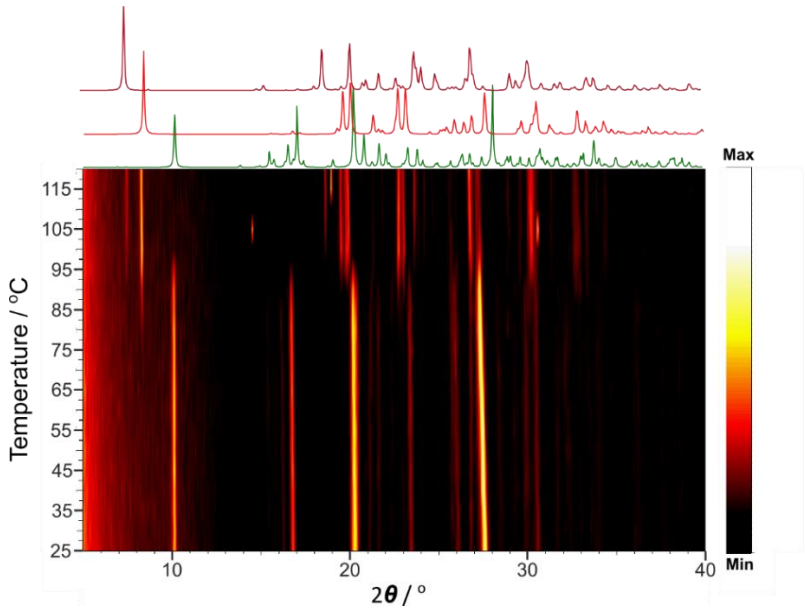

Supplementary Figure 4.12. Variable temperature PXRD taken of (naph)(*trans*-azo)$_2$ co-crystals, with a ΔT of 5 Cº per scan, taken over a temperature range of 25–120 ºC. The green trace is a simulated PXRD of (napht)(*trans*-azo)$_2$, the light red trace is a simulated PXRD of *trans*-azo **II**, and the dark red trace is a simulated PXRD of *trans*-azo **I**.

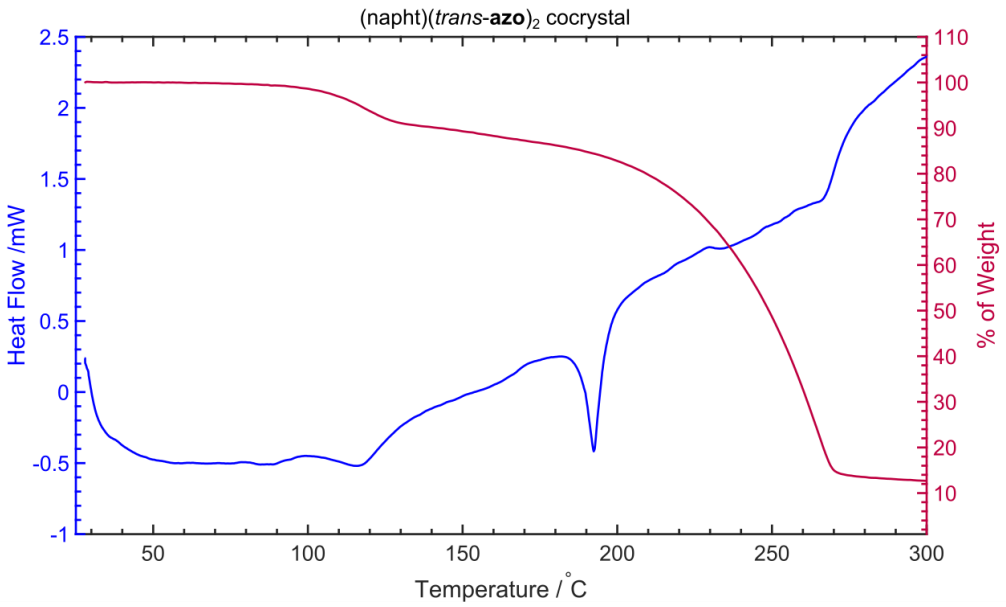

Supplementary Figure 4.13. TGA (red) and DSC (blue) traces of (naph)(*trans*-azo)$_2$, performed on a Mettler-Toledo TGA/DSC 1 Star system thermobalance. Both runs were performed under a stream of nitrogen (50 cm^3 min^{-1}) gas, at a heating rate of 1 C° min^{-1}.

4.7.7 Single crystal analysis of daughter crystal following irradiation with IR light

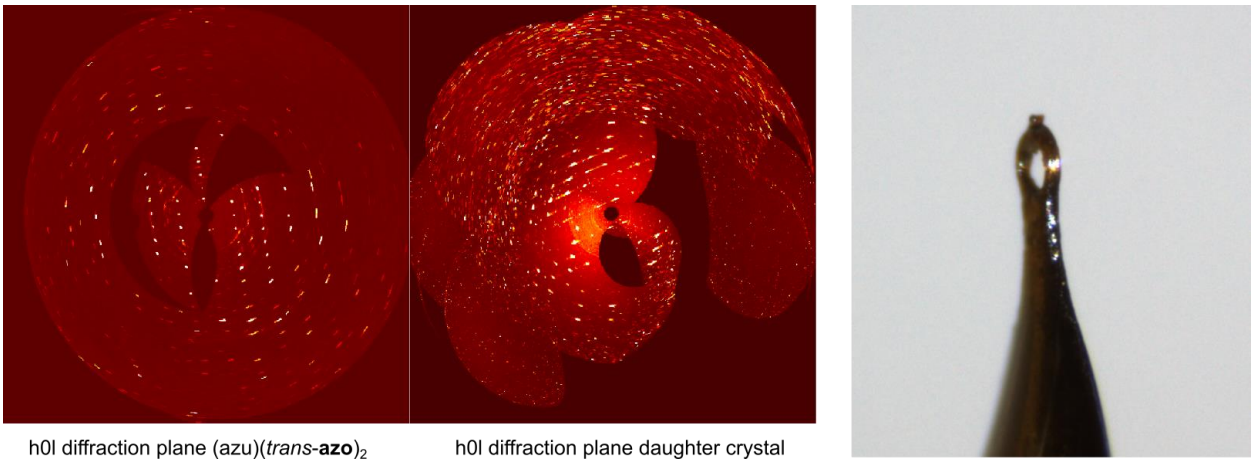

Supplementary Figure 4.14. Left) h0l Diffraction images of a 'mother crystal' (azu)(*trans*-azo)$_2$ and a 'daughter crystal' (confirmed as *trans*-azo **I**) recovered from the surface of the mother crystal after irradiation from a 785 nm 20 mW laser. Right) the *trans*-azo **I** crystal used for diffraction collection.

4.7.8 Scanning electron microscopy of an irradiated (azu)(*trans*-azo)$_2$ co-crystal

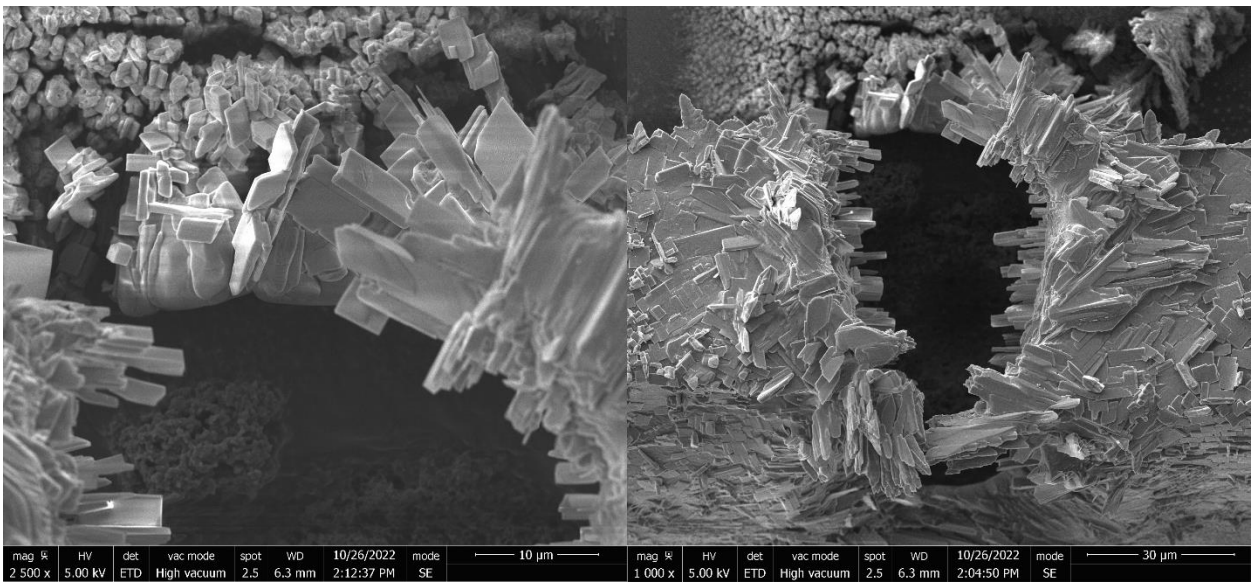

Supplementary Figure 4.15. Scanning electron microscopy image of (azu)(*trans*-azo)$_2$ co-crystal after irradiation by a 50 mW 785 nm IR laser.

4.7.9 UV-Vis absorbance and reflectance spectroscopy

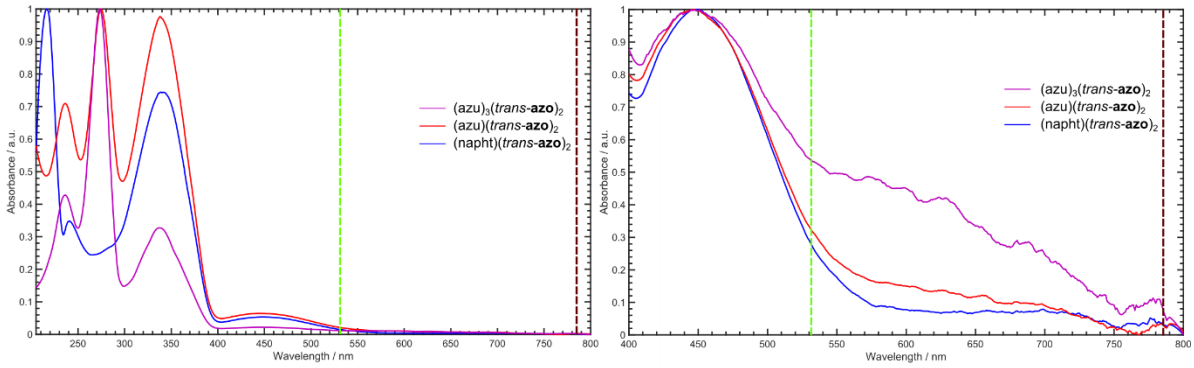

Supplementary Figure 4.16. UV-Vis absorbance spectra of (azu)$_3$(*trans*-azo)$_2$, (azu)(*trans*-azo)$_2$, and (naph)(*trans*-azo)$_2$ co-crystals dissolved in acetonitrile. Green trace represents location of 532 nm irradiation, dark red trace represents location of 785 nm irradiation.

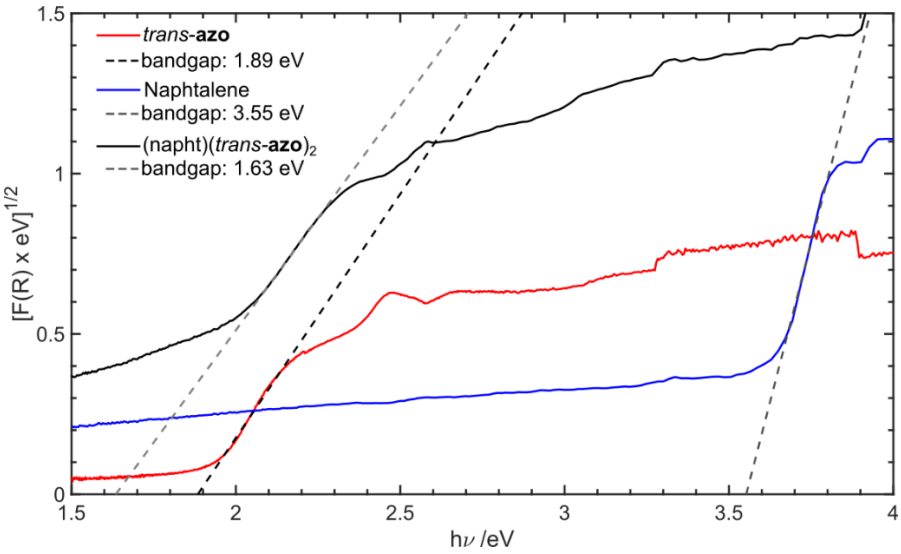

Supplementary Figure 4.17. Tauc plots of naphthlene, *trans*-azo, and (naph)(*trans*-azo)$_2$ co-crystals calculated through % R *vs* wavelength spectra taken on a Lambda 750 UV/Vis/NIR spectrometer from Perkin-Elmer. $BaSO_4$ (ACS) was used as a standard for instrumental calibration (autozero corrections). Samples were placed into a 1 cm quartz cuvette. Full spectra were recorded in reflectance in the range of 2500–300 nm with 5 nm intervals and between 620–300 nm with 0.5 nm intervals.

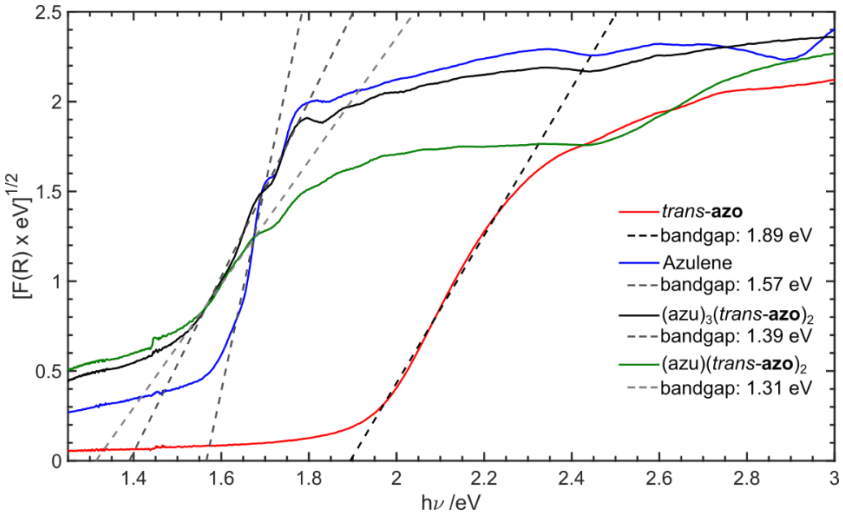

Supplementary Figure 4.18. Tauc plots of azulene, *trans*-azo, (azu)(*trans*-azo)$_2$, and (azu)$_3$(*trans*-azo)$_2$ co-crystals calculated through %R *vs* wavelength spectra taken on a Lambda 750 UV/Vis/NIR spectrometer from Perkin-Elmer. $BaSO_4$ (ACS) was used as a standard for instrumental calibration (autozero corrections). Samples were placed into a 1 cm quartz cuvette. Full spectra were recorded in reflectance in the range of 2500–300 nm with 5 nm intervals and between 620–300 nm with 0.5 nm intervals.

4.7.10 Additional images and data

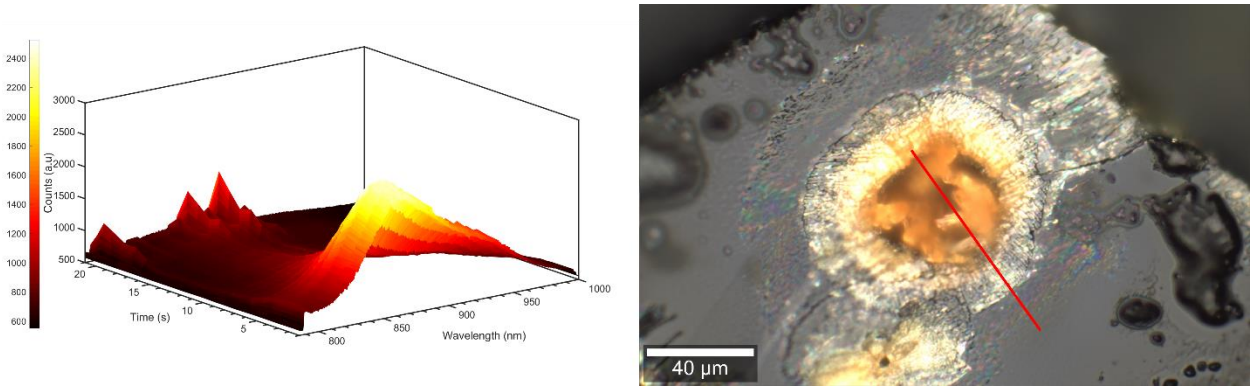

Supplementary Figure 4.19. Left) Time-resolved Raman spectrum of (azu)(*trans*-azo)$_2$ under constant irradiation with a 785 nm 25 mW probe. Right) optical image of the resultant crystal showing the formation of new orange crystals growing from the surface of the original crystal.

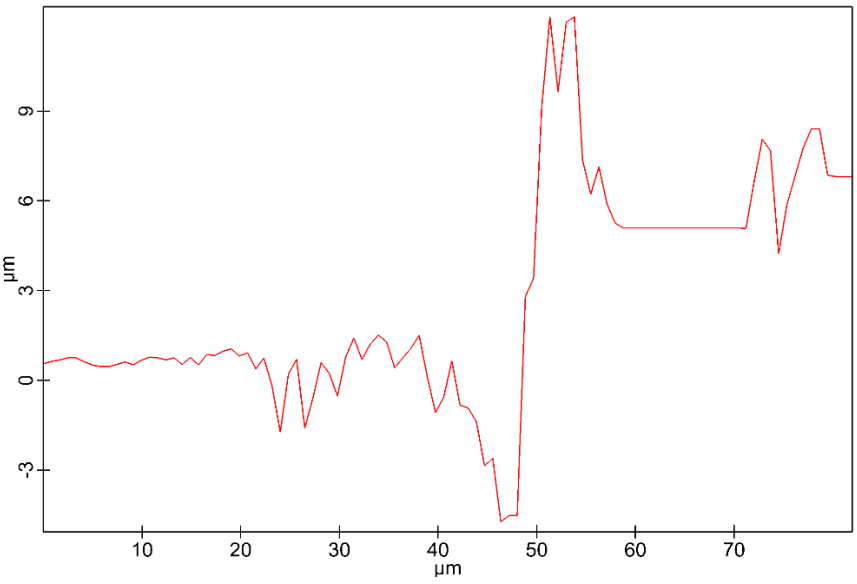

Supplementary Figure 4.20. Confocal Z-mapping of the surface of a crystal used for photo-induced crystallization of *trans*-azo **I**. The red line in **Figure S4** above shows the cross-section location for the mapping.

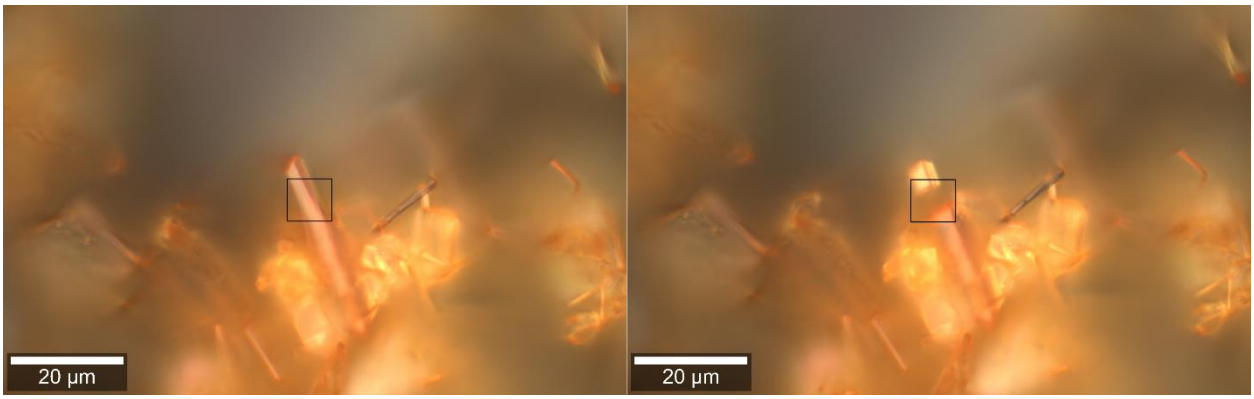

Supplementary Figure 4.21. Left) (naph)(*trans*-azo)$_2$ before and Right) after irradiation from a 1 mW 532 nm laser with 1 s irradiation time. Black box highlights area of irradiation.

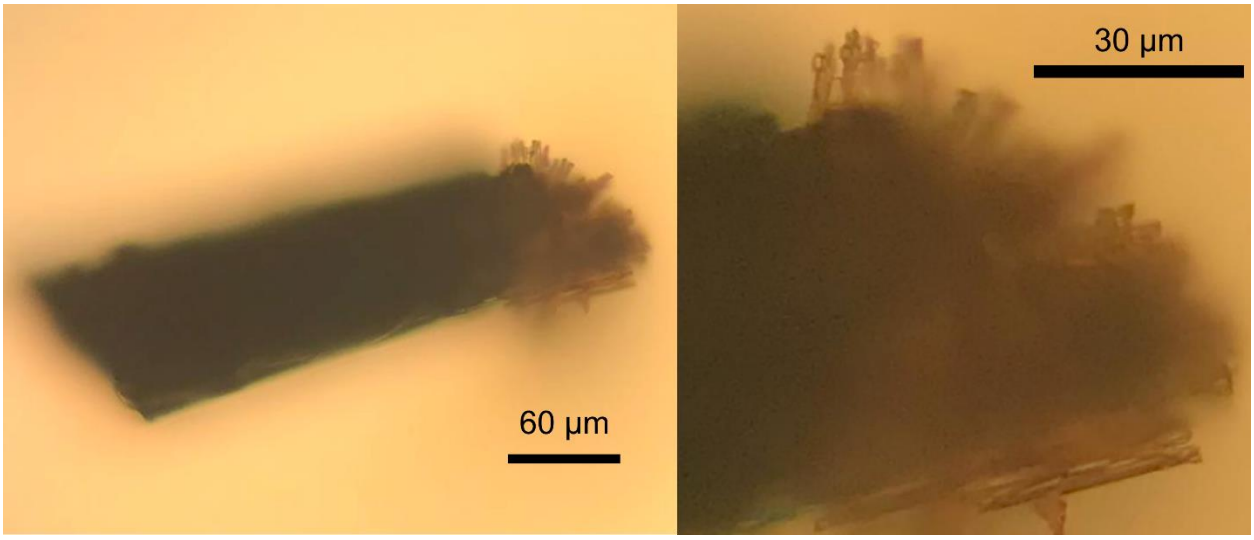

Supplementary Figure 4.22. Example of IR laser induced growth of *trans*-azo **I** crystals from a (azu)(*trans*-azo)$_2$ co-crystal. The co-crystal was irradiated with a 20 mW 785 nm IR laser for 10 seconds to induce crystallization.

Rationale for Chapter 5

Previous chapters (Chapters 2–4) focused on the photo-responsive nature of organic co-crystals, consisting of an organic photo-switch and a volatile component. Here in Chapter 5, we investigate the photo-responsive nature of inorganic crystalline materials, to complement the organic studies. Specifically the inorganic salts studied here are sodium hypochlorite pentahydrate, and hypobromite pentahydrate ($NaOCl{\cdot}5H_2O$, and $NaOBr{\cdot}5H_2O$). The crystallographic structure of the hypochlorite and hypobromite ions have only recently been reported by our team, for the first time, despite these hypohalites being used as bleaching agents for nearly 200 years (Topić, *et al*.[20] *Angew Chemie* **2021**). Additionally, to date no photo-responsive study has been published for solid state hypohalite ions. Therefore, this Chapter is the first report to investigate the photo-responsive nature of these inorganic bleaching agents in the solid state. We report new topochemical reactions occurring in the solid state, where the hypohalites convert to combination of halite and most likely, halide species upon irradiation with visible and UV light. Additionally, the yellow-coloured hypobromite is investigated as an inorganic material that can be machined using low-powered laser light, similar to the materials presented in the previous three Chapters, now extending this phenomenon from organic materials into inorganic. This is not only the first report highlighting the photo-responsive nature of hypohalite species in the solid state, but also a discovery that the photo-response differs from what has been reported in solution or solid state heating studies.

Chapter 5 is being prepared as a manuscript for submission, after this Thesis submission. Citation: Borchers, T. H., Marrett, J. M., Shields, D. J., Barrett, C. J., & Friščić., T. "New Photochemistry of Hypohalites: a Topochemical, Light-Induced Solid-State Conversion of Hypohalites (ClO^-, BrO^-) into Halites (ClO_2^-, BrO_2^-)" manuscript in preparation (2022).

New Photochemistry of Hypohalites: a Topochemical, Light-Induced Solid-State Conversion of Hypohalites (ClO^-, BrO^-) into Halites (ClO_2^-, BrO_2^-)

T. H. Borchers, J. M. Marrett, D. J. Shields, C. J. Barrett, and T. Friščić**

Department of Chemistry, McGill University, Montreal, QC, Canada

5.1 Abstract

We report that the crystalline hypohalite salts $NaClO·5H_2O$ and $NaBrO·5H_2O$ undergo disproportionate to their corresponding halites and halide salts when irradiated with laser light, leading to a complete, selective photo-transformation. This solid state photochemical transformation contrasts the analagous thermally-induced process, and the well-established reactivity in solution, which all lead to the corresponding halates (ClO_3^-, BrO_3^-) as the final products. This unexpected solid state photochemistry, which is here readily monitored *in situ* through Raman spectroscopy, is rationalized by the confinement and organization of anions in the solid state. We propose that this unexpected solid state behaviour, not observed for these materials when in solution, is due to their unique crystal structures, where hypohalite anions are aligned head-to-tail and separated by less than 4 Å, primed for ready conversion.

5.2 Introduction

Hypohalite ions (XO-, where X = halogen) are among the central species in the chemistry of halogens, and are ubiquitous in discussions of systematic trends in textbooks of general and inorganic chemistry.[1-3] Moreover, hypochlorite (ClO-) and hypobromite (BrO-) ions have been extensively used as oxidizing agents, with the hypochlorite ion being the first industrially manufactured chemical bleaching agent since being discovered by Berthelot back in the 18th century.[4–6] Aqueous solutions of sodium hypochlorite (NaOCl), commercially known as liquid bleach or *eau de Javel*, remain one of the most widely used bleaching agents. The manufacture of aqueous bleach today is being estimated at over 2 billion gallons annually.[7] The BrO^- ion is known as an intermediate in the Hoffmann rearrangement,[8] and as an *in situ* generated water disinfection agent.[9] Solid hypobromite ($NaOBr \cdot 5H_2O$) was first reported by Sholder and Krauss in 1952.[10] Consistent with their long history and extensive industrial use, the reactivity of hypohalites has also been extensively studied,[11–13] and is generally considered to be well understood. A staple of hypohalite chemistry is the disproportionation to form corresponding halates (XO_3^-, where X = Cl, Br, I, **Figure 5.1a**). Mechanistic and kinetic studies of this well-known transformation have revealed that the disproportionation can take place either thermally, or photochemically. For example the thermal conversion of hypochlorite or hypobromite in solution proceeds to chlorate, or bromate, respectively.[14,15] Similarly, the photochemical conversion of a hypohalite in solution is known to produce the corresponding halite as the final product.[16,17]

To the best of our knowledge, all reports of hypohalite disproportionation describe the formation of the halate and halide (X^-) ions. In particular, detailed studies exemplified by those conducted by Lister,[14] and by Buxton and Williams,[18] reveal the appearance of a small, steady-state amount of halite (XO_2^-) during such process, indicating that the disproportionation reaction

to form the XO_3^- species is mediated by short-lived XO_2^-.[14,18] Such thermal reaction studies indicate that the formation of XO_3^- involves a slower step in which the hypohalite is converted to the halite which, subsequently and rapidly, converts into the final halate product.[14] In case of hypobromite, these reactions proceed rapidly even in the dark, at room temperature.[15]

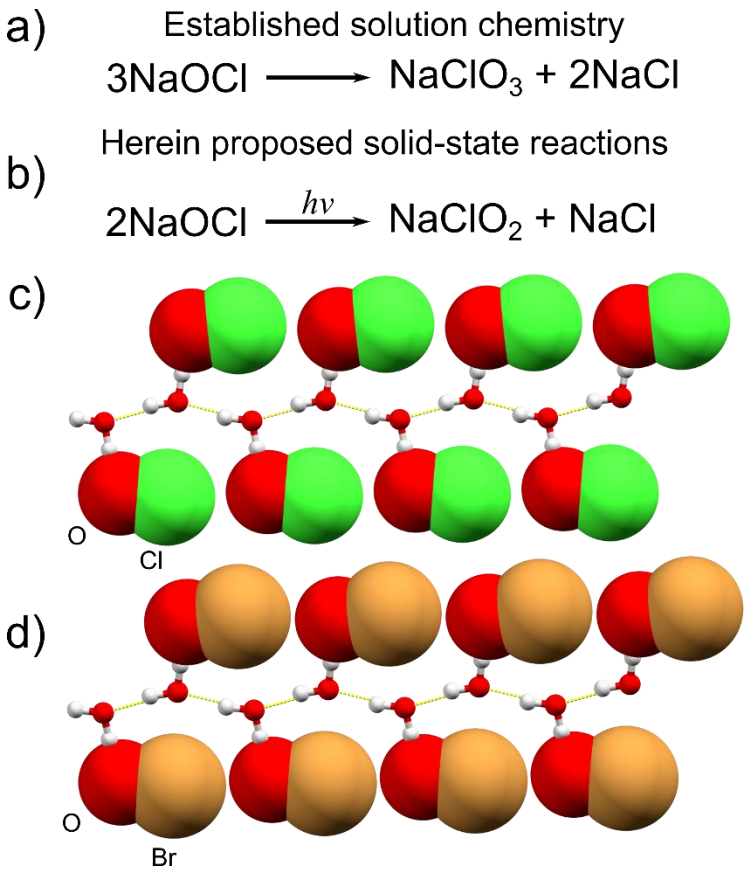

Figure 5.1. Solution and solid state transformations of hypohalites. a) Schematic of established solution decomposition of hypochlorite. **b)** Schematic of herein proposed solid state photo-reaction of hypochlorite. **c)** Example of the hydrogen bonding network between the water and the oxygen atoms leading to near linear alignment of hypochlorite ions. **d)** Example of the hydrogen bonding network between the water and the oxygen atoms leading to near linear alignment of hypobromite ions.

The light-driven hypohalite disproportionation reactions in solution were found to be considerably more complicated, with prolonged photolysis of the hypochlorite ion producing oxygen gas, chlorate, as well as chloride ions.[16,17] In the case of such photolysis, the formation of chlorite was also identified as the initial step of the disproportionation.[8] It should be noted that the total photolysis pathways also include different back-conversions involving the halate, halite ions, and hypohalites ions, leading to photoproducts $Cl^{\cdot}$, Cl^{-}, O^{-} and $O(^3P)$.[19] However after a period of steady-state irradiation, the overall final products remained halate and halide ions, in addition to molecular oxygen.

In contrast to reactions in aqueous solution, the chemistry of hypohalites in the solid state has been significantly less explored. The investigations of solid state reactivity appear to be dominated by a small number of reports on using hypohalites as oxidants in solid state mechano-chemical oxidation protocols.[10] The lack of understanding on the reactivity of hypohalite solids is not surprising, however, considering that the first report of the crystal structures of hypohalite salts, specifically of $NaOCl{\cdot}5H_2O$ and $NaOBr{\cdot}5H_2O$, have only been reported in 2021.[20] That work, as well as others,[21–23] has described that thermal decomposition of solid state crystalline hypohalites leads directly to the formation of halates, with no observed intermediates. To the best of our knowledge, there have not yet been any reports on potential photochemical reactions of hypohalites in the crystalline solid state.

Here we report the first observation of the photochemical transformation of hypohalite salts in the crystalline solid state. In particular, we find that exposure of solid $NaOCl{\cdot}5H_2O$ and $NaOBr{\cdot}5H_2O$ to ultraviolet (UV) or visible light leads to the unexpected, selective solid state formation of the halite ions ClO_2^- and BrO_2^-, with no detectable trace of other halogen oxoanions, such as halate or perhalate. This transformation, which is qualitatively different from either the

thermal or solution-based hypohalite disproportionations to form the corresponding halate ions, proceeds to completion in the case of $NaOCl \cdot 5H_2O$ and is near-complete in the case of $NaOBr \cdot 5H_2O$. Samples of $NaOCl \cdot 5H_2O$ were obtained commercially from TCI, while samples of $NaOBr \cdot 5H_2O$ were prepared following a procedure modified from previous reports by Schloder and Krauss,[10] and by Levason *et al*.[24]

5.3 Results and Discussion

5.3.1 Raman spectroscopy reveals halite conversion upon irradiation

Raman spectroscopy was used as the main characterization technique, which allowed us to use a single wavelength laser to probe Raman vibrational spectra while simultaneously using the laser to induce a photo-response in the hypochlorite solid. The experiments were carried out using a confocal Raman microscope equipped with a laser source of 532 nm wavelength and an output power of 11 mW. The laser was focused on the surface of a single crystal of hypochlorite cooled to -30 ^{o}C by using a THMS600 Linkam stage to ensure no thermal degradation. A Raman spectrum was acquired every 1 second continuously over the duration of the experiment (**Figure 2**). It was found that the Raman bands would quickly evolve upon irradiation, with the characteristic stretching band of the hypochlorite ion ν(Cl-O) at 711 cm^{-1} being replaced by a new, prominent band at 787 cm^{-1} and a minor band at 401 cm^{-1}. Both of these new Raman bands are consistent with the ν(Cl-O) stretches found in sodium chlorite.[25] In addition to those stretches, other changes were also observable in the Raman spectra of the irradiated material, including low frequency bands (< 200 cm^{-1}) suggesting the occurrence of a phase transition, as well as ν(O-H) stretching bands. With prolonged irradiation times (> 5 min) the new Raman bands remained constant, suggesting no further phase change occurs.

To ensure the reaction would occur uniformly in a larger amount of material, a 20 mg sample of crystalline powder $NaOCl \cdot 5H_2O$ was cooled to -30 ºC using a THMS 600 Linkam stage and then irradiated with a 385 nm wavelength light-emitting diode (LED) array. The solid state transformation upon irradiation was monitored continuously using a Raman spectroscopy probe laser of 785 nm (**Supplementary Figures 5.1, 5,2**). Spectra were acquired at 25 separate and random locations across the sample, and the resulting spectra were then averaged to ensure a uniform distribution of data collection over the entire sample. After 10 minutes of irradiation, such monitoring of the microcrystalline $NaOCl \cdot 5H_2O$ powder revealed the characteristic ν(Cl-O) stretching bands of the hypochlorite ion, but also the appearance of bands characteristic of chlorite ions. After further 10 minutes of irradiation, the Raman spectra of the sample contain largely the bands associated with the chlorite ion, with only weak bands of the starting hypochlorite. Finally, after a total of 30 minutes irradiation, Raman spectra of the irradiated sample revealed only stretching bands that matched those of sodium chlorite. While the sample remained a solid throughout the entire process, the irradiation also induced a clear change in the appearance of the sample, which transformed from small yellow crystallites into an off-white powder. This experiment clearly demonstrated the possibility to completely and selectively convert a sample of a hypochlorite salt into a chlorite through solid state irradiation. Upon warming to room Temperature, the irradiated sample was found to liquify.

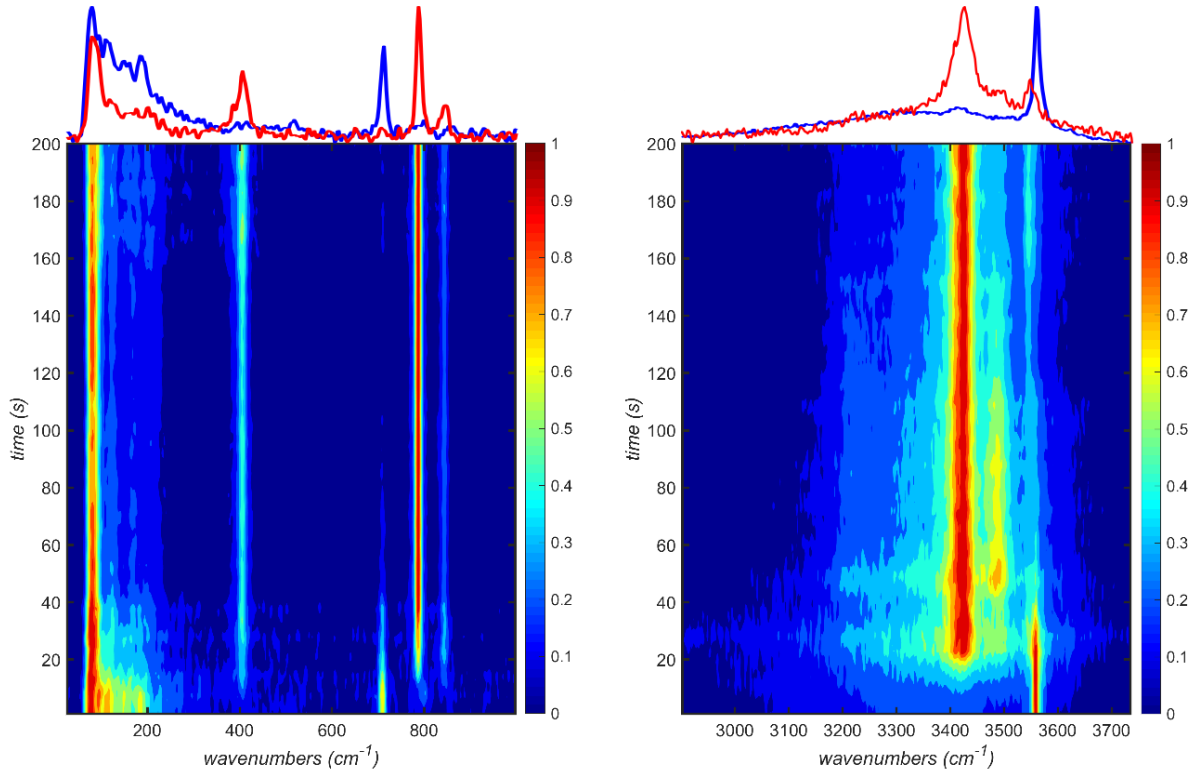

Figure 5.2. Time-resolved Raman spectra. Real-time *in situ* monitoring of the photo-induced disappearance of OCl^- and appearance of ClO_2^- upon irradiation of a crystal of $NaOCl \cdot 5H_2O$ with a laser of 532 nm wavelength and 11 mW power. The spectra have been obtained using a 1 second integration time, on a Witec alpha300 R Confocal Raman microscope.

5.3.2 Heating of solid state hypochlorite pentahydrate

The observed complete and selective transformation of solid $NaOCl \cdot 5H_2O$ to a ClO_2^--based material upon irradiation is surprising and is very different from the reactivity observed upon heating of a sodium hypochlorite sample (**Supplementary Figure 5.3**). In particular, we have again used a 785 nm wavelength Raman spectroscopy laser probe to follow changes in a 20 mg sample of polycrystalline $NaOCl \cdot 5H_2O$ upon heating from 0 ^oC to 120 ^oC. While the sample was found to liquify upon heating to 20 ^oC, there are no changes to the region of the Raman spectrum

associated with the ν(Cl-O) stretching vibrations, except for the broadening and reduction in intensity of the hypochlorite band at 711 cm^{-1}. Upon reaching 80 ^{o}C, however, a new band at 938 cm^{-1} appears, which is an excellent match for sodium chlorate. Upon further heating, the new 938 cm^{-1} ν(Cl-O) band continues to gain prominence, with the 711 cm^{-1} band gradually disappearing until a crystalline solid forms again. Raman spectroscopy reveals ClO_3^- as the only chlorine oxoanion present in the resulting solid. Importantly, Raman spectroscopy throughout the entire heating experiment did not reveal any sign of chlorite, in contrast to the behaviour observed upon solid state irradiation.

5.3.3 Photo-irradiation of solution-based hypochlorite

In order to evaluate the importance of the crystalline arrangement on the course of the observed photochemical $ClO^- \rightarrow ClO_2^-$ transformation, we explored the behaviour of a 10 M concentration aqueous solution of sodium hypochlorite upon irradiation with either a 532 nm laser of 100 mW power, or a 375 nm laser of 50 mW power (**Supplementary Figure 5.4**). In each case, the process was followed in real time through Raman spectroscopy using a 785 nm laser probe, which revealed no change upon exposure to 532 nm laser light, even after 24 hours of irradiation. In contrast, Raman spectroscopy monitoring of the solution that was irradiated at 375 nm revealed transformation from hypochlorite to chlorate within 24 hours. Overall, the described solid state and solution studies indicate that the unexpected $ClO^- \rightarrow ClO_2^-$ transformation in solid $NaOCl \cdot 5H_2O$ is distinct from the reaction that takes place upon external heating of the sample, and also requires the reactant to be present in the form of a crystal. These observations suggest a topochemically-controlled reaction mechanism, in which the alignment of ClO^- ions in crystalline

$NaOCl \cdot 5H_2O$ facilitates an oxygen transfer reaction leading exclusively to chlorite ions (**Figure 5.1c,d**)

5.3.4 Theoretical structural models

To gain further insight into the solid state conversion of hypochlorite to chlorite, we considered that the irradiation of solid $NaOCl \cdot 5H_2O$ might take place through an intermolecular oxygen transfer process (**Figure 5.1b**), which would initially produce solid solutions in which some of the pairs of ClO^- ions are replaced by a combination of a Cl^- and a ClO_2^- ions. Models for these putative mixed-salt structures were built by reducing the symmetry of the experimentally obtained crystallographic structures from the orthorhombic and monoclinic space groups *Pbca* and $P2_1/n$ for the hypochlorite and hypobromite crystal structures respectively, to the triclinic *P*-1. This was followed by developing a supercell through joining of two crystallographic unit cells along crystallographic α-axis, after which selected oxygen atoms would be removed from the hypohalites and placed on neighbouring hypohalites to form halites and halides.

The resulting structural models were then optimized *via* periodic density-functional theory (DFT, Fig. 3, also see ESI) using plane-wave DFT code CASTEP.[26] The calculations were performed using Perdew-Burke-Ernzerhof (PBE)[27] functionals combined with a Grimme D3 semiempirical dispersion correction scheme.[28] The functional and dispersion corrections were chosen, because they have previously been used to model these hypohalite crystal structures, and have shown only minor variations when compared to the experimental crystal structure.[20] A total of four structural models were investigated, for which the structures were developed for different ratios (χ) of ClO_2^- to ClO^- ions of 0.25, 0.50, 0.75 and 1. The energies for the optimized structures

were calculated and compared to that calculated of the original $NaOCl \cdot 5H_2O$ crystal structure (**Figure 5.3, Table 5.1, Supplementary Table 5.1**).

Table 5.1. Theoretically obtained energies. Calculated energies between differing models of χ compared to the calculated energies of the optimized experimentally obtained hypohalite structures.

Initial structure	$\chi=(XO_2^-/XO^-)$	ΔE ($kJ \cdot mol^{-1}$)
$NaOBr \cdot 5H_2O$	0	0.00
	0.25	16.10
	0.50	29.49
	0.75	67.77
	1	70.17
$NaOCl \cdot 5H_2O$	0	0.00
	0.25	-2.07
	0.50	12.03
	0.75	7.10
	1	22.11

The calculations showed that the replacement of pairs of ClO^- ions with a set of Cl^- and ClO_2^- ions led to little distortion in the overall structure — an inspection of the optimized models revealed the retention of similar hydrogen-bonding chains between layers of the chlorite/chloride and hypochlorite layers as the original structures. The energies of the respective models trended enthalpically positive with increasing χ for all models except for $\chi = 0.25$, which was found to be exothermic with respect to the crystal structure of $NaOCl \cdot 5H_2O$.

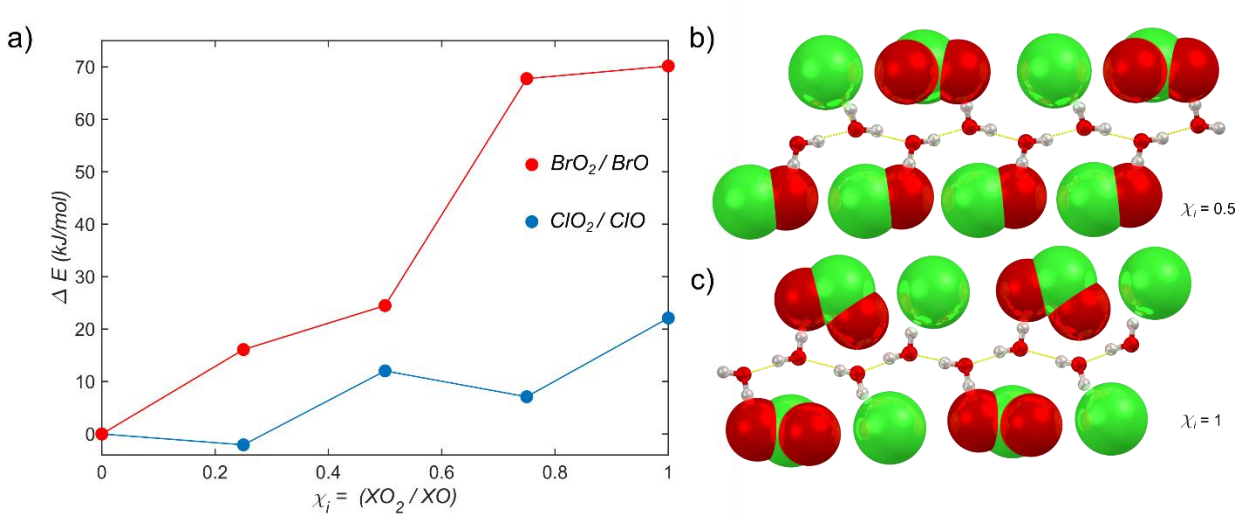

Figure 5.3. Theoretical studies of halite/hypohalite mixed salt models. a) Calculated periodic DFT determined enthalpies of mixed salt models with values χ = 0, 0.25, 0.50, 0.75 and 1. **b)** Optimized crystal structure for χ = 0.50 mixed salt model, highlighting the arrangement of hypochlorite, chlorite, and chloride ions, and connectivity of the hydrogen-bonded framework within calculated mixed salt model. **c)** Optimized crystal structure for χ = 1 mixed salt model, highlighting the arrangement of chlorite, and chloride ions, as well as connectivity of the hydrogen-bonded framework within calculated salt model.

5.3.5 Photo-responsive properties of hypobromite pentahydrate

The unexpected photochemical transformation observed in solid $NaOCl·5H_2O$ was also observed in the analogous hypobromite salt. Specifically, irradiation of a crystal of $NaOBr·5H_2O$ using a laser source of green visible 532 nm wavelength and 1 mW power led to a significant loss in intensity of the hypobromite ν(Br-O) Raman band at 622 cm^{-1}, and the appearance of a new ν(Br-O) signal at 708 cm^{-1}, which is consistent with the bromite ion.

It remained difficult however to obtain Raman spectra demonstrating complete disappearance of hypobromite signal (**Figure 5.4a**). Even when using a very low-powered laser

source (power below 0.5 mW), the irradiation led to rapid physical deterioration of the crystal, resulting in a hole and loss of Raman signal (**Figure 5.4c**). The ability to induce the formation of bromite ions in $NaOBr \cdot 5H_2O$ using green light, whereas the formation of chlorite $NaOCl \cdot 5H_2O$ required the use of UV radiation, reflects the differing UV-Vis absorbance spectra of the two hypohalite salts (**Supplementary Figures 5.5, 5.6**). Specifically, measuring the UV-Vis spectrum of $NaOCl \cdot 5H_2O$ in aqueous solution revealed a major absorbance band centred at 300 nm. Similarly, measuring the absorbance spectrum of an aqueous solution of $NaOBr \cdot 5H_2O$ revealed that the major absorbance band was centred around 350 nm. The red-shifted absorbance of $NaOBr \cdot 5H_2O$ can explain well why the hypobromite sample reacts more quickly to visible light compared to the hypochlorite sample. The bandgaps of hypochlorite and hypobromite species were also calculated from their absorbance spectra through developing Tauc plots. The hypobromite sample (bandgap of 2.95 eV, corresponding to 420 nm wavelength) was found to exhibit a lower band gap compared to the hypochlorite (bandgap of 3.36 eV, corresponding to 370 nm wavelength) and, consequently, irradiation with green light would be expected to readily induce reactivity in a hypobromite sample.

We also explored the thermal behaviour of $NaOBr \cdot 5H_2O$ using a confocal Raman microscope combined with a THMS600 Linkam stage. The initially solid yellow crystalline sample was heated from -50 ^{o}C to +50 ^{o}C, which led to two sequential transformations. While the sample is first observed to liquify around 0 ^{o}C, no chemical changes were detected in the Raman spectra throughout the melting process, with the observed ν(Br-O) band at 622 cm^{-1} being consistent with the presence of the hypobromite ion only. Further heating led to sample crystallization at ca. 50 ^{o}C, with concomitant disappearance of the ν(Br-O) band assigned to the hypobromite ion and the emergence of a new band at 802 cm^{-1} that was consistent with the bromate

ion (**Supplementary Figure 5.7**). Notably, the measured Raman spectra also revealed no sign of any bromite intermediate throughout the heating experiment, again indicating that the observed formation of BrO_2^- upon green light irradiation is a light-enabled solid state process, different from thermal disproportionation that also involves a liquid phase.

We also used periodic DFT modelling to investigate the possibility of forming solid solutions based on the crystal structure of $NaOBr \cdot 5H_2O$, in which pairs of OBr^- ions would be replaced with a combination of Br^- and BrO_2^- (**Figure 5.3, Table 5.1**). Compared to analogous calculations for $NaOCl \cdot 5H_2O$, the formation of such solid solutions was found to be much less favourable for $NaOBr \cdot 5H_2O$, as the resulting structural models were significantly more endothermic. Such results, which indicate a rapid loss of stability upon replacing OBr^- ions with a combination of Br^- and BrO_2^-, provide a potential explanation for the observed rapid physical degradation of the $NaOBr \cdot 5H_2O$ upon irradiation.

5.3.6 Gas-phase transition state modeling

To further investigate the observed solid state transformation of hypohalite to halite, we also evaluated the gas-phase transition state energies for a transformation resembling the proposed $2XO^- \rightarrow X^- + XO_2^-$ process. Specifically, we used gas-phase calculations to investigate the difference in transition state energies between hypochlorite- and hypobromite-based reactions in which an oxygen atom is transferred from one hypohalite ion to a neighbouring one, with the two starting ions arranged in a way resembling that in the crystal structures of solid $NaOCl \cdot 5H_2O$ and $NaOBr \cdot 5H_2O$. The gas-phase calculations involved the calculation of the intrinsic reaction coordinate (IRC). The IRC calculation was used to show that the reactant side of the transition state closely resembles the two hypohalites sitting linearly to each other as seen in the solid state,

while the product side of the transition state resembles a halide ion and a newly formed halite ion (**Supplementary Figures 8 and 9**). Because the photo-reaction occurs in the solid state, a point of the IRC that most closely resembled the experimentally determined X-ray structure was chosen for which to compare the energy of the transition state. Using this treatment, the transition state for the transformation of two hypohalite ions into a halide-halite pair was estimated to be 87 kJ/mol for OCl^-, and 55 kJ/mol for OBr^-. The lower value obtained in case of hypobromite is consistent with the observed faster reactions compared to analogous hypochlorite-based processes.

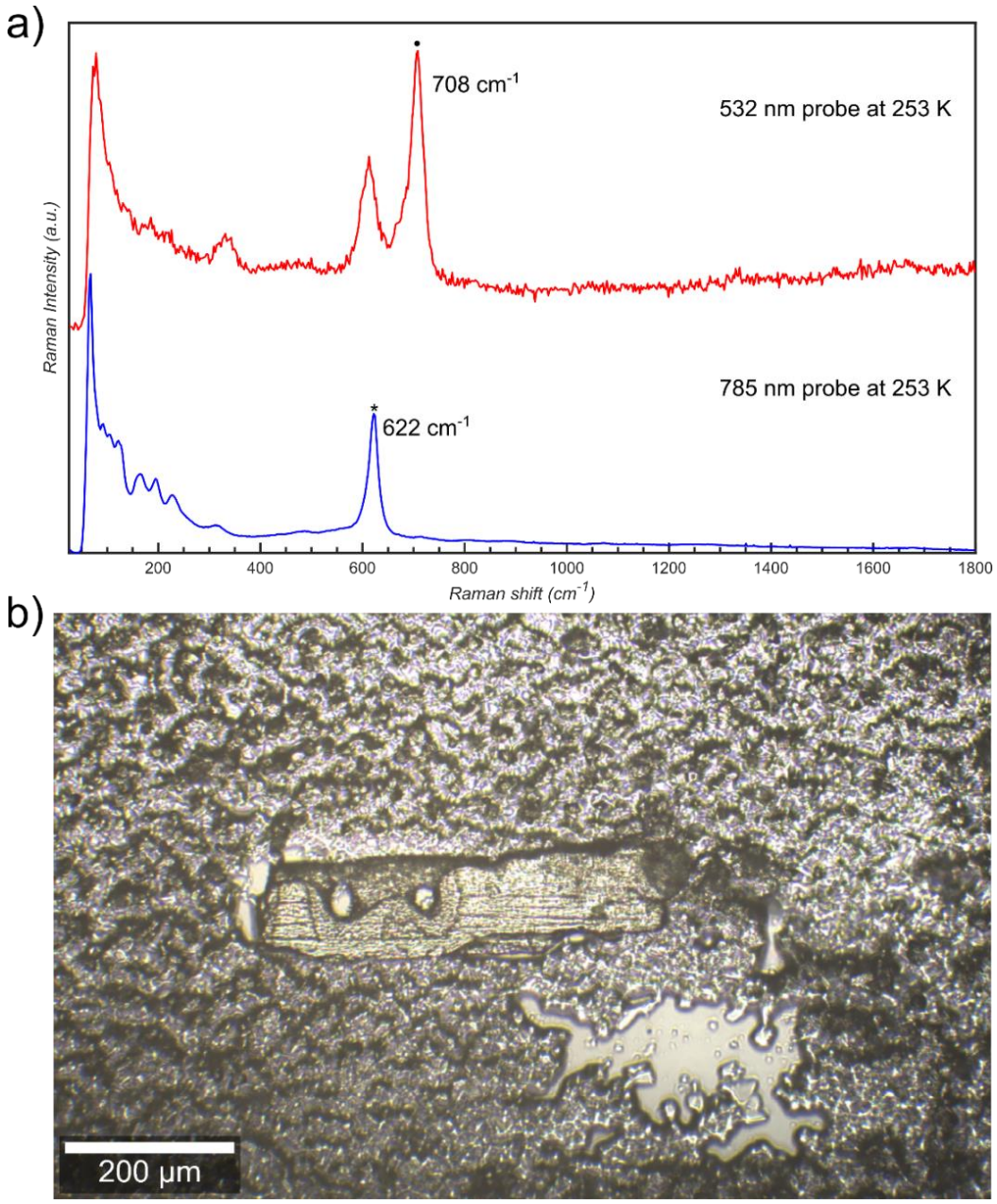

Figure 5.4. Photo-responsive nature of hypobromite ions in the solid state. a) Resultant Raman spectra using either a 785 nm 20 mW probe with 10 s of integration (red), showing only hypobromite stretches, or a 532 nm 1 mW probe with 2 s integration (blue), showing stretches associated with hypobromite but also with bromite. **b)** Resultant hypobromite crystal following Raman experiments, with holes a result of using a 532 nm 1 mW 2s integration laser probe.

We believe that the light-induced reactivity of hypochlorites described here in the solid state represents an example of such topochemically-controlled transformations in a purely inorganic system. Specifically, in the herein investigated crystalline salts, the hypohalites are arranged in a head-to-tail fashion to form chains in which the interionic distance between the halogen atom of one ion and the oxygen atom on a neighbouring one are placed at 3.656 Å and 3.522 Å for Cl···O and Br···O, respectively.[20] These distances slightly exceed those calculated for the sum of the accepted van der Waals radii of the hypochlorite and hypobromite ions of 3.27 Å and 3.37 Å respectively. Due to the short distance between neighboring ions, we suggest that the laser acts as a localized heating source to convert the two hypohalite ions into their respective halite and halide, with the reaction not progressing further due to sufficient space of the remaining ions.

5.4 Conclusions

We have reported the first solid state photo-reaction of hypohalites, in which we have spectroscopic evidence of full conversion from hypochlorite to chlorite. This result differs from previous decomposition experiments of hypohalites in solution or in the solid state, in which the major product converted to the resultant halite. We found that even after continuous irradiation the photo-product would remain as the halite form and would not progress to halate. These results were supported by both Raman spectroscopy and theoretical calculations. Control experiments using thermal means in the solid state shows that the reaction indeed progresses photochemically. Furthermore, the necessity of the solid state structure in promoting the photochemical transformation is confirmed both by solution irradiation control experiments and quantum mechanical calculations. The quantum mechanical calculations suggest that the solid state

structure of these hypohalites works to stabilize the photochemical transition state, which is an important factor to explain the difference between solution and solid state photochemistry in this case. Lastly, these hypohalite reactions have been shown to be the first inorganic crystals able to be cold-carved, which represents further progress in the field of cold photo-carving of crystalline materials.

5.5 References

1. Pauling L. General Chemistry. *Dover Publications, New York, (1988*).
2. Lang, J.-P. Chlorine, Bromine, Iodine & Astatine: Inorganic Chemistry: in *Encyclopedia of Inorganic Chemistry*, Wiley, Online, (2005).
3. King, R. B. Inorganic Chemistry of Main Group Elements. Wiley-VCH, Weinheim, (1994).
4. Berthollet, C. L. Description du Blanchiment des Toiles et des Fils par l'Acide Muriatique Oxygéné, et de Quelques Autres Propriétés de Cette Liqueur Relatives Aux Arts, *Annales de Chimie*, ***2***, 151–190, (1789).
5. Dorveaux, P. L'invention de l'eau de Javel. *Revue d'Histoire de la Pharmacie*, **63**, 286–287, (1929).
6. Scott, J. On the Disinfecting Properties of Labarraque's Preparations of Chlorine. 3rd Edition, Published by S. Highley, 174 Fleet Street, London (1828).
7. https://www.fortunebusinessinsights.com/sodium-hypochlorite-market-105064 (accessed December 1, 2022)
8. Wang, Z. Comprehensive Organic Name Reactions and Reagents. John Wiley & Sons, 1447–1450, (2010)
9. Alternative drinking-water disinfectants: bromine, iodine and silver. World Health Organization, Geneva, 2018.
10. Scholder, R., & Krauss, K. Über kristallisierte Alkalihypobromite. *Zeit. Anorg. Allg. Chem.* **268**, *279290*, (1952).
11. Lister, M. W. The Decomposition of Hypochlorous Acid. *Can. J. Chem.* **30**, 879–889, (1952).

12. Chapin, R. M. The effect of hydrogen-ion concentration on the decomposition of Hypohalites. *J. Am. Chem. Soc*. **56**, 11, 2211–2215, (1934).

13. Adam, L. C., & Gordon, G. Hypochlorite Ion Decomposition: Effects of Temperature, Ionic Strength, and Chloride ion. *Inorg. Chem.* **38**, 6, 1299–1304 (1999).

14. Lister, M. W. Decomposition of sodium hypochlorite the uncatalyzed Reaction. *Can. J. Chem.* **34**, 465–478, (1956).

15. Farkas, L., & Klein, F. S. On the Photo-Chemistry of Some Ions in Solution. *J. Chem. Phys.* **16**, 886–893, (1948).

16. Allmand, A. J., Cunliffe, P. W., & Maddison, R. E. W. The Photodecomposition of Chlorine water and of Aqueous Hypochlorous Acid Soluitions Part I. *J. Chem. Soc.*, **127**, 822, (1925).

17. Allmand, A. J., Cunliffe, P. W., & Maddison, R. E. W. The Photodecomposition of Chlorine water and of Aqueous Hypochlorous Acid Soluitions Part II. *J. Chem. Soc.*, **127**, 655–669, (1927).

18. G. V. Buxton and R. J. Williams, Photochemical decom positions of aqueous solutions of oxyanions of chlorine and chlorine dioxide. *Proc. Chem Soc.* **141**, **(**1962).

19. Buxton. G. V., & Subhani, M. S. Radiation Chemistry and photochemistry of oxychlorine ions. Part 2. –Photodecomposition of aqueous solutions of hypochlorite ions. ***J***. *Chem. Soc., Faraday trans.* **68**, 958–969, (1972).

20. Topić, F., Marrett, J. M., Borchers, T. H., Titi, H. M., Barrett, C. J., & Friščić, T. After 200 Years: The Structure of Bleach and Characterization of Hypohalite Ions by Single-Crystal X-ray Diffraction. *Angew. Chem. Int. Ed.* **60**, 24400, (2021).

21. Kirhara, M., Okada, T., Sugiyama, Y., Akiyoshi, M., Matsunaga, T., & Kimura, Y. Sodium hypochlorite pentahydrate crystals ($NaOCl{\cdot}5H_2O$): A convenient and environmentally benign oxidant for organic synthesis. *Org. Process Res. Dev.* **21**, 12, 1925–1927, (2017).

22. Okada, T., Asawa, T., Sugiyama, Y., Iwai, T., Kirihara, M., & Kimura, Y. Sodium hypochlorite pentahydrate ($NaOCl{\cdot}5H_2O$) crystals; An effective re-oxidant for TEMPO oxidation. *Tetrahedron*. **72**, 22, 2818–2827 (2016).

23. US 3498924, Walsh RH, Dietz A, "Process for preparing stable sodium hypochlorites", issued (1966).

24. Levason, W., Ogden, J. S., Spicer, M. D., & Young, N. A. Characterisation of the oxo-anions of bromine BrO_x^-(x=1-4) by Infrared, Raman, Nuclear Magnetic Resonance, and Bromine K-edge extended X-ray Absorption fine Structure Techniques. *J. Chem. Soc., Dalton Trans*. 349–353, (1990).

25. John Wiley & Sons, Inc. SpectraBase; SpectraBase Compound ID=5gBeGCbBjA2 SpectraBase Spectrum ID=AwIhJ1yCjnj https://spectrabase.com/spectrum/AwIhJ1yCjnj (accessed 2022-12-14).

26. Clark, S. J., Segall, M. D., Pickard, C. J., Hasnip, P. J., Probert, M. I. J., Refson, K., & Payne, M. C. First principles methods using CASTEP. *Z. Kristallogr. Cryst. Mater.* **220**, 5/6, 567–570 (2005).

27. Perdew, J. P., Burke, K., & Ernzerhof, M. Generalized gradient approximation made simple. *Phys. Rev. Lett.* **77**, 3865 (1996).

28. Grimme, S., Antony, J., Ehrlich, S., & Krieg, H. A consistent and accurate *ab initio* parametrization of density functional dispersion correction (DFT-D) for the 94 elements H-Pu. *J. Chem. Phys.* **132**, 154104 (2010).

5.6 Appendix 4: Supporting information for Chapter 5

5.6.1 Bulk Raman study

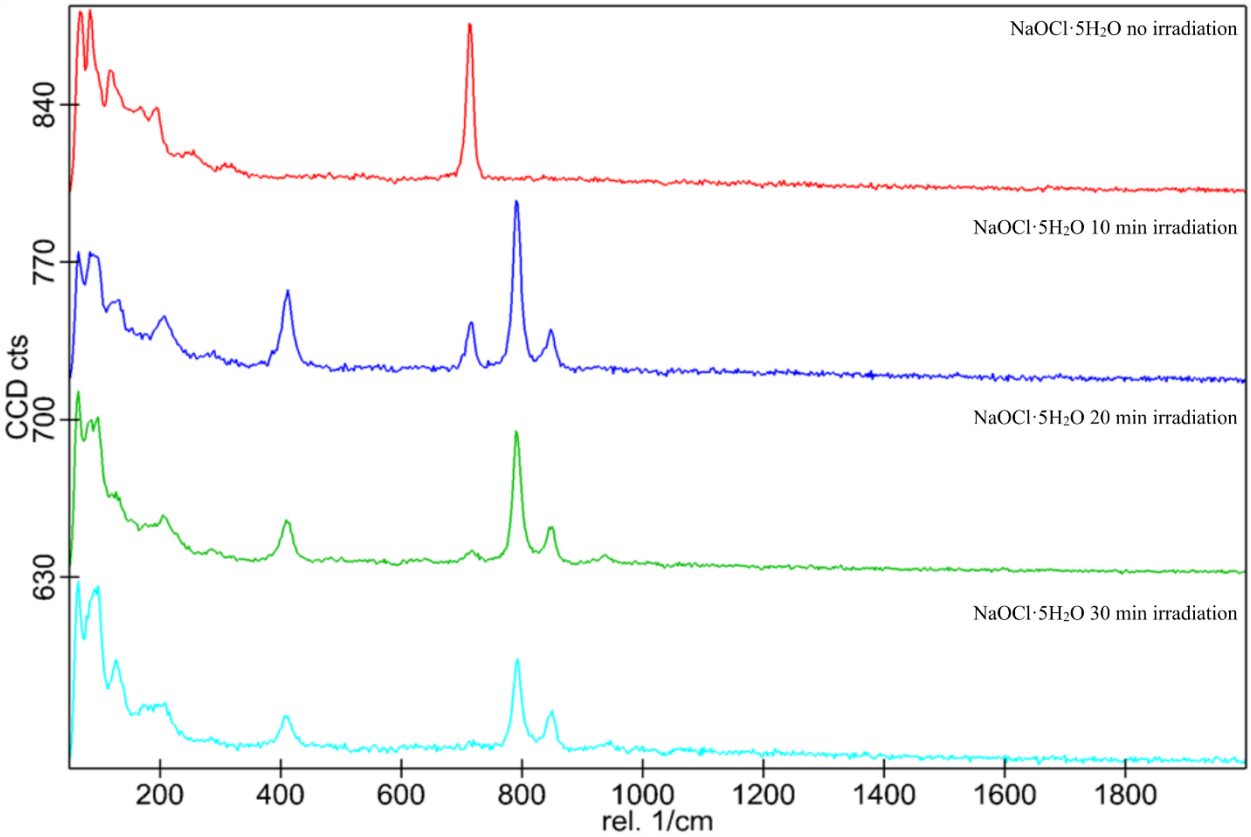

Supplementary Figure 5.1. Individual Raman spectra of NaOCl·5H$_2$O before and after 10 min, 20min, and 30 min of irradiation by a 385 nm LED, and heating to 20 ^{o}C. Each spectrum is the sum of 25 individual spectra acquired at random locations throughout the sample. A 785 nm 20 mW laser was used as the Raman probe. For the irradiation studies the sample was cooled to -30 ^{o}C using a TSMS600 Linkem stage.

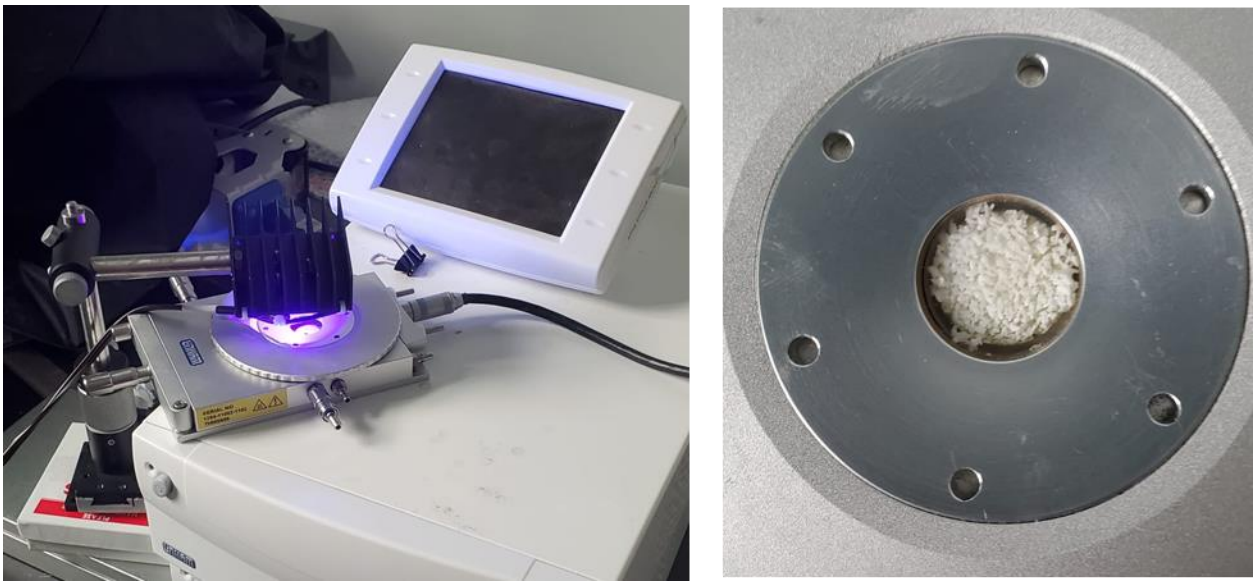

Supplementary Figure 5.2: left) Photographs of the experimental set up using a 400 mA, 14.5 V, 385 nm LED, cooled to -30 ºC using a TSMS600 Linkem stage attached to a nitrogen dewar. right) Photograph of sample following 30 mins of irradiation.

5.6.2 Monitoring of heating solid-state hypochlorite by Raman spectroscopy

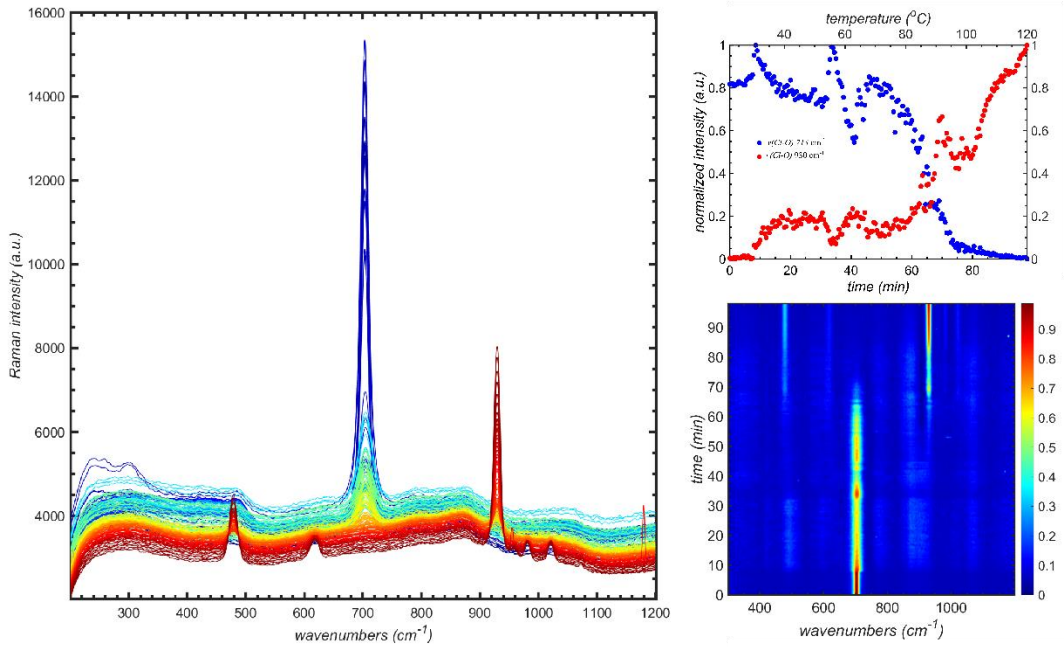

Supplementary Figure 5.3. *in situ* Raman monitoring of heating of a solid $NaOCl \cdot 5H_2O$ from 0–120 ºC. Using a 785 nm 400 mW Raman probe.

5.6.3 Montoring of solution-based photo-reaction of hypochlorite

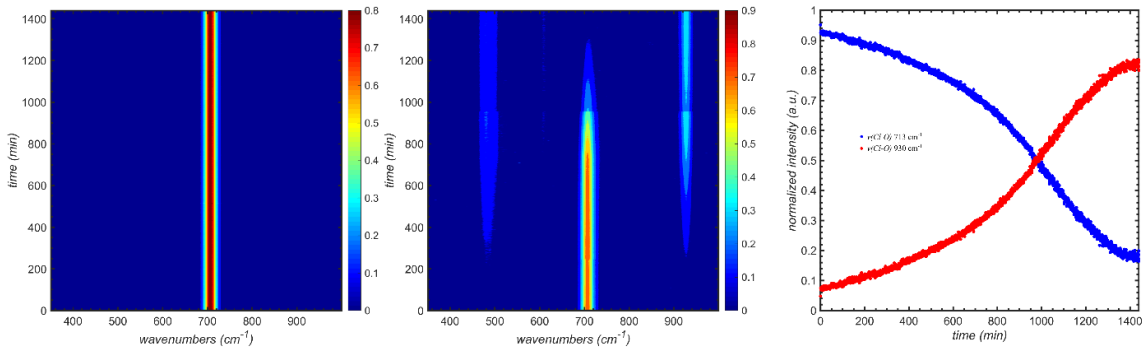

Supplementary Figure 5.4. *in situ* Raman monitoring of a pre-dissolved 10 M solution of $NaOCl{\cdot}5H_2O$ under constant irradiation by either a 100 mW 532 nm laser (left) or 50 mW 375 nm laser (right), both experiments used a 785 nm Raman probe.

5.6.4 Periodic DFT computational studies

Periodic DFT calculations were performed using the plane-wave DFT code CASTEP .[1] The input files were prepared from the CIFs of the experimentally-determined crystal structures using the program cif2cell.[2] For the 8 mixed salt models, they were generated from the original crystal structures of either hypochlorite or hypobromite. Each model was generated by reducing symmetry from *Pbca* and $P2_1/n$ to *P-1*, and creating a [2 0 0] supercell, after which the oxygen atoms would be removed from predetermined hyphohalites and placed on neighbouring hypohalites to form halites and halides.

Crystal structures of all models were geometry-optimized with respect to atom positions and unit cell parameters, subject to the space group symmetry constraints. The calculations were performed with PBE[3] functionals combined with Grimme D3 semiempirical dispersion correction schemes.[4] The plane-wave basis set was truncated at a 750 eV cutoff and the 1st electronic Brillouin zone was sampled with the 2πx0.07 $Å^{-1}$ Monkhorst-Pack grid k-point spacing.[5] Tight convergence criteria were used in the optimization, namely: 5×10^{-6} eV $atom^{-1}$ for total energy, 0.01 eV $Å^{-1}$ for atomic forces, 5×10^{-4} Å for atomic displacement and 0.02 GPa for residual stress.

Supplementary Table 5.1: Calculated energies of different mixed salt models

	Model %Halite	Energy /eV	ΔE / kJ•mol^{-1}
Hypobromite	0	-18296.83	0.00
	25	-18296.67	16.10
	50	-18296.53	29.49
	75	-18296.13	67.77
	100	-18296.11	70.17
Hypochlorite	0	-36266.42	0.00
	25	-36266.44	-2.07
	50	-36266.29	12.03
	75	-36266.34	7.10
	100	-36266.19	22.11

.

5.6.5 UV-Vis absorbance studies

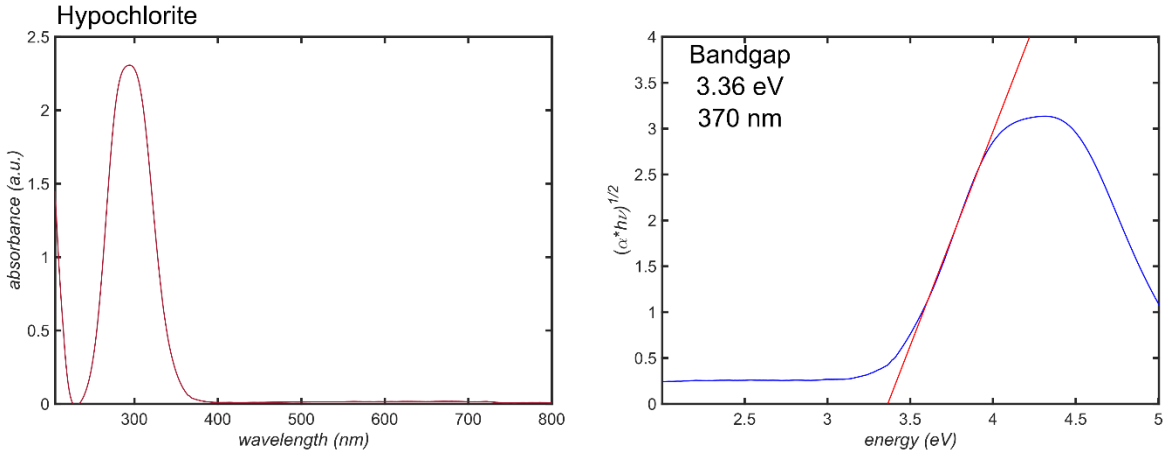

Supplementary Figure 5.5. UV-Vis absorption spectra of hypochlorite desolved in water (left), and calculated tauc plot (right).

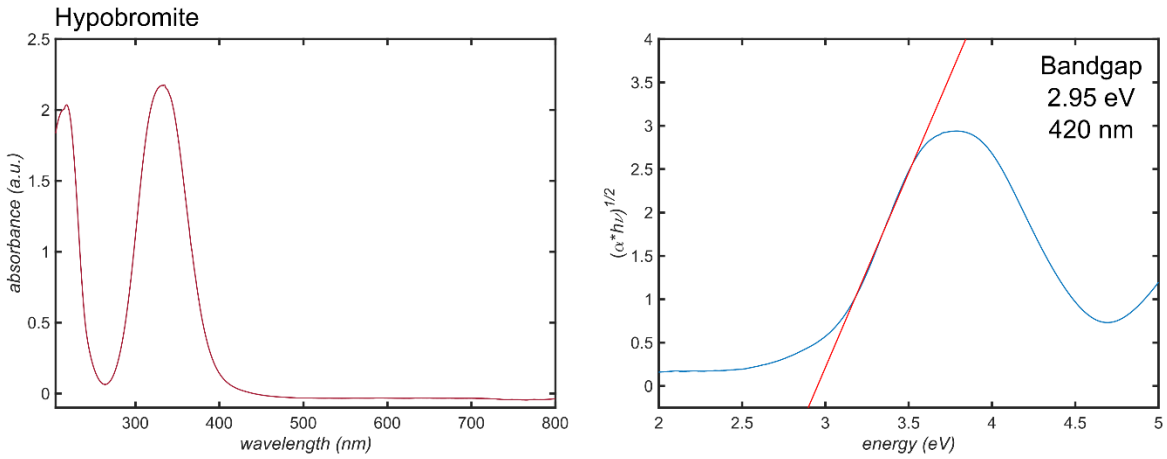

Supplementary Figure 5.6. UV-Vis absorption spectra of hypobromite dissolved in water (left), and calculated from a tauc plot (right).

5.6.6 Monitoring heating response of solid hypobromite

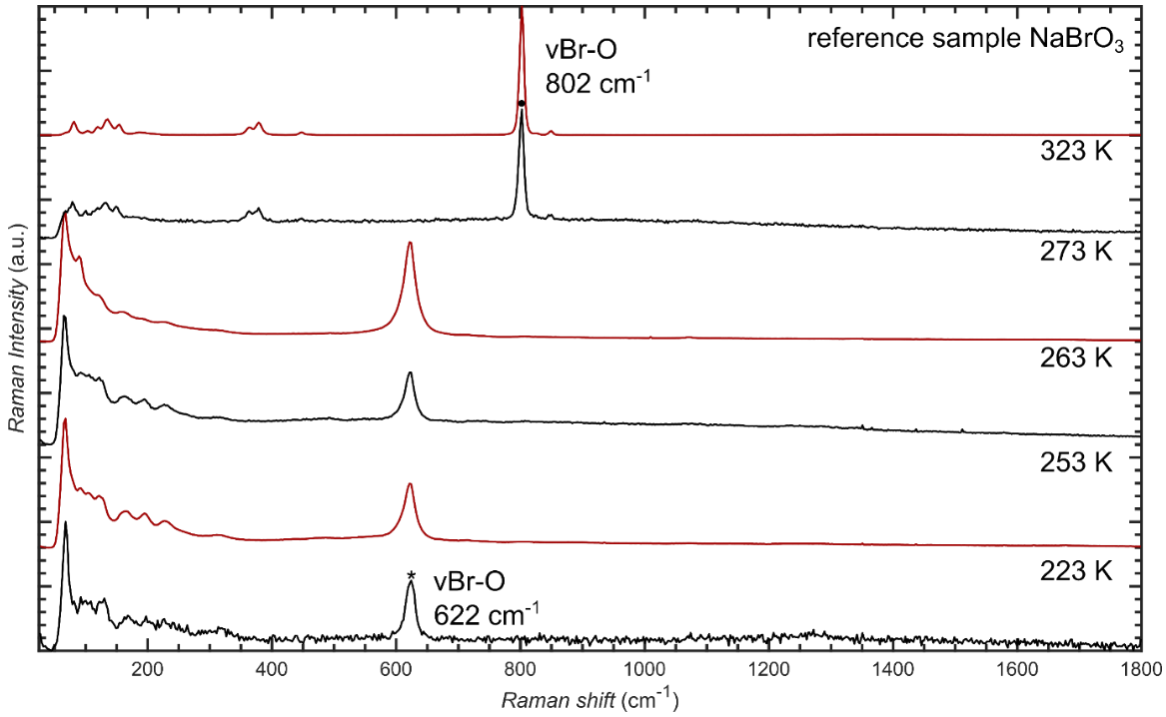

Supplementary Figure 5.7. Individual Raman spectra of $NaBrO{\cdot}5H_2O$ at variable Temperatures, with the single crystal heated from -50 ºC to +50 ºC using a TSMS600 Linkem stage. Raman spectra were acquired using a 785 nm 20 mW Raman probe.

5.6.7 Gas-phase calculations

Structures of hypochlorite, hypobromite, chlorite, and bromite were optimized using the B3LYP theory level with a 6-31G+(d) basis set with Gaussian16 Software[6-10]. The initial transition state calculation was performed by adopting a geometry the experimentally determined crystal structure for each hypohalite, and further refined until a valid transition state calculation was produced. The observation of one imaginary frequency as determined by the second derivative of the of the energy with respect to the internal energy was seen as confirmation of a valid transition state. The transition state geometry was determined to be at a maximum of energy between the reactant and product by Internal Reaction Coordinate (IRC) calculations[11-14]. The geometry of the reactant side of the IRC calculation were those of hypohalite molecules, and the geometry of product side of the IRC was one halide ion and one halite ion. To obtain a suitable energy for the transition state, a point from the IRC calculation that matched the interatomic distances from the experimentally determined X-ray structure for each hypohalite was chosen. The resulting energies from the calculation are shown in the table below.

Supplementary Table 5.2: Calculated energy values of the gas-phase components.

Energies of components (Au)					
Chloride ion	Hypochlorite ion	Chlorite ion	TS	Transition State vs Starting Materials (kcal/mol)	Products vs Reactants (kcal/mol)
-460.27	-1070.77	-610.52	-1070.64	82.65	-17.47
Bromide Ion	Hypobromite ion	Bromite ion	TS	Transition State vs Starting Materials (kcal/mol)	Products vs Reactants (kcal/mol)
-2571.80	-5293.84	-2722.07	-5293.73	71.04	-19.19

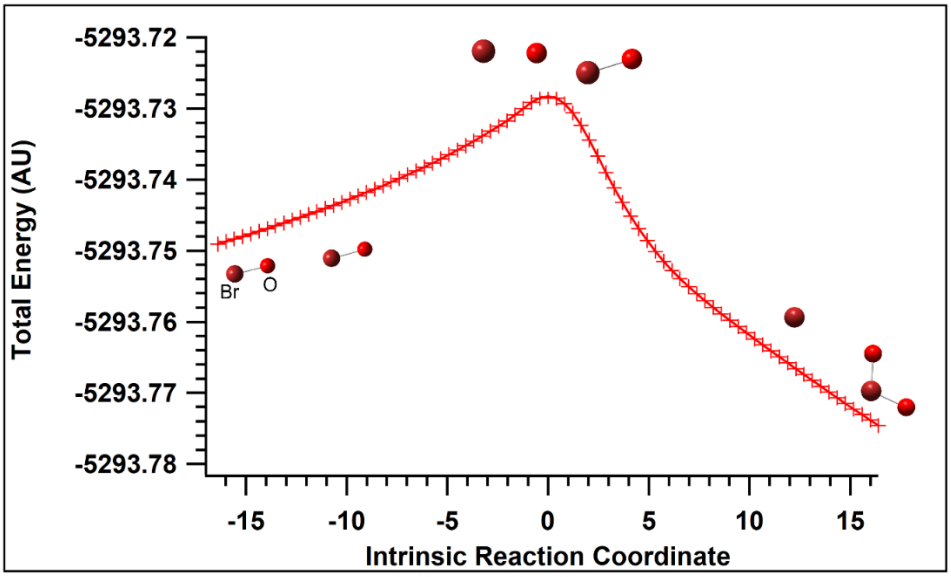

Supplementary Figure 5.8. Intrinsic reaction coordinate energies of a transition state between two hypobromite molecules and bromite + bromine and the corresponding total energy of the system.

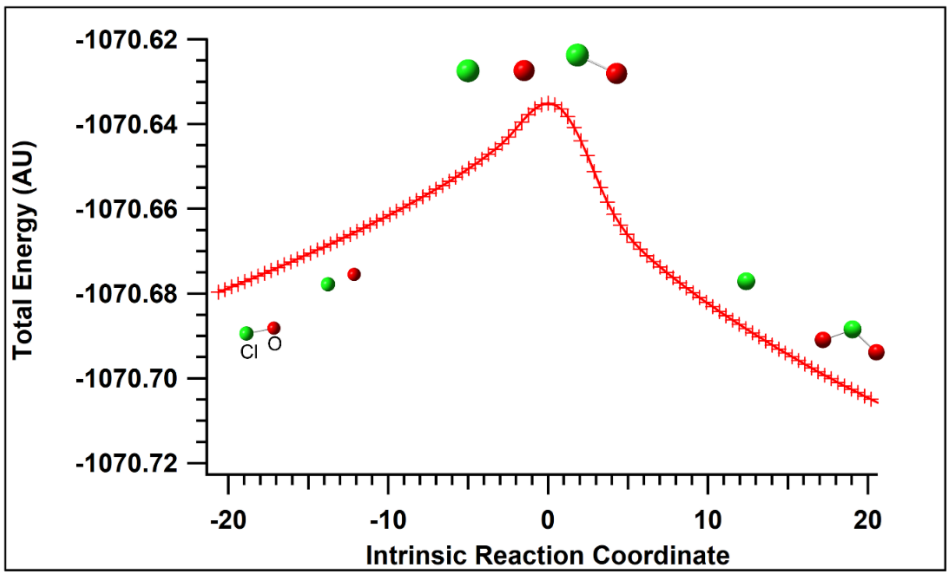

Supplementary Figure 5.9. Intrinsic reaction coordinate energies of a transition state between two hypochlorite molecules and chlorite + chlorine and the corresponding total energy of the system.

5.6.8 Supplementary references

1. Clark, S. J., Segall, M. D., Pickard, C. J., Hasnip, P. J., Probert, M. I. J., Refson, K. & Payne, M. *Kristallogr. Cryst. Mater.* **220**, 5/6, 567–570, (2005).
2. Bjorkman, T. *Comput. Phys. Commun.* **182**, 5, 1183–1186, (2011).
3. Perdew, J. P., Burke, K. & Ernzerhof, M. *Phys. Rev. Lett.* **77**, 3865, (1996).
4. Grimme, S., Antony, J., Ehrlich, S. & Krieg, H. *J. Chem. Phys.* **132**, 154104, (2010).
5. Monkhorst, H. J. & Pack, J. D. *Phys. Rev. B.* **13**, 5188, (1976).
6. Becke, A. D. *J. Chem. Phys.* **98**, 5648–5652, (1993).
7. Lee, C., Yang, W., & Parr, R. G., *Phys. Rev. B: Condens. Matter Mater. Phys.* **37**, 785–789, (1988).
8. Mackenzie, C. F., Spackman, P. R., Jayatilaka, D., & Spackman, M. A. *IUCrJ.* **4**, 575–587, (2017).
9. Frisch, M. J., *et al*., J. *Gaussian 16*, Revision C.01; Gaussian, Inc.: Wallingford, CT, (2016).
10. J. B. Foresman, M. Head-Gordon, J. A. Pople, and M. J. Frisch, *J. Phys. Chem.* **96**, 135–149, (1992).
11. Bauernschmitt, R., & Ahlrichs, R. *Chem. Phys. Lett.* **256**, 454–464, (1996).
12. Mennucci, B., Tomasi, J., Cammi, R., Cheeseman, J. R., Frisch, M. J., Devlin, F. J., Gabriel, S., & Stephens, P. J. *J. Phys. Chem. A.* **106**, 6102–6113, (2002).

Discussion, Summary, and Conclusions

6.1 Discussion

Throughout this Thesis a variety of new photo-active materials and photo-responsive effects have been described in detail. Principally, a completely new and unique photo-mechanical effect coined 'Cold Photo-Carving' (CPC) has been discovered and developed, along with advances in the same materials of already-reported effects of photo-mechanics and photo-chromism in organic crystals and co-crystals. A new photochemistry of inorganic hypohalite ions has also been described here, all of which will now be discussed in a broader context. Chapter 1 provided new insights into previous work on photo-responsive organic solids, and their unique behaviour upon light irradiation, such as photo-mechanical bending. The important role that the crystallographic arrangement has on the potential photo-response has also been discussed, and how one can use crystal engineering tools to mediate chemical reactions,[1] tune luminescent properties,[2] and optimize photo-mechanical properties.[3] The question has been addressed of how using volatile or structurally unstable molecules in crystalline materials as either co-crystals or multicomponent salts can enable a large scale mechanical photo-response of the material as a whole. This Thesis is hoped to lay groundwork for future research which can advance the understanding of photo-responsive solids and how they can be harnessed to provide designer functional optically-responsive materials.

Chapter 2 introduced a pair of halogen-bonded co-crystals of fluorinated azobenzene dyes (*trans*-azo) and a volatile co-crystal former (coformer), either 1,4-dioxane or pyrazine. A single crystal of either (*trans*-azo)(dioxane) or (*trans*-azo)(pyrazine) could be selectively disassembled through irradiation with low-power visible light at room Temperature, shown to be cut, carved,

or engraved with micrometer precision upon laser irradiation. The low-power light required is orders of magnitudes less in intensity than traditional laser beam machining or photo-lithography techniques used to carve metals,[4] ceramics,[5] or polymer resins.[6] It is hypothesized here that the reason that these crystals undergo cold photo-carving, as opposed to other crystalline solids, is due to the unique combination of the thermo- and photo-active properties molecules making up the co-crystals. *Trans*-azo is a light-responsive chromophore, which will convert incident photons to excited state energy sufficient to isomerization to its *cis* geometric form, while pyrazine and dioxane are volatile conformer molecules that can readily sublime away by the input of this energy. These molecules are held together by weak supramolecular interactions through the halogen bonds formed between the iodine of the *trans*-azo and the nitrogen or oxygen atoms of the pyrazine and dioxane respectively. Using weak, soft-bonded supramolecular interactions rather than stronger covalent bonds substantially reduces the required input of energy for laser machining to occur, to wavelengths and intensities low and gentle enough to approach just sunshine. In essence, optimizing both factors described above are key to why CPC can occur in these crystalline solids, under just mild visible irradiation, at just room Temperature.

The process of CPC was characterized by powder X-ray diffraction (PXRD), Raman spectroscopy, high-speed camera photography, and scanning electron microscopy (SEM). Based on these results a mechanism of decomposition was proposed, in which the incident light causes isomerization of the azo component, structural disruption of the crystal packing, and then evaporation of the volatile coformer and recrystallization of *trans*-azo at the edges of the incident beam, all at room Temperature. This proved particularly interesting as the process of irradiation of the co-crystal would lead to decomposition of the co-crystal into a new polymorph of *trans*-azo (*trans*-azo **II**). *Trans*-azo **II** was identified as a kinetic polymorph, which will convert to the more

stable thermodynamically favoured polymorph (*trans*-azo **I**) upon heating to 135 ^{o}C. The fact that the final photo-product is the kinetic polymorph is a clear indication that CPC occurs below 135 ^{o}C, as opposed to traditional laser machining techniques which have been described as "explosive boiling",[7] in which Temperatures over femtoseconds of machining can theoretically reach several thousand Kelvin.[8] The various co-crystals studied possessed different photo-stabilities, with the (*trans*-azo)(pyrazine) co-crystal being the more photo-stable of the two. In PXRD irradiation experiments the pyrazine co-crystal would require a total of 18 hours of continuous irradiation by visible light to convert to *trans*-azo **II**, while the subsequent (*trans*-azo)(dioxane) co-crystal would convert within just 2 hours of irradiation. It was hypothesized that the increased interaction energy (halogen-bond strength) between the chromophore and the volatile coformer is the reason for the enhanced stability of the pyrazine co-crystals.

Chapter 3 introduced two new photo-carvable co-crystals: (*cis*-azo)(dioxane) and (*cis*-azo)(pyrazine), with the halogen-bond donor *cis*-azo being the higher energy, less-stable *cis* isomer of the fluorinated *trans*-azo (*cis*-(*p*-iodoperfluorophenyl)azobenzene) discussed in Chapter 2. Similar to the *trans* co-crystals, experimental results indicated that the (*cis*-azo)(pyrazine) co-crystal offered greater photo-stability than its dioxane counterpart. In addition to the experimental results, the stability of the four co-crystals were explored through theoretical calculations using CASTEP, a periodic density functional theory (DFT) code. These calculations focused on the decomposition energy, for which the predictions were of the enthalpic difference between the respective co-crystals and *trans*-azo **II** crystal + gaseous coformer (dioxane or pyrazine). In both cases the calculations suggested that the pyrazine co-crystals were more stable than their dioxane counterparts, in agreement with experimental results. Additionally, halogen-bond energies between the chromophores and the coformers where calculated, and as expected the pyrazine co-

crystal interaction energies predicted were higher than those of the dioxane co-crystals, suggesting that the stability seen in the photo-studies was related to the halogen-bond strength of the co-crystals. The stability studies also indicated that periodic DFT can be considered a valid technique for comparing decomposition energies of different co-crystals that decompose back into solid and gaseous components.

Cis-azobenzenes are known to be less stable then their *trans*-azobenzene counterparts, and will readily isomerize from *cis* to *trans* through light irradiation or thermal relaxation. The fluorinated *cis*-azo crystals described in Chapter 3 possess enhanced thermal stability against back-isomerization due to the fluorination, and therefore this allows for crystallization as stable solids as either single crystals or as co-crystals. Differing co-crystals of *cis*-azo have been shown to undergo significant mechanical motion upon visible light irradiation. It was proposed that tuning the intensity of light would provide selective control over desired photo-responses of these (*cis*-azo)(dioxane) or (*cis*-azo)(pyrazine) co-crystals. This was indeed found possible when irradiating the co-crystals with either green or blue visible light, as it was observed that the *cis* co-crystals will undergo three separate and distinct intensity-dependent photo-responses. Irradiation with low-intensity (<1 $mW \cdot cm^{-2}$) light irradiation leads to a colour change from a bright yellow to dark red crystals, due to low levels of surface *cis*→*trans* isomerization. Irradiation at higher intensities (150 $mW \cdot mm^{-2}$), causes more extensive azo dye isomerization sufficient to produce photo-mechanical bending driven by a significant near-surface force. At still higher irradiation intensities (2.25 $W \cdot mm^{-2}$) the co-crystals undergo photo-carving, *i.e.* they are readily shaped, punctured, and cut with micrometer precision similar to the *trans* co-crystals, at deep depths.

The photochromic and photo-mechanical responses were directly related to the total *cis* to *trans* isomerization extents occurring within the material. To quantify the amount of isomerization

occurring during these processes, single crystals of (*cis*-azo)(dioxane) were irradiated using either a low intensity source (to induce a colour change) or a higher intensity source (to induce photo-mechanical bending), after which the extent of isomerization for a single crystal was estimated by ^{19}F nuclear magnetic resonance spectroscopy (NMR). The NMR results suggested that the photo-chromic process caused an extent of only 8% isomerization from the *cis* isomer to the *trans* isomer, while the NMR spectra for the photo-mechanical process showed a larger extent of isomerization, with the integration of the peaks assigned as *trans*-azo indicating 17% of the sample was isomerized. A rationalization of the extent of isomerization for the two different processes is as follows: the higher intensity light will induce a larger, more deeply penetrqating amount of *cis* to *trans* isomerization resulting in the photo-mechanical bending due to sufficient internal strain of reorganization of the crystallographic arrangement, while in contrast the lower intensity light leads to a lower, insufficient, surface-confined extent of isomerization, unable to pass a threshold to induce enough strain of the crystal through the *cis* to *trans* isomerization to bend, instead causing the isomerization to be localized to the surface of the crystal causing only the optical change to occur.

An explanation towards the third photo-response (CPC) is that the *cis* co-crystals undergo similar isomerization to that of the *trans*-azo co-crystals *i.e.* the light absorbing dye and volatile coformers combine in such a way that the dye can convert incident photons to mechanical energy sufficient to reach the barrier to crystal re-structuring, allowing the volatile coformers to sublime. To induce this structural photo-response required the highest intensity of light, which could be expected, as opposed to the lower intensity light driven responses, as the change occurring is decomposition of the co-crystal rather than just reversible isomerization-induced photo-chromic or photo-bending of the co-crystals. Raman spectroscopy was used to study the CPC process of

(*cis*-azo)(dioxane) and suggested that the mechanism of the photo-driven process occurs through isomerization of the *cis* co-crystal prior to evaporation of the coformer. Interestingly, a combination of differential scanning colorimetry (DSC), Raman spectroscopy, and optical microscopy revealed that the 'heating process' undergoes a different mechanism of decomposition, in which the evaporation of the coformer occurs prior to isomerization of *cis*-azo. The difference between the two mechanisms could be potentially explained by the heating process inputting energy into the system as a whole, while the photo-process inputs energy specifically to the chromophore, therefore driving the isomerization of the meta stable *cis* back to the thermodynamically favoured *trans* before evaporation of the coformer.

Chapter 4 introduced three additional different co-crystals that undergo CPC with low-powered visible light. The co-crystals are made from the halogen-bond donating *trans*-azo, and halogen-bond accepting azulene (azu) or naphthalene (naph) coformers acting as the volatile components. The co-crystals differ from the previously described co-crystals highlighted in Chapters 2 and 3, as rather than the halogen bond occurring through the iodine atom to heteroatoms (oxygen or nitrogen) the halogen bonding occurs in this case from the C-I···π system of the azu or naph acceptors. The azu co-crystals can form in two separate stoichiometric morphs: a 1:2 (azu)(*trans*-azo)$_2$, and a 3:2 (azu)$_3$(*trans*-azo)$_2$. The azu acts as a second chromophore in these structures as the strongly blue-coloured molecule absorbs red/near-IR light. These co-crystals were designed to investigate how the CPC properties are affected by an additional chromophore, since we had questioned if CPC was strictly a thermal process related to the absorption of the chromophore, or if the azobenzene plays a more pronounced geometric role. If the process is more linked only to the absorption of the molecule, it was hypothesized that the addition of a red absorbing component could have an effect of altering the excitation energy needed to induce CPC.

Naph is the constitutional (structural) isomer of azulene, and forms a 1:2 co-crystal (naph)(*trans*-azo)$_2$ isostructural to (azu)(*trans*-azo)$_2$. Unlike its structural isomer azu, naph does not absorb visible light, and therefore is used as a colourless control throughout the experiments.

All three co-crystals undergo CPC upon irradiation of low powered green light, and the crystals can be cut, carved, and punctured with similar precision to the co-crystals described in Chapters 2 and 3. A 785 nm IR laser was used to test the photo-responsive nature of the co-crystals to low frequency light, and as expected the non-absorbing (naph)(*trans*-azo)$_2$ co-crystal exhibited no inherent photo-response to the IR light even at maximum power. Similarly, azu co-crystals showed no photo-response to low power IR light, however as the power of the laser was increased, the two azu co-crystals underwent a large surface structural modification in the form of epitaxial growth of yellow/orange crystals from the location of irradiation. This response was completely different compared to CPC, in which the laser allows fine control of the surface modification of the crystal, with small *trans*-azo **II** crystallites growing parallel to the surface spot of irradiation. Instead, this IR induced evaporation of azulene is much more pervasive with crystallites of 10+ microns in size growing in an uncontrolled manner in all directions. Interestingly, the resultant crystallites of the IR irradiation were also assigned as *trans*-azo **I**, instead of *trans*-azo **II** (the photo-product of CPC). It is proposed that this is due to the higher power/intensity required to enable the surface modulation when using the IR laser, that would induce greater heating of the surface of the crystal, and therefore cause the crystallization of the higher Temperature polymorph *trans*-azo **I**. Additionally we rationalize the larger modification as also due to the higher power IR laser's larger beam diameter that could evaporate greater areas of the crystal and therefore allowed *trans*-azo to recrystallize as tens of microns-sized *trans*-azo **I** crystallites. Due to the disruptive nature of the IR-based photo-response, we do not consider this a form of CPC, and instead consider

the effect being strictly photo-thermal, in which the high powered IR laser acts as a localized heat source on the area of the irradiation.

Chapters 2–4 have described a total of 7 different co-crystals that exhibit the necessary properties to undergo CPC, and we have shown that CPC isn't reliant on either the halogen-bond donor or acceptor, as long as the components contain both a photo-switch and a volatile conformer molecule. Additionally, the results described in Chapter 4 indicate that halogen-bonding to a π-system is also a plausible crystal engineering approach to form co-crystals that are able to undergo CPC, while adding additional chromophores can allow for more precise optical addressing of the co-crystal through a second distinct response achievable by IR irradiation. Using *cis*-azo rather than *trans*-azo as the photo-switch, the co-crystals will undergo three distinct photo-responses dependant on the intensity of the incoming light. Overall this proof-of-principle work presents a two-fold advance in materials science: it introduces co-crystals of a photo-reversible dye with a volatile co-former as a new class of materials that can be shaped and machined with micrometre precision using low-power visible light, and introduces a new process with clear advantages over those currently used to shape and machine polymers, ceramics, and metals lithographically.

Using the knowledge gained from developing this photo-responsive process for crystalline organic solids, we next wanted to investigate how inorganic salts might respond similarly to visible light. More specifically, in Chapter 5 the photo-responsive nature of crystalline hypochlorite ($NaOCl·5H_2O$) and crystalline hypobromite ($NaOCl·5H_2O$) was described. Despite hypohalites being used as common bleaching agents worldwide for over 200 years,[9] the crystal structures of hypochlorite or hypobromite have only recently been reported, by myself and our Group.[10] Additionally the stability of solid hypohalites had rarely been studied, with only a few thermal stability studies to date, and no studies of any potential photo-response had been published, leading

to a clear lack of understanding of how these common bleaching agents decompose in the solid state. Previous thermal and photo-studies of hypohalites were primarily conducted in solution, and it was found in both cases that hypohalites would decompose into their respective halate, halide, and oxygen components upon photo-irradiation or heating. In both cases the halate formation occurs through a halite intermediate, which remained in low concentration throughout experiments.

Raman spectroscopy investigations revealed that heating of solid state hypohalites leads to decomposition of the hypohalite into halate and halide, the decomposition pathway occurring *via* a melt of the hypohalite and recrystallization into their respective halite forms. Although there was no spectral evidence of any halite intermediate, it was postulated that the reaction progressed with a short-lived halite intermediate. This hypothesis was in good agreement with previously reported solution experiments, suggesting that the melt acts as a saturated solution of hypohalites. In contrast, the photo-studies described here indicated a differing final product, as rather than decomposing into halate as seen in the heating experiments, upon irradiation by UV or visible light the hypohalite would convert to halite. Even with continuous irradiation the resultant halite would not convert to halate.

We believe that the results obtained from these irradiation experiments are a consequence of the unique crystallographic arrangement of these hypohalites in the solid state, in which hypohalite ions of both hypochlorite and hypobromite arrange in linear rows connected by hydrogen-bonding chains of water molecules. Within each row the hypohalites exhibit an intermolecular distance between the halogen atom on one molecule and its neighbouring oxygen atom of 3.656 Å for Cl···O and 3.522 Å for Br···O, which slightly exceeds the accepted van der Waals radii of the molecules of 3.27 Å and 3.37 Å respectively. Due to this proximity of the

molecules, we believe that the laser induces localized heating at the point of irradiation sufficient to cause a transition from the hypohalite to halite and halide, through the oxygen 'leaping' from one hypohalite to the next. We also believe that the crystallographic arrangement is the reason why the reaction doesn't progress further towards a halate final product, with either multiple hypohalite ions or halite ions being too far apart from each other to react within the rigid structure. This differs from solution or melt experiments in which these ions have far larger freedom to form the thermodynamically favoured halate product.

Interestingly, irradiation of hypobromite produced visible holes in the single crystals, similar to the cold photo-carving of the organic co-crystals studied in Chapters 2–4. Even at low powers (< 0.5 mW), the process of conversion of hypobromite to bromite and bromide decomposed the crystal so rapidly that Raman spectra of a fully converted bromite photo-product could not be obtained. The more rapid decomposition of the hypobromite crystal compared to the hypochlorite crystal can be explained through a combination of theoretical results and bandgap studies. Periodic DFT code CASTEP analysis provided insight into the potential stability of several mixed salt models (containing a combination of halite, hypohalite, and halide), in which the models containing a combination of hypobromite, bromite, and bromide were predicted to be less stable than their hypochlorite counterparts, when compared to the stability of the initial crystal structure. Additional gas-phase calculations were used to estimate proposed transition states from hypohalite to halite + halide, and in this case the transition state of the hypobromite system was lower in energy than that of the hypochlorite system, and therefore it can be assumed that the formation of bromite would progress more quickly than the formation of chlorite. Finally, bandgap estimates through the experimentally obtained absorbance spectra of hypobromite and hypochlorite dissolved in water indicated that hypobromite possessed the lower bandgap and would absorb

blue/green light as opposed to the UV absorbing hypochlorite ion. Therefore through the absorbance of the hypobromite solid, the green laser would be expected to induce more heating as opposed to with the hypochlorite solid. The combination of the instability of the product, the lower energy transition state, and the absorbance of the hypobromite ion all may potentially play a role in why the 'photo-carving' occurs in this inorganic salt. We have demonstrated here the first-ever report of photo-reactivity of hypohalites in the solid state, in which hypohalites decompose into halite and halide species upon photo-irradiation, as opposed to the halate and halide forms reported upon thermal heating of solids or solutions. We believe that the unique crystallographic arrangement of the hypohalites is the reason for this specific photo-reactivity, and that the light acts as a localized heat source to induce the reaction.

6.2 Summary and Conclusions

Overall this Thesis outlined how light irradiation can be used to induce a variety of effects in crystalline materials, from *cis* to *trans* isomerization leading to photo-chromic and photo-mechanical responses, to photo-decomposition leading to materials that can be cut, carved, and engraved precisely with low powered light, through evaporation of a volatile component (CPC) or due to decomposition of an inorganic hypobromite to bromite and bromide. In a broader context, this Thesis not only introduces CPC as a new photo-mechanical effect, but it also demonstrates the potential of crystal engineering in optimizing desired photo-responsive materials. It was shown here that one can fine-tune the stability of co-crystals by using a variety of halogen-bond acceptors, which was investigated both theoretically and experimentally. Additionally, varying the halogen-bond donor (*i.e. cis*-azo for *trans*-azo) introduced new controllable photo-responses, triggered

selectively with the intensity of the irradiation of the light. We also explored new photo-responsive properties that are introduced by adding a second chromophore as the volatile component, in which we have developed a wavelength-dependent multi-responsive crystalline material. Lastly, we discovered new chemistry occurring in the solid state by using a laser beam as a localized heating source. Inorganic topochemical reactions were enabled, converting hypohalites to halites plus halides in the solid state, a reaction which previously showed only minor conversion in solution studies. In addition to expanding development of the process of CPC into inorganic materials, we have introduced a new way to convert hypohalites to halites photo-chemically in the solid state, a process which can be scaled up in the future. Perhaps more importantly, we have shown that when these OXO ions are arranged in a head-to-tail fashion to form chains, they can undergo an unusual photo-response, not seen in solution. This process may be further investigated with a large range of different OXO ions that arrange in a similar manner in the solid state, allowing us to better understand these aspects of fundamental inorganic solid state photo-chemistry.

This Thesis has attempted to highlight the potential of using molecular photo-switches to engineer materials that will undergo CPC. Two specific azobenzene dyes (*cis*-azo, and *trans*-azo) have been reported here, though many more photo-switchable dyes remain to be studied, including additional azobenzenes, but also perhaps different types of photo-switches such as stilbenes, hydrazones, spiropyrans, or diarylethenes might also be successful. Using such dyes and volatile molecules in the development of future materials might be beneficial as a 'bottom-up' molecular approach for shaping future optoelectronics materials by CPC. Materials that can be shaped and engraved precisely to micrometer or higher resolution in a controlled low-energy process using low-powered visible light, as introduced and discussed throughout this Thesis, may well enable

significant advances to a wide variety of micro-optical and nano-engineering materials applications in the future.

It is hoped that this Thesis lays groundwork for future research that can advance the understanding of photo-responsive solids and how they can be optimized to provide advanced functional materials. CPC has exclusively been studied with specific systems (halogen-bonding organic co-crystals), yet perhaps future research can explore how CPC might be adapted to different supramolecular systems, such as hydrogen-bonding crystalline materials, or even coordination polymers. Further understanding of the CPC process may also allow for implementation of the technique to other non-crystalline systems, such as polymers, liquid crystals, and molecular glasses. A basic understanding of how CPC occurs in the solid state has been presented and addressed throughout this Thesis, and it is now hoped that from this work, a wider variety of materials that can undergo CPC might be discovered and developed in the future.

6.3 References

1. MacGillivray, L. R., *et al*. Supramolecular Control of Reactivity in the Solid State: From Templates to Ladderanes to Metal–Organic Frameworks. *Acc. Chem. Res.* **41**, 280–291 (2008).
2. Bhowal, R., Biswas, S., Adiyeri Saseendran, D. P., Koner, A. L. & Chopra, D. Tuning the solid-state emission by co-crystallization through σ- and π-hole directed intermolecular interactions. *CrystEngComm.* **21**, 1940-1947, (2019).
3. Bushuyev, O. S., Corkery, T. C., Barrett, C. J. & Friščić, T. Photo-mechanical Azobenzene Cocrystals and *in situ* X-ray Diffraction Monitoring of their Optically-Induced Crystal-to-Crystal Isomerisation. *Chem. Sci.* **5**, 3158–3164 (2014).
4. Bei, H., Shim, S., Miller, M. K., Pharr, G. M. & George, E. P. Effects of Focused Ion Beam Milling on the Nanomechanical Behavior of a Molybdenum-alloy Single Crystal. *Appl. Phys. Lett.* **91**, 111915 (2007).
5. Samant, A. N. & Dahotre, N. B. Laser Machining of Structural Ceramics-A Review. *J. Eur. Ceram. Soc.* **29**, 6, 969–993 (2009).
6. Yao, Y., Zhang, L., Leydecker, T. & Samorì, P. Direct Photolithography on Molecular Crystals for High Performance Organic Optoelectronic Devices. *J. Am. Chem. Soc.* **140**, 6984–6990 (2018).
7. Wood, M. J. *et al*. Femtosecond Laser Micromachining of Co-polymeric Urethane Materials. *Appl. Surf. Sci.* **483**, 633–641 (2019).
8. Cerezo, A. & Smith, G. D. W. Measurement of Temperature Rises in the Femtosecond Laser Pulsed Three-Dimensional Atom Probe. *Appl. Phys. Lett.* **88**, 154103 (2006).
9. Scott, J. On the Disinfecting Properties of Labarraque's Preparations of Chlorine, 3rd ed. *Published by S. Highley,* London (1828).
10. Topić, F., Marrett, J. M., Borchers, T. H., Titi, H. M., Barrett, C. J. & Friščić, T. After 200 Years: The Structure of Bleach and Characterization of Hyphalite Ions by Single-Crystal X-ray Diffraction. *Angew. Chem. Int. Ed.* **60**, 24400 (2021).

Appendix 5: Master Bibliography

1. Szymański, W., Beierle, J. M., Kistemaker, H. A. V., Velema, W. A. & Feringa, B. L. Reversible Photocontrol of Biological Systems by the Incorporation of Molecular Photoswitches. *Chem. Rev.* **113**, 6114-6178, (2013).
2. Andjaba, J. M., Rybak, C. J., Wang, Z., Ling, J., Mein, J., & Uyeda, C. Catalytic Synthesis of Conjugated Azopolymers from Aromatic Diazides. *J. Am. Chem. Soc.* **143**, 3975-3982, (2021).
3. Fang, L. Zhang, H., Li, Z., Zhang, Y., Zhang, Y., & Zhang, H. Synthesis of Reactive Azobenzene Main-Chain Liquid Crystalline Polymers via Michael Addition Polymerization and Photomechanical Effects of Their Supramolecular Hydrogen-Bonded Fibers. *Macromolecules* **46**, 7650-7660, (2013).
4. Thum, M. D., Ratchford, D. C., Casalini, R., Wynne, J. H. & Lundin, J. G. Azobenzene-Doped Liquid Crystals in Electrospun Nanofibrous Mats for Photochemical Phase Control. *ACS Appl. Nano Mater.* **4**, 297-304, (2021).
5. Russew, M.-M. & Hecht, S. Photoswitches: From Molecules to Materials. *Advan. Mater.* **22**, 3348-3360, (2010).
6. Hemmer, J. R. *et al.* Tunable Visible and Near Infrared Photoswitches. *J. Am. Chem. Soc.* **138**, (2016).
7. Kim, D. Li, L., Jiang, X. L., Shivshankar, V., Kumar, J., & Tripathy, S. K. Polarized laser induced holographic surface relief gratings on polymer films. *Macromolecules* **28**, 8835-8839 (1995).
8. Yager, K. G. & Barrett, C. J. All-optical patterning of azo polymer films. *Current Opinion in Solid State and Materials Science* **5**, 487-494, (2001).
9. Barrett, C. J., Mamiya, J.-i., Yager, K. G. & Ikeda, T. Photo-mechanical effects in azobenzene-containing soft materials. *Soft Matter* **3**, 1249-1261, (2007).
10. Banghart, M. R., Mourot, A., Fortin, D. L., Yao, J. Z., Kramer, R. H., & Trauner, D. Photochromic Blockers of Voltage-Gated Potassium Channels. *Angew. Chem. Int. Ed.* **48**, 9097-9101, (2009).
11. Liu, D., Xie, Y., Shao, H. & Jiang, X. Using Azobenzene-Embedded Self-Assembled Monolayers To Photochemically Control Cell Adhesion Reversibly. *Angew. Chem. Int. Ed.* **48**, 4406-4408, (2009).
12. Ferri, V. Elbing, M., Pace, G., Dickey, M. D., Zharnikov, & M., Samori, P. Light-Powered Electrical Switch Based on Cargo-Lifting Azobenzene Monolayers. *Angew. Chem. Int. Ed.* **47**, 3407-3409, (2008).
13. Wang, Y., Han, P., Zu, H., Wang, Z., Zhang, X., & Kabonov, A. V. Photocontrolled Self-Assembly and Disassembly of Block Ionomer Complex Vesicles: A Facile Approach toward Supramolecular Polymer Nanocontainers. *Langmuir* **26**, 709-715, (2010).

14. Baroncini, M., Groppi, J., Corra, S., Silvi, S. & Credi, A. Light-Responsive (Supra)Molecular Architectures: Recent Advances. *Adv. Opt. Mater.* **7**, 1900392, (2019).

15. Bandara, H. D. & Burdette, S. C. Photoisomerization in different classes of azobenzene. *Chem. Rev.* **41**, 1809-1825, (2012).

16. Castellanos, S. Goulet-Hanssens, A., Zhao, F., Dikhtiarenko, A., Pustovarenko, A., Hect, S., Gascon, J., Kapteijn, F., & Bleger D. Structural Effects in Visible-Light-Responsive Metal–Organic Frameworks Incorporating ortho-Fluoroazobenzenes. *Eur. J. Chem.* **22**, 746-752, (2016).

17. Goulet-Hanssens, A. & Barrett, C. J. Photo-control of biological systems with azobenzene polymers. *Journal of Polymer Science Part A: Polymer Chemistry* **51**, 3058-3070, (2013).

18. Lee, K. M., Koerner, H., Vaia, R. A., Bunning, T. J. & White, T. J. Relationship between the Photomechanical Response and the Thermomechanical Properties of Azobenzene Liquid Crystalline Polymer Networks. *Macromolecules* **43**, 8185-8190, (2010).

19. Ikeda, T. & Tsutsumi, O. Optical switching and image storage by means of azobenzene liquid-crystal films. *Science* **268**, 1873-1875 (1995).

20. Pang, X., Lv, J.-a., Zhu, C., Qin, L. & Yu, Y. Photodeformable Azobenzene-Containing Liquid Crystal Polymers and Soft Actuators. *Adv. Mater.* **31**, 1904224, (2019).

21. Yamada, M., Kondo, M., Mamiya, J.-I., Yu, Y., Kinoshita, M., Barrett, C. J., Photomobile Polymer Materials: Towards Light-Driven Plastic Motors. *Angew. Chem. Int. Ed.* **47**, 4986-4988, (2008).

22. Zeng, H., Wani, O. M., Wasylczyk, P. & Priimagi, A. Light-Driven, Caterpillar-Inspired Miniature Inching Robot. *Macromolecular Rapid Communications* **39**, 1700224, (2018).

23. Tanchak, O. M. & Barrett, C. J. Light-Induced Reversible Volume Changes in Thin Films of Azo Polymers: The Photomechanical Effect. *Macromolecules* **38**, 10566-10570, (2005).

24. Kim, K., Park, H., Park, K. J, Park, S. H., Kim, H. H., & Lee, S. Light-Directed Soft Mass Migration for Micro/Nanophotonics. *Adv. Opt. Mater.* **7**, 1900074, (2019).

25. Liang, X., Nishioka, H., Takenaka, N. & Asanuma, H. A DNA Nanomachine Powered by Light Irradiation. *ChemBioChem* **9**, 702-705, (2008).

26. Klajn, R., Wesson, P. J., Bishop, K. J. M. & Grzybowski, B. A. Writing Self-Erasing Images using Metastable Nanoparticle "Inks". *Angew. Chem. Int. Ed.* **48**, 7035-7039, (2009).

27. Landry, M. J., Gu, K., Harris, S. N., Al-Alwan, L., Gutsin, L., De Biasio, D., Jiang, B., Nakamura, D., S. Corkery, T. C., Kennedy, T. E., & Barrett, C. J. Tunable Engineered Extracellular Matrix Materials: Polyelectrolyte Multilayers Promote Improved Neural Cell Growth and Survival. *Macromol Biosci.* **19**, 1900036, (2019).

28. Landry, M. J., Applegate, M. B., Bushyev, O., S., Omenetto, F. G., Kaplan, D. L, Cronin-Golomb, M., & Barrett, C. J. Photo-induced structural modification of silk gels containing azobenzene side groups. *Soft Matter* **13**, 2903-2906, (2017).

29. Comstock, M. J., Levy, N. Kirakosian, A., Cho, J., Lauterwasser, F., Harvey, J. H., Strubbe, D. A., Frechet, J. M. J., Trauner, D., Louie, S. G., & Crommie, M. F. Reversible Photomechanical Switching of Individual Engineered Molecules at a Metallic Surface. *Phys. Rev. Lett.* **99**, 038301, (2007).

30. Borowiak, M., Nahoboo, W., Reynders, M., Nekolla, K., Jalinot, P., Hasserodt, J., Rehberg, M., Delattre, M., Zahler, S., Vollmar, A., Trauner, D., & Thorn-Seshold, O. Photoswitchable Inhibitors of Microtubule Dynamics Optically Control Mitosis and Cell Death. *Cell* **162**, 403-411, (2015).

31. Fortin, D. L., Banghart, M. R., Dunn, T. W., Borges, K., Wagenaar, D. A., Gaudry, Q., Karakossian, M. H., Otis, T. S., Kristan, W. B., Trauner, D. & Kramer, R. H. Photochemical control of endogenous ion channels and cellular excitability. *Nat. Methods* **5**, 331-338, (2008).

32. Koshima, H. & Ojima, N. Photomechanical bending of 4-aminoazobenzene crystals. *Dyes Pigm* **92**, 798-801, (2012).

33. Taniguchi, T., Asahi, T. & Koshima, H. Photomechanical Azobenzene Crystals. *Crystals* **9**, 437 (2019).

34. Sun, S., Liang, S., Xu, W.-C., Xu, G. & Wu, S. Photoresponsive polymers with multi-azobenzene groups. *Polym. Chem.* **10**, 4389-4401, (2019).

35. Bléger, D., Schwarz, J., Brouwer, A. M. & Hecht, S. o-Fluoroazobenzenes as Readily Synthesized Photoswitches Offering Nearly Quantitative Two-Way Isomerization with Visible Light. *J. Am. Chem. Soc.* **134**, 20597-20600, (2012).

36. Aggarwal, K., Kuka, T. P., Banik, M., Medellin, B. P., Ngo, C. Q., Xie, D., Fernandes, Y., Dangerfield, T. L., Ye., E., Bouley, B., Jounson, K. A., Zhang, Y. J., Eberhart, J. K., & Que, E. L. Visible Light Mediated Bidirectional Control over Carbonic Anhydrase Activity in Cells and in Vivo Using Azobenzenesulfonamides. *J. Am. Chem. Soc.* **142**, 14522-14531, (2020).

37. Bushuyev, O. S., Corkery, T. C., Barrett, C. J. & Friščić, T. Photo-mechanical azobenzene cocrystals and in situ X-ray diffraction monitoring of their optically-induced crystal-to-crystal isomerisation. *Chem. Sci.* **5**, 3158-3164, (2014).

38. Stumpel, J. E. *et al.* Surface-Relief Gratings in Halogen-Bonded Polymer–Azobenzene Complexes: A Concentration-Dependence Study. *Molecules* **22**, 1844 (2017).

39. Kravchenko, A., Shevchenko, A., Ovchinnikov, V., Priimagi, A. & Kaivola, M. Optical Interference Lithography Using Azobenzene-Functionalized Polymers for Micro- and Nanopatterning of Silicon. *Adv. Mater.* **23**, 4174-4177, (2011).

40. Desiraju, G. R. Crystal Engineering: From Molecule to Crystal. *J. Am. Chem. Soc.* **135**, 9952-9967, (2013).

41. Biradha, K. & Santra, R. Crystal engineering of topochemical solid state reactions. *Chem. Soc. Rev.* **42**, 950-967, (2013).

42. Mir, N. A., Dubey, R. & Desiraju, G. R. Strategy and Methodology in the Synthesis of Multicomponent Molecular Solids: The Quest for Higher Cocrystals. *Acc. Chem. Res.* **52**, 2210-2220, (2019).

43. Aitipamula, S. *et al.* Polymorphs, Salts, and Cocrystals: What's in a Name? *Cryst. Growth Des.* **12**, 2147-2152, (2012).

44. Thakuria, R. & Sarma, B. Drug-Drug and Drug-Nutraceutical Cocrystal/Salt as Alternative Medicine for Combination Therapy: A Crystal Engineering Approach. *Crystals* **8**, 101 (2018).

45. Duggirala, N. K., Perry, M. L., Almarsson, Ö. & Zaworotko, M. J. Pharmaceutical cocrystals: along the path to improved medicines. *Chem. Commun.* **52**, 640-655, (2016).

46. Kavanagh, O. N., Croker, D. M., Walker, G. M. & Zaworotko, M. J. Pharmaceutical cocrystals: from serendipity to design to application. *Drug Discov. Today* **24**, 796-804, (2019).

47. MacGillivray, L. R. Papaefstathiou, G., Friščić, T., Hamilton, T. D., Bucar, D.-K., Chu, Q., Varshney, D. B., & Georgiev, I. G. Supramolecular Control of Reactivity in the Solid State: From Templates to Ladderanes to Metal−Organic Frameworks. *Acc. Chem. Res.* **41**, 280-291, (2008).

48. Lu, B., Fang, X. & Yan, D. Luminescent Polymorphic Co-crystals: A Promising Way to the Diversity of Molecular Assembly, Fluorescence Polarization, and Optical Waveguide. *ACS Appl. Mater. Interfaces* **12**, 31940-31951, (2020).

49. Christopherson, J. C., Topić, F., Barrett, C. J. & Friščić, T. Halogen-Bonded Cocrystals as Optical Materials: Next-Generation Control over Light–Matter Interactions. *Cryst. Growth. Des.* **18**, 1245-1259, doi:10.1021/acs.cgd.7b01445 (2018).

50. Liu, C.-H., Niazi, M. R. & Perepichka, D. F. Strong Enhancement of π-Electron Donor/Acceptor Ability by Complementary DD/AA Hydrogen Bonding. *Angew. Chem. Int. Ed.* **58**, 17312-17321, (2019).

51. Bora, P., Saikia, B. & Sarma, B. Regulation of π···π Stacking Interactions in Small Molecule Cocrystals and/or Salts for Physiochemical Property Modulation. *Cryst. Growth. Des.* **18**, 1448-1458, (2018).

52. Karki, S., Friščić, T. & Jones, W. Control and interconversion of cocrystal stoichiometry in grinding: stepwise mechanism for the formation of a hydrogen-bonded cocrystal. *CrystEngComm* **11**, 470-481, (2009).

53. Cinčić, D., Friščić, T. & Jones, W. Isostructural Materials Achieved by Using Structurally Equivalent Donors and Acceptors in Halogen-Bonded Cocrystals. *Chem. Eur. J.* **14**, 747-753, (2008).

54. Xiao, Y., Liu, Y. Q., Li, G. & Huang, P. Microwave-assisted synthesis, structure and properties of a co-crystal compound with 2-ethoxy-6-methyliminomethyl-phenol. *Supramol Chem.* **27**, 161-166, (2015).

55. Steiner, T. The hydrogen bond in the solid state. *Angew. Chem. Int. Ed.* **41**, 48-76 (2002).

56. Gilli, G. & Gilli, P. *The nature of the hydrogen bond: outline of a comprehensive hydrogen bond theory*. Vol. 23 (Oxford university press, 2009).

57. Kollman, P. A. & Allen, L. C. Theory of the hydrogen bond. *Chem. Rev.* **72**, 283-303 (1972).

58. Desiraju, G. R. Supramolecular Synthons in Crystal Engineering—A New Organic Synthesis. *Angew. Chem. Int. Ed.* **34**, 2311-2327, (1995).

59. Saikia, B., Bora, P., Khatioda, R. & Sarma, B. Hydrogen Bond Synthons in the Interplay of Solubility and Membrane Permeability/Diffusion in Variable Stoichiometry Drug Cocrystals. *Cryst. Growth Des.* **15**, 5593-5603, (2015).

60. Bavishi, D. D. & Borkhataria, C. H. Spring and parachute: How cocrystals enhance solubility. *Prog. Cryst. Growth. Charact. Mater.* **62**, 1-8, (2016).

61. Bolla, G. & Nangia, A. Pharmaceutical cocrystals: walking the talk. *Chem. Commun.* **52**, 8342-8360, doi:10.1039/C6CC02943D (2016).

62. Gala, U., Chuong, M. C., Varanasi, R. & Chauhan, H. Characterization and Comparison of Lidocaine-Tetracaine and Lidocaine-Camphor Eutectic Mixtures Based on Their Crystallization and Hydrogen-Bonding Abilities. *AAPS PharmSciTech* **16**, 528-536, (2015).

63. McNamara, D. P. *et al.* Use of a Glutaric Acid Cocrystal to Improve Oral Bioavailability of a Low Solubility API. *Pharm. Res.* **23**, 1888-1897, (2006).

64. MacGillivray, L. R., Reid, J. L. & Ripmeester, J. A. Supramolecular Control of Reactivity in the Solid State Using Linear Molecular Templates. *J. Am. Chem. Soc.* **122**, 7817-7818, (2000).

65. Sarma, B. & Saikia, B. Hydrogen bond synthon competition in the stabilization of theophylline cocrystals. *CrystEngComm* **16**, 4753-4765, (2014).

66. Mukherjee, A., Tothadi, S. & Desiraju, G. R. Halogen Bonds in Crystal Engineering: Like Hydrogen Bonds yet Different. *Acc. Chem. Res.* **47**, 2514-2524, (2014).

67. Cavallo, G. *et al.* The Halogen Bond. *Chem. Rev.* **116**, 2478-2601, (2016).

68. Clark, T. Halogen bonds and σ-holes. *Faraday. Discuss.* **203**, 9-27 (2017).

69. Forni, A., Pieraccini, S., Rendine, S., Gabas, F. & Sironi, M. Halogen-Bonding Interactions with π Systems: CCSD(T), MP2, and DFT Calculations. *ChemPhysChem* **13**, 4224-4234, (2012).

70. Huber, S. M., Scanlon, J. D., Jimenez-Izal, E., Ugalde, J. M. & Infante, I. On the directionality of halogen bonding. *Phys. Chem. Chem. Phys.* **15**, 10350-10357, (2013).

71. Metrangolo, P., Meyer, F., Pilati, T., Resnati, G. & Terraneo, G. Halogen Bonding in Supramolecular Chemistry. *Angew. Chem. Int. Ed.* **47**, 6114-6127, (2008).

72. Metrangolo, P. & Resnati, G. Type II halogen···halogen contacts are halogen bonds. *IUCrJ* **1**, 5-7, (2014).

73. Siram, R. B. K., Karothu, D. P., Guru Row, T. N. & Patil, S. Unique Type II Halogen···Halogen Interactions in Pentafluorophenyl-Appended 2,2′-Bithiazoles. *Cryst. Growth. Des.* **13**, 1045-1049, (2013).

74. Ford, M. C., Saxton, M. & Ho, P. S. Sulfur as an Acceptor to Bromine in Biomolecular Halogen Bonds. *J. Phys. Chem. Lett.* **8**, 4246-4252, (2017).

75. Daniliuc, C. G., Hrib, C. G., Jones, P. G. & du Mont, W.-W. Directed Selenium–Iodine Halogen Bonding and Se···H–C Contacts in Solid Iododiisopropylphosphane Selenide. *Cryst. Growth. Des.* **12**, 185-188, (2012).

76. Lisac, K. *et al.* Halogen-bonded cocrystallization with phosphorus, arsenic and antimony acceptors. *Nat. Commun.* **10**, 61, (2019).

77. Robertson, C. C. *et al.* Hydrogen bonding vs. halogen bonding: the solvent decides. *Chem. Sci.* **8**, 5392-5398, (2017).

78. Gullo, M. C., Baldini, L., Casnati, A. & Marchiò, L. Halogen Bonds Direct the Solid State Architectures of a Multivalent Iodopropargylcalix[4]arene. *Cryst. Growth Des.* **20**, 3611-3616, (2020).

79. Gurbanov, A. V. *et al.* Halogen bonding in cadmium(ii) MOFs: its influence on the structure and on the nitroaldol reaction in aqueous medium. *Dalton Trans.* **51**, 1019-1031, (2022).

80. Amombo Noa, F. M., Bourne, S. A., Su, H., Weber, E. & Nassimbeni, L. R. Hydrogen Bonding versus Halogen Bonding in Host–Guest Compounds. *Cryst. Growth Des.* **16**, 4765-4771, (2016).

81. Saccone, M. *et al.* Photoresponsive Halogen-Bonded Liquid Crystals: The Role of Aromatic Fluorine Substitution. *Chem. of Mater.* **31**, 462-470, (2019).

82. Bushuyev, O. S., Friščić, T. & Barrett, C. J. Controlling Dichroism of Molecular Crystals by Cocrystallization. *Cryst. Growth Des.* **16**, 541-545, (2016).

83. Xiao, L. *et al.* Room-Temperature Phosphorescence in Pure Organic Materials: Halogen Bonding Switching Effects. *Chem. Eur. J.* **24**, 1801-1805, (2018).

84. Priimagi, A. *et al.* Halogen Bonding versus Hydrogen Bonding in Driving Self-Assembly and Performance of Light-Responsive Supramolecular Polymers. *Adv. Funct. Mater.* **22**, 2572-2579, (2012).

85. Hirshfeld, F. L. & Schmidt, G. M. J. Topochemical control of solid-state polymerization. *Journal of Polymer Science Part A: General Papers* **2**, 2181-2190, (1964).

86. Cohen, M. D. & Schmidt, G. M. J. 383. Topochemistry. Part I. A survey. *Journal of the Chemical Society (Resumed)*, 1996-2000, (1964).

87. Cohen, M. D., Schmidt, G. M. J. & Sonntag, F. I. 384. Topochemistry. Part II. The photochemistry of trans-cinnamic acids. *Journal of the Chemical Society (Resumed)*, (1964).

88. Bhogala, B. R., Captain, B., Parthasarathy, A. & Ramamurthy, V. Thiourea as a Template for Photodimerization of Azastilbenes. *J. Am. Chem. Soc.* **132**, 13434-13442, (2010).

89. Sinnwell, M. A. & MacGillivray, L. R. Halogen-Bond-Templated [2+2] Photodimerization in the Solid State: Directed Synthesis and Rare Self-Inclusion of a Halogenated Product. *Angew. Chem. Int. Ed.* **55**, 3477-3480, (2016).

90. Liu, D. *et al.* Single-Crystal-to-Single-Crystal Transformations of Two Three-Dimensional Coordination Polymers through Regioselective [2+2] Photodimerization Reactions. *Angew. Chem. Int. Ed.* **49**, 4767-4770, (2010).

91. Gao, X., Friščić, T. & MacGillivray, L. R. Supramolecular Construction of Molecular Ladders in the Solid State. *Angew. Chem. Int. Ed.* **43**, 232-236, (2004).

92. Rath, B. B. & Vittal, J. J. Single-Crystal-to-Single-Crystal [2 + 2] Photocycloaddition Reaction in a Photosalient One-Dimensional Coordination Polymer of Pb(II). *J. Am. Chem. Soc.* **142**, 20117-20123, doi:10.1021/jacs.0c09577 (2020).

93. Medishetty, R., Koh, L. L., Kole, G. K. & Vittal, J. J. Solid-State Structural Transformations from 2D Interdigitated Layers to 3D Interpenetrated Structures. *Angew. Chem. Int. Ed.* **50**, 10949-10952, (2011).

94. Li, C., Campillo-Alvarado, G., Swenson, D. C. & MacGillivray, L. R. Exploiting Aurophilic Interactions in a [2 + 2] Photocycloaddition: Single-Crystal Reactivity with Changes to Surface Morphology. *Inorg. Chem.* **58**, 12497-12500, (2019).

95. Alfuth, J., Jeannin, O. & Fourmigué, M. Topochemical, Single-Crystal-to-Single-Crystal [2+2] Photocycloadditions Driven by Chalcogen-Bonding Interactions. *Angew. Chem. Int. Ed.* **61**, e202206249, (2022).

96. Quentin, J., Reinheimer, E. W. & MacGillivray, L. R. Halogen-Bond Mediated [2+2] Photodimerizations: À la Carte Access to Unsymmetrical Cyclobutanes in the Solid State. *Molecules* **27**, 1048 (2022).

97. Li, M., Schlüter, A. D. & Sakamoto, J. Solid-State Photopolymerization of a Shape-Persistent Macrocycle with Two 1,8-Diazaanthracene Units in a Single Crystal. *J. Am. Chem. Soc.* **134**, 11721-11725, (2012).

98. Servalli, M., Trapp, N. & Schlüter, A. D. Single-Crystal-to-Single-Crystal (SCSC) Linear Polymerization of a Desymmetrized Anthraphane. *Chem. Eur. J.* **24**, 15003-15012, (2018).

99. Morimoto, K. *et al.* Correlating Reaction Dynamics and Size Change during the Photomechanical Transformation of 9-Methylanthracene Single Crystals. *Angew. Chem. Int. Ed.* **61**, e202114089, (2022).

100. Matsumoto, A., Nagahama, S. & Odani, T. Molecular Design and Polymer Structure Control Based on Polymer Crystal Engineering. Topochemical Polymerization of 1,3-Diene Mono- and Dicarboxylic Acid Derivatives Bearing a Naphthylmethylammonium Group as the Countercation. *J. Am. Chem. Soc.* **122**, 9109-9119, (2000).

101. Nagahama, S., Inoue, K., Sada, K., Miyata, M. & Matsumoto, A. Two-Dimensional Hydrogen Bond Networks Supported by CH/π Interaction Leading to a Molecular Packing Appropriate for Topochemical Polymerization of 1,3-Diene Monomers. *Cryst. Growth Des.* **3**, 247-256, (2003).

102. Sun, A., Lauher, J. W. & Goroff, N. S. Preparation of Poly(diiododiacetylene), an Ordered Conjugated Polymer of Carbon and Iodine. *Science* **312**, 1030-1034, (2006).

103. Luo, L. *et al.* Poly(diiododiacetylene): Preparation, Isolation, and Full Characterization of a Very Simple Poly(diacetylene). *J. Am. Chem. Soc.* **130**, 7702-7709, (2008).

104. Xu, R., Schweizer, W. B. & Frauenrath, H. Perfluorophenyl–Phenyl Interactions in the Crystallization and Topochemical Polymerization of Triacetylene Monomers. *Chem. Eur. J.* **15**, 9105-9116, (2009).

105. Itoh, T. *et al.* Cis-Specific Topochemical Polymerization: Alternating Copolymerization of 7,7,8,8-Tetrakis(methoxycarbonyl)quinodimethane with 7,7,8,8-Tetracyanoquinodimethane in the Solid State. *Angew. Chem. Int. Ed.* **50**, 2253-2256, (2011).

106. Samanta, R. *et al.* Mechanical Actuation and Patterning of Rewritable Crystalline Monomer−Polymer Heterostructures via Topochemical Polymerization in a Dual-Responsive Photochromic Organic Material. *ACS. Appl. Mater. Interfaces* **12**, 16856-16863, (2020).

107. Qi, A. *et al.* Hydroxypropyl Cellulose Methacrylate as a Photo-Patternable and Biodegradable Hybrid Paper Substrate for Cell Culture and Other Bioapplications. *Adv. Healthc. Mater.* **3**, 543-554, (2014).

108. Scott, J. L. & Tanaka, K. Photochromic Crystals: Toward an Understanding of Color Development in the Solid State. *Cryst. Growth Des.* **5**, 1209-1213, (2005).

109. Irie, M., Fukaminato, T., Matsuda, K. & Kobatake, S. Photochromism of Diarylethene Molecules and Crystals: Memories, Switches, and Actuators. *Chem. Rev.* **114**, 12174-12277, (2014).

110. Li, X., Xu, Y., Li, F. & Ma, Y. Organic light-emitting diodes based on an ambipolar single crystal. *Org. Electron.* **13**, 762-766, (2012).

111. Huang, R., Wang, C., Wang, Y. & Zhang, H. Elastic Self-Doping Organic Single Crystals Exhibiting Flexible Optical Waveguide and Amplified Spontaneous Emission. *Adv. Mater.* **30**, 1800814, (2018).

112. Cariati, E. *et al.* Tuning second-order NLO responses through halogen bonding. *Chem. Commun.* 2590-2592, (2007).

113. Christopherson, J.-C. *et al.* Assembly and dichroism of a four-component halogen-bonded metal–organic cocrystal salt solvate involving dicyanoaurate(I) acceptors. *Faraday Discuss.* **203**, 441-457, (2017).

114. Vainauskas, J., Topić, F., Bushuyev, O. S., Barrett, C. J. & Friščić, T. Halogen bonding to the azulene π-system: cocrystal design of pleochroism. *Chem. Commun.* **56**, 15145-15148, (2020).

115. Natansohn, A. & Rochon, P. Photoinduced Motions in Azo-Containing Polymers. *Chem. Rev.* **102**, 4139-4176, (2002).

116. Zhao, Y. & Ikeda, T. *Smart light-responsive materials: azobenzene-containing polymers and liquid crystals*. (John Wiley & Sons, 2009).

117. Schönhoff, M., Mertesdorf, M. & Lösche, M. Mechanism of photoreorientation of azobenzene dyes in molecular films. *J. Phys. Chem.* **100**, 7558-7565 (1996).

118. Campillo-Alvarado, G., Liu, R. J., Davies, D. W. & Diao, Y. Enhancing Single-Crystal Dichroism of an Asymmetric Azo Chromophore by Perfluorophenyl Embraces and Boron Coordination. *Cryst. Growth Des.* **21**, 3143-3147 (2021).

119. Morimoto, K., Tsujioka, H., Kitagawa, D. & Kobatake, S. Photoreversible Birefringence Change of Diarylethene Single Crystals as Revealed by Change in Molecular

Polarizability Anisotropy. *J. Phys. Chem. A* **124**, 4732-4741, doi:10.1021/acs.jpca.0c02774 (2020).

120. Liu, H., Lu, Z., Zhang, Z., Wang, Y. & Zhang, H. Highly Elastic Organic Crystals for Flexible Optical Waveguides. *Angew. Chem. Int. Ed.* **57**, 8448-8452, (2018).

121. Gierschner, J. *et al.* Luminescence in Crystalline Organic Materials: From Molecules to Molecular Solids. *Adv. Opt. Mater.* **9**, 2002251, (2021).

122. Tang, S. *et al.* Organic Crystalline Optical Waveguides That Remain Elastic from −196 to ≈200 °C. *Adv. Opt. Mater.* 2200627, (2022).

123. Hayashi, S. & Koizumi, T. Elastic Organic Crystals of a Fluorescent π-Conjugated Molecule. *Angew. Chem. Int. Ed.* **55**, 2701-2704, (2016).

124. Panda, M. K. *et al.* Spatially resolved analysis of short-range structure perturbations in a plastically bent molecular crystal. *Nat. Chem.* **7**, 65-72, (2015).

125. Lan, L. *et al.* Organic Single-Crystal Actuators and Waveguides that Operate at Low Temperatures. *Adv. Mater.* **34**, 2200471, (2022).

126. Karothu, D. P. *et al.* Mechanically robust amino acid crystals as fiber-optic transducers and wide bandpass filters for optical communication in the near-infrared. *Nat. Commun.* **12**, 1326, (2021).

127. Di, Q. *et al.* Fluorescence-based thermal sensing with elastic organic crystals. *Nat. Commun.* **13**, 5280, (2022).

128. Chu, X. *et al.* Engineering Mechanical Compliance of an Organic Compound toward Flexible Crystal Lasing Media. *J. Phys. Chem. Lett.* **11**, 5433-5438, (2020).

129. Du, S., Ma, S., Xu, B. & Tian, W. Optical Waveguide and Photoluminescent Polarization in Organic Cocrystal Polymorphs. *J. Phys. Chem. Lett.* **12**, 9233-9238, (2021).

130. Shao, B. *et al.* Luminescent switching and structural transition through multiple external stimuli based on organic molecular polymorphs. *J. Mater. Chem. C* **7**, 3263-3268, (2019).

131. Ma, Y.-X., Wei, G.-Q., Chen, S., Lin, H.-T. & Wang, X.-D. Self-assembled organic homostructures with tunable optical waveguides fabricated via “cocrystal engineering”. *Chem. Commun.* **57**, 11803-11806, (2021).

132. Feng, Q. *et al.* Tuning solid-state fluorescence of pyrene derivatives via a cocrystal strategy. *CrystEngComm* **15**, 3623-3629, (2013).

133. Shen, Q. J., Wei, H. Q., Zou, W. S., Sun, H. L. & Jin, W. J. Cocrystals assembled by pyrene and 1,2- or 1,4-diiodotetrafluorobenzenes and their phosphorescent behaviors modulated by local molecular environment. *CrystEngComm* **14**, 1010-1015, (2012).

134. Yan, D. *et al.* A Cocrystal Strategy to Tune the Luminescent Properties of Stilbene-Type Organic Solid-State Materials. *Angew. Chem. Int. Ed.* **50**, 12483-12486, (2011).

135. Bhowal, R., Biswas, S., Adiyeri Saseendran, D. P., Koner, A. L. & Chopra, D. Tuning the solid-state emission by co-crystallization through σ- and π-hole directed intermolecular interactions. *CrystEngComm* **21**, 1940-1947, (2019).

136. Salunke, J. K. *et al.* Halogen-Bond-Assisted Photoluminescence Modulation in Carbazole-Based Emitter. *Sci. Rep.* **8**, 14431, (2018).

137. d'Agostino, S., Grepioni, F., Braga, D. & Ventura, B. Tipping the Balance with the Aid of Stoichiometry: Room Temperature Phosphorescence versus Fluorescence in Organic Cocrystals. *Cryst. Growth Des.* **15**, 2039-2045, (2015).

138. Shen, Q. J. *et al.* Phosphorescent cocrystals constructed by 1,4-diiodotetrafluorobenzene and polyaromatic hydrocarbons based on C–I···π halogen bonding and other assisting weak interactions. *CrystEngComm* **14**, 5027-5034, (2012).

139. Naumov, P. *et al.* The Rise of the Dynamic Crystals. *J. Am. Chem. Soc.* **142**, 13256-13272, (2020).

140. Vogelsberg, C. S. & Garcia-Garibay, M. A. Crystalline molecular machines: function, phase order, dimensionality, and composition. *Chem. Soc. Rev.* **41**, 1892-1910, (2012).

141. Yu, Q. *et al.* Photomechanical Organic Crystals as Smart Materials for Advanced Applications. *Chem. Eur. J.* **25**, 5611-5622, (2019).

142. Khalil, A., Ahmed, E. & Naumov, P. Metal-coated thermosalient crystals as electrical fuses. *Chem. Commun.* **53**, 8470-8473, (2017).

143. Kobatake, S., Takami, S., Muto, H., Ishikawa, T. & Irie, M. Rapid and reversible shape changes of molecular crystals on photoirradiation. *Nature* **446**, 778-781 (2007).

144. Tong, F., Liu, M., Al-Kaysi, R. O. & Bardeen, C. J. Surfactant-Enhanced Photoisomerization and Photomechanical Response in Molecular Crystal Nanowires. *Langmuir* **34**, 1627-1634, (2018).

145. Tong, F., Kitagawa, D., Bushnak, I., Al-Kaysi, R. O. & Bardeen, C. J. Light-Powered Autonomous Flagella-Like Motion of Molecular Crystal Microwires. *Angew. Chem. Int. Ed.* **60**, 2414-2423, (2021).

146. Tong, F., Al-Haidar, M., Zhu, L., Al-Kaysi, R. O. & Bardeen, C. J. Photoinduced peeling of molecular crystals. *Chem. Commun.* **55**, 3709-3712, (2019).

147. Uchida, E., Azumi, R. & Norikane, Y. Light-induced crawling of crystals on a glass surface. *Nat. Commun.* **6**, 7310, (2015).

148. Bushuyev, O. S., Tomberg, A., Friščić, T. & Barrett, C. J. Shaping Crystals with Light: Crystal-to-Crystal Isomerization and Photomechanical Effect in Fluorinated Azobenzenes. *J. Am. Chem. Soc.* **135**, 12556-12559, (2013).

149. Bushuyev, O. S., Singleton, T. A. & Barrett, C. J. Fast, Reversible, and General Photomechanical Motion in Single Crystals of Various Azo Compounds Using Visible Light. *Adv. Mater.* **25**, 1796-1800, (2013).

150. Bushuyev, O. S. *et al.* Azo...phenyl stacking: a persistent self-assembly motif guides the assembly of fluorinated cis-azobenzenes into photo-mechanical needle crystals. *Chem. Commun.* **52**, 2103-2106, (2016).

151. Bartholomew, A. K., Stone, I. B., Steigerwald, M. L., Lambert, T. H. & Roy, X. Highly Twisted Azobenzene Ligand Causes Crystals to Continuously Roll in Sunlight. *J. Am. Chem. Soc.* (2022).

152. Qian, H., Pramanik, S. & Aprahamian, I. Photochromic Hydrazone Switches with Extremely Long Thermal Half-Lives. *J. Am. Chem. Soc.* **139**, 9140-9143, (2017).

153. Ryabchun, A., Li, Q., Lancia, F., Aprahamian, I. & Katsonis, N. Shape-Persistent Actuators from Hydrazone Photoswitches. *J. Am. Chem. Soc.* **141**, 1196-1200, (2019).

154. Shao, B., Qian, H., Li, Q. & Aprahamian, I. Structure Property Analysis of the Solution and Solid-State Properties of Bistable Photochromic Hydrazones. *J. Am. Chem. Soc.* **141**, 8364-8371, (2019).

155. Shao, B. *et al.* Solution and Solid-State Emission Toggling of a Photochromic Hydrazone. *J. Am. Chem. Soc.* **140**, 12323-12327, (2018).

156. Karothu, D. P. *et al.* Exceptionally high work density of a ferroelectric dynamic organic crystal around room temperature. *Nat. Commun.* **13**, 2823, (2022).

157. Naumov, P., Sahoo, S. C., Zakharov, B. A. & Boldyreva, E. V. Dynamic Single Crystals: Kinematic Analysis of Photoinduced Crystal Jumping (The Photosalient Effect). *Angew. Chem. Int. Ed.* **52**, 9990-9995, (2013).

158. Seki, T., Sakurada, K., Muromoto, M. & Ito, H. Photoinduced single-crystal-to-single-crystal phase transition and photosalient effect of a gold(i) isocyanide complex with shortening of intermolecular aurophilic bonds. *Chem. Sci.* **6**, 1491-1497, (2015).

159. Medishetty, R. *et al.* Single Crystals Popping Under UV Light: A Photosalient Effect Triggered by a [2+2] Cycloaddition Reaction. *Angew. Chem. Int. Ed.* **53**, 5907-5911, (2014).

160. Medishetty, R., Sahoo, S. C., Mulijanto, C. E., Naumov, P. & Vittal, J. J. Photosalient Behavior of Photoreactive Crystals. *Chem Mater.* **27**, 1821-1829, (2015).

161. Yao, Y., Zhang, L., Leydecker, T. & Samorì, P. Direct Photolithography on Molecular Crystals for High Performance Organic Optoelectronic Devices. *J. Am. Chem. Soc.* **140**, 6984-6990, (2018).

162. Sun, J. & Litchinitser, N. M. Toward Practical, Subwavelength, Visible-Light Photolithography with Hyperlens. *ACS Nano* **12**, 542-548, (2018).

163. Desbiolles, B. X. E., Bertsch, A. & Renaud, P. Ion beam etching redeposition for 3D multimaterial nanostructure manufacturing. *Microsyst.Nanoeng.* **5**, 11, (2019).

164. Wang, Z. *et al.* Patterning Organic/Inorganic Hybrid Bragg Stacks by Integrating One-Dimensional Photonic Crystals and Macrocavities through Photolithography: Toward Tunable Colorful Patterns as Highly Selective Sensors. *ACS Appl. Mater. Interfaces* **4**, 1397-1403, (2012).

165. Ghorai, S. *et al.* From co-crystals to functional thin films: photolithography using [2+2] photodimerization. *Chem. Sci.* **4**, 4304-4308, (2013).

166. Zaworotko, M. J. Molecules to Crystals, Crystals to Molecules … and Back Again? *Cryst. Growth Des.* **7**, 4–9 (2007).

167. Aakeroy, C. B., Wijethunga, T. K., Benton, J. & Desper, J. Stabilizing Volatile Liquid Chemicals using Co-Crystalization. *Chem. Commun.* **51**, 2425-2428 (2015).

168. Raatikainen, K. & Rissanen, K. Breathing Molecular Crystals: Halogen- and Hydrogen-Bonded Porous Molecular Crystals with Solvent Induced Adaptation of the Nanosized Channels. *Chem. Sci.* **3**, 1235–1239 (2012).

169. Metrangolo, P. *et al*. Nonporous Organic Solids Capable of Dynamically Resolving Mixtures of Diiodoperfluoroalkanes. *Science* **323**, 1461–1464 (2009).

170. Catalano, L. *et al*. Dynamic Characterization of Crystalline Supramolecular Rotors Assembled through Halogen Bonding. *J. Am. Chem. Soc.* **137**, 15386–15389 (2015).

171. Szell, P. M. J., Zablotny, S. & Bryce, D. L. Halogen Bonding as a Supramolecular Dynamics Catalyst. *Nat. Commun.* **10**, 916 (2019).

172. Cavallo, G. *et al*. Superfluorinated Ionic Liquid Crystals Based on Supramolecular, Halogen-Bonded Anions. *Angew. Chem. Int. Ed.* **55**, 6300–6304 (2016).

173. Priimagi, A., Cavallo, G., Metrangolo, P. & Resnati, G. The Halogen Bond in the Design of Functional Supramolecular Materials: Recent Advances. *Acc. Chem. Res.* **46**, 2686–2695 (2013).

174. Saccone, M. & Catalano, L. Halogen Bonding beyond Crystals in Materials Science. *J. Phys. Chem. B*, **123**, 9281–9290 (2019).

175. Naumov, P., Chizhik, S., Panda. M. K., Nath, N. K. & Boldyreva, E. Mechanically Responsive Molecular Crystals. *Chem. Rev.* **115**, 12440–12490 (2015).

176. Natarajan, A. *et al*. The Photoarrangement of α-Santonin is a Single-Crystal-to-Single-Crystal Reaction: A Long Kept Secret in Solid-State Organic Chemistry Revealed. *J. Am. Chem. Soc.* **129**, 9846–9847 (2007).

177. Chu, Q., Swenson, D. C. & MacGillivray, L. R. A Single-Crystal-to-Single-Crystal Transformation Mediated by Argentophilic Forces Converts a Finite Metal Complex into an Infinite Coordination Network. *Angew. Chem. Int. Ed.* **44**, 3569–3572 (2005).

178. Toh, N. L., Nagarathinam, M. & Vittal, J. J. Topochemical Photodimerization in the Coordination Polymer $[\{(CF_3CO_2)(\mu\text{-}O_2CCH_3)Zn\}_2(\mu\text{-bpe})_2]_n$ through Single-Crystal to Single-Crystal Transformation. *Angew. Chem. Int. Ed.* **117**, 2277–2281 (2005).

179. Kitagawa, D. *et al*. Control of Photomechanical Crystal Twisting by Illumination Direction. *J. Am. Chem. Soc.* **140**, 4208–4212 (2018).

180. Halabi, J. M., Ahmed, E., Sofela, S. & Naumov, P. Performance of Molecular Crystals in Conversion of Light to Mechanical Work. *Proc. Natl. Acad. Sci. U.S.A.* **118**, e2020604118 (2021).

181. Halabi, J. M. *et al*. Spatial Photocontrol of the Optical Output from an Organic Crystal Waveguide. *J. Am. Chem. Soc.* **141**, 14966–14970 (2019).

182. Grobelny, A. L., Verdu, F. A., & Groeneman, R. H. Solvent-free Synthesis and Purification of a Photoproduct *via* Sublimation of a Tetrahalogenated Template. *CrystEngComm* **19**, 3562–3565 (2017)

183. Li, W. *et al*. Shaping Organic Microcrystals Using Focused Ion Beam Milling. *Cryst. Growth Des.* **20**, 1583–1589 (2020).

184. Wood, M. J. *et al*. Femtosecond Laser Micromachining of Co-polymeric Urethane Materials. *Appl. Surf. Sci*. **483**, 633–641 (2019).

185. Kandidov, V.P., Dormidonov, A. E., Kosareva, O. G., Chin, S. L. & Liu, W. in *self-focusing: Past and Present: Fundamentals and Prospects* (eds Robert W. Boyd, Sventiana G. Lukisova, & Y. R. Shen) 371–298 (springer New York, 2009).

186. Guan, L., Peng, K., Yang, Y., Qiu, X. & Wang, C. The Nanofabrication of Polydimethylsiloxane using a Focused Ion Beam. *Nanotechnology* **20**, 145301 (2009).

187. Alias, M. S., *et al*. Enhanced Etching, Surface Damage Recovery, and Submicron Patterning of Hybrid Perovskites using a Chemically Gas-Assisted Focused-Ion Beam for Subwavelength Grating Photonic Applications. *J. Phys. Chem. Lett.* **7**, 137–142 (2016).

188. Bei, H., Shim, S., Miller, M. K., Pharr, G. M. & George, E. P. Effects of Focused Ion Beam Milling on the Nanomechanical Behavior of a Molybdenum-alloy Single Crystal. *Appl. Phys. Lett.* **91**, 111915 (2007).

189. Vesseur, E. J. R. *et al*. Surface Plasmon Polariton Modes in a Single-Crystal Au Nanoresonator Fabricated using Focused-ion-beam Milling. *Appl. Phys. Lett.* **92**, 083110 (2008).

190. Yager, K. G., Barrett, C. J. Temperature Modeling of Laser-Irradiated Azo-Polymer Thin Films. *J. Chem. Phys.* **120**(2), 1089–1096 (2004)

191. Lommerse, J. P. M., Stone, A. J., Taylor, R. & Allen, F. H. The Nature and Geometry of Intermolecular Interactions between Halogens and Oxygen or Nitrogen. *J. Am. Chem. Soc.* **118**, 3108–3116 (1996).

192. Mantina, M., Chamberlin, A. C., Valero, R., Cramer, C. J. & Truhlar, D. G. Consistent van der Waals Radii for the Whole Main Group. *J. Phys. Chem. A* **113**, 5806–5812 (2009).

193. Salzillo, T. & Brillante, A. Commenting on the Photoreactions of Anthracene Derivatives in the Solid State. *CrystEngComm* **21**, 3127–3136 (2019).

194. Kitamura, I., Oishi, K., Hara, M., Nagano, S. & Seki, T. Photoinitiated Marangoni Flow Morphing in a Liquid Crystalline Polymer Film Directed by Super-Inkjet Printing Patterns. *Sci. Rep.* **9**, 2556 (2019).

195. Cheng, Y.-C., Lu, H.-C., Lee, X., Zeng, H. & Priimagi, A. Kirigami-Based Light-Induced Shape-Morphing and Locomotion. *Adv. Mater.* **32**, 1906233 (2020).

196. Braga, D., Grepioni, F. & Lampronti, G. I. Supramolecular Metathesis: Co-former Exchange in Co-crystals of Pyrazine with (*R*,*R*)-, (*S*,*S*)-, (*R*,*S*)- and (*S*,*S*/*R*,*R*)-tartaric acid. *CrystEngComm* **13**, 3122–3124 (2011).

197. Antoine, J. A. & Lin, Q. Synthesis of Azobenzenes Using *N*-Chlorosuccinimide and 1,8-Diazabicyclo[5.4.0]undec-7-ene (DBU). *J. Org. Chem.* **82**, 9873–9876 (2017).

198. Bruker, APEX3, Bruker AXS Inc., Madison, Wisconsin, USA, 2012.

199. Krause, L., Herbst-Irmer, R., Sheldrick, G. M. & Stalke, D. Comparison of Silver and Molybdenum Microfocus X-ray Sources for Single-crystal Structure Determination. *J. Appl. Cryst.* **48**, 3–10 (2015).

200. Sheldrick, G. M. SHELXT - Integrated Space-Group and Crystal-Structure Determination. *Acta Cryst.* **A71**, 3–8 (2015).

201. Sheldrick, G. M. Crystal Structure Refinement with SHELXL. *Acta Cryst.* **C71**, 3–8 (2015).

202. Dolomanov, O. V., Bourhis, L. J., Gildea, R. J., Howard, J. A. K. & Puschmann, H. OLEX2: A Complete Structure Solution, Refinement and Analysis Program. *J. Appl. Cryst.* **42**, 339–341 (2009).

203. Farrugia, L. J. WinGX and ORTEP for Windows: an Update. *J. Appl. Cryst.* **45**, 849–854 (2012).

204. Frisch, M. J. *et al*. Gaussian 16, Revision C.01, Gaussian, Inc., Wallingford, CT, 2016.

205. Becke, A. D. Density-functional Thermochemistry. III. The Role of Exact Exchange. *J. Chem. Phys.* **98**, 5648–5652 (1993).

206. Lee, C., Yang, W. & Parr, R. G. Development of the Colle-Salvetti Correlation-Energy Formula into a Functional of the Electron Density. *Phys. Rev. B* **37**, 785–789 (1998).

207. Ditchfield, R., Hehre, W. J. & Pople, J. A. Self-Consistent Molecular-Orbital Methods. IX. An Extended Gaussian-Type Basis for Molecular-Orbital Studies of Organic Molecules. *J. Chem. Phys.* **54**, 724–728 (1971).

208. Glukhovtsev, M. N., Pross, A., McGrath, M. P. & Radom, L. Extension of Gaussian-2 (G2) Theory to Bromine- and Iodine-containing Molecules: Use of Effective Core Potentials. *J. Chem. Phys.* **103**, 1878–1885 (1995).

209. Pritchard, B. P., Altarawy, D., Didier, B., Gibson, T. D. & Windus, T. L. New Basis Set Exchange: An Open, Up-to-Date Resource for the Molecular Sciences Community. *J. Chem. Inf. Model.* **59**, 4814–4820 (2019).

210. Shields, D. J., Karothu, D.-P., Sambath K., Ranaweera, R. A. A. U., Schramm, S., Duncan, A., Duncan, B., Krause, J. A., Gudmundsdottir, A. D. & Naumov, P. Cracking

under Internal Pressure: Photodynamic Behavior of Vinyl Azide Crystals through N2 Release. *J. Am. Chem. Soc.* **142**, 18565–18575 (2020).

211. Taniguchi, T., Kubota, A., Moritoki, T., Asahi, T. & Koshima, H. Two-step photomechanical motion of a dibenzobarrelene crystal. *RSC. Adv.* **8**, 34314–34320 (2018).

212. Yue, Y., Shu, Y., Ye, K., Sun, J., Liu, C., Dai, S., Jin, L., Ding, C., Lu, R. Molecular twisting affects the solid-state photochemical reactions of unsaturated ketones and the photomechnical effects of molecular crystals. *Chem. Eur. J.* (2022).

213. Kitagawa, D., Kawasaki, K., Tanaka, R. & Kobatake, S. Mechanical Behavior of Molecular Crystals Induced by Combination of Photochromic Reaction and Reversible Single-Crystal-to-Single-Crystal Phase Transition. *Chem. Mat.* **29**, 7524–7532 (2017).

214. Xu, T., Gao, W., Xu, L.-P., Zhang, X. & Wang, S. Fuel-Free Synthetic Micro-/Nanomachines. *Adv. Mater.* **29**, 1603250 (2017).

215. Xu, L., Mou, F., Gong, H., Luo, M. & Guan, J. Light-driven micro/nanomotors: from fundamentals to applications. *Chem. Soc. Rev.* **46**, 6905–6926 (2017).

216. So, M. C., Wiederrecht, G. P., Mondloch, J. E., Hupp, J. T. & Farha, O. K. Metal–organic framework materials for light-harvesting and energy transfer. *Chem. Commun.* **51**, 3501–3510 (2015).

217. Black, H. T. & Perepichka, D. F. Crystal Engineering of Dual Channel p/n Organic Semiconductors by Complementary Hydrogen Bonding. *Angew. Chem. Int. Ed.* **53**, 2138–2142 (2014).

218. Xu, T.-Y., Tong, F., Xu, H., Wang, M.-Q., Tian, H., Qu, D.-H. Energineering Photomechanical Molecular Crystals to Achieve Extraordinary Expansion Based on Solid-State [2+2] Photocycloaddition. *J. Am. Chem. Soc.* **144**, 14, 6278–6290 (2022).

219. Anthony, J. E., Brooks, J. S., Eaton, D. L. & Parkin, S. R. Functionalized Petacene: Imporved Elctronic Properties from Control of Solid-State Order. *J. Am. Chem. Soc.* **123**, 9482–9483 (2001).

220. Trask, A. V., Motherwell, W. D. S. & Jones, W. Pharmaceutical Cocrystallization: Engineering a Remedy for Caffeine Hydration. *Cryst. Growth. Des.* **5**, 1013–1021 (2005).

221. Gao, G., Chen, M., Roberts, J., Feng, M., Xiao, C., Zhang, G., Parkin, S., Risko, C., & Zhang, L. Rational Functionalization of a C_{70} Buckybowl to Enable a C_{70}:Buckybowl Cocrystal for Organic Semiconductor Applications. *J. Am. Chem. Soc.* **142**, 5, 2460–2470 (2020).

222. Wang, J., Zhang, S. T., Xu, S. P., Li, A. S., Li, B., Ye, L., Geng, Y. J., Tian, Y., & Xu, W. Q. Morphology-Dependent Luminescence and Optical Waveguide Property in Large-

Size Organic Charge Transfer Cocrystals with Anisotropic Spatial Distibution of Transition Dipole Moment. *Adv. Optical. Mater.* **8**, 1901280 (2020).

223. Liu, Y. *et al.* Reversible Luminescent Switching in an Organic Cocrystal: Multi-Stimuli-Induced Crystal-to-Crystal Phase Transformation. *Angew. Chem. Int. Ed.* **59**, 15098–15103 (2020).

224. Clark, S. J., Segall, M. D., Pickard, C. J., Hasnip, P. J., Probert, M. I. J., Refson, K., & Payne, M. C. First principles methods using CASTEP. *Z. Kristallogr. Cryst. Mater.* **220**, 5/6, 567–570 (2005).

225. Bjorkman, T. Generating geometries for electronic structure programs. *Comput. Phys. Commun.* **182**, 5, 1183–1186 (2011).

226. Perdew, J. P., Burke, K., & Ernzerhof, M. Generalized gradiet approximation made simple. *Phys. Rev. Lett.* **77**, 3865 (1996).

227. Grimme, S., Antony, J., Ehrlich, S., & Krieg, H. A consistent and accurate *ab initio* parametrization of density functional dispersion correction (DFT-D) for the 94 elements H-Pu. *J. Chem. Phys.* **132**, 154104 (2010).

228. Monkhorst, H. J., Pack, J. D. Special points for the brillouin-zone integrations. *Phys. Rev. B.* **13**, 5188 (1976).

229. Huang, K. S., Britton, D., Etter, M., C., & Byrn, S. R. A Novel Class of Phenol-Pyridine Co-crystals for Second Harmonic Generation. *J. Mater. Chem.* **5**, 713-720, (1997).

230. Adamo, C. Toward Reliable Density Functional Methods without Adjustable Parameters: The PBEO Model. J. *Chem. Phys*. **110**, 6158 (1999).

231. Dunning, T. H. Gaussian Basis Sets for use in Correlated Molecular Calculations. 1. The Atoms Boron Through Neon and Hydrogen. *J. Chem. Phys.* **90**, 1007, (1989).

232. Pauling L. General Chemistry. *Dover Publications, New York, (*1988).

233. Lang, J.-P. Chlorine, Bromine, Iodine & Astatine: Inorganic Chemistry: in *Encyclopedia of Inorganic Chemistry*, Wiley, Online, (2005).

234. King, R. B. Inorganic Chemistry of Main Group Elements. Wiley-VCH, Weinheim, (1994).

235. Berthollet, C. L. Description du Blanchiment des Toiles et des Fils par l'Acide Muriatique Oxygéné, et de Quelques Autres Propriétés de Cette Liqueur Relatives Aux Arts, *Annales de Chimie*, ***2***, 151–190, (1789).

236. Dorveaux, P. L'invention de l'eau de Javel. *Revue d'Histoire de la Pharmacie*, **63**, 286–287, (1929).

237. Scott, J. On the Disinfecting Properties of Labarraque's Preparations of Chlorine. 3rd Edition, Published by S. Highley, 174 Fleet Street, London (1828).

238. https://www.fortunebusinessinsights.com/sodium-hypochlorite-market-105064 (accessed December 1, 2022)

239. Wang, Z. Comprehensive Organic Name Reactions and Reagents. John Wiley & Sons, 1447–1450, (2010)

240. Alternative drinking-water disinfectants: bromine, iodine and silver. World Health Organization, Geneva, 2018.

241. Scholder, R., & Krauss, K. Über kristallisierte Alkalihypobromite. *Zeit. Anorg. Allg. Chem.* **268**, *279290*, (1952).

242. Lister, M. W. The Decomposition of Hypochlorous Acid. *Can. J. Chem.* **30**, 879–889, (1952).

243. Chapin, R. M. The effect of hydrogen-ion concentration on the decomposition of Hypohalites. *J. Am. Chem. Soc*. **56**, 11, 2211–2215, (1934).

244. Adam, L. C., & Gordon, G. Hypochlorite Ion Decomposition: Effects of Temperature, Ionic Strength, and Chloride ion. *Inorg. Chem.* **38**, 6, 1299–1304 (1999).

245. Lister, M. W. Decomposition of sodium hypochlorite the uncatalyzed Reaction. *Can. J. Chem.* **34**, 465–478, (1956).

246. Farkas, L., & Klein, F. S. On the Photo-Chemistry of Some Ions in Solution. *J. Chem. Phys.* **16**, 886–893, (1948).

247. Allmand, A. J., Cunliffe, P. W., & Maddison, R. E. W. The Photodecomposition of Chlorine water and of Aqueous Hypochlorous Acid Soluitions Part I. *J. Chem. Soc.*, **127**, 822, (1925).

248. Allmand, A. J., Cunliffe, P. W., & Maddison, R. E. W. The Photodecomposition of Chlorine water and of Aqueous Hypochlorous Acid Soluitions Part II. *J. Chem. Soc.*, **127**, 655–669, (1927).

249. G. V. Buxton and R. J. Williams, Photochemical decom positions of aqueous solutions of oxyanions of chlorine and chlorine dioxide. *Proc. Chem Soc.* **141**, **(**1962).

250. Buxton. G. V., & Subhani, M. S. Radiation Chemistry and photochemistry of oxychlorine ions. Part 2. –Photodecomposition of aqueous solutions of hypochlorite ions. ***J***. *Chem. Soc., Faraday trans.* **68**, 958–969, (1972).

251. Topić, F., Marrett, J. M., Borchers, T. H., Titi, H. M., Barrett, C. J., & Friščić, T. After 200 Years: The Structure of Bleach and Characterization of Hypohalite Ions by Single-Crystal X-ray Diffraction. *Angew. Chem. Int. Ed.* **60**, 24400, (2021).

252. Kirhara, M., Okada, T., Sugiyama, Y., Akiyoshi, M., Matsunaga, T., & Kimura, Y. Sodium hypochlorite pentahydrate crystals ($NaOCl{\cdot}5H_2O$): A convenient and environmentally benign oxidant for organic synthesis. *Org. Process Res. Dev.* **21**, 12, 1925–1927, (2017).

253. Okada, T., Asawa, T., Sugiyama, Y., Iwai, T., Kirihara, M., & Kimura, Y. Sodium hypochlorite pentahydrate ($NaOCl{\cdot}5H_2O$) crystals; An effective re-oxidant for TEMPO oxidation. *Tetrahedron*. **72**, 22, 2818–2827 (2016).

254. US 3498924, Walsh RH, Dietz A, "Process for preparing stable sodium hypochlorites", issued (1966).

255. Levason, W., Ogden, J. S., Spicer, M. D., & Young, N. A. Characterisation of the oxo-anions of bromine BrO_x^-(x=1-4) by Infrared, Raman, Nuclear Magnetic Resonance, and Bromine K-edge extended X-ray Absorption fine Structure Techniques. *J. Chem. Soc., Dalton Trans*. 349–353, (1990).

260. John Wiley & Sons, Inc. SpectraBase; SpectraBase Compound ID=5gBeGCbBjA2 SpectraBase Spectrum ID=AwIhJ1yCjnj https://spectrabase.com/spectrum/AwIhJ1yCjnj (accessed 2022-12-14).

261. Samant, A. N. & Dahotre, N. B. Laser Machining of Structural Ceramics-A Review. *J. Eur. Ceram. Soc.* **29**, 6, 969–993 (2009).

262. Cerezo, A. & Smith, G. D. W. Measurement of Temperature Rises in the Femtosecond Laser Pulsed Three-Dimensional Atom Probe. *Appl. Phys. Lett.* **88**, 154103 (2006).